Fundamentals of laser modelling

A dissertation submitted for the
degree of Doctor of Philosophy
at the University of Cambridge

Dominique David Marcenac
St. Catharine's College

December 1993

Fundamentals of laser modelling

Dominique David Marcenac

Summary

This dissertation presents a new "time domain model" to design and invent advanced laser diodes for optical fibre communications. It is securely based on quantum theory. This new model describes the optical fields in the time domain, allowing it to simulate large signal responses for Fabry-Perot and Distributed Feedback (DFB) lasers, in addition to calculating the laser linewidth and the Relative Intensity Noise (RIN). The quantum basis for this time domain model justifies the noise treatment of some other recent semiclassical laser models. However, it indicates that these models are incapable of simulating lasers with sub-Poissonian photon statistics (squeezing). The time domain model is implemented with new algorithm, which uses a transfer matrix method to simulate DFB lasers with much greater accuracy than previously.

New applications for two numerical methods are then introduced, providing tools to study the spectra of lasers simulated by the time domain model. Firstly, the Wigner distribution is shown to be the time-frequency representation, for modulated optical laser signals, which has the highest resolution. Secondly, the maximum entropy method of spectral estimation is shown to reduce noise and windowing effects, thus allowing small features in the spectra of simulated lasers to be displayed, without being obscured as with Fourier transform-based methods.

Comparisons of the time domain model are carried out. The first detailed comparison of simulated multimode DFB lasers, under large signal modulation, is performed: the time domain model and the Power Matrix Model show excellent agreement, increasing confidence in the validity of both these models. A comparison of the time domain model, with simulation results from the European COST laser workshop, further increases confidence in the accuracy of the algorithm. Finally, the first detailed simulation of self-pulsating DFB lasers is carried out. Its agreement with reported experimental results shows the potential and power of the present model.

The time domain model is then extended, using a novel formalism, to allow the simulation of intensity squeezed light: simulations for different laser structures are carried out. A new analytic formula for the RIN in Fabry-Perot lasers is derived. Predictions of the model are that low facet reflectivities and DFB structures make squeezing difficult, but that lasers with a Distributed Bragg reflector are promising.

Finally, a new concept of spectrometer, which uses computer interpretation of two-pinhole diffraction patterns, is demonstrated experimentally. It uses the maximum entropy method to resolve the spectrum of a two moded DFB laser, and is potentially a cheaper and more robust alternative to commercial spectrometers which use diffraction gratings.

Contents

Preface

Communications systems using optical fibres have already taken over as the main way to transfer information rapidly, with rates of Gigabits per second, and over long distances, with more than 100km between repeaters. The potential capacity of optical fibre communications is sufficient to satisfy increasing needs in the future, but the current systems must be improved to keep up with the growing demands for information transfer.

Semiconductor laser diodes are key components of optical fibre communication systems. They are the sources for the pulses of light which travel along the fibres to convey information, and are also used in the optical switches which redirect the signals. To provide the best performance, the structures of these lasers are increasingly complex. This has made it too expensive to design new lasers by directly fabricating and testing them. Simulation tools must be therefore be used to understand their operation, to help with their design, and in particular to calculate the quantum noise which often limits the performance of communication systems.

A number of models have been developed to simulate various aspects of laser diodes. Chapter 1 looks at some different approaches to modelling them, and concludes that laser models with an in-depth quantum mechanical treatment of noise, apply mostly to simple lasers with uniform structures, whereas potentially useful models for lasers with complex structures have not been based securely on quantum theory. There is therefore scope for a model capable of simulating complicated laser diodes, which at the same time provides a detailed quantum mechanical treatment of noise.

Chapters 2 and 3 describe the theory and implementation respectively, of a new time-domain model for laser diodes. Based on quantum mechanical theory, the model takes into account longitudinal variations of the photon and carrier densities, and changes in refractive index. This model can simulate large signal dynamics of semiconductor lasers with many modes, and at the same time calculate noise properties in agreement with accepted theories, for both Fabry-Perot and Distributed Feedback (DFB) laser structures. The quantum formalism presented justifies the noise treatment of some current semiclassical models, but indicates that these semiclassical models are incapable of simulating lasers with sub-shot noise intensity fluctuations.

In Chapter 4, new applications are suggested for two numerical tools. The first application concerns the Wigner distribution, which provides in quantum mechanics,

a simultaneous description of the position and momentum of a particle, and which has received much attention in signal processing as a representation of signals in both time and frequency. A new use of the Wigner distribution is suggested here: it provides the highest resolution time-dependent spectrum for modulated, simulated laser diodes. The second new application concerns the maximum entropy method of spectral estimation, which is ideally suited to displaying the spectra of lasers simulated using the time domain model: this method eliminates the windowing effect, and reduces the noise, which have obscured the spectra calculated until now using discrete Fourier transform methods.

In Chapter 5, the first detailed comparison of two different large signal models for multimoded DFB lasers, is carried out. The Time Domain Model, presented in Chapters 2 and 3, directly calculates the evolution of the optical fields in time, and it is compared with the Power Matrix Method, which describes the fields in the frequency domain. The programming and simulations using the Power Matrix Method were carried out by C. F. Tsang. The excellent agreement between these two very different programmes increases confidence in the simulations of both models.

In Chapter 6, two further comparisons are carried out. The static and noise calculations of the time-domain model are compared against the results of the COST European laser modelling exercise, further increasing confidence in the accuracy of the time domain algorithm. Next, the first detailed simulations of self-pulsating Distributed Feedback (DFB) lasers are carried out with the time domain model, and they are compared with some published experimental results. A mechanism for this type of self-pulsation is suggested. The good qualitative agreement obtained here underlines the potential usefulness of the model in researching complex behaviour of DFB lasers.

Chapter 7 suggests a new, if speculative, formalism which enables the time domain model to simulate light output with sub-Poissonian photon statistics (amplitude squeezed light), and therefore to simulate accurately relative intensity noise. Different laser structures are examined to find the one with the lowest intensity noise, and analytic expressions for intensity noise in Fabry-Perot lasers are derived. The predictions of the model are that intensity squeezing can be impossible to obtain in symmetric Fabry-Perot lasers with low facet reflectivities, or in symmetric Distributed Feedback lasers, but that lasers with Distributed Bragg Reflectors appear a promising source of squeezed light.

The experimental demonstration of a new type of spectrometer is presented in Chapter 8. It uses computer interpretation of optical interference patterns with the

maximum entropy method, and it can estimate the spectrum of a two moded DFB laser with a 2nm mode separation at a wavelength of 1.55μm. The resulting instrument is potentially a cheaper and more robust alternative to the monochromators commonly used in optoelectronics laboratories.

Declaration

The work described in this dissertation is believed to be original, except where acknowledgement to others is given, and no part of it is a result of work done in collaboration with anyone else, except for the comparison presented in Chapter 5, where C. F. Tsang carried out those simulations which used the Power Matrix laser model. The contents have not been submitted, in whole or in part, for any other University degree or diploma.

Acknowledgements

I would like to thank my supervisor, Prof. John Carroll, for his generous and expert help, advice and encouragement.

To Natascha, my fiancée, I am grateful for being such a delightful companion during the course of this Ph.D.

To my parents, I am grateful for their support and guidance throughout my education.

I would like to thank the Schiff foundation and S.E.R.C. for my financial support.

I am grateful to all the members of the optoelectronics group for their pleasant and interesting company, and to C. F. Tsang and L. M. Zhang for stimulating discussions.

Chapter 1

Laser diodes for communication systems

Optical fibres have now taken over as the main medium for long distance communications: several submarine optical fibre cables are in place below the Atlantic, Pacific and Indian oceans, and land based fibre links span the continents. The national telecommunications backbones of most industrialized countries use optical fibres to transmit information faster, and at a lower cost than would be possible using any other competing technology.

The demand for communication systems with greater capacities is strong, due to the increasing traffic generated by inter-computer links and Fax transmission. Newer services like video conferencing, tele-working and remote shopping are not yet widespread, but, coupled with new leisure services, their use is likely to increase, adding to the demand on the telecommunications networks.

The optical fibre cables already in place can potentially satisfy this demand for greater capacities. The bandwidth of communication systems is ultimately limited by the frequency of the carrier. Now the range of frequencies which can be transmitted with low losses down optical fibres, and amplified by the current Erbium-doped fibre amplifiers, is about a thousand times the frequency of the microwaves used by telecommunication satellites. However, in order to use this potential bandwidth, technological improvements are necessary: firstly, the sources which send light down the fibres need to be improved, and secondly, all-optical switching systems, which do not rely on slower electronics, have to be constructed. Laser diodes are key components of these sources and switching systems, and they need to be improved.

The laser diodes used in communication systems have increasingly complex structures, and intricate aspects of their behaviour are being exploited to improve their

performance. To understand the behaviour of these laser diodes and to facilitate their design, computer models are very useful. As computing power becomes cheaper and more abundant, these computer models can be more sophisticated and powerful: this dissertation presents new powerful simulation tools for laser diodes, based on quantum mechanical physical theories.

1.1 The need for modelling tools

Reliable laser diodes with high performances are needed, and the structures of the lasers have gradually become more and more complicated.

Material improvements have been instrumental in determining progress: the use of quantum wells to confine the carrier, later followed by strained quantum wells, has permitted large improvements in some of the relevant material parameters, such as the differential gain and the linewidth enhancement factor. These material improvements have resulted in lower threshold currents, higher efficiencies, and have promised higher modulation bandwidths for laser diodes.

Improved designs for the laser structure have also been important: the initial Fabry-Perot lasers, which suffered from multimode operation, have now largely given way for distributed feedback (DFB) lasers for the long haul communications. The first DFB lasers, which had uniform gratings, lased in two degenerate modes, provided the carrier density is uniform and incontrolable facet reflections are reduced by anti-reflective coatings. To ensure single mode operation, new laser structures were designed: first, the $\lambda/4$ phase shifted DFB, which lases in one mode only up to high powers, and then structures with multiple phase-shifts which provide a more controllable single mode operation at higher powers.

Structures with Fabry-Perot and grating sections, and multiple section structures driven by separate current sources may also find applications were they are superior to single contact, more simple devices. Present commercial research is also considering laser devices with integrated external modulators.

The effort towards developing improved optical sources for optical communications is thus considering complex structures, as well as improved materials. The aim of these complex structures is to improve the parameters of the laser sources which are relevant to the applications concerned. The laser structures have a profound influence on the characteristics of the laser, giving rise for example to linewidth rebroadening in DFB lasers as the optical power is increased. The complexity of these structures makes predicting their characteristics almost impossible to a designer

without extensive experience, and mere guesswork to even the most experienced engineer, without detailed computer models.

Furthermore, powerful, fast and accurate computer models, rather than just tools used to evaluate operation characteristics for preconceived designs, can be used as very low cost "experiments", which can be performed to give the design engineer a feel for the operation of the laser sources. As well as an aid to optimizing precise design parameters, the simulation program can become a computer aided invention tool, which may stimulate the designer to have new ideas, and which then lets the designer try out these ideas.

1.2 Specifications for laser models

Computer models of laser diodes are potentially very useful, or even indispensable to the design engineer. They should be fast, so that ideas may be checked quickly. They should be easy to use, so that the energy of the designer is expended on productive tasks rather than learning how to operate the tools, or typing obscure commands which demand concentration and time, and cause frustration. They should present the essential results in a form which can be understood easily. Above all else, they should be powerful, realistic and correct.

A powerful program enables a wide range of designs to be simulated, and most of the relevant laser characteristics to be calculated.

To be realistic, a computer program must take into account the major factors which influence the operation of a laser. This is essential if the program is to be used as a design tool to find the best parameters before fabrication. The sensitivity of the design to the inevitable external influences to which a real laser is exposed to can then be evaluated.

The most important aspect of a computer model is that it should be correct. The only way to verify this is ultimately to check all of the predictions of the model against carefully designed experiments. This cannot be done, due to the considerations of cost, time, and possibly unavailable technology. Checking of the predictions against a limited set of experimental results is nevertheless indispensable. Agreement with other computer models is not a gage of correctness. If different models based on a similar set of assumptions predict identical results, however, the agreement minimizes the likelihood of implementation errors as well as the use of inaccurate algorithms.

Aside from a comparison between predicted and experimental results, a careful

inspection of the assumptions made in formulating the model is necessary. It is important to base the model on accepted physical theories, which have been tested individually against experiment. The assumptions behind the model are generally of two kinds: the first is the agreement with fundamental physical theories, which are consistent with one another. The second kind is the use of numerical parameters derived from experiment, which due to the complexity of the phenomena involved cannot be derived by calculation from a set of fundamental physical laws. In both cases, the assumptions made must be based on accepted physical laws, whether obtained from experimental measurements or derived from a set of fundamental concepts.

1.3 Laser models

A wide range of models, with varying degrees of complexity and performance, have been used to simulate laser diodes and to explain their behaviour.

1.3.1 The laser rate equations

The most well known of these are the laser rate equations developed by Statz and deMars [1], which relate the number of photons P inside the laser cavity and the number of excited carriers N responsible for the optical gain:

$$\frac{d}{dt}P = g(N - N_0)P - P/\tau_P + \beta N/\tau_N, \tag{1.1}$$

$$\frac{d}{dt}N = I/q - N/\tau_N - g(N - N_0)P. \tag{1.2}$$

Here N_0 is the transparency carrier number, g is the gain constant, τ_P is the photon lifetime for the cavity mode, I is the drive current, q is the charge of the electron, τ_N is the lifetime of the excited electrons, and β is the spontaneous emission coupling factor. These equations have been used extensively for the analysis of transients in laser diodes. With the addition of various terms such as nonlinear gain (by making $g \rightarrow g/(1 + \epsilon P)$ to model carrier diffusion effects and gain compression due to spectral hole burning [2]), an extra equation for the phase of the optical mode [3], another carrier density term to account for carrier transport effects [4], the rate equations can explain a considerable range of the behaviour of laser diodes.

1.3.2 Quantum approaches to simulating laser noise

The laser rate equations above do not give us any information concerning the statistical properties of the emitted light. Quantum noise, being the main source of noise in laser diodes, is important: not only does it determine the laser linewidth and intensity fluctuations, but it also affects the transient behaviour also, by causing timing jitter for example. Inclusion of noise in the laser rate equations was performed by Shimoda *et al* [5, 6] by only allowing the carrier and photon numbers N and P to take on integer values, and thus obtained information concerning photon number distributions. After this pioneering work, three main theoretical approaches to laser noise were developed:

- The density matrix approach of Scully and Lamb [7].
- The quantum Langevin approach [7].
- The Fokker-Planck or Langevin approach using distribution functions [8–10].

Though not specifically developed for semiconductor lasers, these approaches are sufficiently general to have been adapted and used for laser diodes. Figure 1 summarizes these approaches. All three consider quantized optical fields, in order to discuss all aspects of the light statistics. They start from 'first principles' by considering a Hamiltonian which describes the interaction of the optical field with the atoms or carriers. Optical fields and carrier populations are described by quantum mechanical operators. Quantum expectation values of these operators describe the statistics of the emitted light, and equations of motion for these operators are obtained from the Hamiltonian. Reservoir theory [7, 10, 11] deals with the losses and damping in a statistical fashion: reservoirs are systems with many degrees of freedom, and appear to be the most successful way to include losses in quantum theory [12]. All three approaches agree for high photon numbers, as is the case in lasers.

The Fokker-Planck (or classical Langevin approach) and the quantum Langevin approach have been the most popular with laser diodes, as they are more suited to computation. In the Fokker-Planck models, the quantum operators, or the density operator which describes the quantum state, are expressed in terms of distributions of classical variables. The distribution changes in time following a Fokker-Plank equation, but the equivalent classical Langevin formulation can be used to obtain the distribution function by stochastic simulations which are more easily solved using a computer.

In the quantum Langevin approach, equations of motion for the operators describing the field and carriers are obtained which include operator "noise" sources with prescribed expectation values. In certain cases, these equations of motion for operators can be transformed into stochastic equations of motion for classical quantities like the photon and carrier numbers, by taking expectation values [7, 13].

From the Distribution function or the quantum Langevin approaches, equations of motion with stochastic noise sources are obtained for classical numbers describing the carriers and optical field. Because of their simplicity, they have been used extensively to analyse the noise properties of laser diodes [13–15].

These models, derived from the quantum theory of lasers with high Q-factors, rely on parameters like the photon lifetime for the cavity, which are not known for the more complex DFB structures, and indeed vary with the carrier concentration. The structure of the cavity is not explicitly taken into account, and correction factors must be used to calculate noise properties accurately [16, 17]. This limits their usefulness for simulating realistic laser diodes.

1.3.3 Travelling wave models for complex laser structures

With the increasing importance of laser diode sources with complicated DFB or DBR sources, it has become necessary to take into account explicitly at least the longitudinal structure of the laser. A number of models were therefore developed, which consider the propagation of the optical fields along the laser cavity [18–23]. Concerning the noise properties, these models were for the most part based on the semiclassical Langevin sources obtained from the distribution function approach.

One result of this evolution is that the concepts used by some current sophisticated laser models are removed from those originally used in the quantum mechanical theories from which their treatment of noise is derived. It is therefore difficult to determine exactly how far these newer models agree with the quantum theory they derive from. Some work is required to point out the extent of the validity of these newer models. These could then be extended to simulate characteristics of light not previously considered, such as amplitude squeezed light which cannot be described semiclassically.

To remedy this situation, where the old quantum laser models cannot simulate realistic laser diodes, and where the treatment of noise in the newer semiclassical models is uncertain, a new laser model is presented in this dissertation. It provides a quantum mechanical treatment of noise, thus agreeing with the older models, while taking into account the laser structure and the presence of more than one laser

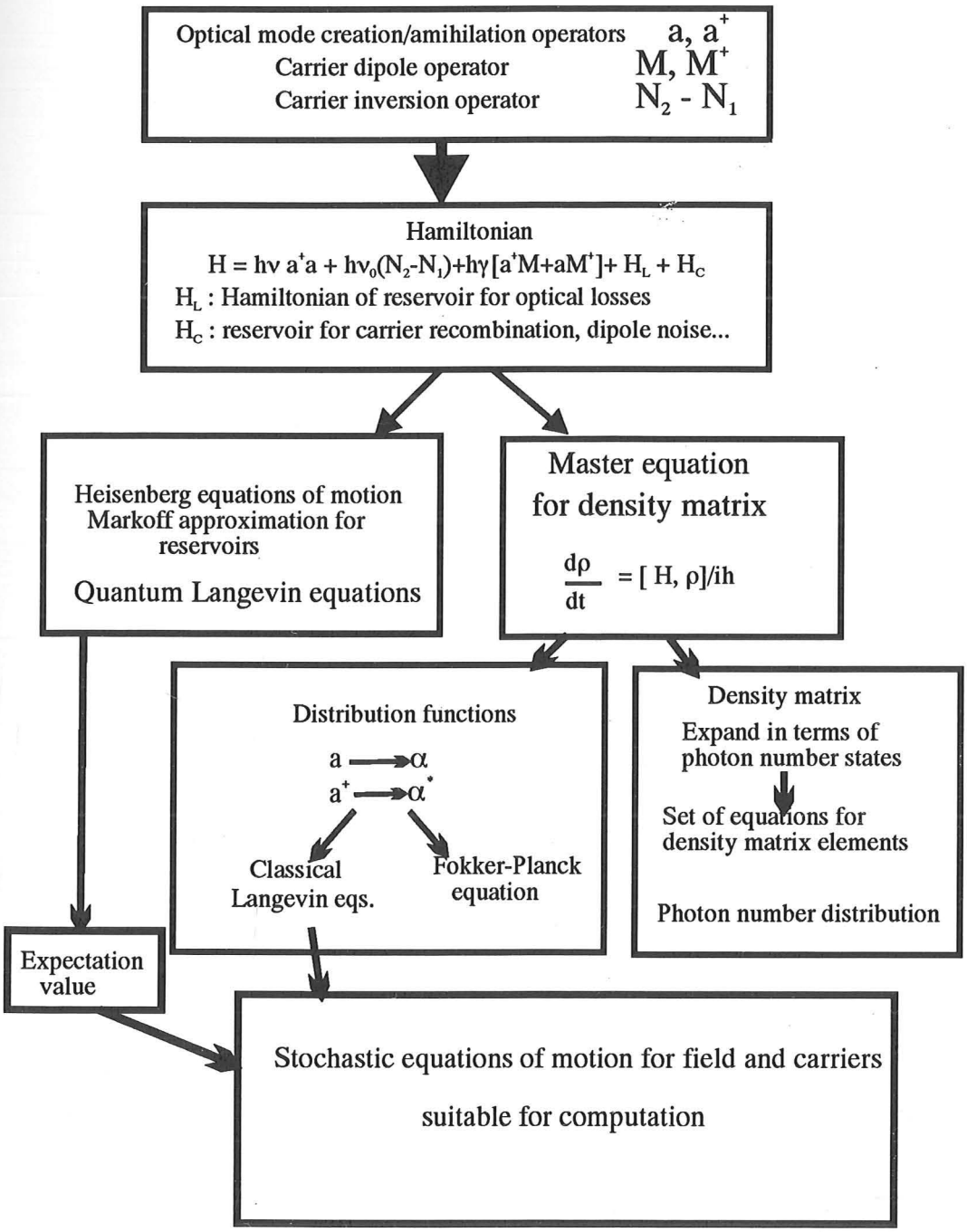

Figure 1-1: Quantum approaches to modelling noise in lasers

mode. In addition, the time domain algorithm used to implement the model allows simulations of laser diodes under large signal modulation.

Chapter 2

Quantum basis of the laser model

This chapter presents the theory for a new quantum mechanical travelling wave, time domain model for DFB and Fabry-Perot laser diodes.

This is the route followed in this chapter:

1.) The propagating optical fields are quantized.

2.) Simple models for quantum amplification and attenuation are introduced, to be used in the laser model.

3.) The operators describing the carriers and the field are replaced by classical variables (Glauber function for the field), and the noise sources required by this replacement are given.

The implementation of this theory into a time-domain model for Fabry-Perot lasers and lasers with Bragg gratings will be presented in chapter 3.

The resulting large signal model will take into account longitudinal spatial hole burning, multimoded behaviour, and will provide a quantum treatment of linewidth and intensity noise.

2.1 Introduction

Noise is important in determining the performance of optical communication and sensor systems: for example, intensity noise limits the signal-to-noise ratio for analogue transmission, and narrow laser linewidths are required by coherent communication systems. Since the main source of noise in laser diodes is quantum noise, a better understanding of it can only come from quantum theory. This motivates the development of the quantum laser model presented in this chapter.

The quantum theory of the laser has been explored in detail in the 1960's and 1970's [7, 9, 10, 24], and general noise properties of laser light have been pointed out. This early work, however, was relevant mainly to lasers with high Q-factor resonators, and in some cases only applicable to class A lasers (e.g. Ar^+ gas lasers where the field decay rate is much slower than either the population or the dipole moment decay rates).

For laser diodes, this early quantum theory requires a number of correction factors (e.g. linewidth enhancement factor [25], excess spontaneous emission factors [16, 17, 26–30]) to simulate the experimentally observed results.

However, with the increasingly complex laser diodes for communications, which use Bragg gratings and can be made of different sections performing different tasks, the early quantum theory can no longer be directly applied. Recent semiclassical models for laser diodes have therefore been developed which take better into account the laser diode structure, [21, 23, 31, 32], and which are of great use in researching and developing new lasers for optical fibre communications. These semiclassical models have distanced themselves from the quantum theory which governs the lasing processes. As a result, in some models (e.g. [21, 31]) the emphasis is more on calculating the more "classical" properties of the light, such as power and frequency variations during modulation, or the shape of the optical spectrum as determined by the cavity structure; the noise properties of the fields are not taken into account in depth. Others of these models like CLADISS [23] feature a thorough noise analysis, shown by the work in this dissertation to be essentially correct, but are limited to D.C. or small signal simulations. In addition they cannot simulate noise for non-classical states of the fields, like amplitude squeezed light [33], because of their semiclassical background.

Therefore, a model which can simulate the large signal behaviour of lasers with complex structures, together with a quantum treatment of field noise would constitute a powerful and desirable tool: the model presented in this chapter can do this. Because of the field representation used, it cannot simulate intensity squeezed light, but is the grounding for the extension in chapter 7, which can.

2.2 Representation of the optical Field

A typical laser diode used for optical communications is shown schematically in Figure (2-1).

The active region layer (dashed) is composed of material with a narrower bandgap

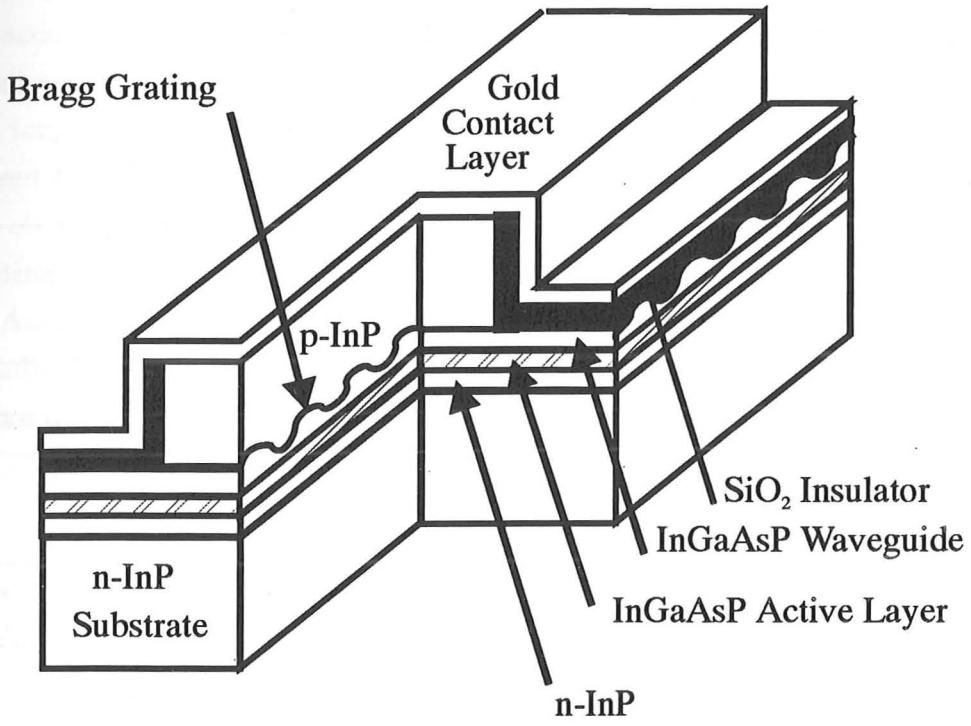

Figure 2-1: Structure of a Ridge waveguide InP DFB laser diode.

than the surrounding p and n doped layers. This heterojunction confines the electrons and the holes within the active layer, and thus achieves higher carrier concentrations leading to higher optical gain.

The active region with a narrower bandgap also has a higher refractive index than the surrounding layers. Above the active region, the refractive index is higher inside the ridge: a dielectric waveguide is formed which confines the optical energy close to the confinement region for the carriers.

A Bragg grating is etched into the waveguide layer and couples the forward and reverse longitudinally propagating optical fields. This provides the optical feedback necessary for lasing. Because this feedback is frequency dependent, the grating can also ensure single longitudinal mode selection.

2.2.1 Transverse modes

Index guided laser structures are currently preferred over gain guided structures as they provide better control of the optical field. The waveguide is generally designed so that only the fundamental mode for each polarization is supported, by making the transverse waveguide dimensions sufficiently small. Because the confinement

factor, the facet reflectivities [34], and the optical gain in quantum well material differ according to polarization, only one polarization is generally excited. The full three-dimensional optical field can then be described completely by a scalar function of the longitudinal coordinate z only. This section describes the variables used to represent the optical field.

To obtain a good picture of the fields inside the laser, consider first the waveguide neglecting material gain, scattering losses, and refractive index changes due to carriers. Assuming a harmonic time variation with frequency $\omega = ck$, and a harmonic longitudinal spatial variation $\mathbf{E}(x, y, z) = \exp(i\beta z)\mathbf{E}(x, y)$, the electric field satisfies the time-independent wave equation:

$$\nabla_T^2 \mathbf{E} + (\epsilon k^2 - \beta^2)\mathbf{E} = 0, \tag{2.1}$$

together with the usual boundary conditions at the material interfaces and at infinity [35]. The propagation constant β and the mode profile $\mathbf{E}(x, y)$ can often be determined roughly and simply, as a function of k using the effective index approximation ([36], chap. 2).

Once the transverse mode profiles have been calculated for a lossless waveguide, the effect of gain in the active region is included as a perturbation [36]. The resulting gain for the waveguide mode is the gain in the active region, multiplied by the confinement factor Γ which describes the overlap of the optical field and the carrier density confined by the heterojunction or a quantum well structure, as depicted in Fig. (2-2).

Considering one polarization only along the unit vector $\hat{e}$, the electric fields can be written:

$$\mathbf{E}(x, y, z, t) = \hat{e}S(x, y) \int \Big\{ F'(\omega) \exp(i\beta z - i\omega t) + R'(\omega) \exp(-i\beta z - i\omega t) \Big\} d\omega, \tag{2.2}$$

where $F'(\omega)$ and $R'(\omega)$ are for propagation in the the $+z$ and $-z$ directions. The dispersion curve relating β to ω depends on the waveguide structure, and also on the material dispersion. Because of the short dimensions of laser diodes, group velocity dispersion can be neglected, and around the operating frequency ω_0, the propagation constant β can be determined by the group and the phase velocities v_g and v_p, as depicted in Figure (2-3), by:

$$\beta = \omega_0 / v_p + (\omega - \omega_0)/v_g \tag{2.3}$$

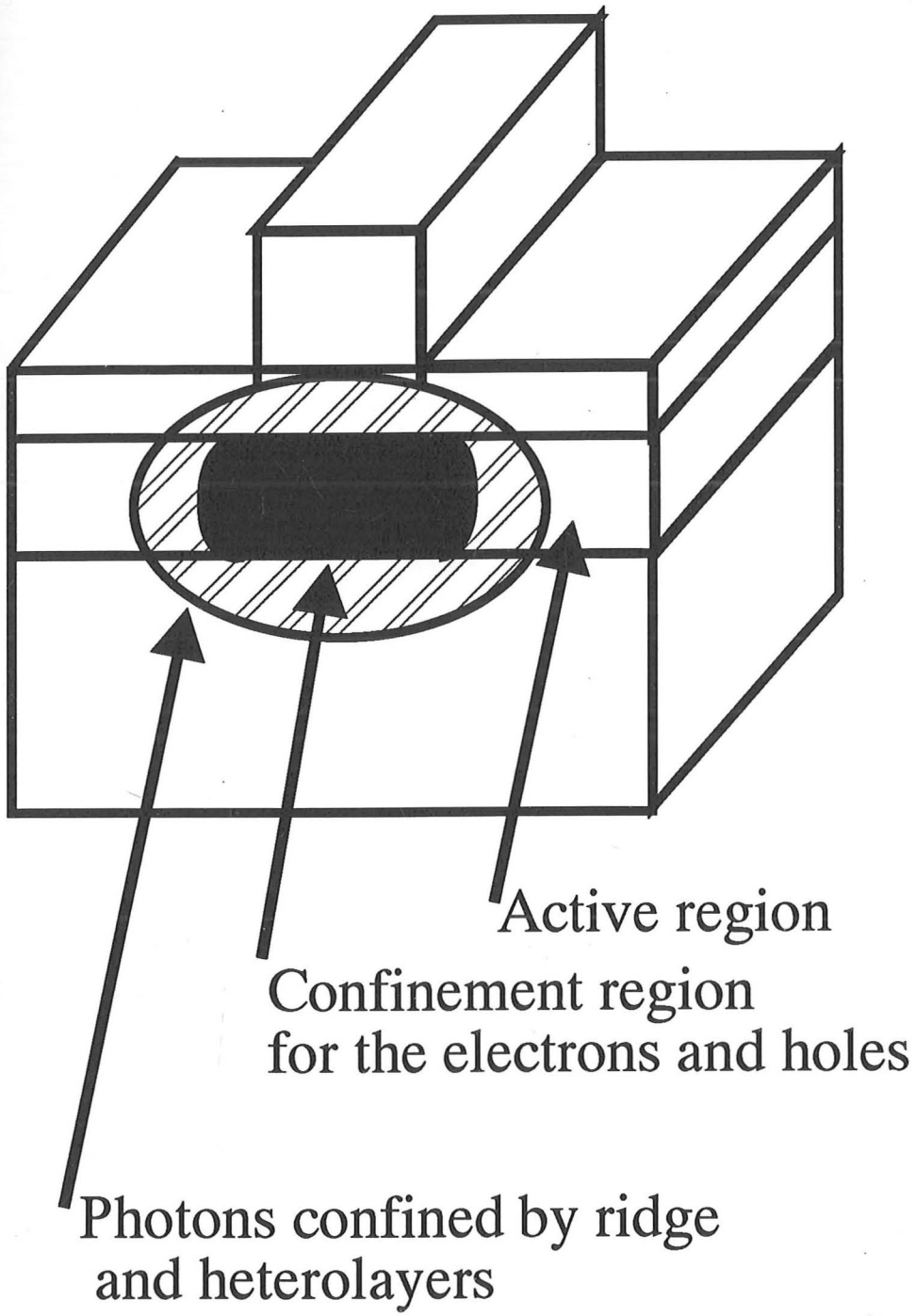

Figure 2-2: Overlap of the photon density and the carriers in the active region which determines the waveguide gain through the confinement factor Γ.

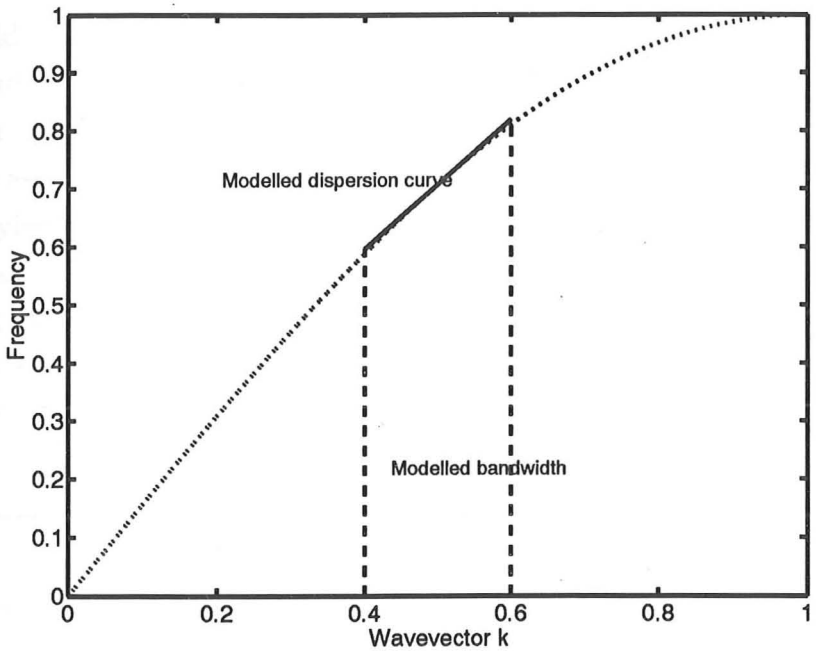

Figure 2-3: Modelled dispersion curve, with a constant group velocity to approximate the real laser dispersion curve.

The transverse mode profile $S(x, y)$ is normalised to make the forward and reverse wave magnitudes $|F'(\omega)|^2$ and $|R'(\omega)|^2$ equal to the spectral energy density of the optical fields.

2.2.2 Forward and reverse wave operators

In a semiconductor laser, effectively scalar, one dimensional forward and reverse propagating optical fields are subject to gain, loss, and material and waveguide dispersion; effects which should be taken into account. It is easier, for computation, to separate these effects rather than use a general quantum theory where they are all included together [37].

The model therefore considers a material, which instead of being treated as a continuum, has gain, loss and reflections which are all concentrated at a number of discrete points along laser cavity. Sections of material lie between these points where the optical propagation is lossless and has a constant group velocity. These sections are referred to as *free* sections. It is easier to quantize the propagating fields in these free sections.

In order to quantize the fields, however, dispersion must still be dealt with. This is because in a medium with dispersion, the material polarization depends on the electric field values at previous times. The dynamic field equations are then non-local in time, and this non-locality prevents quantization [38] when only the field degrees of freedom are considered. As discussed in the previous section, a constant group velocity is assumed for the waveguide. This assumption together with a change of variables, yields equations of motion which are local in time and *can* be quantized. The expressions obtained for the quantized electric and magnetic fields agree with other work on quantum fields with dispersion [38, 39].

Within the free sections, the quantized optical fields thus obtained are characterized by forward and reverse wave operators. Fourier transformation into the frequency domain then leads to new destruction/creation field operators, whose commutation rules are sculpted by the cavity structure, and which enable us to use frequency domain techniques to analyze optical systems.

Next, straightforward quantum models for the processes of reflection and amplification of the travelling waves which occur between adjacent "free" sections, will be presented. By linking the fields in neighbouring sections, these processes allow for spatial variations in all the significant laser properties along the length of the laser. But first, in this section, the propagating optical fields are quantized. This is the first step in deriving the field description used by the model. The usual (canonical) method of quantization is used here: once the classical equations of motion are derived, it involves first describing the dynamic properties of the system by a Hamiltonian. The Hamiltonian formalism is the "gateway" between classical and quantum descriptions of a system, and the classical dynamic variables of the Hamiltonian formalism can be converted directly into the new quantum operators.

As discussed in the previous section, the fields inside the laser are

$$\mathbf{E}(x,y,z,t) = \hat{e}S(x,y)\int \big(F'(\omega)\exp(i\beta z - i\omega t) + R'(\omega)\exp(-i\beta z - i\omega t)\big)d\omega, \quad (2.4)$$

Including the phase factors $\exp(\pm i\beta z)$ with F' and R' to redefine

$$\mathbf{E}(x,y,z,t) = \hat{e}S(x,y)\int \exp(-i\omega t)\big(F'(\omega,z) + R'(\omega,z)\big)d\omega. \quad (2.5)$$

F' and R' now obey the equations of motion

$$\frac{i\omega}{v_p(\omega)}F'(\omega,z) = -\frac{\partial F'}{\partial z}, \quad (2.6)$$

$$\frac{i\omega}{v_p(\omega)}R'(\omega,z) = \frac{\partial R'}{\partial z}. \tag{2.7}$$

The phase velocity $v_p(\omega) = c/n(\omega)$ changes with ω to keep the group velocity $v_g = c/n_g$ constant, within a bandwidth centered on the frequency ω_0. The phase velocity at the frequency ω_0 is defined to be n_p, so that

$$n(\omega) = n_g + (n_p - n_g)\frac{\omega_o}{\omega}. \tag{2.8}$$

Through the unitary transformation:

$$F(\omega,z) = F'(\omega,z)\exp(i\Delta kz), \tag{2.9}$$
$$R(\omega,z) = R'(\omega,z)\exp(-i\Delta kz). \tag{2.10}$$

where $\Delta k = \omega_o(n_p - n_g)/c$, using the constant group velocity property Eq.(2.8), "dispersion-less" equations of motion (see Appendix A) are found:

$$\frac{\partial F}{\partial t} = -v_g\frac{\partial F}{\partial z} \quad \text{and} \quad \frac{\partial R}{\partial t} = v_g\frac{\partial R}{\partial z}. \tag{2.11}$$

Define new "slowly varying" field operators $E(z,t)$ and $B(z,t)$, in analogy with the electric and magnetic fields $\mathbf{E}(z,t)$ and $\mathbf{B}(z,t)$, by

$$E(z,t) = \frac{1}{\sqrt{2\epsilon_g}}\Big(F(z,t) + R(z,t)\Big), \tag{2.12}$$
$$B(z,t) = \frac{1}{v_g\sqrt{2\epsilon_g}}\Big(F(z,t) - R(z,t)\Big). \tag{2.13}$$

The equations of motion for these variables are similar to those in a medium without dispersion:

$$\epsilon_g\frac{\partial E}{\partial t} = -\frac{1}{\mu_o}\frac{\partial B}{\partial z}, \tag{2.14}$$
$$\frac{\partial B}{\partial t} = -\frac{\partial E}{\partial z}. \tag{2.15}$$

These field equations are quantized in the usual way [40]: first, a "vector" potential $A(z)$ is defined by:

$$E = -\frac{\partial A}{\partial t} \quad \text{and} \quad B = \frac{\partial A}{\partial z}. \tag{2.16}$$

This ensures that Eq.(2.15) is always satisfied, while Eq.(2.14) becomes the wave

equation:

$$\frac{\partial^2 A}{\partial t^2} = \frac{1}{\epsilon_g \mu_o} \frac{\partial^2 A}{\partial z^2}. \tag{2.17}$$

Following Abram *et al* [41], we use the field Lagrangian density

$$\mathcal{L}(z) = \frac{\epsilon_g}{2} \left(\frac{\partial A}{\partial t} \right)^2 - \frac{1}{2\mu_o} \left(\frac{\partial A}{\partial z} \right)^2. \tag{2.18}$$

The conjugate momentum to $A(z)$ is found to be

$$\Pi(z) = \frac{\partial \mathcal{L}}{\partial(\partial A/\partial t)} = \epsilon_g \frac{\partial A(z)}{\partial t} = -\epsilon_g E(z). \tag{2.19}$$

The unitary transformations (2.9,2.10) ensure (Appendix A) that the Hamiltonian density remains the correct energy density for the medium:

$$\begin{aligned} \mathcal{H}(z) &= \frac{1}{2\epsilon_g} \Pi(z)^2 + \frac{1}{2\mu_o} \left(\frac{\partial A}{\partial z} \right)^2 \\ &= \frac{1}{2} \left(\epsilon_g E(z)^2 + B(z)^2/\mu_o \right). \end{aligned} \tag{2.20}$$

Quantization is achieved by transforming the field variables $A(z)$ and $\Pi(z)$ into operators and imposing the equal time commutation rule

$$[A(z,t), \Pi(z',t)] = i\hbar \delta(z - z'). \tag{2.21}$$

From this, the commutator for the E and B fields is obtained:

$$[E(z',t), B(z,t)] = \frac{1}{\epsilon_g} [\frac{\partial}{\partial z} A(z,t), \Pi(z',t)] = \frac{i\hbar}{\epsilon_g} \frac{\partial}{\partial z} \delta(z - z'). \tag{2.22}$$

The forward and reverse wave operators are, from Eqs.(2.12,2.13), given by

$$F(z,t) = \sqrt{\frac{\epsilon_g}{2}} \Big(E(z,t) + v_g B(z,t) \Big), \tag{2.23}$$

$$R(z,t) = \sqrt{\frac{\epsilon_g}{2}} \Big(E(z,t) - v_g B(z,t) \Big). \tag{2.24}$$

The slightly unusual commutation rules for these operators are found to be:

$$[F(z,t), F(z',t)] = \frac{v_g \epsilon_g}{2} \Big([E(z,t), B(z',t)] + [B(z,t), E(z',t)] \Big)$$

$$= \frac{i\hbar v_g}{2}\left(\frac{\partial}{\partial z'}\delta(z'-z) - \frac{\partial}{\partial z}\delta(z-z')\right)$$
$$= i\hbar v_g \frac{\partial}{\partial z'}\delta(z'-z). \tag{2.25}$$

Similarly,

$$[R(z,t), R(z',t)] = -i\hbar v_g \frac{\partial}{\partial z'}\delta(z'-z) \tag{2.26}$$
$$[F(z,t), R(z',t)] = 0. \tag{2.27}$$

Using the field Hamiltonian density Eq.(2.150), the following equations of motion for the forward and reverse operators are derived

$$\begin{aligned}\frac{\partial F(z,t)}{\partial t} &= \frac{1}{i\hbar}[F(z,t), H(t)] \\ &= \frac{1}{i\hbar}\int dz' \,[F(z,t), F(z',t)^2]/2 \\ &= -v_g \frac{\partial F(z,t)}{\partial z},\end{aligned} \tag{2.28}$$

where the integral has to cover only the points around $z = z'$, and similarly

$$\frac{\partial R(z,t)}{\partial t} = v_g \frac{\partial R(z,t)}{\partial z}. \tag{2.29}$$

These equations signify that $F(z,t)$ and $R(z,t)$ propagate without distortion at the velocity v_g.

2.2.3 Time and frequency operators

The forward and reverse wave operators $F(z,t)$ and $R(z,t)$, valid only for free sections, are characterized by their equal time commutators Eqs.(2.25,2.26) provided that

$$z_1 < z < z_2, \tag{2.30}$$

where z_1 and z_2 are the end points of a free section. The forward and reverse wave operators propagate, from Eqs.(2.28, 2.29), according to

$$R(z,t) = R(z + v_g t, 0) \quad \text{and} \quad F(z,t) = F(z - v_g t, 0). \tag{2.31}$$

Through a change of variables, we may then derive the equal space, different time commutators

$$[F(z,t),F(z,t')] = -\frac{i\hbar}{v_g}\frac{\partial}{\partial t'}\delta(t'-t), \tag{2.32}$$

$$[R(z,t),R(z,t')] = -\frac{i\hbar}{v_g}\frac{\partial}{\partial t'}\delta(t'-t). \tag{2.33}$$

The spatial restriction (2.30) implies that these equal space, different time commutators will be valid only for $|t-t'| \leq (z_2-z_1)/v_g$. When the time difference between t and t' is greater than $(z_2-z_1)/v_g$, reflections may prevent commutation.

The equal space, different time commutators are used to obtain the commutation rules for the frequency domain operators defined below:

$$a_f(\omega) = -i\sqrt{\frac{v_g}{2\pi\hbar\omega}}\int_{-\infty}^{+\infty} dt\; F(z,t)\exp[i\omega(t-z/v_g)], \tag{2.34}$$

$$a_f^\dagger(\omega) = i\sqrt{\frac{v_g}{2\pi\hbar\omega}}\int_{-\infty}^{+\infty} dt\; F(z,t)\exp[-i\omega(t-z/v_g)], \tag{2.35}$$

$$a_r(\omega) = -i\sqrt{\frac{v_g}{2\pi\hbar\omega}}\int_{-\infty}^{+\infty} dt\; R(z,t)\exp[i\omega(t+z/v_g)], \tag{2.36}$$

$$a_r^\dagger(\omega) = i\sqrt{\frac{v_g}{2\pi\hbar\omega}}\int_{-\infty}^{+\infty} dt\; R(z,t)\exp[-i\omega(t+z/v_g)], \tag{2.37}$$

where $\omega \geq 0$.

The coefficients above are chosen to give commutation rules for the operators $a(\omega)$ and $a^\dagger(\omega)$ which correspond to those commonly used [39]. Indeed, for waves which propagate freely over an infinite distance — so that Eqs.(2.32,2.33) are valid for all times — these are seen to be

$$\begin{aligned}[a_f(\omega),a_f^\dagger(\omega')] &= \frac{v_g}{2\pi\hbar\sqrt{\omega\omega'}}\int_{-\infty}^{+\infty} dt \int_{-\infty}^{+\infty} dt'\; [F(z,t),F(z,t')]\exp(i\omega t - i\omega' t') \\ &= \frac{-i\hbar}{2\pi\hbar\sqrt{\omega\omega'}}\int_{-\infty}^{+\infty} dt \int_{-\infty}^{+\infty} dt'\; \frac{\partial}{\partial t'}\{\delta(t-t')\}\;\exp(i\omega t - i\omega' t')) \\ &= \delta(\omega-\omega'),\end{aligned} \tag{2.38}$$

and $[a_r(\omega),a_r^\dagger(\omega')] = \delta(\omega-\omega')$. The inverse relationships for the Fourier transform operators are

$$F(z,t) = \int_0^\infty d\omega\; i\sqrt{\frac{\hbar\omega}{2\pi v_g}}\left(a_f(\omega)e^{-i\omega(t-z/v_g)} - a_f^\dagger(\omega)e^{i\omega(t-z/v_g)}\right), \tag{2.39}$$

and

$$R(z,t) = \int_0^\infty d\omega\, i\sqrt{\frac{\hbar\omega}{2\pi v_g}}\left(a_r(\omega)e^{-i\omega(t+z/v_g)} - a_r^\dagger(\omega)e^{i\omega(t+z/v_g)}\right). \tag{2.40}$$

Using the transformation Eqs.(2.139,2.140), together with Eqs.(2.135,2.136) in the appendix, "equivalent" electric and magnetic fields $\mathbf{E}(z,t)$ and $\mathbf{B}(z,t)$ for 1-D propagation can be expressed as

$$\mathbf{E}(z,t) = \int_0^\infty d\omega\, i\sqrt{\frac{\hbar\omega}{4\pi c\epsilon_o n(\omega)}}\left(a_f(\omega)e^{-i\omega(t-z/v_p(\omega))} + a_r(\omega)e^{-i\omega(t+z/v_p(\omega))}\right) + \text{Herm. conj.}, \tag{2.41}$$

$$\mathbf{B}(z,t) = \int_0^\infty d\omega\, i\sqrt{\frac{\hbar\omega n(\omega)}{4\pi c^3\epsilon_o}}\left(a_f(\omega)e^{-i\omega(t-z/v_p(\omega))} - a_r(\omega)e^{-i\omega(t+z/v_p(\omega))}\right) + \text{Herm. conj.}. \tag{2.42}$$

These expressions are similar to the expressions used by Blow *et al* [39], and also agree with the expressions derived by Hüttner *et al* [38] who use a canonical quantization where the dielectric matter is explicitly included.

The energy flux in the material is given by the Poynting vector (Eq.(2.146) in Appendix A):

$$\mathbf{S}(z,t) = \frac{1}{\mu_o}\mathbf{E}(z,t)\mathbf{B}(z,t) \tag{2.43}$$

$$= \frac{v_g}{2}\int_{-\infty}^{\infty}\frac{d\omega}{2\pi}\int_{-\infty}^{\infty}\frac{d\omega'}{2\pi}\sqrt{\frac{v_p(\omega)}{v_p(\omega')}}\Big(F'(\omega,z)F'(\omega',z) - R'(\omega,z)R'(\omega',z)$$

$$+ F'(\omega,z)R'(\omega',z) - F'(\omega',z)R'(\omega,z)\Big)\exp\left(i(\omega+\omega')t\right). \tag{2.44}$$

We define in a similar way the transformed energy flux $S(z,t)$:

$$S(z,t) = \frac{1}{\mu_o}E(z,t)B(z,t)$$

$$= \frac{v_g}{2}\int_{-\infty}^{\infty}\frac{d\omega}{2\pi}\int_{-\infty}^{\infty}\frac{d\omega'}{2\pi}\Big(F(\omega,z)F(\omega',z) - R(\omega,z)R(\omega',z)\Big)$$

$$\times \exp\left(i(\omega+\omega')t\right)$$

$$= \frac{v_g}{2}\Big(F(z,t)^2 - R(z,t)^2\Big). \tag{2.45}$$

These two fluxes are equal up to second order in $\omega - \omega_o$.

The travelling wave operators $F(z)$ and $R(z)$ can be written as the sum of positive frequency, destruction operators $F^+(z)$ and $R^+(z)$ and their Hermitian conjugates, the negative frequency creation operators $F^-(z)$ and $R^-(z)$, where

$$F^+(z,t) = \int_0^{+\infty} d\omega \left\{ i\sqrt{\frac{\hbar\omega}{2\pi v_g}} a_f(\omega) e^{-i\omega(t-z/v_g)} \right\}, \tag{2.46}$$

$$R^+(z,t) = \int_0^{+\infty} d\omega \left\{ i\sqrt{\frac{\hbar\omega}{2\pi v_g}} a_r(\omega) e^{-i\omega(t+z/v_g)} \right\}, \tag{2.47}$$

and similarly for $F^-(z,t)$ and $R^-(z,t)$. The positive and negative frequency operators can express the normally ordered field operators which are convenient for describing most experiments [42]. In particular, the normally ordered power fluxes S^+ and S^- in the $+z$ and $-z$ directions are written as

$$S^+(z,t) = v_g F^-(z,t) F^+(z,t), \tag{2.48}$$

$$S^-(z,t) = v_g R^-(z,t) R^+(z,t). \tag{2.49}$$

A harmonic oscillator of frequency ω, described by the destruction and creation operators a and $a^\dagger$, still possesses, in the ground state, a zero point energy $\hbar\omega/2$, which results from the commutation relation $aa^\dagger - a^\dagger a = 1$. The symmetrically ordered energy operator, $H = \hbar\omega(aa^\dagger + a^\dagger a)/2$, includes this ground state energy, which cannot be extracted from the system. The photon number operator, $n = a^\dagger a$ is normally ordered, with destruction operators to the right of creation operators, and consequently does not include the ground state energy. In the same way, every mode of the electromagnetic field possesses a ground state energy, which is included in the symmetrically ordered flux operators $v_g\, F(z,t)^2/2$ and $v_g\, R(z,t)^2/2$ in Eq.(2.45), but is not included by the normally ordered fluxes (2.48,2.49). These normally ordered flux operators are useful because they do not include the contribution from the vacuum fluctuations, which is proportional to the field bandwidth, but which cannot be extracted from the field.

2.2.4 Reflections

A real laser has facets from which the optical fields are either partially or totally reflected. Partial reflection is modelled by a two-port formalism [43]. A forward wave $F_1(z,t)$ and a reverse wave $R_2(z,t)$ are incident upon the partially transmitting,

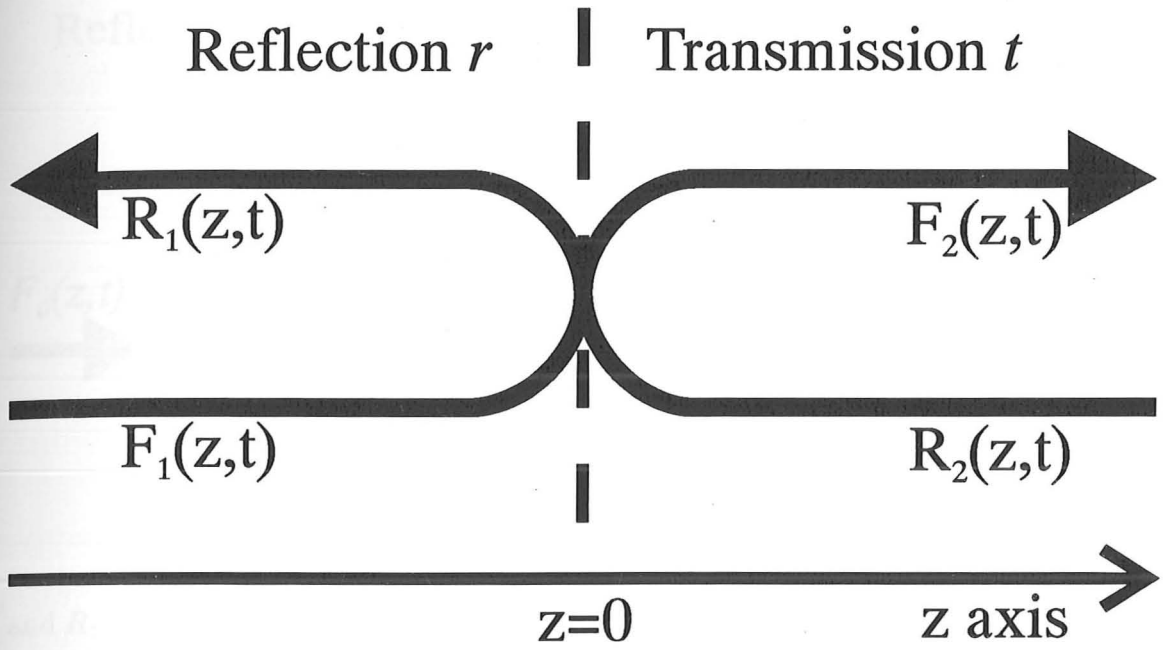

Figure 2-4: Partial reflection of the travelling-wave fields at an interface.

lossless facet at $z = 0$ (see Fig. 2-4). The commutators for the emerging partially reflected waves $F_2(z,t)$ and $R_1(z,t)$ must be preserved. We achieve this by writing:

$$F_2(z,t) = t\,F_1(z,t) + r\,R_2(-z,t), \tag{2.50}$$

$$R_1(z,t) = -r\,F_1(-z,t) + t\,R_2(z,t). \tag{2.51}$$

The transmission and reflection coefficients r and t, are real numbers in order to preserve the Hermitian nature of the field operators, and they satisfy the relationship:

$$r^*r + t^*t = 1. \tag{2.52}$$

Equation (2.52) is equivalent to power conservation, but the coefficients in Eqs.(2.51) also satisfy the usual relations implied by time reversal [43]. Because these coefficients are real numbers, and not operators, this two-port model describes reflection and transmission which is uniform over all (relevant) frequencies.

The incident and reflected waves now no longer commute with each other at all times:

$$[R_1(z,t), F_1(z,t')] = r\,\frac{i\hbar}{v_g}\frac{\partial}{\partial t'}\delta(t - t' + \frac{2z}{v_g}). \tag{2.53}$$

Using Eqs.(2.50,2.51) we see that the commutators for the outgoing waves $F_2(z,t)$

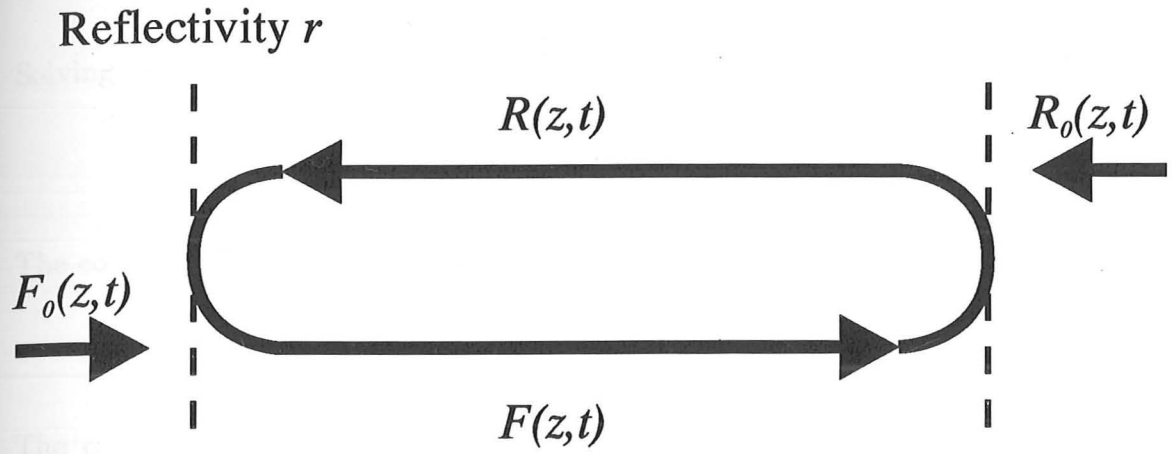

Figure 2-5: Field commutator inside a Fabry-Perot cavity.

and $R_1(z,t)$ are respectively the commutators for forward and reverse waves, Eqs.(2.25, 2.26). These outgoing forward and reverse waves also commute with each other at all points in space:

$$[F_2(z,t), R_1(z',t)] = 0. \tag{2.54}$$

2.2.5 Field commutator inside a resonant cavity

Because the incident and reflected fields no longer commute with each other at all times, the field commutation relations inside a Fabry-Perot cavity are changed. Consider a FP cavity with two reflecting mirrors at $z = -L/2$ and $z = +L/2$, with, for simplicity, the same reflection and transmission coefficients r and $t = \sqrt{1-r^2}$. The forward and reverse fields $F(z,t)$ and $R(z,t)$ inside the cavity can be written in terms of each other at earlier times, and of the incoming external fields $F_0(z,t)$ and $R_0(z,t)$ (Fig. 2-5).

The expressions are (at z=0):

$$F(0,t) = rR(0,t-T) + tF_0(0,t), \tag{2.55}$$

$$R(0,t) = rF(0,t-T) + tR_0(0,t). \tag{2.56}$$

where $T = L/v_g$ is half the cavity round trip time. In the frequency domain, these equations become

$$a_f(\omega) = r\, e^{i\omega T} a_r(\omega) + t\, a_{f0}(\omega), \tag{2.57}$$

$$a_r(\omega) = r\, e^{i\omega T} a_f(\omega) + t\, a_{r0}(\omega). \tag{2.58}$$

Solving for $a_f(\omega)$ we get

$$a_f(\omega) = \frac{t\, a_{f0}(\omega) + rt\, e^{i\omega T} a_{r0}(\omega)}{1 - r^2 \exp(i2\omega T)}. \tag{2.59}$$

The commutator can then be calculated:

$$[a_f(\omega), a_f^\dagger(\omega')] = \frac{(1 - r^4)\delta(\omega - \omega')}{1 + r^4 - 2r^2 \cos(2\omega T)}. \tag{2.60}$$

The commutator thus acquires the FP modal structure. In the limit when the reflectivity r tends to unity, the commutator exists only at the Fabry-Perot modes, and the usual discrete cavity mode formalism is recovered. The outgoing fields, however, display the normal, free field, commutation rules (2.25,2.26).

Open resonant structures are usually analyzed in terms of energy eigenstates, which are obtained by quantizing the classical field modes of the cavity [44, 45]. Our approach, where the field is quantized before the boundary conditions of the structure are imposed, is an alternative to this analysis. The structure imposed by the cavity on the commutators for the boson field operators may be used in calculating the modified spontaneous emission rates when an atom is placed inside a resonant 1-D cavity [46], for example.

2.2.6 Amplification

Following Loudon and Jeffers *et al* [47, 48], the amplification of travelling waves is modelled using an "amplifying beamsplitter". This is derived from a general model for phase insensitive amplification originally based on the inverted harmonic oscillator, as presented by Glauber [49].

In this model's simplest form, an optical mode is described by the harmonic oscillator operators a and $a^\dagger$ which satisfy the usual commutation rule

$$[a, a^\dagger] = 1. \tag{2.61}$$

Amplification is modelled by writing the amplified a operator as

$$a' = g\, a + \sqrt{|g|^2 - 1}\, b^\dagger, \tag{2.62}$$

$$a^{\dagger\prime} = g^*\, a^\dagger + \sqrt{|g|^2 - 1}\, b. \tag{2.63}$$

Here $|g| > 1$ is the amplitude gain of the process, with g a c-number, and b and $b^\dagger$ are the inverted harmonic oscillator operators, which also satisfy the boson commutation rule

$$[b, b^\dagger] = 1. \tag{2.64}$$

The inverted harmonic oscillator is in a thermal state, so that

$$< b >=< b^\dagger >= 0 \qquad \text{and} \qquad < b^\dagger b >= \bar{n} = \frac{1}{\exp(-\hbar\omega/kT) - 1}. \tag{2.65}$$

The negative temperature T describes the inversion of the amplifying medium. The commutation rule for the amplified operators a' and $a^{\dagger'}$ is seen to be preserved

$$[a', a^{\dagger'}] = |g|^2[a, a^\dagger] - (|g|^2 - 1)[b, b^\dagger] = 1. \tag{2.66}$$

The energy of the amplified state is

$$< a^{\dagger'}a' >= |g|^2 < a^\dagger a > +(|g|^2 - 1)(\bar{n} + 1). \tag{2.67}$$

The last term in equation (2.67) is the mean amplified spontaneous emission energy.

This model is modified slightly so as to apply it to the bandwidth-limited amplification of travelling waves. In Figure 2-6, the forward wave $F_1(z,t)$ is incident to an "amplifying beamsplitter" placed at $z = z_o$. The transmission t and reflection coefficient r of the amplifying beamsplitter no longer satisfy the usual power conservation relation $t^*t + r^*r = 1$. Instead, to provide gain, the transmission $t = g$ becomes larger than 1, and the relation becomes $t^*t - r^*r = 1$. A "noise" forward travelling wave $B(z,t)$ is incident into the other arm of the beamsplitter, and is combined to the transmitted wave $g\,F_1(z,t)$. The output wave $F_2(z,t)$:

$$F_2(z,t) = g\,F_1(z,t) + \sqrt{|g^*g - 1|}B(z,t). \tag{2.68}$$

The noise field $B(z,t)$ possesses the reverse wave commutation rule:

$$[B(z,t), B(z',t)] = -i\hbar v_g \frac{\partial}{\partial z'}\delta(z - z'). \tag{2.69}$$

If the power gain g^*g is made smaller than 1, attenuation rather than gain is modelled: the noise field must then assume forward wave commutation rules. The

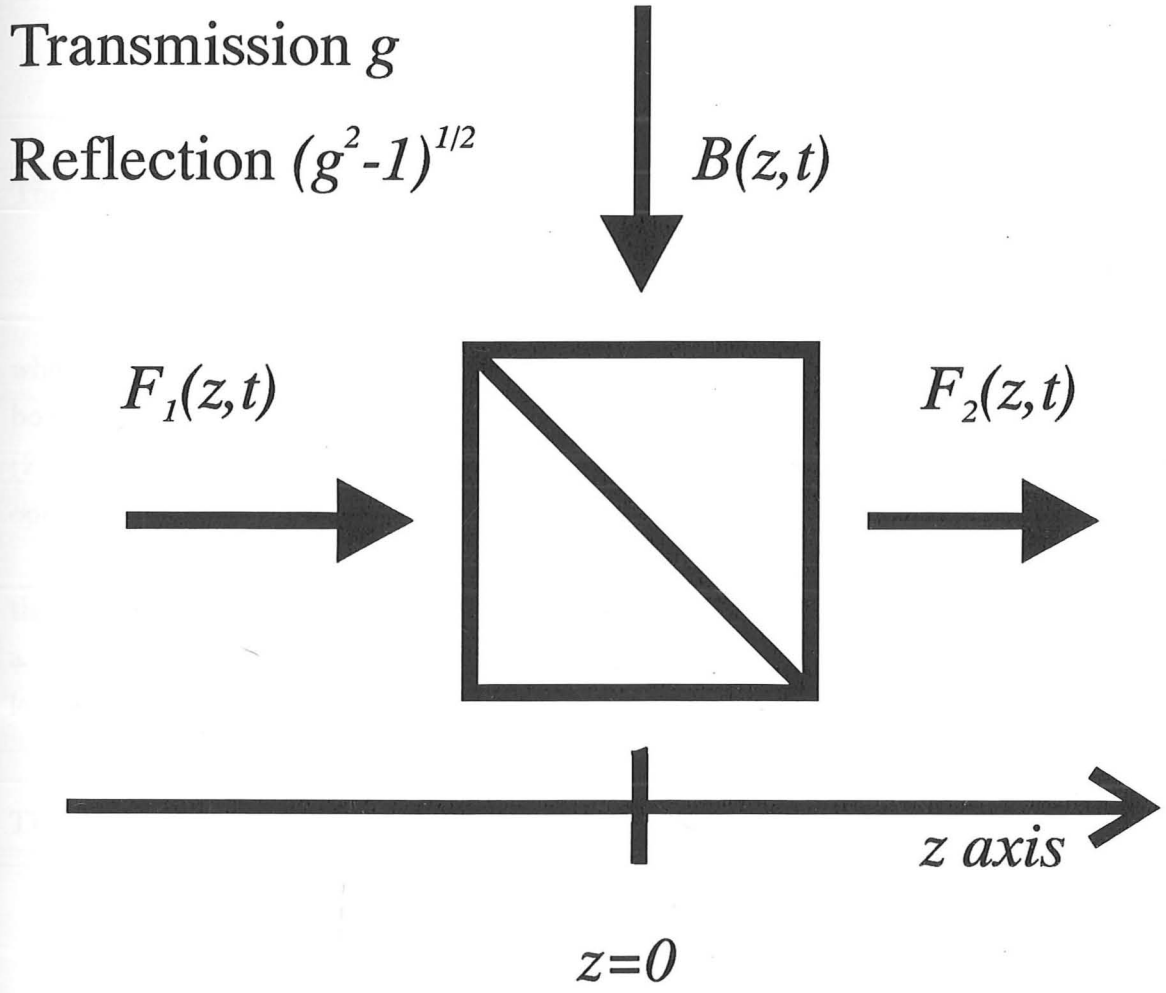

Figure 2-6: 'Amplifying beamsplitter' for a forward wave, adding amplification noise $B(z,t)$.

commutator of the amplified forward wave $F_2(z,t)$ is seen to be preserved:

$$\begin{aligned}[F_2(z,t),F_2(z',t)] &= g^*g\,[F_1(z,t),F_1(z',t)] + (|g^*g-1|)[B(z,t),B(z',t)] \\ &= i\hbar v_g \frac{\partial}{\partial z'}\delta(z-z'). \end{aligned} \tag{2.70}$$

The forward wave noise field $B(z,t)$ is synthesized from positive and negative frequency operators $b(\omega)$ and $b^\dagger(\omega)$ as:

$$B(z,t) = \int_0^\infty d\omega\, i\sqrt{\frac{\hbar\omega}{2\pi v_g}}\left\{b(\omega)e^{-i\omega(t-z/v_g)} - b^\dagger(\omega)e^{i\omega(t-z/v_g)}\right\}. \tag{2.71}$$

Their commutation rule is

$$[b(\omega),b^\dagger(\omega')] = -\delta(\omega-\omega'), \tag{2.72}$$

when the power gain $g^*g > 1$. The operators $b(\omega)$ and $b^\dagger(\omega)$ thus behave like the boson operators $a(\omega)$ and $a^\dagger(\omega)$, apart from the negative sign in their commutator (2.72): $b(\omega)$ therefore becomes the creation operator, while $b^\dagger(\omega')$ is the destruction operator.

Bandwidth limited gain is obtained by making the gain g frequency dependent, so that terms involving g in Eq.(2.68) should be replaced by convolutions representing a filtering process. Convolution becomes multiplication in the frequency domain leading to:

$$a_{f2}(\omega) = g(\omega)\,a_{f1}(\omega) + \sqrt{|g(\omega)^*g(\omega)-1|}b(\omega). \tag{2.73}$$

The commutator Eq.(2.72) then becomes, in the case of frequency dependent gain:

$$\begin{aligned}[b(\omega),b^\dagger(\omega')] &= \delta(\omega-\omega')\ ,\ \text{if}\ |g(\omega)^2| \geq 1 \\ &= -\delta(\omega-\omega')\ ,\ \text{if}\ |g(\omega)^2| < 1, \end{aligned} \tag{2.74}$$

so that the output wave commutator is preserved. For a gain $|g(\omega)^2| > 1$, if the noise field is to have a ground state, the minimum eigenvalue of the number operator $b(\omega)b^\dagger(\omega)$ must be zero, and using the commutation rule Eq.(2.74), the expectation value of the normally ordered operator $b^\dagger(\omega)b(\omega')$ is:

$$< b^\dagger(\omega)b(\omega') >= \delta(\omega-\omega'). \tag{2.75}$$

This noise power is the quantum limit for amplification, and is achievable only when

the medium is totally inverted. This is not the case in a real laser medium, where stimulated emission and absorption rates $E(\omega)$ and $A(\omega)$ compete to provide a net gain. The noise field $B(z,t)$ is then in a thermal state, with

$$< b^{\dagger}(\omega)b(\omega') >= \frac{E(\omega)}{E(\omega) - A(\omega)}\delta(\omega - \omega') = n_{sp}(\omega)\delta(\omega - \omega'). \tag{2.76}$$

This noise power spectral density Eq.(2.76) is valid for both gain and loss. Using it together with Eqs.(2.71) and (2.73), the total spontaneous power added to the amplified wave is found to be

$$v_g \int_0^{\infty} \frac{d\omega}{2\pi} \hbar\omega \left(g^*(\omega)g(\omega) - 1 \right) n_{sp}(\omega). \tag{2.77}$$

This "spontaneous emission" noise power is determined by the amplifier gain and the inversion of the amplifying medium, through the requirement of the preservation of commutation rules. It agrees with the power derived by Henry [27] for laser amplifiers, and which has been used by some workers to analyze lasers [22]. When this amplifier model is used to analyze laser structures, the quantum mechanical treatment already takes into account the "longitudinal excess spontaneous emission factor", so linewidths of arbitrary laser structures are straight-forwardly obtained.

2.2.7 Computing averages of quantum operators

To compute the averages of the quantum mechanical field operators, the *Glauber function* is used. The Glauber function is a classical distribution function which represents a quantum mechanical state of a harmonic oscillator. All the quantum mechanical averages of the oscillator's operators can be calculated from this distribution: these averages are the classical expectation values of the variables corresponding to the operators.

Consider a harmonic oscillator, of resonant frequency ω. The position x and the momentum p for the oscillator, obey Heisenberg's uncertainty principle:

$$< \Delta x >< \Delta p >\geq \hbar. \tag{2.78}$$

The position and momentum cannot therefore be classical variables. In order to enforce Eq.(2.78), x and p are operators which do not commute: it becomes impossible to set up a state of the harmonic oscillator for which the uncertainty in momentum and position is less than in Eq.(2.78). "Destruction" and "creation"

operators a and $a^\dagger$ can be defined as linear combinations of p and x. They contain the same information as p and x, they also do not commute with one another, and their averages are in general complex: they are similar to the classical phasor description of the Harmonic oscillator. A quantum mechanical state can be described completely by specifying the averages of all combinations and powers of a complete set of operators, like (x, p), or $(a, a^\dagger)$ (for example, by knowing all the expectation values $< a(a^\dagger)^m >$, $m, n = 0, 1, 2 \ldots$). The Glauber function describes the state of the oscillator by a real distribution $P(\alpha)$. The expectation values for a and $a^\dagger$ are then simply the classical averages for α and α^*. Two examples are shown in Fig. (2-7). The Glauber function corresponding to a coherent ("classical") state is a δ-function, and is like our view of a classical harmonic oscillator state, with x and p well defined. In contrast, the Glauber function for a thermal state has a Gaussian distribution, with zero mean: the mean values of x and p are zero, but $< x^2 >$ and $< p^2 >$ are non zero.

For a single boson system described by the destruction and creation operators a and $a^\dagger$, the quantum mechanical expectation value of an operator $M(a, a^\dagger)$ at time t is computed by evaluating its trace with the density matrix $\rho(t)$ of the system:

$$< M(a, a^\dagger) >= \mathrm{tr}\left[\rho(t) M(a, a^\dagger)\right]. \tag{2.79}$$

The coherent states

$$|\alpha >= e^{\alpha a^\dagger - \alpha^* a}|0 >$$

are the eigenstates of the destruction operator a: $a|\alpha >= \alpha|\alpha >$. While the coherent states are not mutually orthogonal, they form a complete set. The completeness relation for the coherent states is [10]:

$$\int \frac{d^2\alpha}{\pi} |\alpha >< \alpha| = 1, \tag{2.80}$$

where the integration is over the whole complex plane. The density operator of the system is expanded as a power series of a and $a^\dagger$ in antinormal order:

$$\rho(t) = \sum_{n,m} c_{nm}(t) a^n a^{\dagger m}. \tag{2.81}$$

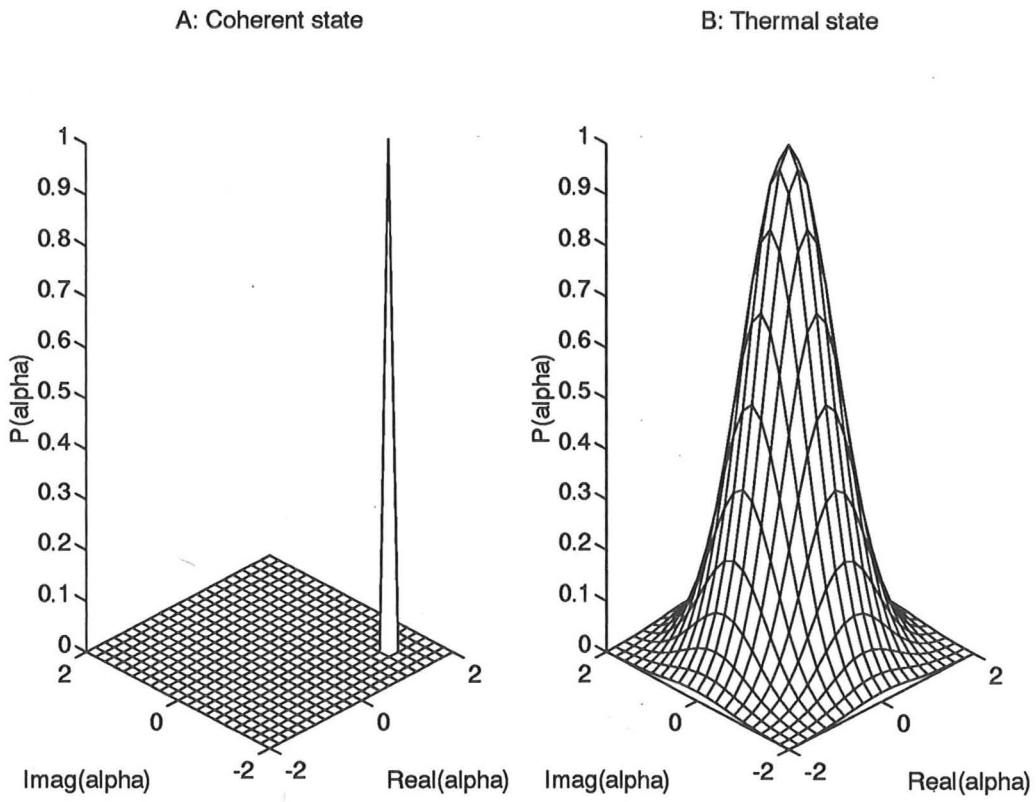

Figure 2-7: Glauber function for:
A) A coherent state (the distribution is a delta-function, $\delta(\alpha - \alpha_0)\delta(\alpha^* - \alpha_0^*)$).
B) A thermal state (the distribution is Gaussian with zero mean).

Using the completeness relation (2.80) gives

$$\begin{aligned}\rho(t) &= \sum_{n,m}\int \frac{d^2\alpha}{\pi} c_{nm}(t) a^n |\alpha><\alpha| a^{\dagger m} \\ &= \int \frac{d^2\alpha}{\pi} \sum_{n,m} c_{nm}(t)\alpha^n \alpha^{*m} |\alpha><\alpha| \\ &= \int d^2\alpha\, P(\alpha,\alpha^*,t)|\alpha><\alpha|, \end{aligned} \tag{2.82}$$

where

$$P(\alpha,\alpha^*,t) = \frac{1}{\pi}\sum_{n,m} c_{nm}(t)\alpha^n\alpha^{*m}, \tag{2.83}$$

is the Glauber function for the oscillator. Provided the operator $M(a,a^\dagger)$ is expanded as the normally ordered power series:

$$M(a,a^\dagger) = \sum_{j,k} M_{jk} a^{\dagger j} a^k. \tag{2.84}$$

Eqs.(2.79) and (2.82) express the quantum mechanical average $< M(a,a^\dagger) >$ as

$$\begin{aligned}< M(a,a^\dagger) > &= \mathrm{tr}\left(\sum_{i,j}\int \frac{d^2\alpha}{\pi} P(\alpha,\alpha^*,t) M_{jk} a^k |\alpha><\alpha| a^{\dagger j}\right) \\ &= \mathrm{tr}\left(\sum_{i,j}\int \frac{d^2\alpha}{\pi} P(\alpha,\alpha^*,t) M_{jk} \alpha^{*j}\alpha^k |\alpha><\alpha|\right) \\ &= \int \frac{d^2\alpha}{\pi} P(\alpha,\alpha^*,t)\mathcal{M}(\alpha,\alpha^*), \end{aligned} \tag{2.85}$$

where the function $\mathcal{M}(\alpha,\alpha^*)$ is

$$\mathcal{M}(\alpha,\alpha^*) = \sum_{j,k} M_{jk}\alpha^{*j}\alpha^k. \tag{2.86}$$

Thus, by expanding the density operator in terms of the coherent states $|\alpha>$, a quantum mechanical average of a normally ordered operator is expressible as a classical average of a function $\mathcal{M}(\alpha,\alpha^*)$ over a quasi-probability function $P(\alpha,\alpha^*,t)$.

The Glauber function $P(\alpha,\alpha^*,t)$ replaces the density operator $\rho(t)$. Under the influence of coupling to external systems, and indeed following the free motion of the boson system itself, the Glauber function $P(\alpha,\alpha^*,t)$ evolves in time. The equation of motion for $P(\alpha,\alpha^*,t)$ is generally a Fokker-Plank equation [10], with drift and

diffusion coefficients which govern the way in which the quasi-probability function is altered in time. We may then use the Langevin formulation equivalent to the Fokker-Plank process, where $\alpha(t)$ and $\alpha^*(t)$ follow stochastic, noise driven equations of motion. The quantum average, expressed as an integral in Eq.(2.85), then becomes the stochastic ensemble average $< \mathcal{M}(\alpha(t), \alpha^*(t)) >$, which is more suitable for computation purposes.

We use the Glauber function, in preference to the Wigner, or Q-functions [10], because we are primarily interested in averages of normally ordered operators, such as the optical power, which does not include the contribution of the vacuum fluctuations. The use of the Wigner or the Q-functions, (which give averages of symmetrically and antinormally ordered operators respectively) would require the subtraction of the vacuum fluctuation energy, proportional to the modelled bandwidth.

In our model, as the fields pass from one "free" section to another, through amplifiers and reflectors, their properties are altered. The z-axis is split into n "free" sections, and within each free section, the boson frequency operators of the field are used in the same way to define a Glauber P-function for the forward and reverse travelling waves. First, continuum coherent states are defined [39], for forward and reverse waves, within the k-th "free" section:

$$|\{\alpha_{fk}(\omega)\}>= \exp\left\{ \int d\omega \left(\alpha_{fk}(\omega) a^{\dagger}_{fk}(\omega) - \alpha_{fk}(\omega)^* a_{fk}(\omega) \right) \right\} |0>, \qquad (2.87)$$

and

$$|\{\alpha_{rk}(\omega)\}>= \exp\left\{ \int d\omega \left(\alpha_{rk}(\omega) a^{\dagger}_{rk}(\omega) - \alpha_{rk}(\omega)^* a_{rk}(\omega) \right) \right\} |0>, \qquad (2.88)$$

where $\alpha_{fk}(\omega)$ and $\alpha_{rk}(\omega)$ are arbitrary functions defined for $\omega \geq 0$. The Glauber P function, already used for fields with an infinite number of discrete modes [50], is extended to continuum fields by expressing the density operator as

$$\begin{aligned} \rho \;=\; & \int P\Big(\{\alpha_{f1}(\omega)\}, \{\alpha_{r1}(\omega)\}, \ldots, \{\alpha_{fn}(\omega)\}, \{\alpha_{rn}(\omega)\} \Big) \times \\ & |\{\alpha_{f1}(\omega)\}> |\{\alpha_{r1}(\omega)\}> \ldots |\{\alpha_{fn}(\omega)\}> |\{\alpha_{rn}(\omega)\}> \times \\ & <\{\alpha_{rn}(\omega)\}| < \{\alpha_{fn}(\omega)\}| \ldots < \{\alpha_{r1}(\omega)\}| < \{\alpha_{f1}(\omega)\}| \times \\ & \prod_{k=1}^{n} d\{\alpha_{fk}(\omega)\} d\{\alpha_{rk}(\omega)\}. \end{aligned} \qquad (2.89)$$

The integrations are now over all possible functions $\alpha_{fk}(\omega)$ and $\alpha_{rk}(\omega)$. Averages of normally ordered field operators, such as the forward wave momentum Eq.(2.48) in the spatial section k,

$$S^+(z_k,t) = \frac{\hbar}{2\pi}\int_0^\infty d\omega \int_0^\infty d\omega' \sqrt{\omega\omega'} a_f^\dagger(\omega') a_f(\omega) e^{i(t-z_k/v_g)(\omega-\omega')}, \tag{2.90}$$

can then be expressed as the classical average:

$$\begin{aligned} < S^+(z_k,t) > \; &= \int P\Big(\{\alpha_{f1}(\omega)\},\{\alpha_{r1}(\omega)\},\ldots,\{\alpha_{fn}(\omega)\},\{\alpha_{rn}(\omega)\}\Big) \times \\ &\mathcal{S}^+_{(z_k,t)}\Big(\{\alpha_{fk}(\omega)\}\Big)\prod_{k=1}^{n} d\{\alpha_{fk}(\omega)\}d\{\alpha_{rk}(\omega)\}, \end{aligned} \tag{2.91}$$

where the function $\mathcal{S}^+_{(z_k,t)}\Big(\{\alpha_{fk}(\omega)\}\Big)$ is

$$\mathcal{S}^+_{(z_k,t)}\Big(\{\alpha_{fk}(\omega)\}\Big) = \frac{\hbar}{2\pi}\int_0^\infty d\omega \int_0^\infty d\omega' \sqrt{\omega\omega'}\alpha_{fk}(\omega')^*\alpha_{fk}(\omega) e^{i(t-z/v_g)(\omega-\omega')}. \tag{2.92}$$

This classical average Eq.(2.91) is replaced, in the Langevin formulation of the problem, by the stochastic ensemble average

$$\begin{aligned} < S^+(z_k,t) > \; &= \; < \mathcal{S}^+_{(z,t)}\Big(\{\alpha_{fk}(\omega)\}\Big) > \\ &= \frac{\hbar}{2\pi}\int_0^\infty d\omega \int_0^\infty d\omega' \sqrt{\omega\omega'} < \alpha_{fk}(\omega')^*\alpha_{fk}(\omega) > e^{i(t-z/v_g)(\omega-\omega')}. \end{aligned} \tag{2.93}$$

The single mode variables $\alpha(t)$ and $\alpha^*(t)$ mentioned above followed stochastic equation of motion describing their time evolution. In contrast, the functions $\alpha_{fk}(\omega)$ and $\alpha_{rk}(\omega)$, which describe the field for all times in the different spatial sections k, are now related to each other by stochastic relations as one progresses from one section to the next, backwards and forwards, for example through an amplifier.

The frequency domain functions $\alpha_{fk}(\omega)$ are not convenient for computation and one requires the forward and reverse complex fields, which from Eqs.(2.46,2.47), now become

$$\mathcal{F}(z_k,t) \; = \; \int_0^\infty d\omega\, i\sqrt{\frac{\hbar\omega}{2\pi v_g}}\alpha_{fk}(\omega)\exp(-i\omega(t-z_k/v_g)), \tag{2.94}$$

$$\mathcal{R}(z_k,t) \;=\; \int_0^\infty d\omega\, i\sqrt{\frac{\hbar\omega}{2\pi v_g}}\alpha_{rk}(\omega)\exp(-i\omega(t+z_k/v_g)). \tag{2.95}$$

The quantum average $< S^+(z_k,t) >$ is then the stochastic ensemble average

$$< S^+(z_k,t) >= v_g < \mathcal{F}(z_k,t)\mathcal{F}^*(z_k,t) > . \tag{2.96}$$

Within each free section, the complex fields propagate in time at the velocity v_g, and are partially reflected at facets, or are amplified and added to noise as they traverse amplifiers.

In the Glauber representation, the complex wave which represents a travelling field in its vacuum state is identically zero. Thus, provided the thermal contributions of the external field to the laser are neglected, no noise need be introduced at the reflecting facets. In contrast, use of the Wigner or Q-functions would require suitable modelling of the influx of the external vacuum fields into the laser by Gaussian noise sources.

2.3 Field and electron population fluctuations

We derive here the equations of motion, and the correlations for the noise sources, of the fields and electron populations in the laser. We first look at a single-mode laser model which uses the Glauber function to represent the optical mode, and we examine the correlations between the various noise sources used. We then extend this stochastic model of amplification in order to apply it to gain for travelling waves.

We take a simplified model of a semiconductor, with N_c degenerate states in the conduction band, and N_v degenerate states in the valence band. There are n_c electrons in the conduction band, together with n_v electrons in the valence band. Charge neutrality requires

$$n_c + N_A = N_v - n_v, \tag{2.97}$$

where N_A is the number of (ionized) acceptor atoms. $N_v - n_v$ is the number of holes in the valence band. The rate of spontaneous and stimulated emission is proportional to

$$g\Gamma\, n_c(N_v - n_v), \tag{2.98}$$

while the rate of stimulated absorption is proportional to $g\Gamma n_v(N_c - n_c)$. This makes

the net gain proportional to

$$g\Gamma N_c N_v(\frac{n_c}{N_c} - \frac{n_v}{N_v}), \tag{2.99}$$

where g is the material gain constant and Γ is the optical confinement factor. Using the charge neutrality expression (2.97) the net gain Eq.(2.99) can be rewritten as $b(n_c - n_t)$, where the gain constant b is $b = g(N_c + N_v)$, and the transparency carrier density n_t is $n_t = N_c(N_v - N_A)/(N_c + N_v)$. Intraband scattering occurs on a femtosecond time-scale, and the models developed by Lax [24], Louisell [10] and Haken [9], using distribution functions, for homogeneously broadened laser media are applicable.

2.3.1 Derivation of the laser noise sources using distribution functions

Lax [24], Louisell [10] and Haken [9], in their laser model, use distribution functions to replace the laser operators a, $a^\dagger$ for the field, N_2, N_1, M and $M^\dagger$ for the atomic population inversion and dipole moments, with the classical variables α, α^*, $\mathcal{N}_2$, $\mathcal{N}_1$, $\mathcal{M}$ and $\mathcal{M}^*$. The complete derivation of the equations of motion for these classical variables is somewhat long and involved. As their results are used, a brief outline of their derivation is given here.

The system they consider consists of an optical mode of a resonant cavity, and a number of "atoms" which have an excited and an absorbing level which couple to the optical mode (see Fig. 2-8). To this system are added two "reservoirs" which provide, respectively, loss for the optical field, and disturbance for the atoms (causing recombination, and dephasing of the atomic dipole moments).

The evolution of the system is determined by the standard Hamiltonian [51]:

$$H = \hbar\omega a^\dagger a + \hbar\omega_0(N_2 - N_1) + \hbar\delta(a^\dagger M + aM^\dagger) + H_O + H_A, \tag{2.100}$$

where δ is the dipole strength, H_O is the contribution of the reservoir for optical loss to the Hamiltonian, and H_A is the contribution of the reservoir which causes atomic recombination and dephasing of the dipole moments. These reservoir terms contain a large number of operators describing the quantum state of the reservoir, corresponding for example either to the modes of the external electromagnetic field, or to the modes of thermal vibrations which disorder the atomic dipole moments. It is the large number of degrees of freedom possessed by the reservoirs which enable

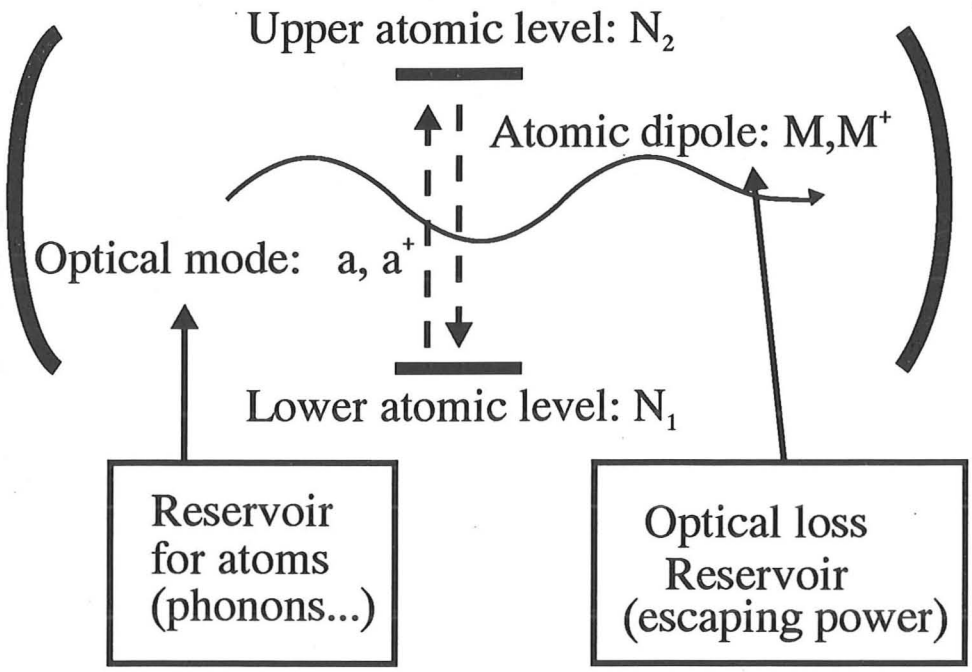

Figure 2-8: System considered by Lax *et al* to derive the laser noise sources.

the irreversible processes like damping to be simulated.

The Schrödinger equation, or the Heisenberg equations of motion could be used with the Hamiltonian to determine the evolution of the quantum state describing the laser, but the immense number of degrees of freedom, together with the complexity of operator algebra, prevent this in practice. Furthermore, the degrees of freedom corresponding to the reservoirs are of no interest to us. To eliminate these degrees of freedom, some statistical assumptions are made concerning the reservoir.

Because of these statistical assumptions, the wavefunction of the system cannot be used, as it can only describe a system in a known "pure" quantum state: it embodies the fundamental uncertainty between momentum and position, for example, but cannot also describe statistical uncertainties due to our incomplete knowledge. The density operator for the system must be used instead, as it embodies both statistical and quantum uncertainties. Reservoir theory considers the density operator, describing the total system (reservoir plus atoms and field), in terms of a reduced density operator for the field and atoms, plus another part, which describes the state of the reservoir. The part of the density operator describing the reservoirs can be eliminated with appropriate statistical assumptions, and an equation of motion for the *reduced* density operator $\rho(t)$, which describes only the field and atom operators,

is obtained. This Master equation is an operator equation of the form:

$$\dot{\rho}(t) = \frac{i}{\hbar}[\rho, H_I] + \left(\frac{\partial \rho}{\partial t}\right)_{Field} + \left(\frac{\partial \rho}{\partial t}\right)_{Atoms}, \tag{2.101}$$

where the square brackets denote the commutator $[a, b] = ab - ba$, H_I contains the first three terms of the Hamiltonian Eq.(2.100), and the other two terms describe the effects of the reservoirs such as loss, and contain the system operators a,$a^\dagger$ etc..., as well as the density operator $\rho(t)$. Some of the operators can only be represented by matrices of infinite dimensions, and so, this Master equation cannot be solved directly either analytically, or numerically.

The method of distribution functions replaces the density matrix by a classical distribution of variables $\alpha, \alpha^*, \mathcal{N}_2$,etc... This distribution $P(\alpha, \alpha^*, \mathcal{N}_1, \mathcal{N}_2, \mathcal{M}, \mathcal{M}^*, t)$ is the Fourier transform of the characteristic function:

$$\begin{aligned} \chi(\eta, \eta^*, \nu_1, \nu_2, \mu, \mu^*, t) &= < \rho(t) \exp(i\eta^* a^\dagger) \exp(i\mu^* M^\dagger) \\ &\quad \times \exp(i\nu_2 N_2) \exp(i\nu_1 N_1) \exp(i\mu M) \exp(i\eta a) >, \end{aligned} \tag{2.102}$$

where the "< .. >" denotes expectation value. The rate of change $d\chi/dt$ is obtained by replacing $\rho(t)$ by $\dot{\rho}(t)$ using Eq.(2.101). The resulting equation of motion for the distribution function $P(t)$ is a Fokker-Plank equation containing terms like

$$\frac{\partial P}{\partial t} = -\gamma/2 \frac{\partial P}{\partial \alpha} - \alpha^* \mathcal{M} \exp(\frac{\partial}{\partial \mathcal{N}_1}) P + \ldots, \tag{2.103}$$

where γ is the damping rate for the field. The exponential terms are simplified by using a power series expansion. The Fokker-Planck equation can then be replaced by the equivalent set Langevin equations [24], one of which is:

$$\dot{\alpha} = -\frac{\gamma}{2}\alpha(t) + \mu\mathcal{M} + \mathcal{G}_\alpha(t), \tag{2.104}$$

where $\mathcal{G}_\alpha(t)$ is a white noise source, which causes α to diffuse in the same way as derivatives like $\partial^2 P/(\partial\alpha\partial\alpha^*)$, in Eq.(2.103), cause the distribution to spread in α.

Assuming a homogeneously broadened medium, so that the atomic dipole moment is disturbed on a time scale much shorter than the rates of change for the field and carrier number, the dipole moment can be eliminated, and the following

Langevin equations of motion are obtained:

$$\dot{\alpha}(t) = \frac{g}{2}(\mathcal{N}_2 - \mathcal{N}_1)\alpha - \frac{\gamma}{2}\alpha + F_\alpha(t), \tag{2.105}$$

$$\dot{\mathcal{N}}_2(t) = D - g(\mathcal{N}_2 - \mathcal{N}_1)\alpha^*\alpha - N_2/\tau_2 + F_{N2}(t), \tag{2.106}$$

$$\dot{\mathcal{N}}_1(t) = \mathcal{N}_2/\tau_{21} - g(\mathcal{N}_2 - \mathcal{N}_1)\alpha^*\alpha - \mathcal{N}_1/\tau_1 + F_{N1}(t), \tag{2.107}$$

$$\tag{2.108}$$

where τ_1, τ_2 and τ_{21} are carrier lifetimes for the populations N_1, N_2 and non-radiative recombinations from N_2 to N_1.

The noise correlations are:

$$< F_\alpha(t)F_\alpha^*(t') > = g\mathcal{N}_2\delta(t-t'), \tag{2.109}$$

$$< F_{N2}(t)F_{N2}(t') > = \Big(D' + \mathcal{N}_2/\tau_2 + g(\mathcal{N}_2 - \mathcal{N}_1)\alpha^*\alpha\Big)\delta(t-t'), \tag{2.110}$$

$$< F_\alpha(t)F_{N2}(t') > = g\mathcal{N}_2\alpha\delta(t-t'). \tag{2.111}$$

2.3.2 Rate equations for semiconductor

Using the results of Louisell, Lax and Haken, we derive the following equations of motion for the laser variables:

$$\dot{\alpha} = \frac{g\Gamma N_c N_v\Big((n_c/N_c) - (n_v/N_v)\Big) - \gamma}{2}\alpha + F_\alpha(t), \tag{2.112}$$

$$\dot{\alpha}^* = \frac{g\Gamma N_c N_v\Big((n_c/N_c) - (n_v/N_v)\Big) - \gamma}{2}\alpha^* + F_{\alpha^*}(t), \tag{2.113}$$

$$\dot{n_c} = D - n_c/\tau_c - g\Gamma N_c N_v\Big((n_c/N_c) - (n_v/N_v)\Big)\alpha^*\alpha + F_{n_c}(t) - \Big(\alpha F_{\alpha^*}(t) + \alpha^* F_\alpha(t)\Big), \tag{2.114}$$

$$\dot{n_v} = -\dot{n_c}. \tag{2.115}$$

Here g is a lumped gain constant, γ is the field damping rate equal to the inverse of the photon lifetime, D is the drive term due to the supply current, while τ_c is the conduction band electron lifetime (for simplicity, quadratic and cubic recombination rates are neglected here).

The noise sources F_α and F_{n_c} are uncorrelated, Gaussian, white noise sources, with the following correlation functions:

$$< F_\alpha(t)F_{\alpha^*}(t') > = g\Gamma\, n_c(N_v - n_v)\,\delta(t-t'), \tag{2.116}$$

$$< F_\alpha(t)F_\alpha(t') > \;=\; 0, \tag{2.117}$$

$$< F_{n_c}(t)F_{n_c}(t') > \;=\; \Big\{ D' + n_c/\tau_c - g\Gamma\, N_c N_v \Big((n_c/N_c) - (n_v/N_v) \Big) |\alpha|^2 \;-\; g\Gamma\, n_c(N_v - n_v) \Big\} \delta(t-t'). \tag{2.118}$$

In Eq.(2.118) above, D' is the magnitude of the drive current fluctuations, and depends on the current injection conditions. In this work the drive current is injected from a high impedance current source, and the value of D' will be specified below. The field noise, according to Eq.(2.116), is in the Glauber representation, proportional to the rate of spontaneous emission, Eq.(2.98). The total electron noise is from Eq.(2.114):

$$F_n(t) = F_{n_c}(t) - \Big(\alpha(t)F_{\alpha^*}(t) + \alpha^*(t)F_\alpha(t) \Big). \tag{2.119}$$

Due to correlations between $\alpha(t)$ and $F_\alpha(t)$, the second term above has a negative D.C. component, equal to $-g\,n_c(N_v - n_v)$, which represents the average spontaneous emission rate. Subtracting this D.C. component gives a zero mean noise $F_n'(t)$, whose correlation function is seen to be

$$< F_n'(t)F_n'(t') > = \Big\{ D' + n_c/\tau_c + g\Gamma\, n_c(N_v - n_v)\{|\alpha^2| + 1\} + g\Gamma\, n_v(N_c - n_c)|\alpha^2| \Big\} \delta(t-t'). \tag{2.120}$$

The terms in this equation (2.120) are recognized as the usual shot noise contributions due to drive, recombination, stimulated & spontaneous emission and stimulated absorption. If we set $\gamma = 0$ in Eqs.(2.112, 2.113), so as not to include facet losses, we see that

$$\frac{d}{dt}(\alpha\alpha^*) = g\Gamma\, N_c N_v (n_c/N_c - n_v/N_v)\alpha^*\alpha + \alpha(t)F_{\alpha^*}(t) + \alpha^*(t)F_\alpha(t), \tag{2.121}$$

The carrier rate equation can then be written

$$\dot{n_c} = D - n_c/\tau_c + F_{n_c}(t) - \frac{d}{dt}(\alpha\alpha^*) \tag{2.122}$$

where the only noise source is $F_{n_c}(t)$. In the Glauber representation, correlations between the carrier and field noise sources can thus be accounted for by subtracting the rate of change of field energy $\alpha\alpha^*$, from a carrier rate equation with only drive and recombination terms.

This single mode model is extended to model amplification of travelling waves: the laser is divided into a number of longitudinal sections, and in each section we use two "amplifying beamsplitters", discussed in section 2.2.6, to provide gain to the forward and the reverse travelling fields as they propagate along the cavity. The carrier concentration is assumed to be uniform within one section, and it determines the gain for the two "amplifying beamsplitters".

The operator equation Eq.(2.73) describes amplification of a travelling wave. The noise field $B(z,t)$, with frequency domain operators $b(\omega)$ and $b^\dagger(\omega)$, is in a thermal state. Equation (2.76) gives the expectation value $< b^\dagger(\omega)b(\omega') >$:

$$< b^\dagger(\omega)b(\omega') >= n_{sp}(\omega)\delta(\omega - \omega'). \tag{2.123}$$

The Glauber function $P(\alpha, \alpha^*)$ for a single mode thermal state with $< a^\dagger a >= \bar{n}$ is a Gaussian distribution with $< \alpha >=< \alpha^* >= 0$ and $< \alpha\alpha^* >= \bar{n}$. Accordingly, the noise field operators $b(\omega)$ and $b^\dagger(\omega)$ are represented by the set of complex numbers $\beta(\omega)$ and $\beta^*(\omega)$ which are Gaussian distributed with

$$< \beta(\omega)\beta^*(\omega') >= n_{sp}(\omega)\delta(\omega - \omega'). \tag{2.124}$$

The positive frequency noise operator $B^+(z,t)$ will therefore be replaced, in the Glauber representation, by the Gaussian distributed complex noise field

$$\mathcal{B}(z,t) = \int_0^\infty d\omega \, i\sqrt{\frac{\hbar\omega}{2\pi v_g}}\beta(\omega)e^{-i\omega(t-z/v_g)}. \tag{2.125}$$

The Glauber representation equivalent of Eq.(2.73) is, in the frequency domain:

$$\alpha_{f2}(\omega) = g(\omega)\,\alpha_{f1}(\omega) + \sqrt{|g(\omega)^* g(\omega) - 1|}\beta(\omega). \tag{2.126}$$

In the time domain, Eq.(2.126) becomes

$$\mathcal{F}_2(z,t) = \int_0^\infty d\tau \; g'(\tau)\mathcal{F}_1(z, t-\tau) \; + \; \mathcal{B}'(z,t), \tag{2.127}$$

where $g'(\tau)$ is the impulse response of a causal filter which implements the frequency response $g(\omega)$, and $\mathcal{B}'(z,t)$ is the total noise added to the amplified wave

(the reflection of the beamsplitter being now included):

$$\mathcal{B}'(z,t) = \int_0^\infty d\omega\, i\sqrt{\frac{\hbar\omega}{2\pi v_g}}\sqrt{|g(\omega)^* g(\omega) - 1|}\beta(\omega)e^{-i\omega(t-z/v_g)}. \qquad (2.128)$$

This equation (2.127) is the travelling wave equivalent to the single mode equation (2.112) integrated over time $\Delta t = \Delta L/v_g$, where it is assumed that during the time short Δt, the gain stays constant. The injected noise $\mathcal{B}'(z,t)$ thus corresponds to the single mode "spontaneous emission" noise $F_\alpha(t)$ in equation (2.112).

The carrier population is also subject to fluctuations during the amplification process. In a given section where the carrier concentration is n_c, the material stimulated emission is proportional to $E = g\Gamma\, n_c(N_v - n_v)$, while the stimulated absorption is proportional to $A = g\Gamma\, n_v(N_c - n_c)$, where charge neutrality requires $n_c + N_A = N_v - n_v$. This gives the material a net gain constant

$$E - A = g\Gamma(n_c N_v - n_v N_c) = b(n_c - n_t),$$

and the amplitude gain for a travelling wave, at centre gain frequency ω_o, along a section length ΔL is set equal to

$$g(\omega_o) = \exp\Big(b\Gamma(n_c - n_t)\Delta L/2\Big). \qquad (2.129)$$

The rate $R(t)$ at which photons are emitted by the material, equals the photon flux of the outgoing amplified waves, minus the photon flux of the incident waves:

$$R(t) = v_g\Big\{|\mathcal{F}_2(z_o,t)^2| + |\mathcal{R}_2(z_o,t)^2| - |\mathcal{F}_1(z_o,t)^2| - |\mathcal{R}_1(z_o,t)^2|\Big\}/\hbar\omega_o. \qquad (2.130)$$

If this rate $R(t)$ is subtracted in the carrier rate equation for the laser section, as for the single mode case in equation (2.122), no other carrier noise sources correlated with the wave noise fields are needed.

Looking again to the single mode model of Eqs.(2.112—2.115), we see that the carrier rate equation must be

$$\dot{n_c} = D - n_c/\tau_c + F_{n_c}(t) - R(t). \qquad (2.131)$$

The carrier noise $F_{n_c}(t)$, which corresponds to $F_{n_c}(t)$ in the single mode model, is uncorrelated with the optical field noise $\mathcal{B}(z,t)$. Its spectrum can be determined

by requiring that the total carrier noise, including contributions hidden in the term $R(t)$, be the usual shot noise expression, as given by Eq. (2.120). We obtain a noise source with the correct spectrum at low frequencies by taking

$$< F_{n_c}(t)F_{n_c}(t') >= \left\{ D' + \Gamma_c n_c - R(t) \right\} \delta(t - t'). \tag{2.132}$$

Again, the factor D', in Eq.(2.132) above depends on the current injection conditions. For a long time, the drive fluctuations were assumed to be Poissonian [10, 24], and so $D' = D$ was used. As pointed out by Yamamoto *et al* [33], the assumption of Poissonian current fluctuations is often misleading. Further work [33, 52] shows that the drive circuit helps to determine these fluctuations. One result which is used here, is to assume that the internal resistance R_S is much higher than the differential resistance R of the laser diode. The injection current fluctuations are then caused by the thermal noise of the drive impedance, and it is appropriate to take $D' = 2k_BT/R_S$ instead of the shot-noise value $D' = D$.

With an appropriate drive circuit, sub-shot noise drive fluctuations may be obtained as demonstrated by Yamamoto *et al* [33, 52] generating squeezed-states from laser diodes. Here this requires $D < D'$ leading to a non-physical negative noise correlation in Eq.(2.132). It is then found that the Glauber distributions become singular, so that squeezed light cannot be simulated in our model. Simulations of squeezed light would require Wigner or Q-functions, which in turn would require altering the amplification noise and adding noise sources at the laser facets, or else the use of the *positive*-P function, which is the subject of chapter 7.

2.4 Conclusion: theory for the quantum laser model

The theoretical basis of a large signal travelling wave model for laser diodes has been presented.

The quantum mechanical treatment of the laser determines the noise sources in a consistent way, so that the fluctuations of the fields are simulated accurately, including effects like the excess spontaneous emission factor. Both intensity and phase noise are calculated correctly by using the Glauber distribution to simulate the quantized optical fields.

As indicated by the quantum theory, the model presented in this chapter cannot

simulate intensity squeezed light. This will be left for the extension of the model presented in chapter 7.

2.5 Appendix A: Treatment of the optical field dispersion

The dispersive field equations are transformed here into dispersion-less equations of motion which can be quantized. We start with the 1-D Maxwell equations (2.133,2.134):

$$i\omega\epsilon(\omega)\mathbf{E}(\omega,z) = -\frac{1}{\mu_o}\frac{\partial \mathbf{B}}{\partial z}, \tag{2.133}$$

$$i\omega\mathbf{B}(\omega,z) = -\frac{\partial \mathbf{E}}{\partial z}. \tag{2.134}$$

Defining

$$F'(\omega,z) = \sqrt{\frac{\epsilon_g v_g}{2v_p(\omega)}}\Big(\mathbf{E}(\omega,z) + v_p(\omega)\mathbf{B}(\omega,z)\Big), \tag{2.135}$$

$$R'(\omega,z) = \sqrt{\frac{\epsilon_g v_g}{2v_p(\omega)}}\Big(\mathbf{E}(\omega,z) - v_p(\omega)\mathbf{B}(\omega,z)\Big), \tag{2.136}$$

these Maxwell equations also describe the propagation in a laser waveguide, assuming single transverse mode operation, as discussed in section 2.2.1.

The choice of the normalization constants above will be justified later. Using Eqs.(2.133,2.134) and the refractive index defined in Eq.(2.8), we get the following equations of motion for the forward and reverse waves:

$$\left(\frac{i\omega}{v_g} + i\omega_o\frac{n_p - n_g}{c}\right)F'(\omega,z) = -\frac{\partial F'}{\partial z}, \tag{2.137}$$

$$\left(\frac{i\omega}{v_g} + i\omega_o\frac{n_p - n_g}{c}\right)R'(\omega,z) = \frac{\partial R'}{\partial z}. \tag{2.138}$$

We now define new forward and reverse field variables through:

$$F(\omega,z) = F'(\omega,z)\exp(i\Delta k z), \tag{2.139}$$

$$R(\omega,z) = R'(\omega,z)\exp(-i\Delta k z), \tag{2.140}$$

where we make the wave-vector Δk equal to $\omega_o(n_p - n_g)/c$. The equations of motion

for the "translated" variables are now:

$$i\omega F(\omega,z) = -v_g\frac{\partial F}{\partial z}, \tag{2.141}$$

$$i\omega R(\omega,z) = v_g\frac{\partial R}{\partial z}, \tag{2.142}$$

which are equivalent to Eq.(2.11) in the time domain.

We will need to have an expression for the field energy associated with the travelling waves to quantize the fields, so first we determine the energy flux in terms of the new variables. The energy flux is given by the Poynting vector $\mathbf{S}(z,t)$:

$$\mathbf{S}(z,t) = \frac{1}{\mu_o}\mathbf{E}(z,t)\mathbf{B}(z,t). \tag{2.143}$$

Using Eqs.(2.135,2.136), we get

$$\mathbf{E}(\omega,z) = \sqrt{\frac{v_p(\omega)}{2\epsilon_g v_g}}\Big(F'(\omega,z)+R'(\omega,z)\Big), \tag{2.144}$$

$$\mathbf{B}(\omega,z) = \sqrt{\frac{1}{2\epsilon_g v_g v_p(\omega)}}\Big(F'(\omega,z)-R'(\omega,z)\Big), \tag{2.145}$$

from which:

$$\begin{aligned}\mathbf{S}(z,t) &= \frac{1}{\mu_o}\int_{-\infty}^{\infty}\frac{d\omega}{2\pi}\int_{-\infty}^{\infty}\frac{d\omega'}{2\pi}\,\frac{1}{2\epsilon_g v_g}\sqrt{\frac{v_p(\omega)}{v_p(\omega')}}\Big(F'(\omega,z)F'(\omega',z)-R'(\omega,z)R'(\omega',z)\\ &+ F'(\omega,z)R'(\omega',z)-F'(\omega',z)R'(\omega,z)\Big)\exp\left(i(\omega+\omega')t\right).\end{aligned} \tag{2.146}$$

Integrating the Poynting vector over all time, we get:

$$\begin{aligned}\int_{-\infty}^{\infty}\mathbf{S}(z,t)dt &= v_g\int_{-\infty}^{\infty}\frac{d\omega}{2\pi}\Big(|F'(\omega,z)|^2-|R'(\omega,z)|^2\Big)\\ &= v_g\int_{-\infty}^{\infty}dt\Big(F'(z,t)^2-R'(z,t)^2\Big).\end{aligned} \tag{2.147}$$

This suggests that the forward and reverse wave momenta can be written respectively as

$$v_g\int_{-\infty}^{\infty}dt\,F'(z,t)^2 \text{ and } -v_g\int_{-\infty}^{\infty}dt\,R'(z,t)^2. \tag{2.148}$$

In a medium with dispersion, the ratio of energy flux to the total energy density is

for the "translated" variables are now:

$$i\omega F(\omega,z) = -v_g\frac{\partial F}{\partial z}, \tag{2.141}$$

$$i\omega R(\omega,z) = v_g\frac{\partial R}{\partial z}, \tag{2.142}$$

which are equivalent to Eq.(2.11) in the time domain.

We will need to have an expression for the field energy associated with the travelling waves to quantize the fields, so first we determine the energy flux in terms of the new variables. The energy flux is given by the Poynting vector $\mathbf{S}(z,t)$:

$$\mathbf{S}(z,t) = \frac{1}{\mu_o}\mathbf{E}(z,t)\mathbf{B}(z,t). \tag{2.143}$$

Using Eqs.(2.135,2.136), we get

$$\mathbf{E}(\omega,z) = \sqrt{\frac{v_p(\omega)}{2\epsilon_g v_g}}\Big(F'(\omega,z)+R'(\omega,z)\Big), \tag{2.144}$$

$$\mathbf{B}(\omega,z) = \sqrt{\frac{1}{2\epsilon_g v_g v_p(\omega)}}\Big(F'(\omega,z)-R'(\omega,z)\Big), \tag{2.145}$$

from which:

$$\begin{aligned}\mathbf{S}(z,t) = \frac{1}{\mu_o}\int_{-\infty}^{\infty}\frac{d\omega}{2\pi}\int_{-\infty}^{\infty}\frac{d\omega'}{2\pi}\,\frac{1}{2\epsilon_g v_g}\sqrt{\frac{v_p(\omega)}{v_p(\omega')}}\Big(&F'(\omega,z)F'(\omega',z)-R'(\omega,z)R'(\omega',z)\\ +\;&F'(\omega,z)R'(\omega',z)-F'(\omega',z)R'(\omega,z)\Big)\exp\left(i(\omega+\omega')t\right).\end{aligned} \tag{2.146}$$

Integrating the Poynting vector over all time, we get:

$$\begin{aligned}\int_{-\infty}^{\infty}\mathbf{S}(z,t)dt &= v_g\int_{-\infty}^{\infty}\frac{d\omega}{2\pi}\Big(|F'(\omega,z)|^2-|R'(\omega,z)|^2\Big)\\ &= v_g\int_{-\infty}^{\infty}dt\Big(F'(z,t)^2-R'(z,t)^2\Big).\end{aligned} \tag{2.147}$$

This suggests that the forward and reverse wave momenta can be written respectively as

$$v_g\int_{-\infty}^{\infty}dt\,F'(z,t)^2 \text{ and } -v_g\int_{-\infty}^{\infty}dt\,R'(z,t)^2. \tag{2.148}$$

In a medium with dispersion, the ratio of energy flux to the total energy density is

the group velocity v_g [53], so that the field energy will be:

$$H(t) = \int_{-\infty}^{\infty} dz \left(F'(z,t)^2 + R'(z,t)^2 \right), \tag{2.149}$$

or, in terms of the translated fields $F(z,t)$ and $R(z,t)$ (the exponential phase factors in Eq.(2.139,2.140) cancel out):

$$H(t) = \int_{-\infty}^{\infty} dz \left(F(z,t)^2 + R(z,t)^2 \right). \tag{2.150}$$

The normalization factors in Eqs.(2.135,2.136) were chosen so as to give this simple expression for the energy density. In terms of the italicized fields of Eqs.(2.12,2.13), the energy in Eq.(2.150) can be written:

$$H(t) = \int_{-\infty}^{\infty} dz \, \frac{1}{2} \left(\epsilon_g E(z,t)^2 + \frac{1}{\mu_o} B(z,t)^2 \right). \tag{2.151}$$

Chapter 3

Time-domain implementation of the model

This chapter presents the implementation of the laser theory described in the previous chapter. The progression followed is:

1.) This laser theory is implemented numerically as a time domain model, for Fabry-Perot lasers.

2.) The model is extended to DFB lasers.

The resulting large signal model takes into account longitudinal spatial hole burning, multimoded behaviour, and gives a quantum treatment of linewidth and intensity noise.

3.1 Fabry-Perot lasers

In the previous chapter, a theoretical framework in which complex travelling waves $\mathcal{F}(z,t)$ and $\mathcal{R}(z,t)$, experience gain as they flow past a number of gain centres in their trip around the laser cavity has been described. This section considers the implementation of this theory using a time domain algorithm, for Fabry-Perot lasers.

The electron populations of each gain centre change according to the rate equations Eq.(2.131) derived above. For computation, these travelling waves $\mathcal{F}(z,t)$ and $\mathcal{R}(z,t)$ are sampled at a fixed interval Δz along the cavity. The interval Δz is related to the simulation time step Δt through the group velocity v_g : $\Delta z = v_g \Delta t$, so that the sampled wave values $\mathcal{F}_n$ and $\mathcal{R}_n$ at $z = n\Delta z$ are moved at the next time step to $\mathcal{F}_{n+1}$ and $\mathcal{R}_{n-1}$, at points $z = (n+1)\Delta z$ and $z = (n-1)\Delta z$ respectively.

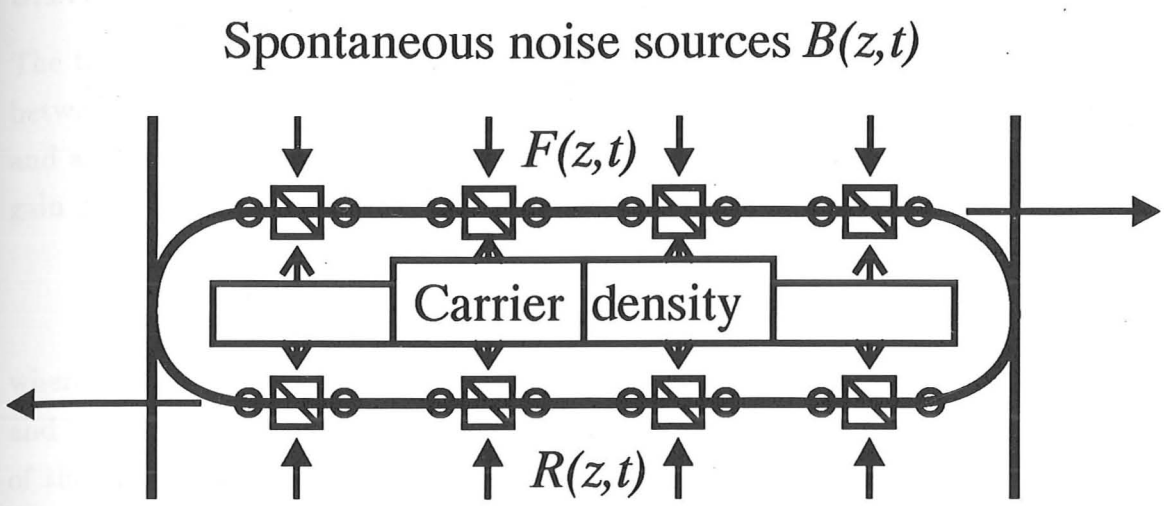

Figure 3-1: Travelling wave laser model showing four gain centres and six field sampling points along the length of the cavity.

Following Lowery [21], Sub-Nyquist field sampling is used to save computing time. In a laser, we are only interested in the field within a bandwidth B around the nominal laser frequency f_0. Outside this bandwidth, the gain and spontaneous emission spectra ensure that the field power is comparatively very small. We focus on this bandwidth by artificially shifting the spectral response of the laser down, from the nominal laser frequency, f_0, to zero frequency $f = 0$. Provided that we then keep the sampling time Δt small enough, so that the Nyquist bandwidth $1/\Delta t$ covers the bandwidth B, we will obtain a faithful picture of the real laser spectrum. To achieve this shift in frequency, both the Fabry-Perot cavity response, and the semiconductor material response must be shifted down to zero frequency.

The frequency response of an empty Fabry-Perot cavity is a periodic function, the period being the mode separation, so that no changes to the cavity structure have to be made. The modelled semiconductor material's gain curve is translated down from f_0 to zero frequency. Because complex fields are used, twice as many Fabry-Perot modes (spacing $1/2N\Delta t$) lie inside the modelled bandwidth $1/\Delta t$ as the number of sampling points N along the cavity.

Figure 3-1 shows a schematic view of the model: the gain centres are separated from each other by a small number of sampling points, so that typically 50 sampling points and 10 gain centres are used along the cavity. This generally gives a sufficiently accurate longitudinal carrier density profile. The separation between the gain centres is ΔL.

3.1.1 Modelling the gain curve

The frequency dependent gain is modelled using a digital filter. There is trade-off between an accurate modelling of the gain peak, requiring complex digital filtering, and a short computation time achieved using a very simple filter. One such simple gain filter is the first order Infinite Impulse Response (IIR) filter implemented by

$$y_n = g(1 - |\gamma|)x_n + \gamma y_{n-1} \tag{3.1}$$

where x_n and y_n are the sampled inputs and outputs respectively, g is the peak gain, and γ is a complex parameter, $|\gamma| < 1$, the amplitude of which controls the width of the gain curve, and whose phase controls the peak frequency of the filter. The power gain and the associated phase change of the filter transfer function $G(\omega)$ is shown as a function of frequency in Fig. (3-2), for $\gamma = 0.7$ and $g = 1$. The phase change is a consequence of the causality of the filter, whose output only depends on inputs at previous times. The relationship between the power and the phase is consistent with the Krammers-Krönig relation linking the real and imaginary parts of the refractive index. It can be expressed as: the real and imaginary parts of $G(\omega)$ form a Hilbert transform pair:

$$\Im m\{G(\omega)\} = \mathcal{H}\Big(\Re e\{G(\omega)\}\Big) = \int_{-\infty}^{\infty} \frac{\Re e\{G(\omega)\}}{\omega - \omega'} d\omega' \tag{3.2}$$

The effect of the this phase change is to introduce dispersion in the model. This results in a variation in the separation of the Fabry-Perot modes across the modelled bandwidth. This effect is generally small (less than 1%) for typical modelled gain curve widths.

The parameters for the digital filters can be determined from numerical fitting of an experimentally measured or a calculated gain curve. Figure (3-3) shows a calculated gain curve for GaAs material, and the dashed lines represent the modelled bandwidth.

The gain curve shown is for a temperature of 300K, with a carrier density of $2.5 \times 10^{18} \mathrm{cm}^{-3}$, assuming momentum-conserving electron-hole recombinations, using the method described in [54]. The numerical fit of the time-domain model filter to this gain curve is shown in Fig. (3-4). The digital filter used had a transfer function of the form

$$T(z) = \frac{A - Bz}{C - Dz} \tag{3.3}$$

For Fabry-Perot lasers, a good fit around the peak of the gain curve is required to

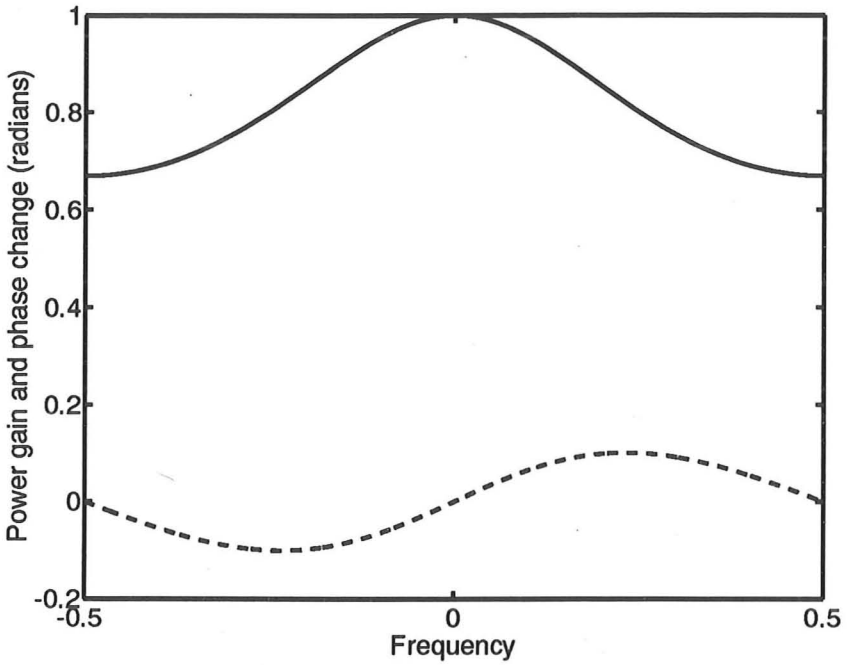

Figure 3-2: Power gain and phase change for the first order IIR digital filter in Eq. (3.1), with $g = 1$ and $\gamma = 0.7$.

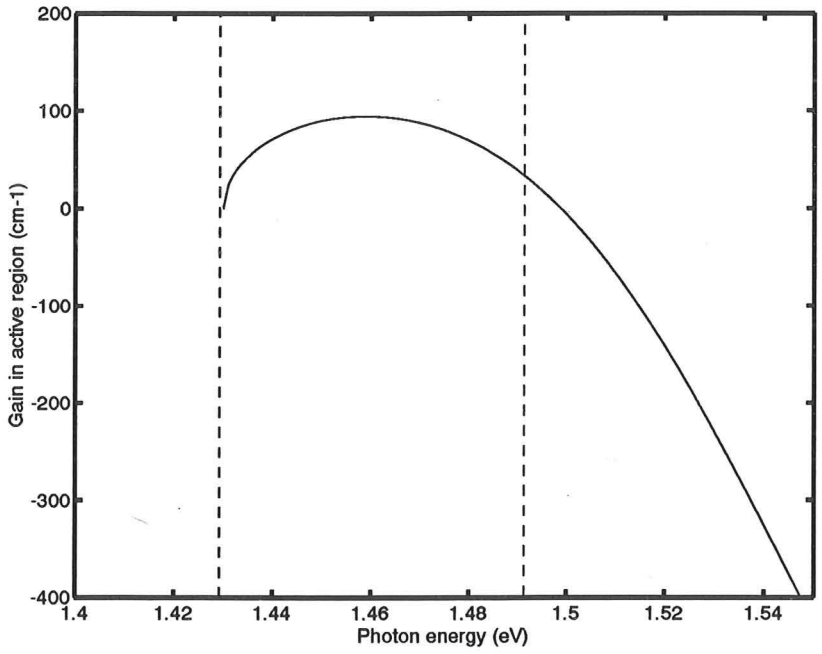

Figure 3-3: Calculated gain curve for GaAs material, for a carrier concentration of $2.5\times10^{18}\text{cm}^{-3}$, and a temperature of 300K. Momentum conserving electron-hole recombinations are assumed. The dashed lines show the bandwidth modelled using 60 section for a 300μm long laser.

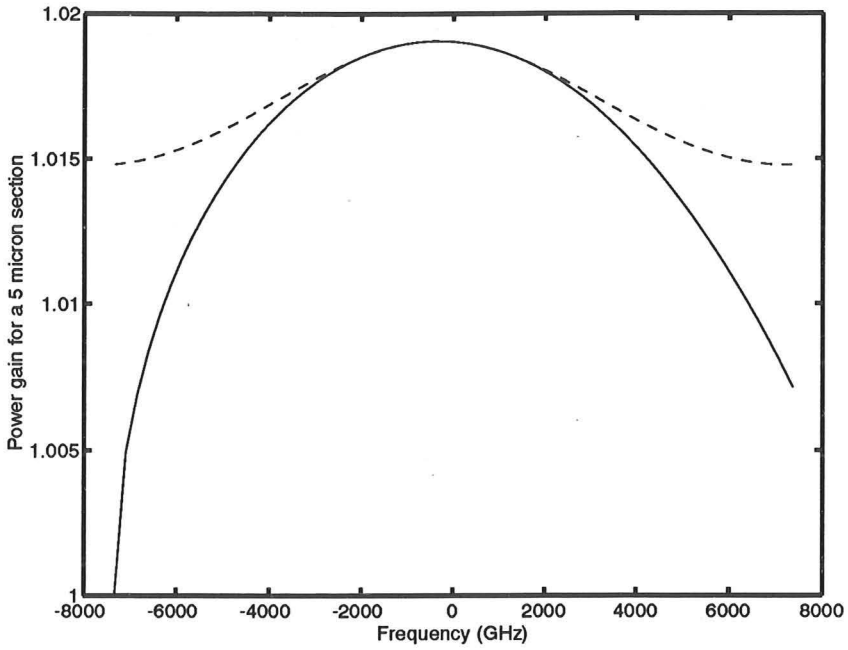

Figure 3-4: Calculated gain for one section for GaAs material (solid line), and best fit to a digital filter with one pole and one zero, over the modelled bandwidth. A 300μm long laser with 60 modelling sections is assumed, and the carrier density is $2.5\times10^{18}\text{cm}^{-3}$.

simulate a realistic spectrum. As seen in Fig. (3-4), this can generally be obtained because the shape of the gain curve away from the peak has little effect on the spectrum, so that the accuracy in these regions can be sacrificed. Higher order filters can be used if greater accuracy in the gain curve is of importance.

In a semiconductor material, changes in the carrier density cause changes in the refractive index, as well as changes in the gain. If the gain filter faithfully reproduced the semiconductor gain spectrum, then causality would ensure, through the Krammers-Krönig relationships, that the correct refractive index changes would also be modelled. However, the gain spectrum of a semiconductor material is too complex to reproduce faithfully with a simple digital filter. Considering the simple filter in Eq.(3.1), where the gain is determined by the parameter g, we see that the phase shift in fact does not change with changing gain: g is simply a scaling parameter with no frequency dependence. The refractive index variations, which are important in determining the performance of laser diodes, must therefore be determined differently. Following Lowery [55], a carrier-density dependent phase

change is introduced in the model.

Rather than using the transmission-line stub technique used by Lowery [55], the complex field representation used here enables the refractive index changes to be included by multiplying the complex wave amplitudes by a phase shift $\exp(i\phi)$ after each gain filter. The phase shift ϕ is calculated from the carrier density n_c and Henry's linewidth enhancement factor α_H [25]. The alpha factor is the change of the real part of the refractive index, over the change of its imaginary part:

$$\alpha_H = \frac{\Re e(dn/dn_c)}{\Im m(dn/dn_c)} \tag{3.4}$$

The complex amplitude gain is therefore

$$\sqrt{G}\exp(i\phi) = \exp(b\Gamma(n_c - n_t)\Delta L/2 + i\phi) = \exp(ink\Delta L) \tag{3.5}$$

where k is the wave vector. The real and imaginary parts of the refractive index are, from Eq.(3.5),

$$\Im m(n) = -b\Gamma(n_c - n_t)\Delta L/2k \quad \text{and} \quad \Re e(n) = \phi/k\Delta L \tag{3.6}$$

This gives the differential changes as

$$\Im m(\frac{dn}{dn_c}) = -b\Gamma\Delta L/2k \quad \text{and} \tag{3.7}$$

$$\Re e(\frac{dn}{dn_c}) = \alpha_H \Im m(\frac{dn}{dn_c}) = -\alpha_H b\Gamma\Delta L/2k \tag{3.8}$$

The phase shift is finally

$$\phi = -\alpha_H b\Gamma\Delta L n_c/2 \tag{3.9}$$

The spontaneous emission noise $\mathcal{B}'(z,t)$ as given by Eq.(2.128) is obtained by passing complex Gaussian white noise with independent real and imaginary parts through a filter with a power spectral response

$$g_n(\omega) = \hbar\omega\, n_{sp}(\omega)\left\{|g(\omega)^2| - 1\right\} \tag{3.10}$$

We approximate this by filtering Gaussian white noise with a Lorentzian digital filter.

The carrier rate equation (2.131), integrated over the timestep Δt gives the

Laser Parameters			
Cavity length	L	300	μm
Active region width	w	5.0	μm
Active region thickness	d	0.1	μm
Gain-slope×confinement fac.	$b\Gamma$	$1.5 * 10^{-16}$	cm^2
Inversion parameter at $n_t h$	n_{sp}	2.5	
Transparency carrier density	n_t	$1.5 * 10^{18}$	cm^{-3}
Gain-refractive index coupling	α_H	5.0	
Free space wavelength	λ	850	nm
Phase refractive index	n_p	3.5	
Group refractive index	n_g	4.0	
Gain curve FWHM	ΔF	3.5	THz
Facet power reflectivity	R	0.3	
Carrier lifetime	τ_n	4.0	ns

Table 3.1: Parameters for the modelled Fabry-Perot laser.

change in carrier density:

$$\Delta n_c(t) = \Big(D - \Gamma_c n_c - R(t)\Big)\Delta t + G_n(t) \tag{3.11}$$

$G_n(t)$ is the noise obtained by integrating $F_{n_c}(t)$ over the timestep Δt, and is Gaussian with mean square

$$< G_n(t)^2 >= \Big\{D + \Gamma_c n_c - R(t)\Big\}\Delta t \tag{3.12}$$

3.1.2 Modelling results for Fabry-Perot laser

Some modelling results are presented here to illustrate the capabilities of the time domain model. A Fabry-Perot index-guided laser diode is modelled, and unless specified otherwise, the parameters used are given in Table 3.1.

Ten gain sections were used along the cavity to show electron density variations and spatial hole burning. The travelling waves are sampled at 50 points along the cavity, making the modelled bandwidth equal to 100 Fabry-Perot mode spacings.

The laser threshold predicted by the model is 10.5 mA.

Consider first the dynamic laser operation: the output power of the laser during a step change in drive current from 10 to 20 mA is shown in Fig. (3-5). The considerable ringing which is shown exists because the gain compression has been left out for simplicity.

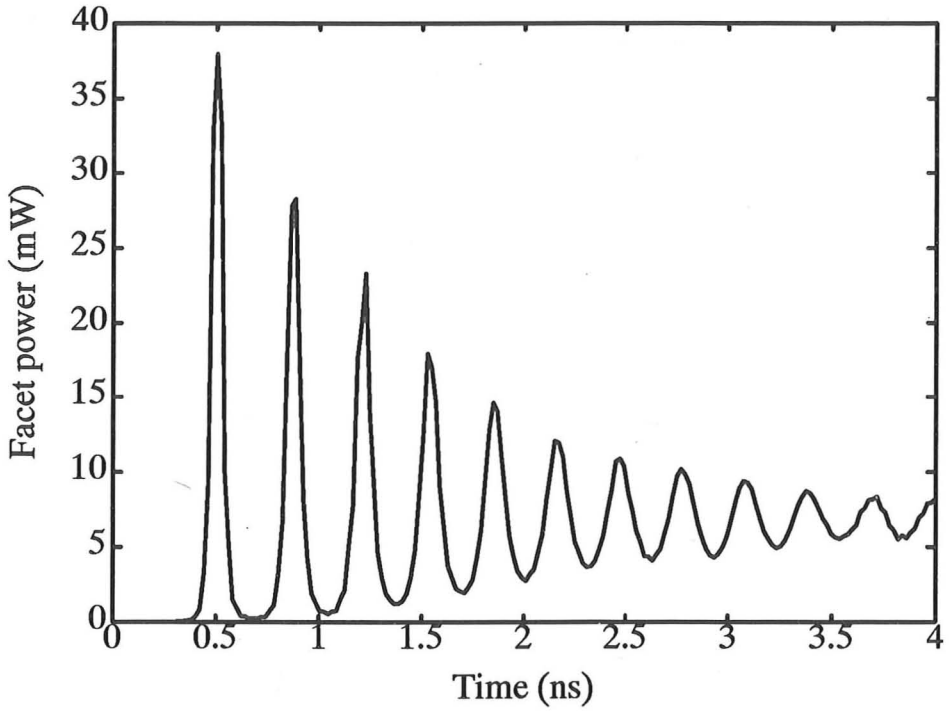

Figure 3-5: Facet power response to a current step from 10 to 20 mA.

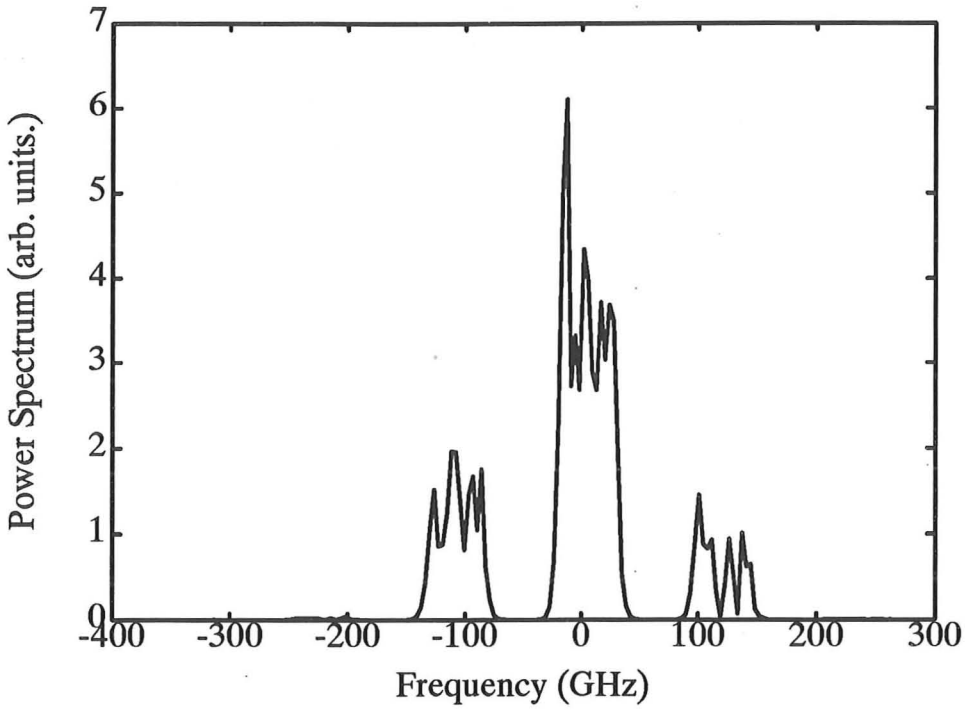

Figure 3-6: Optical spectrum for a gain switched pulse, showing three Fabry-Perot modes broadened by chirp.

The dynamic optical power spectrum is obtained by taking a Fast Fourier Transform spectrum of the complex field amplitude, and the spectral resolution is then limited by the sampling time. Figure (3-6) shows the spectrum of the first pulse of the transient of Fig. (3-5). Three Fabry-Perot modes are seen to be significantly excited, which are considerably broadened due to the frequency chirp caused by the large changes in carrier density. Steady state laser operation is examined by running the simulation until the initial transients have died away: Figure (3-7) shows the steady state electron density for a drive $I_d = 20$ mA, together with forward and reverse optical fluxes inside the cavity. Spatial hole burning occurs near the facets where the optical power density is largest. An important parameter, the CW optical spectrum is evaluated by starting the FFT of the output, once the initial transients have died away. Arbitrary resolution of the spectrum can be achieved by sampling during a sufficient time, and simulation noise must be reduced by averaging together the spectra obtained from different runs. If only every n data points are recorded to save computer memory, care must be taken to avoid aliasing. The spectrum is fitted to a Lorentzian curve to determine the linewidth. For a linewidth around 20 MHz,

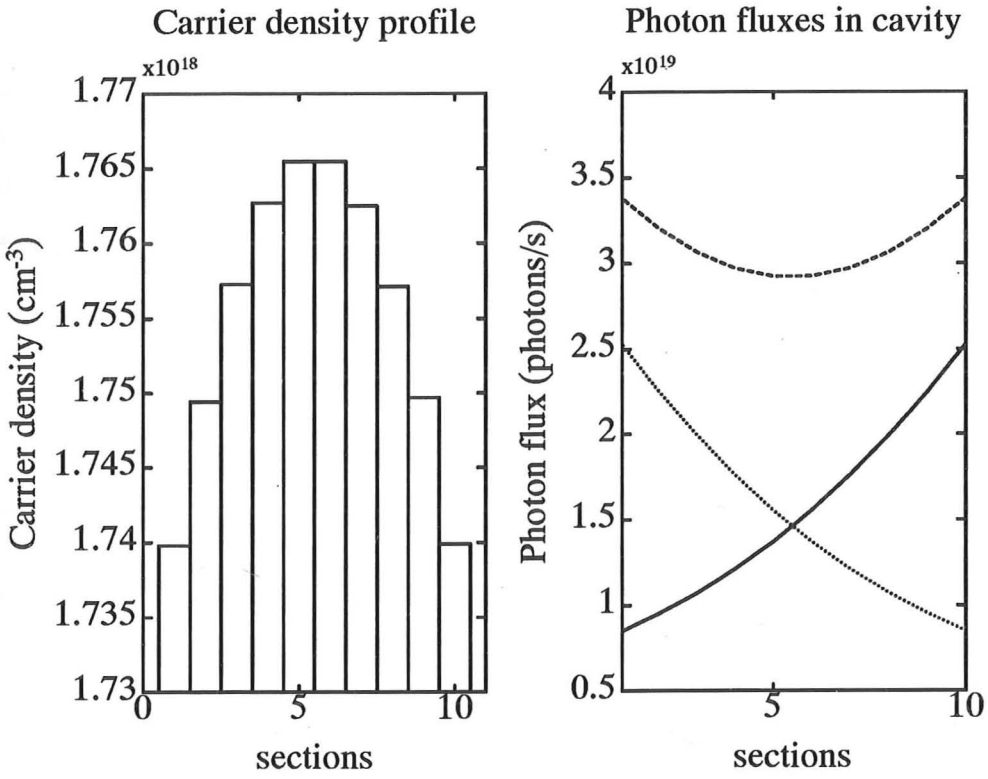

Figure 3-7: Optical power fluxes for forward and reverse propagating fields, and carrier density along the laser cavity.

a spectrum with a resolution of around 5 MHz is needed: a simulated time of 0.2 μs is required which takes 10 minutes on a HP-740 Workstation (with 10 sections along the cavity).

Accepted theories predict a Lorentzian shape for the spectrum of the modes of a Fabry-Perot laser. Below threshold, the full width at half maximum (FWHM) of a given Fabry-Perot mode of centre frequency ω is given by the corrected Schawlow-Townes formula [17]

$$\Delta f = \frac{\hbar\omega(1-R)^2/R}{2\pi P}\left(\frac{v_g}{L}\right)^2 n_{sp}(\omega) \tag{3.13}$$

where P is the total optical power output (both facets) for the mode in question. The partial inversion of the medium is taken into account through the factor $n_{sp}(\omega)$ evaluated at the mode frequency. This formula includes the "longitudinal excess spontaneous emission factor"

$$K = \frac{(1-R)^2}{R}\left(ln\frac{1}{R}\right)^2 \tag{3.14}$$

This factor increases the linewidth by about 12% for cleaved facets, over the Schawlow-Townes linewidth, and becomes large when facets are anti-reflection coated. This factor can be derived by assuming distributed noise sources with delta–function spatial and temporal correlations. A Green's function analysis in the frequency domain is used by Henry to evaluate the spectrum [27]. Expansion of the optical field in terms of non–power–orthogonal cavity modes has also been used to evaluate this factor [16, 17, 28, 30, 56]. Ujihara [26] calculates this factor by integrating the noise following a travelling wave as it propagates through laser the cavity. By contrast, in our model, the noise power is given by the requirement of preservation of the travelling wave commutators during the amplification process.

Note that the one–dimensional theory presented in chapter 2 cannot predict the transverse "Petermann" excess spontaneous emission factor [16], which is a three–dimensional effect. Our linewidths, as the model stands, are therefore only accurate for strongly index-guided lasers. The quantum theory for propagating fields in gain guided waveguides developed by Deutsch *et al* [57] should be used if gain or loss guided lasers are modelled.

Above threshold, gain saturation quells amplitude fluctuations, and effects a twofold reduction in the linewidth, while gain-refractive index coupling enhances the linewidth [25] by the factor $1+\alpha_H^2$. The lineshape predicted also displays side

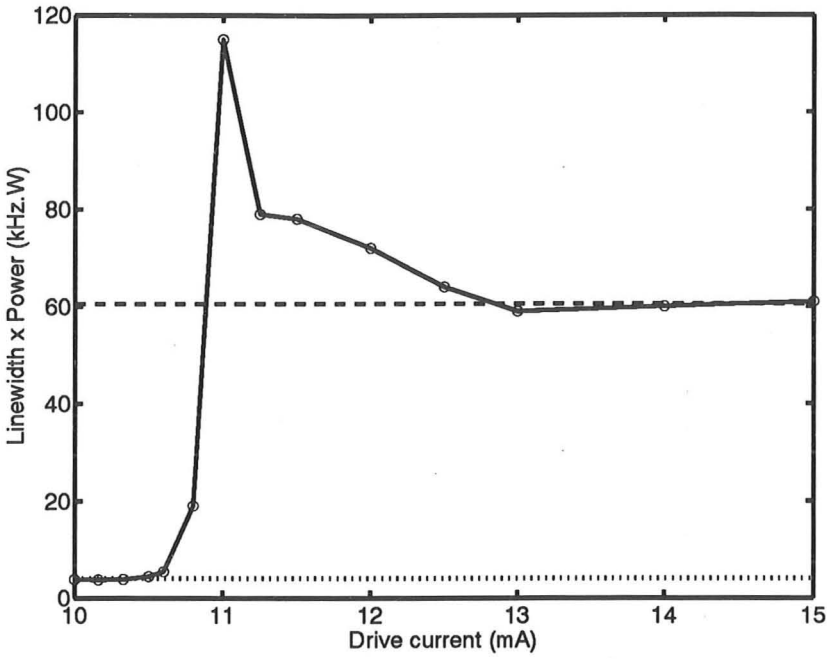

Figure 3-8: Simulated linewidth-facet power product against drive current (solid line), showing the transition around threshold ($I_{th} = 10.6$ mA).
Dotted line: theoretical limit below threshold, including longitudinal excess spontaneous emission factor.
Dashed line: theoretical limit above threshold (enhanced by $(1 + \alpha_H^2)/2$).

modes due to electron-photon resonance, and the FWHM of the central laser mode is given by the new modified Schawlow-Townes formula:

$$\Delta f = \frac{\hbar\omega(1-R)^2/R}{4\pi P}\left(\frac{v_g}{L}\right)^2 n_{sp}(\omega)(1+\alpha_H^2) \tag{3.15}$$

The formula Eq.(3.15) still includes the "excess spontaneous emission factor".

The spectra predicted by our model agree well with these theoretical formulas. Figure (3-8) shows the power $\times$ linewidth product for the main Fabry-Perot mode of the laser, plotted against drive current. The gain-refractive index coupling factor α_H was here set to 5.0, and the simulation data agree well with the theoretical expressions, including the jump at threshold. Figure (3-9) shows the influence of the gain-refractive index coupling factor α_H on the linewidth at a fixed drive of 15 mA. The predicted quadratic dependence of the linewidth Δf on α_H is demonstrated. Our quantum mechanical treatment of the noise associated with the amplification

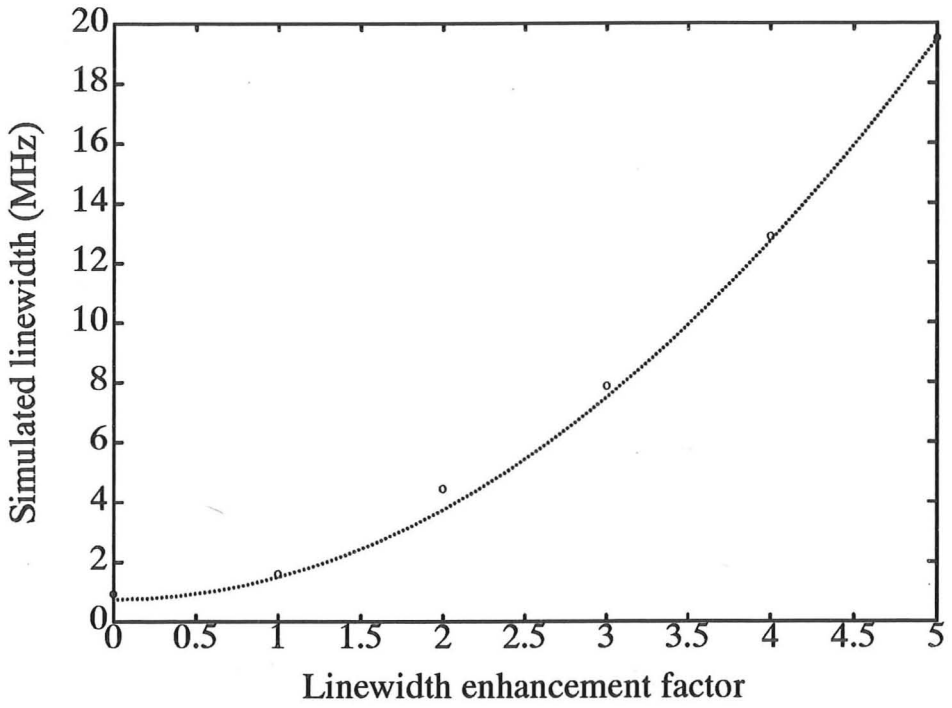

Figure 3-9: Linewidth against Henry's linewidth enhancement factor α_H for a fixed facet power.

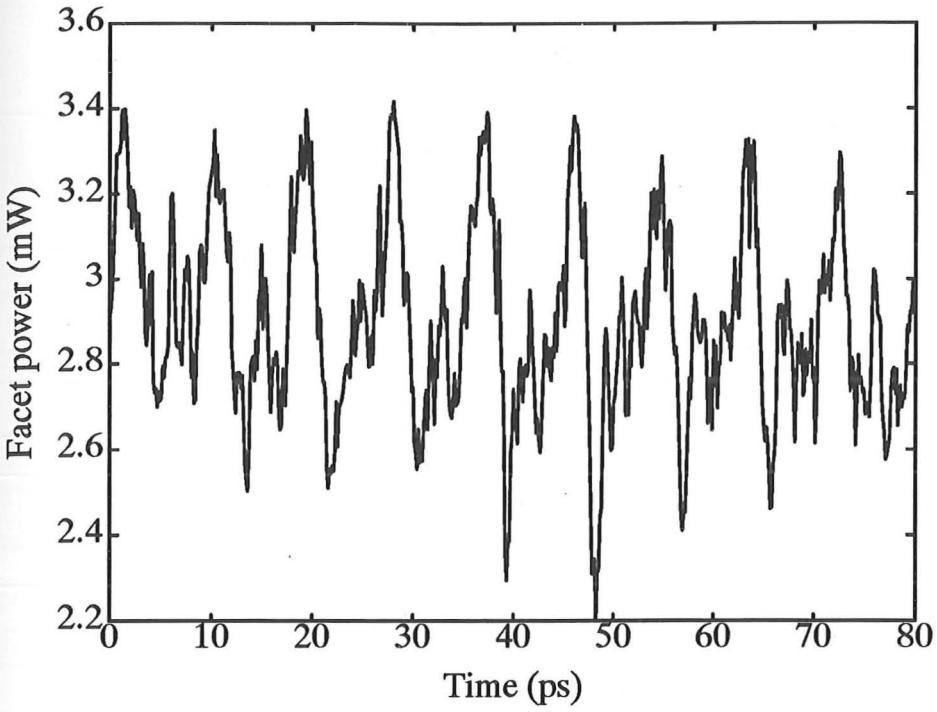

Figure 3-10: Facet power picosecond fluctuations due to beating between the Fabry-Perot modes, for C.W. operation with a side-mode suppression ratio of 25dB. The period is 8ps, corresponding to a longitudinal mode spacing of 125 GHz.

process, given in section 2.5, includes the longitudinal excess spontaneous emission factor. The line-widths predicted will be correct for any facet reflectivities, and for any cavity structure. This can be seen from consideration of a laser below threshold: the gain is then constant, and a spectrum can be derived analytically, in a similar fashion as in section 2.4, which agrees with the corrected line-width formulas.

The optical field simulated by the time-domain model includes the contributions of all the excited laser modes. The field must be filtered in the frequency domain in order to separate the different modes. The different modes beat with each other, leading to large fluctuations on a picosecond timescale, as shown in Fig. (3-10) for CW operation. The periodicity of these fluctuations, 8 ps, corresponds to the cavity round trip time. Sizeable fluctuations occur even when the side modes are strongly suppressed. These fluctuations are not generally given by most laser models, and may have to be considered when using high speed modulation of the optical fields to transmit information.

The beating between modes becomes much more important in dynamic oper-

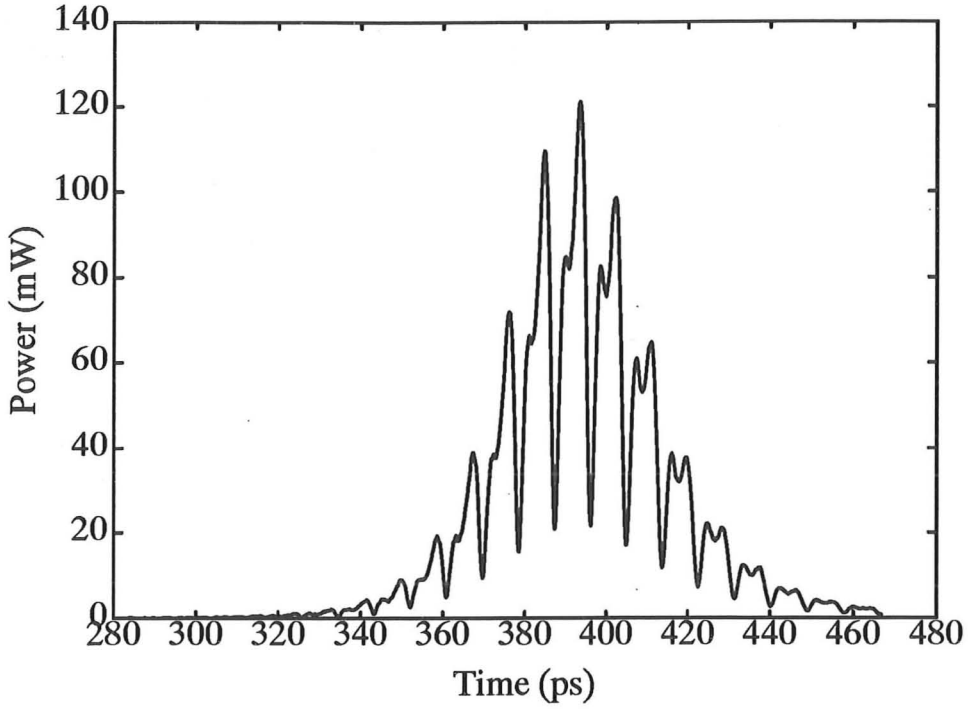

Figure 3-11: Detail of facet power fluctuations on a picosecond time-scale for the first pulse in Fig. (3-5).

ation, when the spectrum is rarely single moded. Figure (3-11) shows a detailed picture of the simulated facet power for the first gain switched pulse of Figure (3-5). Strong fluctuations within the pulse envelope are visible, indicating that side modes are strongly excited. Since the relative phases between different modes are random, averaging the facet powers over a number of simulation runs, smooths out the temporal structure of the pulse, and we are left only with the envelope of the gain switched pulse as in Figure (3-5). This structure of gain switched pulses, with a periodicity of the cavity round trip time, can be observed experimentally using autocorrelation techniques [58, 59].

3.2 Extension to DFB lasers

Single frequency lasers are essential for long distance, high bit-rate optical communications. In most dynamic single mode laser diodes, the frequency selection is due to a Bragg grating written into the waveguide. The periodic variation of the refractive index or the modal gain along the cavity causes a distributed reflection of

the forward and reverse propagating waves, providing the optical feedback, which in Fabry-Perot lasers, is due to the facet reflections. Increasingly complex structures are used to provide stable single mode operation with low chirp, by introducing phase shifts into the gratings ($\lambda/4$ and $2\times\lambda/8$ structures), chirped gratings, or using second order or gain coupled gratings. The photon and carrier densities along the laser interact with each other to affect considerably the laser operation, possibly causing mode jumps or instabilities. Modelling tools are therefore useful for understanding and developing DFB lasers diodes.

The numerical implementation of the laser model just presented for Fabry-Perot lasers, is extended here to lasers with Bragg gratings. Unlike the Fabry-Perot case, where the travelling wave equations of motion can be integrated directly, the time dependent coupled wave equations for the Bragg sections can only be solved approximately when no assumptions are made about the evolution of the fields.

3.2.1 The Coupled Wave Equations

The starting point is the time dependent coupled wave equations, derived from the slowly varying amplitude approximation [36, 60]:

$$\left(\frac{1}{v_g}\frac{\partial}{\partial t}+\frac{\partial}{\partial z}\right)F = -(i\delta - g + \alpha_s)F + i\kappa_{RF}R + G_F(z,t) \qquad (3.16)$$

$$\left(\frac{1}{v_g}\frac{\partial}{\partial t}-\frac{\partial}{\partial z}\right)R = -(i\delta - g + \alpha_s)R + i\kappa_{FR}F + G_R(z,t) \qquad (3.17)$$

Where:

- $F(z,t)$ and $R(z,t)$ are the complex forward and reverse waves, given in section (2.2.7).
- δ expresses changes in the refractive index due to changes in the carrier density,
- g is the gain due to the electrons in the conduction band,
- α_s is the waveguide scattering and absorption loss,
- κ_{RF} and κ_{FR} are the coupling coefficients for reverse-to-forward wave and forward-to-reverse wave respectively. For index gratings, $\kappa_{RF} = \kappa^*_{FR}$, for gain gratings, $\kappa_{RF} = -\kappa^*_{FR}$.

- $G_F(z,t)$ and $G_R(z,t)$ are spontaneous noise sources identical to those for a Fabry-Perot laser.

The coupled wave equations (3.16,3.17) can be grouped into three terms (ignoring the noise terms which do not affect the mean motion):

- On the right hand side, the wave equation part: if the left hand sides were zero, these equations would describe distortionless propagation for forward and reverse waves.
- First terms on the left hand side: a propagation part. These describe gain, losses and variations in refractive index. Including these terms, but without the coupling terms, the equations describe propagation in a Fabry-Perot laser, for example.
- Last, the coupling terms. These describe the effect of the reflections caused by the grating.

3.2.2 Distortionless propagation in the time domain model

In the time domain model, the fields are sampled in space and time, at intervals Δz and $\Delta t = \Delta z / v_g$:

$$F(n\Delta z, k\Delta t) \rightarrow F_{n,k} \tag{3.18}$$

$$R(n\Delta z, k\Delta t) \rightarrow R_{n,k} \tag{3.19}$$

$$\tag{3.20}$$

The laser cavity of length L is thus divided into a number $NSEC = L/\Delta z$ of sections.

The right hand sides of Eqs. (3.16,3.17) can be directly integrated along the paths of propagation for the waves ($dt = v_g dz$ for forward waves, $dt = -v_g dz$ for reverse waves). The fields at time step $k+1$ are related to the fields at the previous time step k by:

$$\int_0^{\Delta t} d\tau \left(\frac{1}{v_g} \frac{\partial}{\partial t} + \frac{\partial}{\partial z} \right) F\Big((n-1)\Delta z + v_g \tau, k\Delta t + \tau\Big) =$$

$$\frac{1}{v_g} \Big[F\Big(n\Delta z, (k+1)\Delta t\Big) - F\Big((n-1)\Delta z, k\Delta t\Big) \Big] = 0 \tag{3.21}$$

and

$$\int_0^{\Delta t} d\tau \left(\frac{1}{v_g}\frac{\partial}{\partial t} - \frac{\partial}{\partial z}\right) R\Big((n+1)\Delta z - v_g\tau, k\Delta t + \tau\Big) =$$

$$\frac{1}{v_g}\left[R\Big(\Delta z, (k+1)\Delta t\Big) - R(\Big(n+1)\Delta z, k\Delta t\Big)\right] = 0 \tag{3.22}$$

Which gives

$$F_{n,k+1} = F_{n-1,k} \tag{3.23}$$

$$R_{n,k+1} = R_{n+1,k} \tag{3.24}$$

The forward and reverse fields thus jump along by one spatial step at every time step, without interfering with each other.

3.2.3 Propagation with gain, losses and refractive index changes

If now the propagation part of Eqs.(3.16,3.17) is taken into account, the fields are subject to gain, loss and phase changes. In the first order, for small enough sampling intervals (i.e. $\Delta z|i\delta - g + \alpha_s| \ll 1$), the left hand sides of Eqs. (3.16,3.17) approximate to

$$\frac{1}{v_g}(F_{n,k+1} - F_{n-1,k}) \tag{3.25}$$

$$\frac{1}{v_g}(R_{n,k+1} - R_{n+1,k}) \tag{3.26}$$

while the left hand sides approximate to

$$-\Delta t(i\delta - g + \alpha_s)F_{n-1,k} \tag{3.27}$$

$$-\Delta t(i\delta - g + \alpha_s)R_{n+1,k} \tag{3.28}$$

Thus, the fields at time step $k+1$ are related to the fields at time step k by:

$$F_{n,k+1} = F_{n-1,k} - \Delta z(i\delta - g + \alpha_s)F_{n-1,k} \tag{3.29}$$

$$R_{n,k+1} = R_{n+1,k} - \Delta z(i\delta - g + \alpha_s)R_{n+1,k} \tag{3.30}$$

This describes propagation in a Fabry-Perot laser, for example. When the gain or losses or refractive index changes are such that the condition $\Delta z|i\delta - g + \alpha_s| \ll 1$ is no longer satisfied, the first order approximation is poor. *An exact solution* can be obtained by integrating along the paths of the forward and reverse waves as above, leading to:

$$F_{n,k+1} = \exp\Big(-\Delta z(i\delta - g + \alpha_s)\Big)\, F_{n-1,k} \tag{3.31}$$

$$R_{n,k+1} = \exp\Big(-\Delta z(i\delta - g + \alpha_s)\Big)\, R_{n+1,k} \tag{3.32}$$

3.2.4 Propagation with coupling of the forward and reverse waves

If the coupling terms are now included in the wave equations, the first order approximation gives, in the same way as for the Fabry-Perot case above:

$$F_{n,k+1} = F_{n-1,k} - \Delta z(i\delta - g + \alpha_s)F_{n-1,k} + i\Delta z\kappa_{RF}R_{n,k} \tag{3.33}$$

$$R_{n,k+1} = R_{n+1,k} - \Delta z(i\delta - g + \alpha_s)R_{n+1,k} + i\Delta z\kappa_{FR}F_{n,k} \tag{3.34}$$

This is the first order approximation, used by Lowery, for instance, in his time domain model.

This first order approximation will be accurate provided both

$$\Delta z|i\delta - g + \alpha_s| \ll 1 \quad \text{and} \tag{3.35}$$

$$\Delta z|\kappa_{FR}|, \Delta z|\kappa_{RF}| \ll 1 \tag{3.36}$$

If these conditions are not satisfied, the first order approximation will be poor, and number of sections in the simulation should be increased. *It is no longer possible* to integrate exactly the coupled wave equations as in the Fabry-Perot case, since both equations are no longer independent, and the paths of integration for the forward and reverse waves are different.

Table 3.2 shows the effect on the accuracy in output power of different numbers of sections. The modelling parameters are taken from the COST exercise no.2, and are for a 1mm long, $\lambda/4$ DFB with $\kappa L = 1$. The drive current is fixed at 100 mA. The error compared with the value ($P = 5.209$ mW) obtained with the CLADISS and TFL programmes is seen to decrease slowly with the number of sections. Dynamic behaviour also is significantly affected by the number of sections, as shown in Figure

Calculated Power (mW) and % error				
Number of sections	First Order Method		Transfer Matrix Method	
10	4.96mW	4.8%	5.178mW	0.5%
20	5.09mW	2.3%	5.198mW	0.2%
40	5.14mW	1.8%	5.207mW	0.1%

Table 3.2: Accuracy of first order and transfer matrix models.

(3-12). The figure shows the facet power response of a 400μm long uniform DFB with κL=3.2, to a current step from 70 to 90 mA. The other device parameters are as in Table (6.2.2). Due to spatial hole burning the laser operates in the (+1) mode. Except for the two bottom curves, the power response is calculated using the first order approximation with different numbers of sections: from top to bottom, 20, 30, 40, 50, 60, 80, 100 and 150 sections. The response is seen to converge only slowly with increasing numbers of sections.

3.2.5 Improvement of the model accuracy: Transfer Matrix Method

Fortunately, by making certain assumptions, it is possible to increase considerably the accuracy of the model. The assumption made is that the fields in a given section, during a given time step, vary in time as:

$$\frac{1}{v_g}\frac{\partial F(z,t)}{\partial t} = \beta F(z,t) \tag{3.37}$$

$$\frac{1}{v_g}\frac{\partial R(z,t)}{\partial t} = \beta R(z,t) \tag{3.38}$$

The meaning of this assumption is that the variations of the fields over the duration of a single time step is smooth: the laser is single moded, or else if multimoded, the period of the beat signal between the modes is significantly longer than the time step. This condition is nearly always satisfied, since the beat period between two adjacent laser modes is of the order of the number of sections modelled multiplied by the modelled time step. The complex parameter β has a similar role, to the μ-factor and the mode frequency combined, in the Power Matrix Method.

Using this assumption, the coupled mode equations (3.16,3.17) can be written

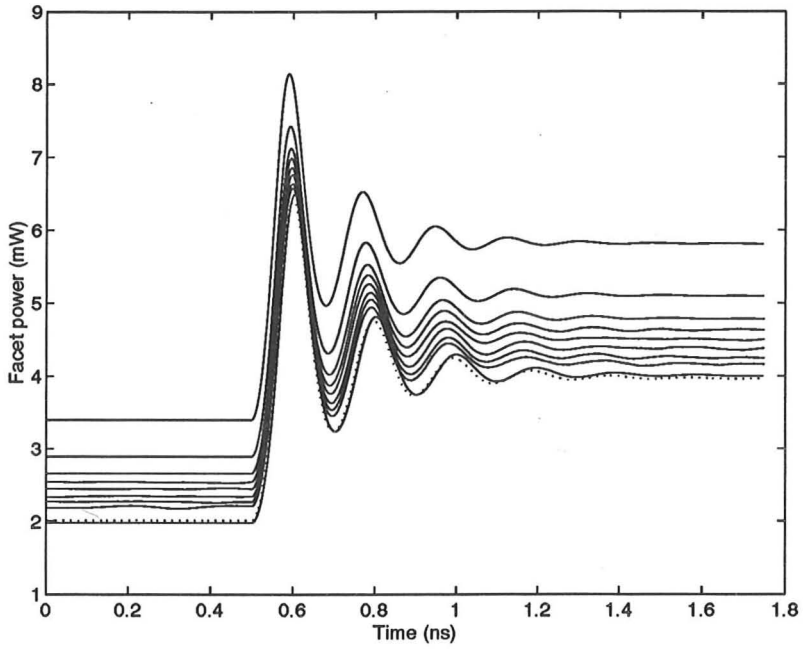

Figure 3-12: Power response of uniform DFB with $\kappa L = 3.2$, to a current step from 70 to 90 mA, calculated using different time domain models. From top to bottom: first order approximation using 20, 30, 40, 50, 60, 80, 100 and 150 sections, and then transfer matrix method, using 10 and 30 sections (dots).

(ignoring the noise terms) as

$$\frac{\partial}{\partial z}F(z,t) = -(i\delta - g + \alpha_s + \beta)F(z,t) + i\kappa_{RF}R(z,t) \tag{3.39}$$

$$-\frac{\partial}{\partial z}R(z,t) = -(i\delta - g + \alpha_s + \beta)R(z,t) + i\,\kappa_{FR}F(z,t) \tag{3.40}$$

Since the time derivatives have vanished, the coupled mode equations can now be integrated between $z = n\Delta z$ and $z = (n+1)\Delta z$, for constant t. Performing the integration, the fields at time step $k+1$ are now given in terms of the fields at time step k by:

$$\begin{bmatrix} F_{n+1,k+1} \\ R_{n,k+1} \end{bmatrix} = \frac{\exp(\beta\Delta z)}{\gamma\cosh(\gamma\Delta z) + (i\delta - g + \alpha_s + \beta)\sinh(\gamma\Delta z)} \times \begin{bmatrix} \gamma & i\kappa_{RF}\sinh(\gamma\Delta z) \\ i\kappa_{FR}\sinh(\gamma\Delta z) & \gamma \end{bmatrix} \begin{bmatrix} F_{n,k} \\ R_{n+1,k} \end{bmatrix} \tag{3.41}$$

where the propagation constant is

$$\gamma^2 = (i\delta - g + \alpha_s + \beta)^2 + \kappa_{RF}\kappa_{FR} \tag{3.42}$$

The number β may vary from section to section, from time step to time step, and may even be different for the forward and reverse waves. It may be estimated in several different ways:

- Simply setting $\beta = 0$. This will be accurate when the fields do not vary significantly over one time step (i.e. $|\ln(F_{n,k+1}/F_{n,k})|, |\ln(R_{n,k+1}/R_{n,k})| \ll 1$) which means that the mode frequency is close to the middle of the stop band.

- Estimate the value for time step k to $k+1$ using the actual changes for the previous time step:

$$\beta = \ln(F_{n,k}/F_{n,k-1})/\Delta z \quad \text{or } \beta = \ln(R_{n,k}/R_{n,k-1})/\Delta z \tag{3.43}$$

- Calculate the value self-consistently, for every section separately; Using a starting guess for β, compute $F_{n+1,k+1}$ and $R_{n,k+1}$ from $F_{n,k}$ and $R_{n+1,k}$. Then take

$$\beta = \ln(F_{n+1,k+1}/F_{n+1,k})/\Delta z \tag{3.44}$$

Obtain new estimates for $F_{n+1,k+1}$ and $R_{n,k+1}$ using this β, and so on until

successive changes are smaller than a set limit.

The last way is the most accurate, and the first way the least accurate. For static modelling, the last two ways should be equivalent. In practice, when considering static and dynamic modelling of the output power, all three methods are almost indistinguishable, and estimating a single instantaneous frequency β constant throughout the laser from the previous time step is a good compromise between excessive computing time and accuracy.

Table 3.2 shows the accuracy of the modelled output power, when using Eq.(3.41). Very few sections can be used to obtain a satisfactory accuracy. Figure (3-12) shows the dynamic responses to a 70 to 90 mA current step, as obtained with this method for 10 and 30 modelled sections: improvement in the dynamic performance is also clearly obtained. Figure (3-13) shows the differences in the reflection and transmission coefficients, estimated using the first order approximation and exactly, using the transfer matrix method, against the frequency deviation from the Bragg frequency. This is a typical case for a 300μm long DFB with $\kappa L = 4$, using 20 sections in the model. Around the Bragg frequency, the reflections given by both methods are very similar, but the transmissions show a noticeable difference. The first order approximation overestimates the transmission, which leads to the poor performance shown in Fig. (3-12).

It is also possible for β in Eqs.(3.37) and (3.38) to be different for the forward and reverse waves. This approach is theoretically more appealing and justifiable, but the improvements in the simulation accuracy were too small to justify the increase in computation time.

3.2.6 Summary

Bragg gratings can be simulated in the time domain model in different ways. The two ways presented here should give the same results, provided enough sections are used. The main advantages and disadvantages are as follows:

- The first order approximation method, Eqs. (3.33,3.34) involves less computation, and is easier to implement. It is however less accurate, especially in the dynamic regime, and for large coupling coefficients.

- The "transfer matrix method", Eq.(3.41), involves more calculation for every time step. For an equal number of sections, it is about 40% slower. However it is more accurate, so that less sections need to be modelled, which can speed

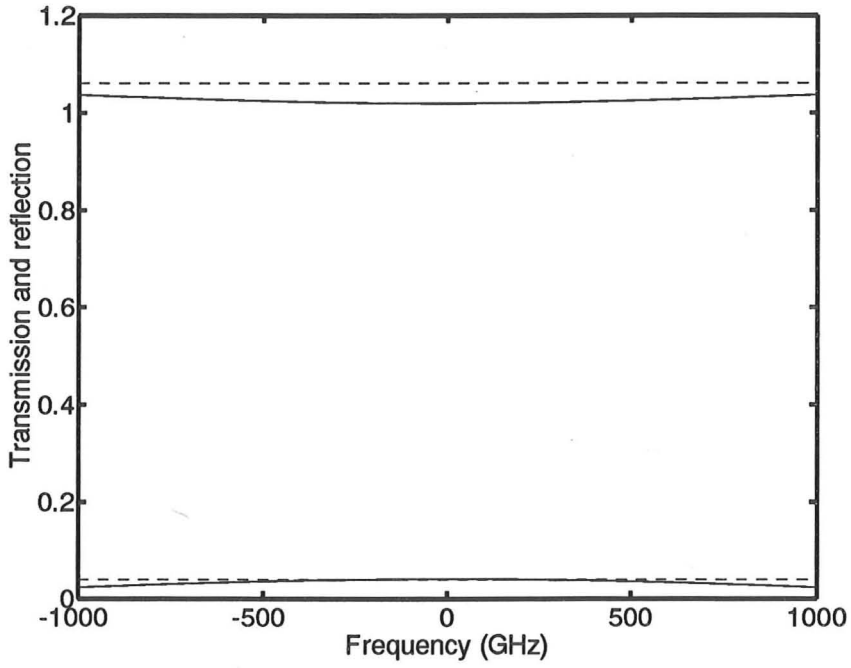

Figure 3-13: Reflection and transmission for one DFB section, calculated using the transfer matrix method (solid), and the first order approximation. A 300μm long DFB laser with $\kappa L = 4$ is modelled. 20 sections are used, and the gain is 40cm^{-1} in this section.

up simulations greatly. One advantage is that the results obtained will be less dependent on the modelling details.

The modelling of the noise sources and carrier rate equations is the same as that presented earlier for the Fabry-Perot laser.

3.3 Noise and small signal analysis

The large signal model can be used to determine small signal and noise characteristics. By suppressing the noise sources, the model becomes deterministic: the dominant laser mode takes over, and the side modes disappear as they are below threshold and no longer driven by spontaneous noise. The response of the laser to different perturbations can then be monitored to obtain information about small signal responses or noise characteristics.

To determine small signal responses like the FM and AM modulation characteristics, an impulse in drive current is applied on top of the normal drive current. The subsequent phase and amplitude transients can then be Fourier transformed to recover the FM and AM modulation characteristics.

For the noise analysis, impulses in the various types of noises are applied to the model, one at a time, in the different sections along the laser. The subsequent transients are analysed. Taking into account the lack of correlation between the individual noise sources, and assuming linearity, the overall mean fluctuations in phase and amplitude can be determined by summing the individual responses. This type of noise analysis is faster than just running the model with the noise sources, and averaging the fluctuations over a very long time. In addition it also gives the contributions of the different noise sources to quantities like the linewidth and intensity noise.

The accurate dynamic response obtained with the Transfer Matrix Method makes a precise small signal and noise analysis possible.

3.4 Conclusion: Time domain algorithm

The implementation and capabilities of a large signal travelling wave model for laser diodes have been presented. The laser model is capable of calculating multimoded C.W., small signal and large signal modulation characteristics, including effects of longitudinal hole burning.

The quantum theory is implemented using the time-domain algorithm pioneered for laser diodes by Arthur Lowery in his Transmission Line Laser Model [21]. The time domain algorithm used here is an improved version:

a) Allowing the optical fields to be represented by *complex* variables instead of real ones brings the implementation conceptually closer to the semiclassical or quantum theories, upon which the model can be based. Practically, the use of complex field variables doubles the simulated optical bandwidth, and makes the phase shifts required to model refractive index changes or gain coupled gratings easier to implement.

b) A transfer matrix method is presented which greatly improves the dynamic and static accuracy when modelling DFB lasers. This enables fewer modelling sections to be used along the laser, and can save considerable computing time, as this increases as the square of the number of sections.

These improvements allow the model to be used interactively, on a personal computer (486-PC). Written in C programming language, and interfacing with the Matlab mathematical processing environment, the laser modelling package operates under Microsoft Windows.

Chapter 4

Wigner distribution and maximum entropy method

Dispersion in optical fibres limits the bandwidth of communications, and the optical spectrum is an important parameter for modulated laser diodes. The time domain model presented in the last two chapters represents the optical output as a series of complex fields sampled in time: the simulated spectral information is not directly available, but must be extracted from the calculated time-series. Up till now, time domain models [21] have relied exclusively on the Discrete Fourier Transform to extract the frequency information. In this chapter, the application of two numerical methods to the study of the spectrum of laser diodes is examined for the first time.

First, the Wigner distribution is shown to display the dynamic power-spectrum of a laser with a combined time-frequency resolution greater than that obtained by linear spectrometers. It is suggested that it could be used as a tool for examining the spectral shifts of modulated or pulsing laser diodes.

The maximum entropy method of spectral estimation is then shown to reduce the noise and minimize the windowing effect, compared to methods based on Discrete Fourier Transforms, when estimating the power spectrum from the time-domain model data.

4.1 Wigner Distribution and Spectral Dynamics of Lasers

The Wigner distribution is a simultaneous representation of a signal in both time and frequency domains. This section discusses the Wigner distribution as an instrument

independent method of displaying the time-frequency response of a laser transmitter. This is important in long haul communication systems using semiconductor lasers, which exhibit chirp. If the type of spectrometer for measuring the spectrum as a function of time is known, so that the instrument's impulse response is known, then the Wigner distribution can be recovered. This distribution is then identical to that obtained using a different instrument with a different resolution. Examples of the time resolved spectra, obtained using two different instruments, are shown for a gain switched laser. They are compared to the Wigner distribution obtained by deconvolution.

4.1.1 Introduction

Chirping in semiconductor laser diodes under large signal modulation, is one of the major limiting factors for improving the bandwidth of long-haul optical fibre communications. For this reason, a considerable amount of research into the spectral dynamics of laser diodes is being carried out: Experimentally, measurements of the time dependent optical spectrum of modulated lasers have been carried out, which provide us with information about how the optical spectrum varies with time [61]. However, the time dependent optical spectra measured in this way depend upon the characteristics of the spectral analysers that are used.

Use of large signal, time domain models of laser diodes, like the ones presented in this dissertation, is helpful for device simulation and design. To access the spectral information in their sampled optical fields, Discrete Fourier Transforms can be used. But again, for modulated lasers, the time dependent spectrum depends on the way that it is calculated.

Since the time-dependent spectrum of an optical signal depends on the characteristics of the system used to measure it, it cannot be a fundamental description of the optical signal itself. But, provided one knew the characteristics of the measuring system, would it not be possible to recover, from the time dependent spectrum, a description of the optical signal which did not depend on the measurement system? Indeed, a possible candidate for this description is the Wigner distribution.

The Wigner distribution, first introduced in quantum mechanics [62], has received much attention in signal processing, as a simultaneous representation of a signal in time and frequency [63, 64]. The Wigner distribution for a continuous

signal $s(t)$ can be defined as:

$$W(t,f) = \int_{-\infty}^{\infty} d\tau\, s(t+\tau/2)s^*(t-\tau/2)\exp(-i2\pi f\tau). \tag{4.1}$$

Properties of the Wigner distribution have already been discussed at length elsewhere [63–67]. We recall only some properties which make the Wigner distribution an attractive time-dependent spectrum:

1) The Wigner distribution is a real function of time and frequency (although it takes negative values for all except Gaussian signals).

2) Its integral over all times is the time-averaged spectrum of the signal.

3) Its integral over all frequencies is the power at a time t.

4) If the signal is translated by a certain amount in time or in frequency, so is its Wigner distribution.

5) If a signal is limited in time or bandwidth, its Wigner distribution also vanishes outside those limits.

6) The modulus square of the inner product of two signals $s(t)$ and $u(t)$ is the integrated product of their respective Wigner distributions $W_s(t,f)$ and $W_u(t,f)$:

$$|\int_{-\infty}^{\infty} d\tau s(\tau)u^*(\tau)|^2 = \int_{-\infty}^{\infty} dt \int_{-\infty}^{\infty} df\, W_s(t,f)W_u(t,f). \tag{4.2}$$

The convolution of two Wigner distributions will therefore be positive everywhere.

8) The instantaneous frequency of the signal, equal to the rate of change of phase, is the first moment in f of the Wigner Distribution:

$$f(t) = \frac{\int_{-\infty}^{\infty} fW(t,f)df}{\int_{-\infty}^{\infty} W(t,f)df}. \tag{4.3}$$

4.1.2 Relation between the experimental time-resolved spectrum and the Wigner distribution

As shown by Brenner *et al* [68], the connection between the Wigner distribution, which can assume negative values, and the squared output of a filtering device

used to measure the physical spectrum of a signal, is a simple one: if $g_f(t)$ is the impulse response of the filtering device (such as a grating), then the experimental time-resolved spectrum $P(t, f)$ of a signal $s(t)$ is:

$$P(t,f) = |\int_{-\infty}^{\infty} d\tau\, s(t-\tau)g(\tau)|^2 = \int_{-\infty}^{\infty} dt \int_{-\infty}^{\infty} df\, W_s(t,f)W_g(t,f), \qquad (4.4)$$

where

$$W_g(t,f) = \int_{-\infty}^{\infty} d\tau\ g_f(t-\tau/2)g_f(t+\tau/2)\exp(-i2\pi f\tau), \qquad (4.5)$$

is the Wigner distribution of the time-inverted impulse response of the measuring device. The time-dependent spectrum is thus the convolution over time and frequency of the signal Wigner distribution with the spectrometer's Wigner distribution.

For the modulated optical field of a laser, the time-resolved spectrum, (as might be measured using a grating and a "2-D" streak camera, for example), is but the smeared Wigner distribution of the field. The smearing depends on the characteristics of the spectrometer: there is an unavoidable trade-off between blurring in time and frequency. The Wigner distribution of the spectrometer's impulse response determines this blurring. The Wigner Distribution, or its 2-D Fourier Transform, the Ambiguity function [69], can be used to design a spectrometer with some specified joint resolution in time and frequency.

Alternatively, if the impulse response of the spectrometer is known, the signal's Wigner distribution can be recovered from its time-resolved spectrum, through a 2-dimensional deconvolution: this enables a great improvement in the joint time-frequency resolution of a signal.

To avoid having to perform a deconvolution, the direct measurement of the Wigner distribution of an optical signal would be convenient. Although methods have been proposed to measure the Wigner distribution of signals written on slides, by optical means [70, 71], its direct measurement seems more difficult for the optical fields of laser diodes. An alternative is to use the complex Ambiguity function, which is the 2-dimensional Fourier transform of the Wigner distribution. Direct measurement of the Ambiguity function of a laser signal is possible [72], by measuring the correlation of the optical signal, after shifts in time and frequency. The amplitude and phase of the autocorrelation can be obtained using a multiport, providing the value of the ambiguity function at one point in the t and f plane. Provided the signal is repeatable, the whole ambiguity function can then be mapped out, and a 2-dimensional Fourier transform then yields the signal's Wigner distribution.

4.1.3 Chirp representation for time-domain modelling

Time domain models describe the simulated optical fields of laser diodes as a time-series of real [21] or complex sampled field amplitudes. For a signal s_n sampled at time intervals Δt, the Wigner distribution at time $n\Delta t$ is now given by

$$W(n\Delta t, f) = \sum_{m=-\infty}^{\infty} s^*_{n-m} s_{n+m} \exp(-i4\pi m f \Delta t). \tag{4.6}$$

In practice, the limits in the summation are finite, and the resulting "Pseudo-Wigner distribution" can be calculated using the efficient Fast Fourier Transform algorithm.

In this discrete-time case, aliasing must be avoided: this is because the Wigner distribution is periodic in frequency f, with a period which is only half of the Nyquist Bandwidth $1/\Delta t$. For a real signal, aliasing can be avoided by first making the signal analytic, using a Hilbert transform to eliminate negative frequencies [73]. For a complex signal, interpolation can be used to obtain another time series, sampled at twice the original rate, but occupying the same bandwidth [74].

Used in conjunction with time-domain models of semiconductor laser diodes, the Wigner distribution enables the chirped optical signals to be displayed simultaneously in the time and frequency domains, as a contour map for example, enabling changes in spectrum to be related to the conditions in the device at the times of the changes. Two alternatives to using the Wigner distribution to follow spectral dynamics could be:

(1) To measure the instantaneous frequency: For single mode signals, the rate of change of phase is the instantaneous frequency. This is, however, no longer meaningful when more than one laser modes are excited. Moreover, the Fourier broadening must be added to the change in instantaneous frequency, to provide a measure of the spectral width of short pulses.

(2) To evaluate the spectrum for short segments of the signal, using a sliding window. The use of a sliding window FFT [75] to determine the time-varying spectrum of the signal has the disadvantage that the spectrum obtained is dependent on the size and shape of the window used. This method, in fact, is equivalent to the experimental measurement of the optical spectrum, using a diffraction grating: the measured time-dependent spectrum is just equal to a smeared Wigner distribution. As discussed above, this leads to an unavoidable trade-off between blurring in the frequency or time resolution. This blurring is of particular importance for very high speed modulation of laser diodes:

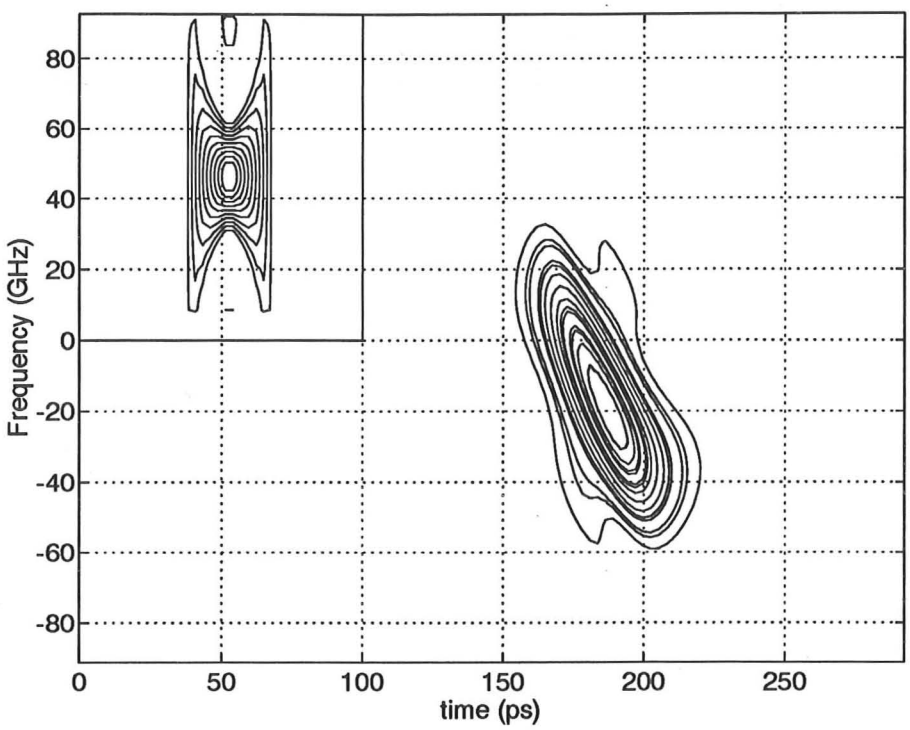

Figure 4-1: Time resolved spectrum as measured using a grating, whose impulse response is a 20ps long step. The inset shows the Wigner distribution corresponding to the grating's impulse response.

higher bit rates can only be obtained by working close to the Fourier limit for the optical pulses: the smearing caused by the experimental measurement or the sliding window FFTs, then extends over an area comparable to the area of the signal's Wigner distribution itself. The loss of resolution is then of great importance.

4.1.4 Examples of the use of the Wigner distribution

A time domain model is used to simulate a 300μm long $\lambda/4$ shifted DFB laser diode, with $\kappa L = 3$ and $\alpha_H = 4$. A gain switched pulse corresponding to a step in drive current from 20 mA to 80 mA is simulated. The time-resolved spectra for this pulse are calculated for two different spectral analysers. Figure (4-1) uses an ideal diffraction grating whose impulse response is a step of 10ps duration. Figure (4-2) uses an ideal Fabry-Perot interferometer whose impulse response is a decaying exponential with a 100ps time constant. The insets in Figs. (4-1) and (4-2) show the Wigner

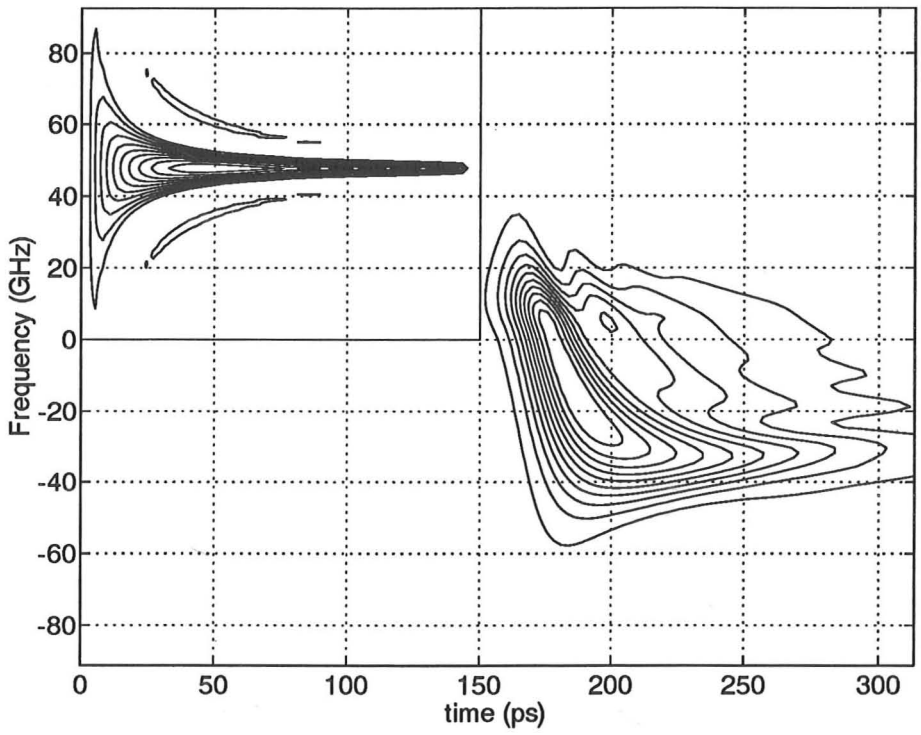

Figure 4-2: Time resolved spectrum as measured using a Fabry-Perot interferometer, whose impulse response is a decaying exponential with a 100ps time constant. The inset shows the Wigner distribution for the interferometer's impulse response.

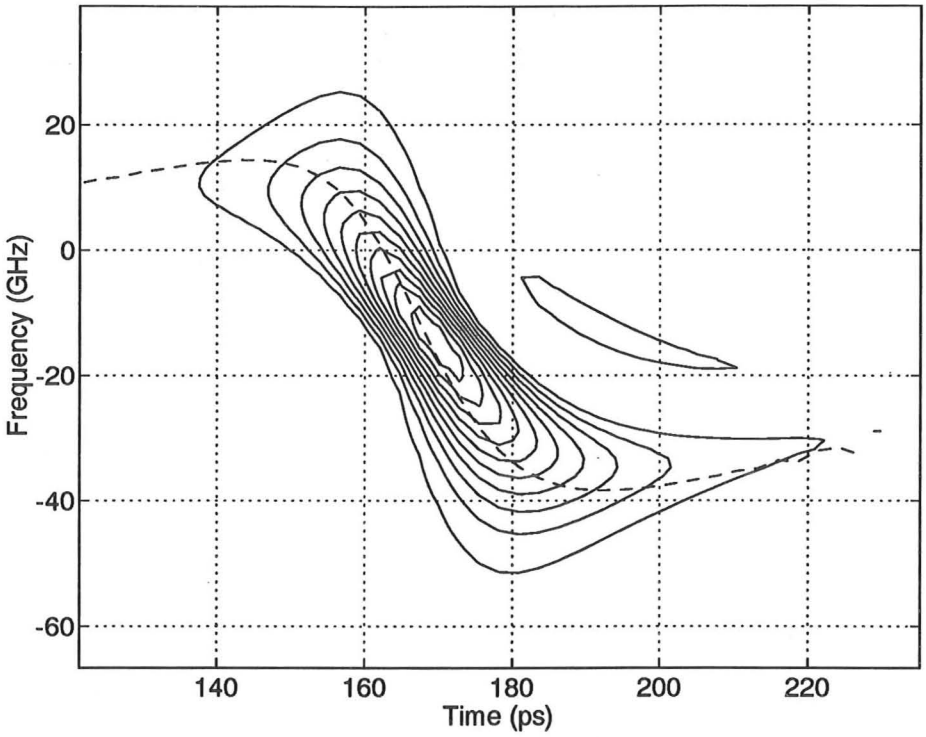

Figure 4-3: Wigner distribution for the same gain switched pulse as in Figures (1) & (2). The dashed line shows the instantaneous frequency during the pulse.

distributions of the respective spectral analysers. In contrast, Fig. (4-3) shows the Wigner distribution of the gain switched pulse, as obtained from a deconvolution of either of the time-resolved spectra. The dashed line is the instantaneous frequency calculated from the Wigner distribution. The small island above the main feature of the Wigner distribution is similar to the side-lobes which are present in the Fourier Transforms of objects with sharp features.

Great improvements in the time and frequency resolution of the measurements are obtained, and the S-shaped red-shift of the frequency, due to carrier depletion in the device, is clearly seen.

4.1.5 Related time-dependent spectra

The Wigner distribution belongs to Cohen's class [76] of time-frequency distributions with correct "marginals" : these distributions, when integrated along the time or frequency axis, give the time-averaged spectrum or the instantaneous power re-

spectively, without any additional broadening. Other functions in Cohen's class can be defined so they are always positive, unlike the Wigner function, with the result that they can be interpreted as a power density in time and frequency.

The Wigner function also suffers from "cross components": the Wigner function of two Gaussian pulses, separated in time, frequency or both, features a series of spikes halfway between the two pulses. These rapidly varying cross components can confuse the interpretation of the Wigner function of a signal. The cross-components can be reduced by suitable smoothing, at the expense of loss of combined resolution in time and frequency: different choices of smoothing functions result in other members of Cohen's class.

The Page distribution [77] is another of Cohen's class of time-frequency distributions, which includes aspects of causality: the Page distribution, at time τ, only depends on the values of the signal at times preceding τ. The Page function has indeed been used to describe the time-dependent spectrum of ultra-short laser pulses [78, 79], by deconvolution similar to the one described earlier.

Thus, alternatives to the Wigner function exist to represent chirped optical signals in optical communication systems. In cases were cross-components confuse our interpretation of the Wigner function, these can be significantly reduced by appropriate smoothing; for example, by using an optimization procedure to design the smoothing function without sacrificing too much time-frequency resolution [80].

4.2 Maximum Entropy Spectrum for the time domain model

The Maximum Entropy Method for estimating the power spectral density is applied to the optical fields of laser diodes simulated using a time domain model. The advantages of this technique over the conventional Discrete Fourier Transform method are discussed.

It is found that the absence of windowing effects enable the shape of the spectrum to be seen clearly, and large side mode suppression ratios to be determined more accurately. The method also suppresses the noise which in the Fourier transform methods can obscure the spectral features unless time consuming averaging is carried out.

4.2.1 Introduction

The Maximum Entropy Method of spectral estimation, closely related to the autoregressive (AR), or All Poles method, was pioneered by Burg [81]. Used originally in geophysics, it has found applications in a wide variety of fields. A variety of methods using the maximum entropy principle or autoregression have been developed, and are reviewed by Kay and Marple [82]. Named the Yule-Walker method, the Burg method, the least-squares or forward-backward method, they vary in their performance (e.g. spectral resolution, immunity to noise). The Yule-Walker method was presented first [81], and has an inferior spectral resolution compared to more modern methods, like the forward-backward least-squares method, but is used here because it is simpler, easy to adapt to complex data and is sufficient for the present purpose.

We recall briefly here the basic principles of the technique, which has been described in detail elsewhere (e.g. in [82]).

The principle is to find the most random (whitest) spectrum of a set of data for which the signal autocorrelations at a number of lags are known [82, 83]. For a time-series x_k, for which the signal autocorrelations $R_{xx}(m)$ are known, or can be estimated, at a number of equally spaced lags:

$$R_{xx}(m) =< x_k^* x_{k+m} >= \frac{1}{N} \sum_{k=0}^{N-1} x_{k+m} x_k^*, \tag{4.7}$$

the Maximum Entropy power spectral density takes the form:

$$S(f) = \frac{\sigma_p^2}{|1 + \sum_{n=1}^{p} a_{pn} \exp(i2\pi n f \Delta t)|^2}, \tag{4.8}$$

where Δt is the sampling interval, p is the model order (number of poles), and $\{a_{p1}, \ldots, a_{pp}\}$ and σ_p^2 are the predictor parameters and the prediction error power respectively.

These parameters can be obtained efficiently using the Levinson-Durbin recursion [84]. Starting with a model order $p = 1$ and initial parameters:

$$a_{11} = -R_{xx}(1)/R_{xx}(0), \tag{4.9}$$

$$\sigma_1^2 = (1 - |a_{11}|^2) R_{xx}(0), \tag{4.10}$$

the model order is increased gradually, with the new parameters for order p estimated

in terms of those for order $p-1$ by

$$a_{pp} = -\left[R_{xx}(p) + \sum_{l=1}^{p-1} a_{p-1,l} R_{xx}(p-l)\right] / \sigma_{p-1}^2, \tag{4.11}$$

$$a_{pi} = a_{p-1,i} + a_{pp} a_{p-1,p-i}^*. \tag{4.12}$$

4.2.2 Estimation of the optical spectrum of laser diodes

Time domain models are useful for research and design of semiconductor laser diodes used in optical fibre communications. These models describe the laser's optical output as a time series of complex fields, sampled at a time interval Δt (which is related to the spatial sampling interval Δz of the fields within the laser through the group velocity, $\Delta z = v_g \Delta t$).

Techniques such as the Fast Fourier Transform must be used to access the spectral information contained in the time-domain data, just as a diffraction grating or a Fabry-Perot interferometer must be used to assess the spectrum of a real laser diode. Using the Discrete Fourier Transform to estimate the power spectrum from the time domain model data, suffers from noise and the windowing effect.

The noise is due to the stochastic nature of the fields: because the Fourier Transform of a Gaussian random process is also a Gaussian random process, the power spectral density for any frequency bin will have a Rayleigh distribution. This noise can obscure the spectral features. It is reduced by repeated averaging, but this is time consuming.

The windowing effect causes the slow fall-off from the main laser mode to obscure the stop-band, and can mask side modes with low powers. This effect can never be eliminated, but can be reduced substantially by pre-windowing the data before Fourier transforming.

The maximum entropy method can reduce both these effects. Since only a few tens of poles are used to describe the spectrum, there are not enough degrees of freedom to model noise, and the envelope of the spectrum is smooth. The windowing effect is minimized because the maximum entropy method, unlike Discrete Fourier Transform based methods, does not assume that the signal autocorrelation vanishes beyond the window length. It is evident that the Maximum Entropy Spectrum shows much more clearly the spectral features, which are obscured, in the FFT case, by noise. The noise reduction away from the peaks is a well known feature of Maximum Entropy spectral estimates, and is mainly due to the restriction of the number of parameters imposed by the model order: the technique tries to "fit" p modes to the

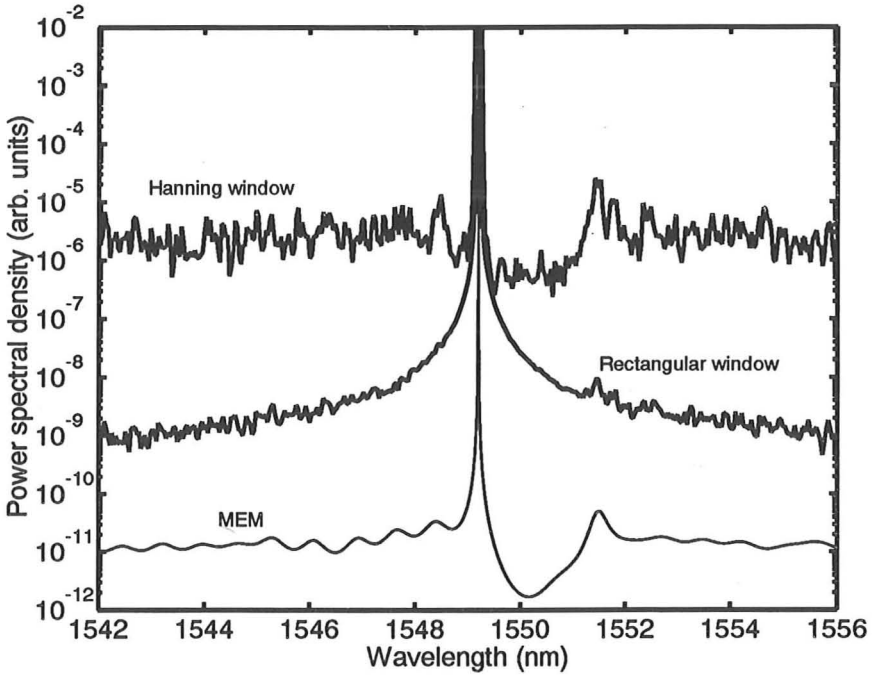

Figure 4-4: CW optical spectrum estimated from the time-domain model data: from top to bottom, using a Discrete Fourier Transform with Hanning window, using the DFT with a rectangular window, and using the Maximum Entropy method (Yule-Walker). The spectra are shifted with respect to one another for clarity.'

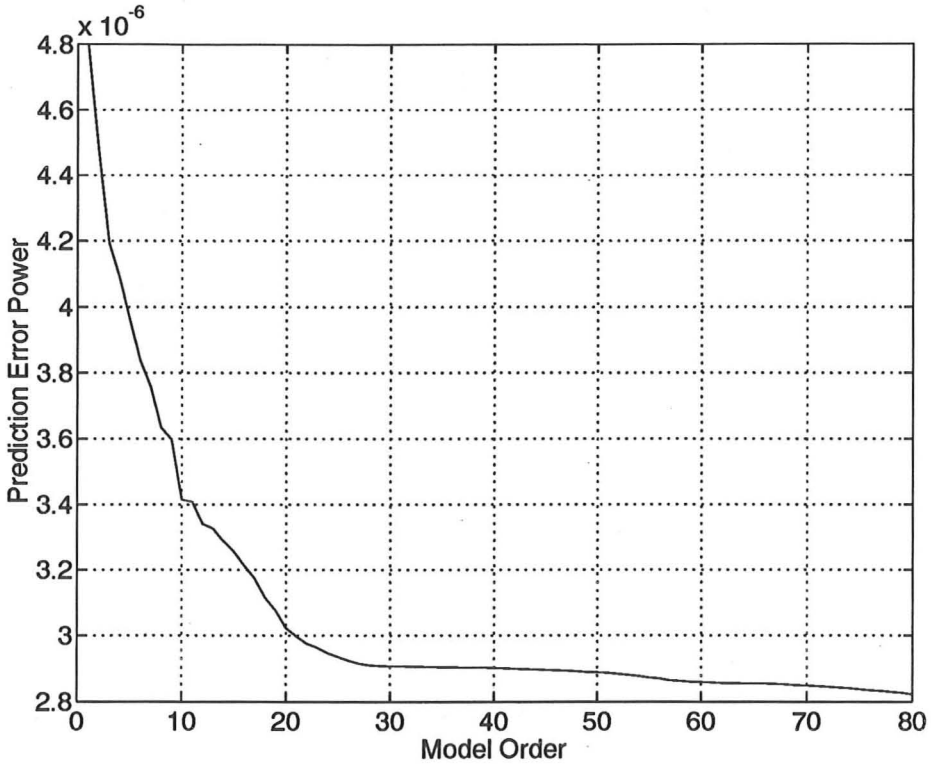

Figure 4-5: Prediction error power against the number of poles. The correct model order was generally found to be the number of poles at which the curve first levels out (here around 25).

spectrum, leaving no degrees of freedom to represent spurious noise.

4.2.3 Model Order Selection

Selection of the correct model order p is a problem encountered using the Maximum Entropy Method. With a number of poles p which is too low, the spectrum will be very smooth and will show few features, whereas when p is too high, the spectra may be contaminated by spurious peaks. Various criteria have been advanced for predicting the correct model order [82, 85], but most of these criteria seem to predict too high a model order for simulated laser fields. Fig. (4-5) shows a plot of the prediction error power σ_p^2 against the model order p. It is seen that σ_p^2 initially decreases before levelling out at $p \approx 25$: this was found empirically to produce a good estimate of the correct model order.

4.2.4 Limitations

The Maximum Entropy Method is not well suited to estimating dynamic spectra (e.g. chirp of gain switched pulses). This is because the optical fields may actually be zero outside the sampling window, whereas the Maximum Entropy Method effectively attempts to extrapolate field autocorrelations beyond the duration of the sampling window. When applied to laser fields with a large number of modes (e.g. Fabry-Perot lasers with around 60 simulated modes), the model order required may be large ($\approx$ 200). The computation time may then be excessive compared to the FFT method, and the number of data samples, which is needed to compute good autocorrelation estimates, may also increase.

4.3 Conclusion: Wigner function and Maximum Entropy Method

The relevance of two numerical methods to laser dynamics and time domain modelling has been demonstrated.

The Wigner distribution is a useful representation of a signal in time and frequency. It is particularly relevant to the analysis of modulated laser signals for optical communications, where dispersion is one of the main obstacles to wider information bandwidths.

The Maximum Entropy Method, or autoregression, is an alternative to using methods based on Discrete Fourier Transforms (DFT) to estimate the power spectra of sampled data, like that generated by the time domain model. It is well suited to calculating the C.W. spectra of laser diodes simulated by the time domain model, since it reduces the windowing effect associated with DFTs, which can obscure the spectral features close to the lasing modes. In addition, it effectively performs a smoothing which removes the noise which can confuse the spectrum.

Chapter 5

Comparing with the Power Matrix Method

If modelling results are to be at all relied on, it is vital to check the modelling tools as thoroughly as possible. This section provides a quantitative comparison between the time domain model, presented in Chapters 2 and 3, and another large signal laser model recently developed at Cambridge University Engineering Department: the Power Matrix Method (PMM).

This comparison serves two purposes:

1.) To rule out both programming errors and wrong assumptions which lead to different predictions.

2.) To highlight differences in approaches, and to determine which approaches are best suited to particular problems.

Although agreement between different models is by no means a proof of their correctness, it does however enhance and qualify our confidence in their predictions, especially when their implementation differ substantially.

The programming of the Power Matrix Method model and the simulations using this model presented in this section were done by C.F. Tsang.

The comparisons in this chapter concern the static, small signal, and large signal multimoded operation of uniform DFB lasers. Simulations of longitudinal instabilities are also compared.

5.1 Description of the Power Matrix Method

The PMM model [31] is a mixed frequency time model driven by the amplification of spontaneous emission. Like the time domain model, it includes modelling of spontaneous emission, and treatment of the longitudinal variation in gain, photon density and refractive index.

As in the time domain model, the evolution of the optical fields inside the laser is described by the coupled wave equations in the slowly-varying approximation:

$$\left(\frac{1}{v_g}\frac{\partial}{\partial t}+\frac{\partial}{\partial z}\right)F = -(i\delta + i\Delta\omega/v_g - g + \alpha_s)F + i\kappa_{RF}R + G_F(z,t), \quad (5.1)$$

$$\left(\frac{1}{v_g}\frac{\partial}{\partial t}-\frac{\partial}{\partial z}\right)R = -(i\delta + i\Delta\omega/v_g - g + \alpha_s)R + i\kappa_{FR}F + G_R(z,t). \quad (5.2)$$

The gain g is a function of the local carrier density, $\Delta\omega = \omega - \omega_0$ is the deviation of the laser mode under consideration from the Bragg frequency ω_0, and $i\delta$ models the change in refractive index caused by changes in carrier density.

The laser cavity is divided into a number of sections, typically around 10, and within each section the carrier density is considered uniform. The facet reflectivities impose the following boundary conditions upon the fields:

$$F(0,t) = r_l R(0,t), \quad (5.3)$$

$$R(L,t) = r_r F(L,t). \quad (5.4)$$

Steady state values for the optical fields can be calculated by setting the time derivatives to zero in Eqs. (5.1,5.2). Assuming a constant value for the gain g (thus implying that the carrier densities in the different sections of the laser do not vary with time), the coupled wave equations can be written:

$$\frac{\partial}{\partial z}\begin{bmatrix} F(z,\omega) \\ R(z,\omega) \end{bmatrix} = \begin{bmatrix} -(i\delta + i\Delta\omega/v_g - g + \alpha_s) & i\kappa \\ i\kappa & (i\delta + i\Delta\omega/v_g - g + \alpha_s) \end{bmatrix} \quad (5.5)$$

$$\times \begin{bmatrix} F \\ R \end{bmatrix} + \begin{bmatrix} G_F \\ G_R \end{bmatrix}, \quad (5.6)$$

where G_F and G_R are the frequency components of the spontaneous noise sources for the forward and reverse waves.

By finding the eigenvalues of the matrix above, its exponential can be calculated,

and the coupled wave equations can be integrated over the section j. The fields at $z = z_j$ can be expressed in terms of the fields at $z = z_{j-1} = z_j - l$ through the transfer matrix bf T_j:

$$\begin{bmatrix} F_j(\omega) \\ R_j(\omega) \end{bmatrix} = \mathbf{T}_j \begin{bmatrix} F_{j-1}(\omega) \\ R_{j-1}(\omega) \end{bmatrix}, \tag{5.7}$$

where bf T_j is:

$$\mathbf{T}_j = \begin{bmatrix} \cosh(\gamma l) - (i\delta + i\Delta\omega/v_g - g + \alpha_s)\sinh(\gamma l)/\gamma, & i\kappa \sinh(\gamma l)/\gamma \\ -i\kappa \sinh(\gamma l)/\gamma, & \cosh(\gamma l) + (i\delta + i\Delta\omega/v_g - g + \alpha_s)\sinh(\gamma l)/\gamma \end{bmatrix}, \tag{5.8}$$

with the propagation constant:

$$\gamma^2 = [i\delta + i(\omega - \omega_0)/v_g - g + \alpha_s]^2 + \kappa^2.$$

The noise terms are included at the end of each section:

$$\begin{bmatrix} F_j(\omega) \\ R_j(\omega) \end{bmatrix} = \mathbf{T}_j \begin{bmatrix} F_{j-1}(\omega) \\ R_{j-1}(\omega) \end{bmatrix} + \begin{bmatrix} Gf_{j-1}(\omega) \\ Gr_{j-1}(\omega) \end{bmatrix}. \tag{5.9}$$

Together with the boundary conditions Eqs.(5.3,5.4), the transfer matrices above, determine the optical field in terms of the spontaneous noise sources. The lack of correlation between the spontaneous sources is exploited to calculate the optical power. Assuming a Lorentzian lineshape for the mode, this optical power can be evaluated rapidly.

A given carrier density profile therefore determines completely the photon distribution of the mode in this static case. In the dynamic case, the time derivatives in Eqs.(5.1,5.2) are no longer zero. Because the instantaneous mode frequency ω_0 appears on the right hand sides of Eqs.(5.1,5.2), the logarithmic rates of change $(1/F)\partial F/\partial t$ and $(1/R)\partial R/\partial t$ do not include changes of phase, but only changes in the magnitude of the fields, and so they are real. By setting within each section of the laser,

$$\frac{1}{v_g F}\frac{\partial F}{\partial t} = \frac{1}{v_g R}\frac{\partial R}{\partial t} = \mu, \tag{5.10}$$

where μ varies from section to section, the partial time derivatives in Eqs.(5.1,5.2) can be replaced by μF and μR, and the same analysis as for the static case can be carried out, provided the gain g is replaced by $g - \mu$. In this dynamic case, a given carrier density profile thus determines the photon distribution profile which is

consistent with the rates of growth μ in the different sections.

The rates of growth μ are determined by iteration: starting with a given photon density distribution $P_{t-\Delta t}$, at time $t - \Delta t$, and μ from the last time step, a new photon density distribution P_t at the next time step is calculated. The new μ factor is estimated as

$$\mu = \frac{P_t - P_{t-\Delta t}}{v_g \Delta t (P_t + P_{t-\delta t})}. \tag{5.11}$$

This procedure is iterated until μ changes less than a set amount.

The carrier density changes in the different sections are calculated using the usual rate equation, where the photon density is summed over all the modes.

5.2 Simulation Results

Two devices were compared, both uniform grating, perfectly anti-reflection coated 300μm long devices. The device parameters, shown in Table (5.1), are identical for both devices with the exception of the coupling. The κL product chosen was 1.5 and 3 which will be labelled device **A** and **B** respectively. The coupling is so chosen to show mode competition between the two degenerate modes outside the stopband. A comparison was made on static, small signal and large signal properties of these devices. The solid lines in all of the figures represent the values obtained by the power matrix method, and the dashed by the time domain model.

5.2.1 Static Characteristics

To generate the light current curve, both models obtained static solutions by allowing the transient response to settle for each current injection. This may be seen for device **A** in Fig.(5-1). The two models show excellent agreement along the whole range of current injection. However a noticeable difference is observed at higher output powers, which can explained by the number of sections the cavity was divided into in the two models. In the power matrix method only 10 sections were used to save computational time as this increases very rapidly with an increasing number of sections. The computation time for the time domain model increases less rapidly, and is proportional to the square of the number of sections. Twenty sections where used with the time domain model, as its algorithm is less accurate than the power matrix method for small section numbers.

Parameter (Uniform DFB)	Bulk
Facet reflectivities R1,R2	0
Grating period [nm]	244.5
Normalised coupling strength κL	1.5, 3
Bragg order m	1
Stripe width w [μm]	1.5
Active layer thickness [μm]	0.2
Laser length L [μm]	300
Confinement factor Γ	0.3
Effective index without injection $n_{e,0}$	3.2
Effective group index n_g	3.6
Internal absorption $\alpha_s[cm^{-1}]$	50
Differential gain a $[10^{-16}cm^2]$	2.5
Transparency carrier density $N_0[cm^{-3}]$	10^{18}
Non-linear gain coefficient $\epsilon[cm^3]$	6.0×10^{-17}
Material enhancement factor α_H	4
Inversion factor n_{sp}	2
Carrier lifetime τ [ns]	10
Bimolecular coefficient B $[10^{-10}cm^3/s]$	1
Auger Coefficient C $[10^{-29}cm^6/s]$	7.5
Spontaneous emission coefficient β_{sp}	5.10^{-5}

Table 5.1: Device Parameters of two Uniform DFBs

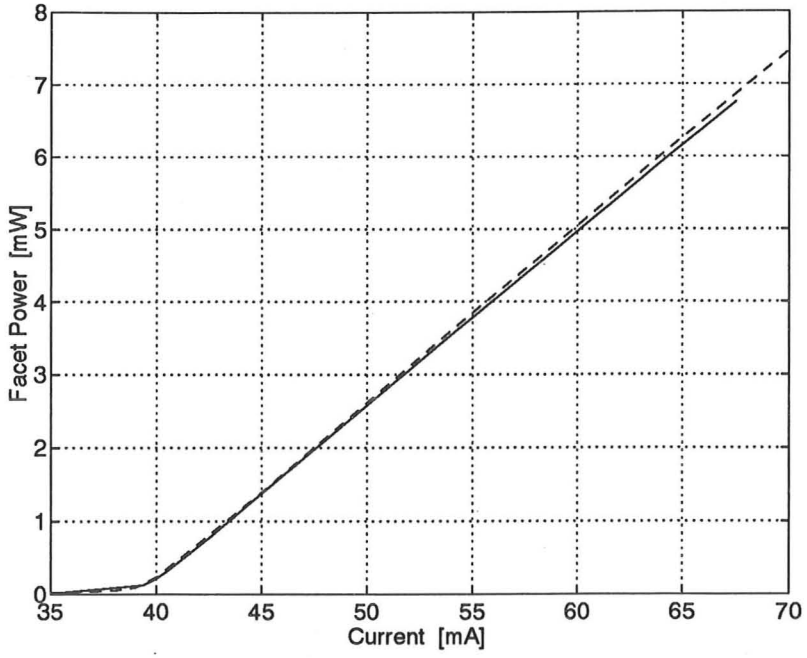

Figure 5-1: Light current characteristic for device A: $\kappa L = 1.5$. The solid line is from the PMM model and dashed from TDM.

5.2.2 CW Optical Spectrum

The optical spectrum in the PMM can be calculated through the amplification of the spontaneous emission in the cavity. The optical power spectrum in the TDM is estimated from the sampled field values, obtained by running the laser at constant power for a period of time. A windowed Fourier transform (FFT) is a straightforward way to estimate the power spectrum, but the resulting spectra suffers from noise, and from the windowing effect due to the finite sampling time. The maximum entropy method described in the previous chapter is therefore used.

In this comparison, 60 poles were used to calculate the spectrum. As shown in Fig.(5-2), the maximum entropy method shows good agreement with the PMM method.

5.2.3 Small Signal AM and FM Responses

Although the two models described here are primarily large signal models, small signal responses can easily be obtained using familiar control theory, as described in Chapter 3 for the time domain model. The power matrix method small signal response is obtained in the same way.

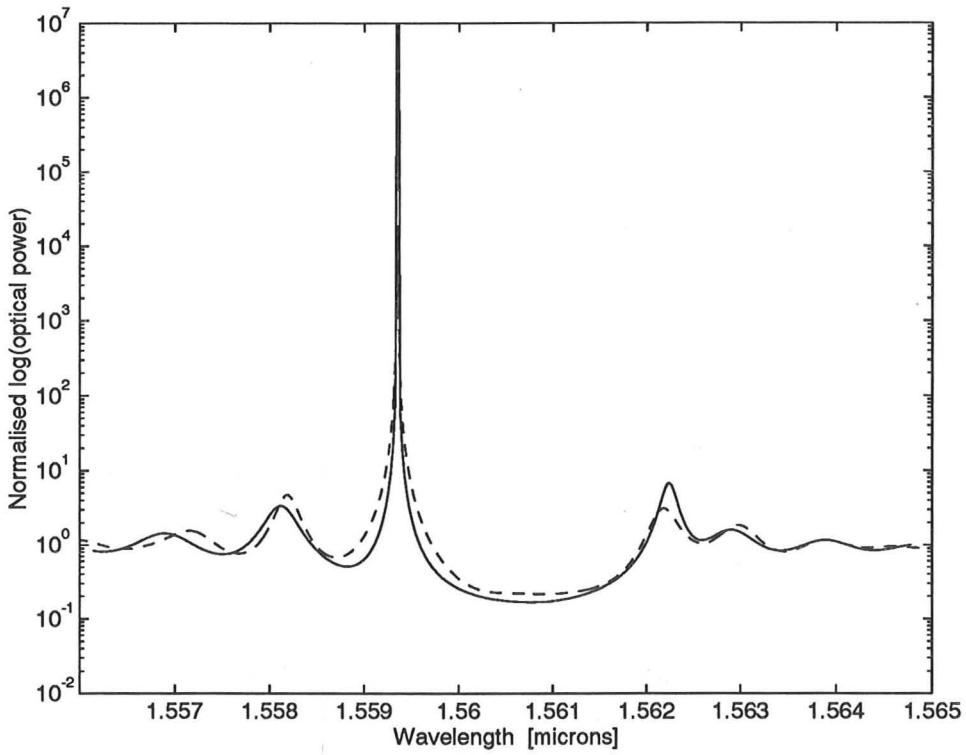

Figure 5-2: CW optical spectrum of device B at 50 mA injection. The solid line is from the PMM model and dashed from TDM.

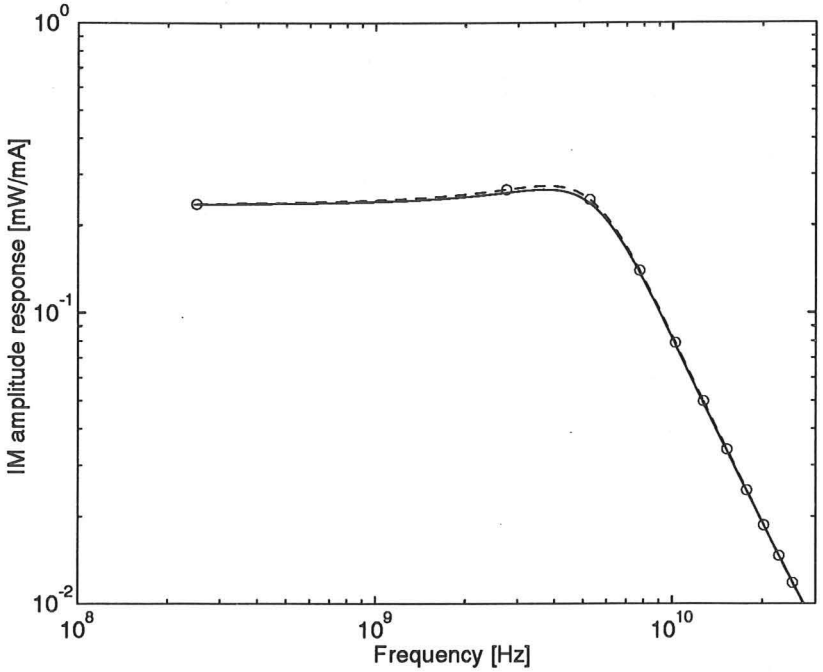

Figure 5-3: IM amplitude response of device A at 67.5 mA; data points 'o' are from TDM

The AM and FM responses are shown in Figs.(5-3, 5-4, 5-5, 5-6): the results from both models are virtually indistinguishable, and to aid visualisation, some of the time domain model points are represented by 'o'. The response at high frequencies, especially its phase, is very dependent on the sampling times and impulse duration Δt, accounting for the slight deviation in that region. The small signal responses given by both models are expected to diverge at high frequencies of the order of the mode separation, not shown on the graph. The time domain model shows resonances in the responses at frequencies corresponding to the mode separations, typically around 100 GHz, which are due to the excitation of other longitudinal modes by the applied impulse in current.

5.2.4 Transient Responses

Switch-on transients are shown in Figs.(5-7) and (5-9) where both devices are switched from around threshold to a much higher injection current (A: 35–60 mA B: 23–50 mA). (The numerical data from the time domain model has been filtered using the Fast Fourier Transform to separate the longitudinal modes, otherwise a beating between the two modes would be observed). The transient for device **A**

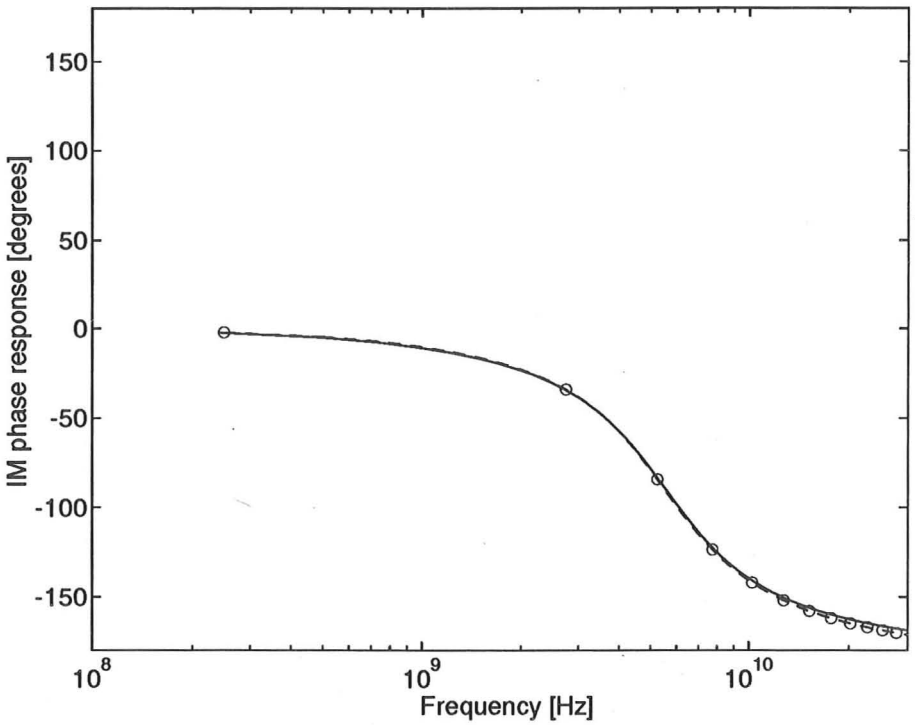

Figure 5-4: IM phase response of device A at 67.5 mA; data points 'o' are from TDM

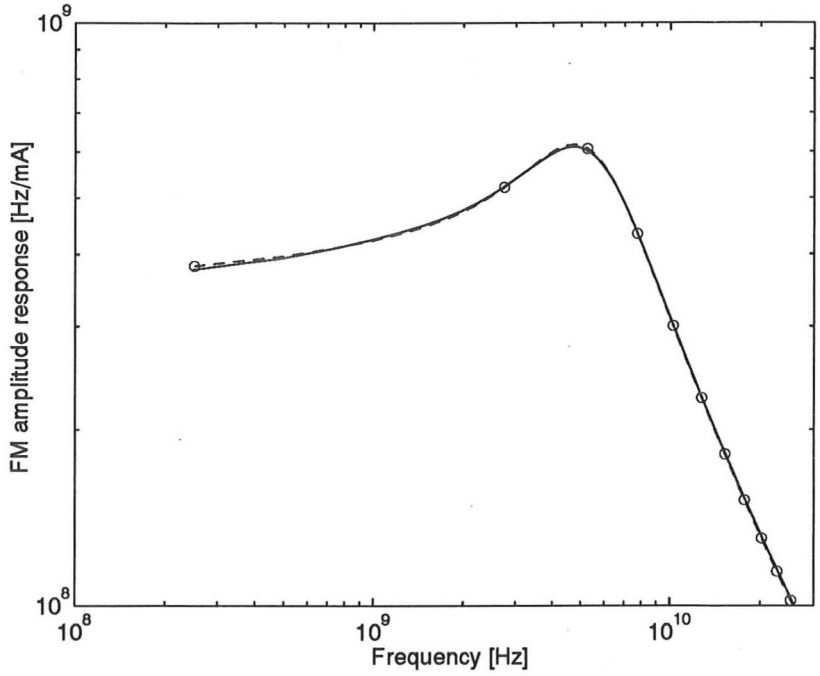

Figure 5-5: FM amplitude response of device A at 67.5 mA; data points 'o' are from TDM

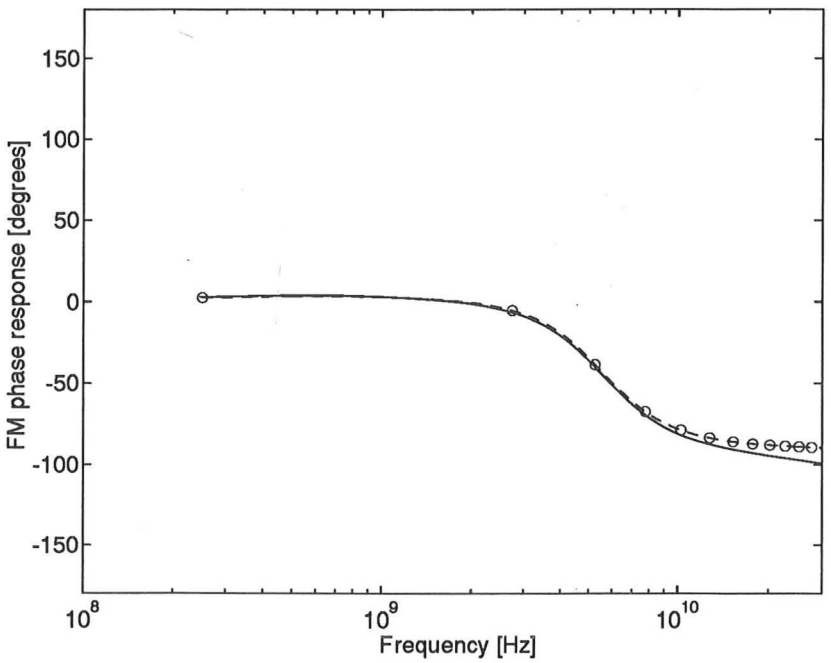

Figure 5-6: FM phase response of device A at 67.5 mA; data points 'o' are from TDM

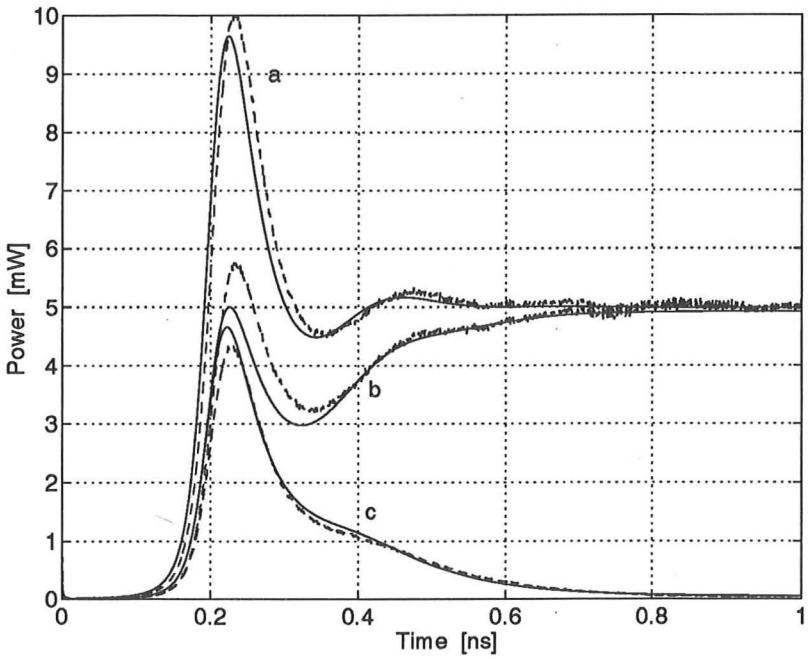

Figure 5-7: Transient response of device A switched from 35 mA to 60 mA. Trace (a) is the total emitted power, (b) is power from the longer wavelength mode and (c) from the shorter wavelength mode. The solid line is from the PMM model and dashed from TDM.

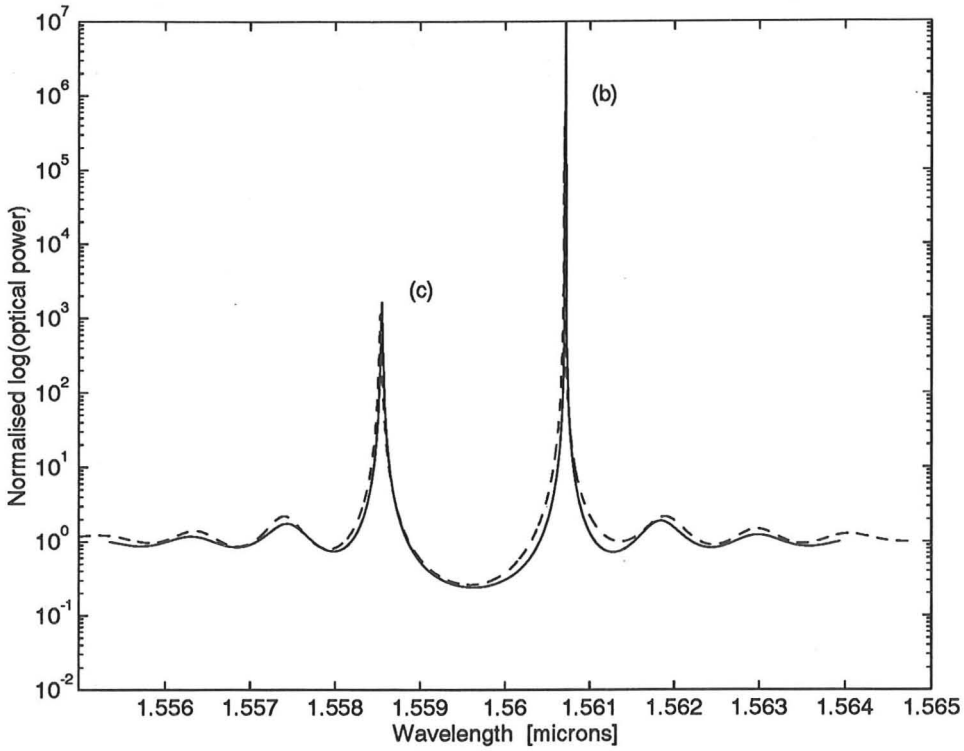

Figure 5-8: CW optical spectrum of device A at 60 mA injection. The solid line is from the PMM model and dashed from TDM.

shows mode competition: both modes come up initially, but the shorter wavelength mode **c** is suppressed after one nanosecond (refer to Figure 5-8 for the labeling of the respective modes). This shows dynamically that devices similar to **A** will inherently exhibit multi-mode behaviour at high modulation rates, whereas in **B** the shorter wavelength mode is dominant.

Laser **B** is initially biased slightly above threshold where the side mode is suppressed. When it is switched from this current level to 50 mA, the carrier density overshoots and the longer wavelength mode lases and peaks at 0.1ns. This is then quickly suppressed by the main lasing mode through spatial hole-burning.

The overall power shown by trace **a** in Fig.(5-7) shows good agreement but the distribution of power in the modes show slight deviation. The discrepancy can be attributed to the simulation of longitudinal spatial hole burning. With an increased number of sections, better modelling of the longitudinal inhomogeneities can be obtained.

The discrepancy for the transient of device **B** in Fig.(5-9) is also probably due in part to the different numbers of sections used in both models. Another possible

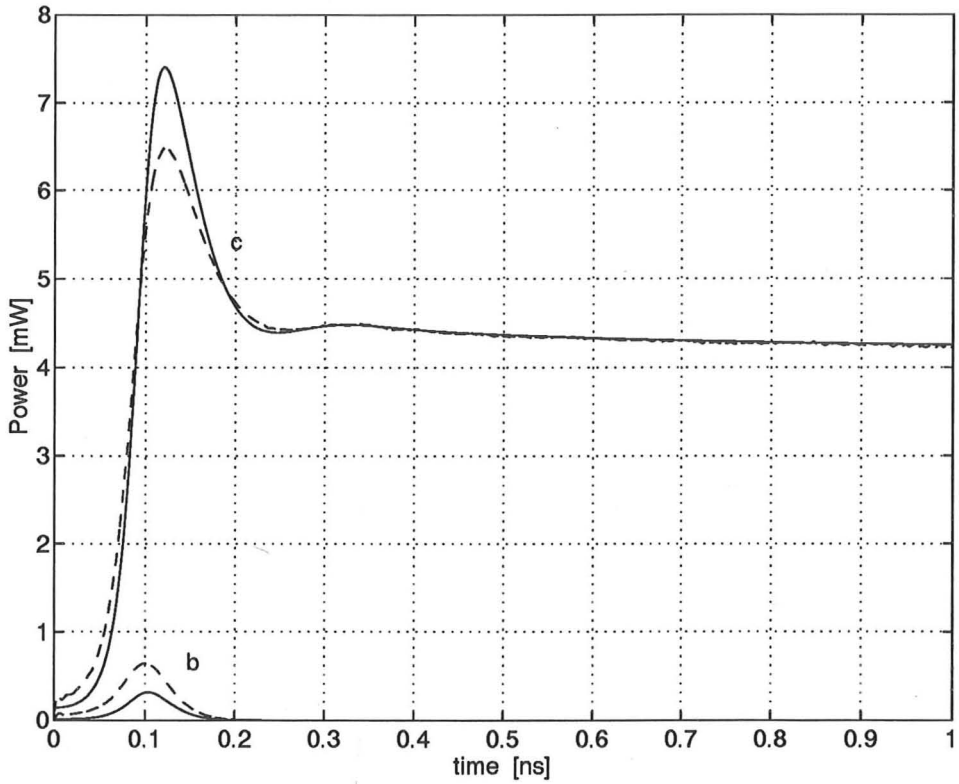

Figure 5-9: Transient response of device B switched from 23 mA to 50 mA. The solid line is from the PMM model and dashed from TDM.

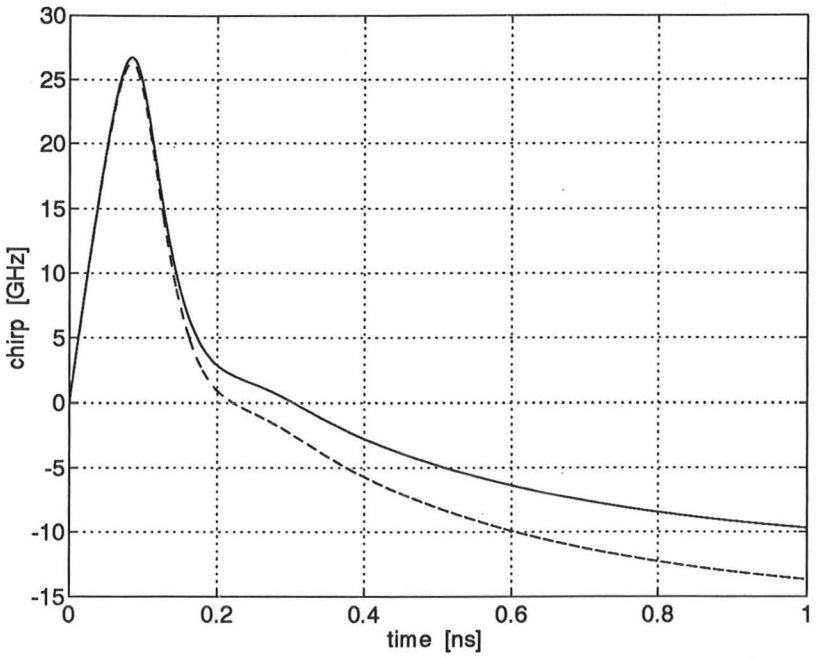

Figure 5-10: Frequency chirp in device B due to switching from 23 mA to 50 mA. The solid line is from the PMM model and dashed from TDM.

cause for the discrepancies are the different treatments of spontaneous emission: the power matrix method only considers the optical power in the modes which are followed, and the optical power away from these modes, due to spontaneous emission, is not taken into account. The time domain model considers spontaneous emission over the entire material spontaneous spectrum. In this comparison, however, the modelled spontaneous spectrum was white, over a modelled bandwidth of about 40nm. At low optical powers, this difference can affect the side mode suppression ratios, resulting in differences in mode competition.

The frequency chirp of the shorter (dominant) wavelength mode for the current step in device **B** is shown in Fig.(5-10). Again good agreement is shown although a slightly larger change in frequency is predicted by the TDM model towards steady state. This is expected since the initial optical power differs slightly in the two models as explained above. This shows that although the modes of a uniform DFB are degenerate, it is possible to obtain single-moded operation using a uniform DFB. A simple explanation of this effect of spatial hole-burning has been given by Whiteaway *et al* [32]. Figure (5-11) shows the SMSR in a number of different κL product devices at 1 mW and 5 mW power output. The positive and negative values of SMSR indicate which mode is dominant. As the power is increased, spatial hole

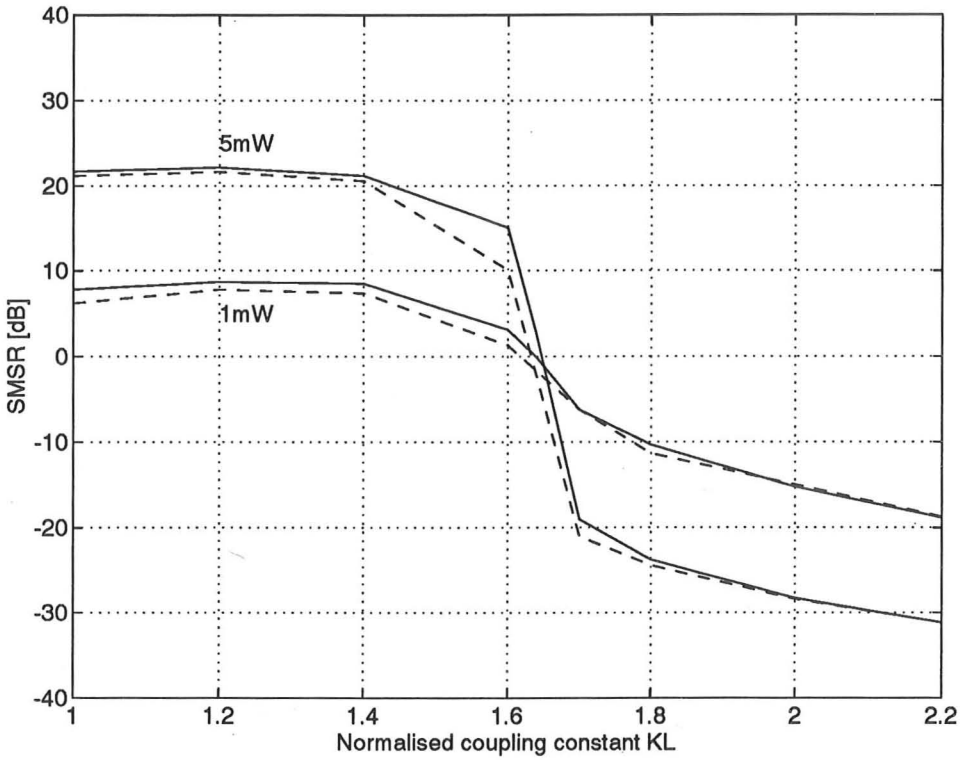

Figure 5-11: SMSR for uniform DFBs with varying κL products at 1 mW and 5 mW output power. Solid lines given by the PMM model and dashed lines are from TDM.

burning effects are stronger and the SMSR increases. A cross-over point is observed around $\kappa L = 1.64$, when both modes are of almost equal intensity. This point is extremely sensitive to many contributing factors such as the number of sections used, the amount of spontaneous emission, facet reflections and other defects. Increasing the power increases this sensitivity, and only a small deviation from the cross-over point is required to give single moded steady state operation. However as shown in the $\kappa L = 1.5$ device, these devices are likely to exhibit multi-mode oscillations.

5.2.5 Instability

Device **B** exhibits longitudinal instability, recently analysed by Schatz [86]. This effect is characterised by an unstable symmetrical longitudinal mode decaying to an asymmetrical stable state due to spatial hole burning effects [87, 88]. Both models predict instability using different techniques. Instability is automatically treated in the time domain method, since the complex fields propagate along the cavity in time. Any deviation from the unstable symmetrical longitudinal mode caused by random noise or other fluctuations would shift the laser to a different state. In the case of the power matrix method, the unsteady state is allowed to converge. However a small noise source can be simulated by including small perturbations in electron density along the cavity and allowing the laser to settle.

The small perturbations can cause an unstable mode to decay into an asymmetrical stable mode (two exist due to geometric symmetry); in the case of a stable mode the cavity profile will correct itself to its original state. The photon and carrier distributions at the instability region are shown in Figs. (5-12) and (5-13) respectively. The distribution of power is asymmetrical and again shows good agreement between the two models on asymmetrical inhomogeneities.

The facet power is shown for different injection currents in Fig. (5-14). The onset of instability is predicted at 60 mA by both models, and the modelled difference in power from both facets is also in good agreement. A kink in the total facet power vs. current is also visible around 70 mA injection, caused by the onset of a side mode.

5.3 Discussion: Comparison with PMM

Good agreement between the PMM and TDM has been demonstrated in static, small and large signal regimes.

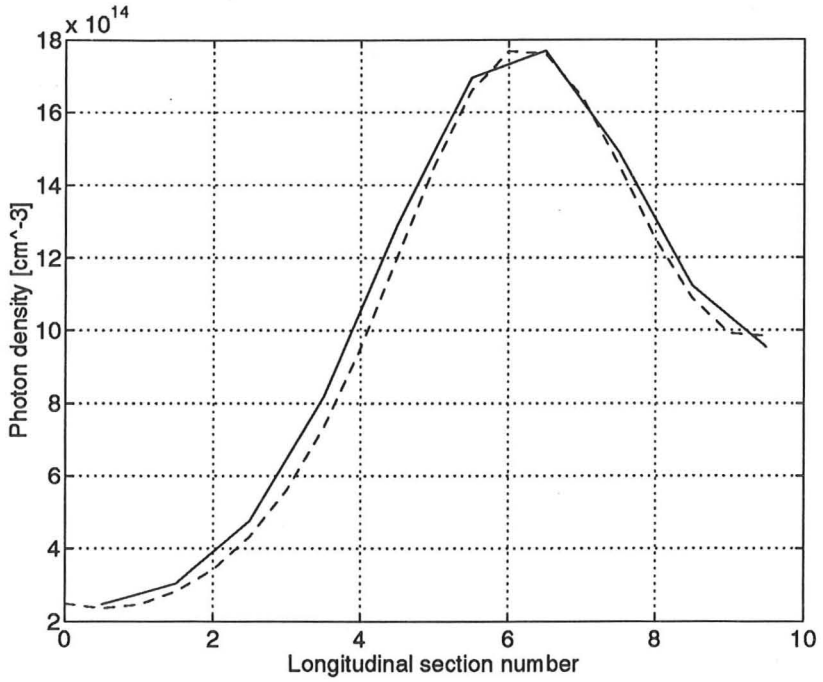

Figure 5-12: Photon density profile of device B at 67 mA showing instability. The solid line is from the PMM model and dashed from TDM.

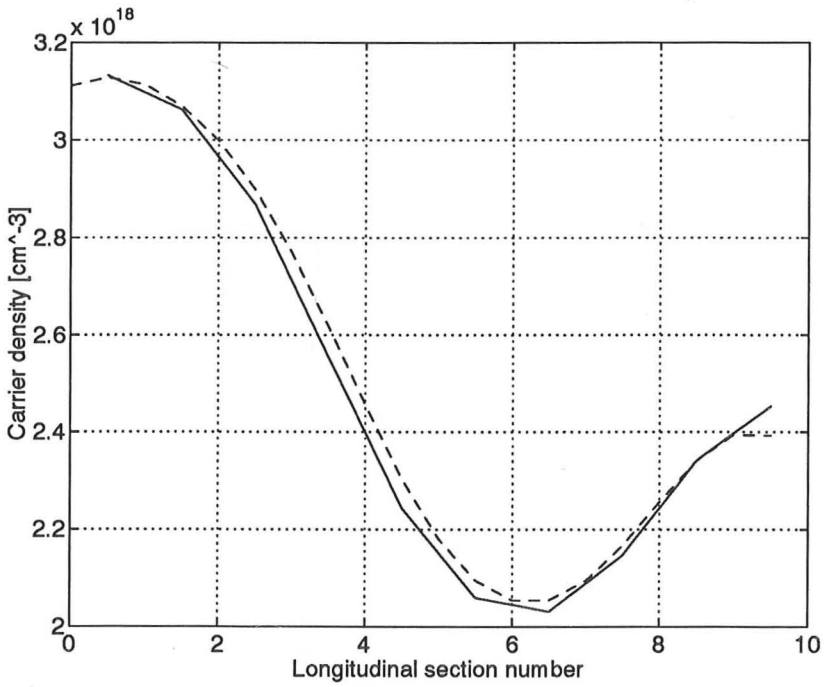

Figure 5-13: Carrier density profile of device B at 67 mA showing instability. The solid line is from the PMM model and dashed from TDM.

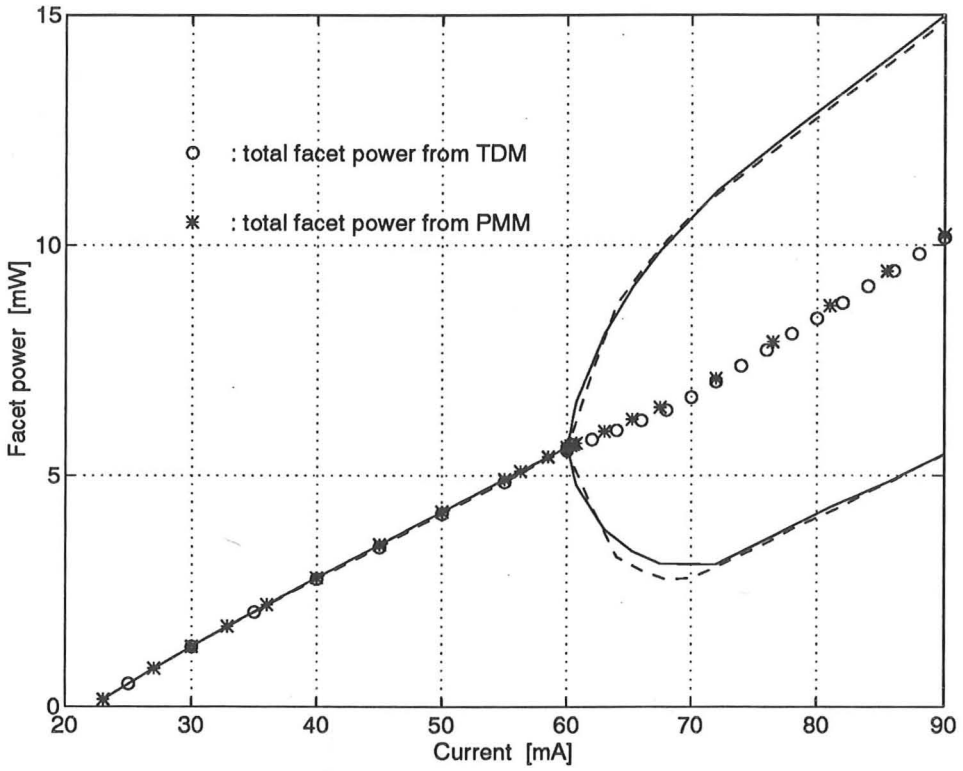

Figure 5-14: Light current characteristic for device B showing regions of splitting in output power. The solid line is from the PMM model and dashed from TDM.

The TDM differs from the PMM in its use of stochastic noise sources. The TDM simulations must be averaged to obtain the mean dynamic response of the laser. In contrast the PMM gives this mean response directly. Suppression of the noise sources in the TDM can be used to calculate a deterministic response, above threshold, for single moded devices where spontaneous power has negligible effect on spectral and dynamic characteristics. Multi-mode operation and modulation close to threshold however, are not accurately modelled without the noise sources.

The validity of the models is demonstrated in uniform DFBs with κL products of 1.5 and 3. In the latter case instability is demonstrated in both models resulting in stable asymmetric longitudinal modes. Both models agree in single and double-moded behaviour. The agreement in dynamic simulations show that both models can be used as powerful tools for designing and optimizing devices, although there are particular advantages in each model dependent on the application.

The comparison with the Power Matrix Method has shown good agreement for laser spectra, small signal responses, instabilities, transients and mode competition. Based on different premises, the agreement of these two large signal models minimizes greatly the likelihood of any programming errors, as well as increasing confidence in the validity of the large signal response simulations. The power matrix method uses the concept of laser modes. Modes are no longer defined when considering travelling wave amplifiers and modulators, and the power matrix method could not, in its present state simulate these devices correctly; these devices are simulated without any difficulties by the time domain model, where optical modes only appear when the optical fields are examined in the frequency domain. The good agreement in this comparison therefore shows that optical modes are useful concepts in modelling many aspects of lasers diodes.

Chapter 6

Comparison with other models and experiment

This chapter presents further comparisons of the time domain model presented in Chapters 2 and 3 with other modelling and experimental results.

Two comparisons are presented in this chapter:

1.) The first is a comparison with the results reported by the European COST 240 workshop on laser modelling, calculated using a variety of models developed by the leading laser modelling groups in Europe. This comparison concerns static, small signal and noise characteristics.

2.) The second compares experimental results concerning self-pulsating DFB laser diodes, reported by the Heinrich Hertz Institute, with simulations using the time domain model.

The first comparison shows that the time domain model calculates accurately the static properties of DFB laser diodes, and that the laser linewidth calculations agree with some other current sophisticated models in showing rebroadening due to spatial hole burning.

The second comparison shows that some complex behaviour in DFB laser diodes can be studied usefully using the time domain model.

6.1 Comparing with results of COST 240

The results presented here concern the first part of the second COST exercise: a 1mm long $\lambda/4$ shifted DFB laser emitting around 1.66μm is considered. The laser parameters are given in Table 6.1.

Parameter ($\lambda/4$ shifted DFB)	Bulk
Facet reflectivities R1,R2	0
Grating period [nm]	244.5
Coupling strength κL [cm^{-1}]	10
Bragg order m	1
Stripe width w [μm]	1.5
Active layer thickness [μm]	0.2
Laser length L [μm]	1000
Confinement factor Γ	0.3
Effective index without injection $n_{e,0}$	3.4
Effective group index n_g	3.6
Internal absorption $\alpha_s[cm^{-1}]$	50
Differential gain a [$10^{-16}cm^2$]	2.5
Transparency carrier density N_0[cm^{-3}]	10^{18}
Non-linear gain coefficient ϵ[cm^3]	0.0
Material enhancement factor α_H	4.51
Inversion factor n_{sp}	2
Carrier lifetime τ [ns]	10
Bimolecular coefficient B [$10^{-10}cm^3/s$]	1
Auger Coefficient C [$10^{-29}cm^6/s$]	7.5

Table 6.1: Device Parameters for the COST DFB

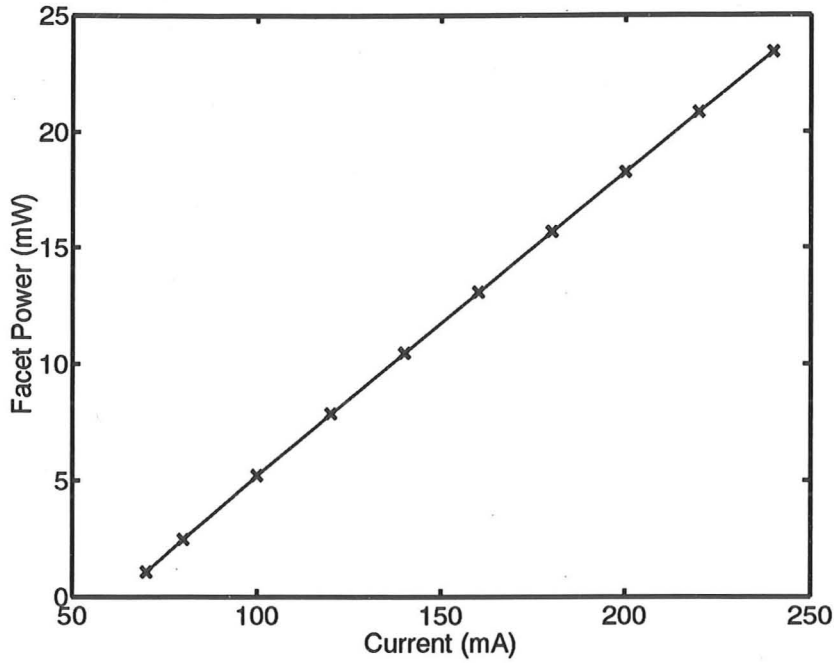

Figure 6-1: Facet power against current for the time domain model (x) and for University of Gent (solid).

Figure(6-1) shows the facet power versus the drive current for both the time domain model results and those of University of Gent. Twenty sections were used in the time-domain model, and the curve was calculated by stepping the current to the different levels and waiting for the transient to settle. On a 486-PC this takes about five minutes for the 10 points. The difference between the models never exceeds 1%, and is well within the spread of results from the other groups.

Figure (6-2) shows the laser linewidth versus the drive current for the device, with the results from the University of Gent, from TFL, and from KTH. The curves for the time domain model, University of Gent and TFL shows a rebroadening occurring around 160 mA, due to an increasing instability of the longitudinal mode. A mode jump is indeed observed using the time domain model around 220 mA: after a relatively long period of time of about 20ns, during which the laser seems to operate in a stable fashion, the carrier density quickly becomes asymmetric and a large transient follows as the laser switches to the (-1) mode (see Fig.(6-3)). The optical power and carrier density distribution are different for the (0) mode before the jump and the final, stable (-1) mode; These are shown in Fig.(6-4). The linewidth of the time domain model agrees very well at low and moderate powers with University of Gent and TFL, and rebroadening is observed. The last point (I=240 mA) for

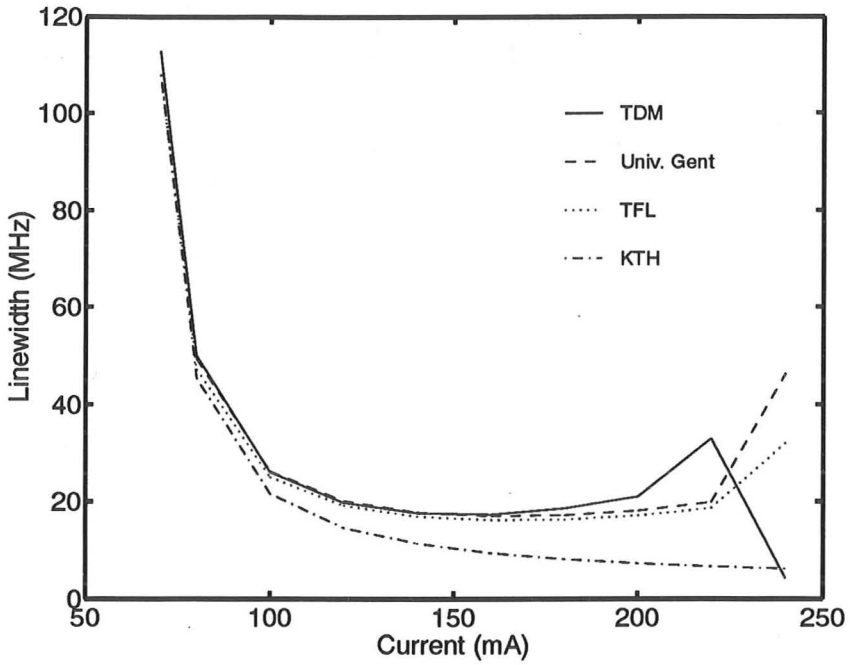

Figure 6-2: Linewidth against current for the time domain model and other models.

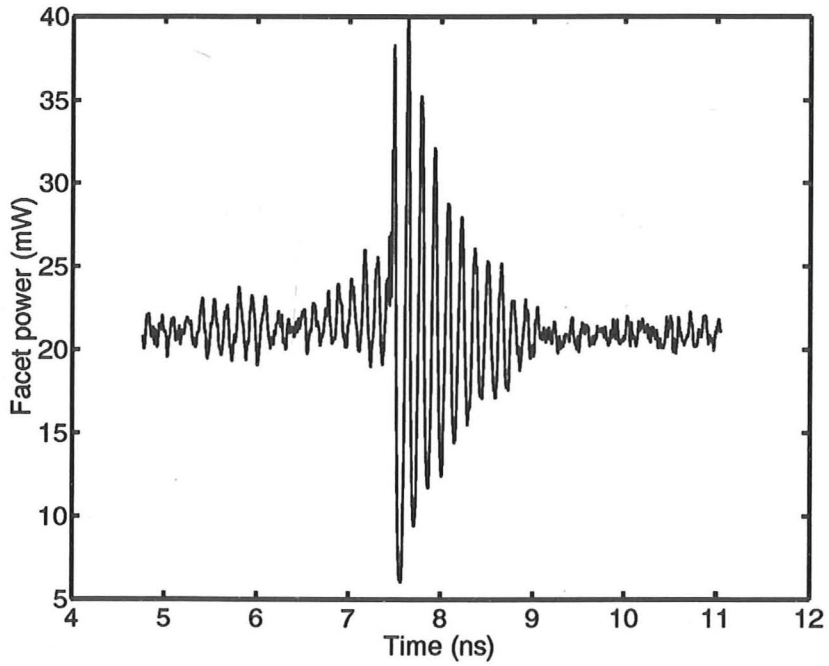

Figure 6-3: Facet power versus time, showing a large transient due to the mode jump.

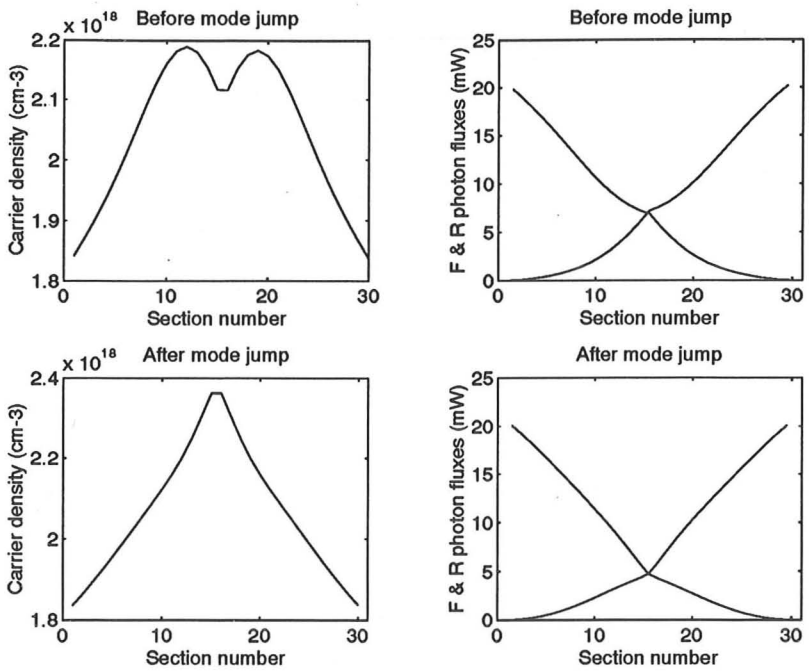

Figure 6-4: Carrier and photon density distributions before and after the mode jump.

the time domain model shows a low linewidth ($\approx$ 5MHz): this is the linewidth of the new stable mode. The time domain model actually predicts the instability at a lower power than the other two models. Thirty sections were used in the time domain model, and the numbers of sections used by the other models is not known: this may explain the discrepancy, as the modelling results are very sensitive to any differences in parameters in the region of instability.

The linewidth calculated by KTH is representative of the results of the other models in the COST exercise, and does not show any rebroadening. This is probably because the variations in the mode profile with increasing power are not taken into account in these models.

The low frequency modulation characteristics calculated by a few models are shown in Fig.(6-5). Again at low powers there is good agreement between the time-domain model and the other models. At higher powers the results from different models seem to diverge. Again, this may be due to the number of sections used in the different models.

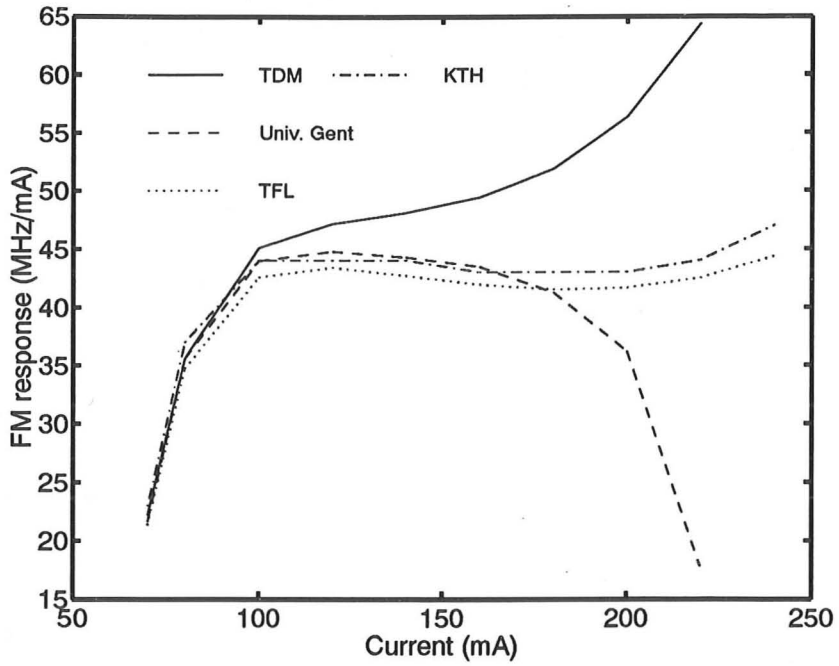

Figure 6-5: FM modulation response at low frequencies against current for the time domain model (solid) and other models in COST-240.

6.2 Simulation of self-pulsating DFB lasers

In this section the time domain model is used to simulate the phenomenon of self-pulsation in DFB lasers, as recently observed by Möhrle *et al* [89]. Möhrle *et al* reported self-pulsation with a repetition rate of several GHz in two section DFB lasers under certain conditions of non-uniform pumping. Self-pulsating DFB lasers were subsequently used by the same research group for all-optical clock-recovery for transmission systems [90].

Self-pulsation was chosen for this comparison in order to test the capabilities of the time domain model to simulate behaviour in DFB lasers unforeseen when the model was developed. Furthermore, the simulation of self-pulsation requires a dynamic model which takes into account longitudinal effects, and therefore tests modelling capabilities more specific to the time domain model, and not shared by a wide variety of models.

6.2.1 Description of the phenomenon of self-pulsation in DFB lasers

Jinno and Matsumoto [91] and Möhrle *et al* [89] first reported the generation of optical pulses at Gigahertz repetition rates in multisection DFB lasers driven by a D.C. current injection.

This phenomenon differs from self-pulsation in multi-section Fabry-Perot lasers [92, 93], where differences in carrier lifetimes in different sections of the laser are at the origin of the pulsations [94]. Lasers with carrier lifetimes varying along the cavity can be fabricated by uneven doping of the semiconductor or by ion bombardment of sections of the laser. The presence of defects can also reduce the carrier lifetime and cause self-pulsation. However, Möhrle et al have shown that the self-pulsation was unaffected by exchanging the current injection levels in a DFB laser with two even sections, and therefore that defects were very unlikely to be the cause of the phenomenon. The cause seems to be due to the shifting of the optical stopbands of the DFB gratings relative to each other in both sections of the laser, when the refractive index changes due to varying carrier densities. As shown by Bandelow *et al* [95] this leads to substantial nonlinear effects which can cause self-pulsation.

6.2.2 Experimental and simulation results

The devices used by Möhrle *et al* are drawn in Fig.(6-6).

The DFB lasers used had a high coupling coefficient $\kappa = 150\text{cm}^{-1}$, and were 400μm long. Devices with different relative lengths of the two sections were used. The laser facets were uncoated. The parameters used in the model are shown in Table 6.2, and are typical of the ridge waveguide structures considered.

The DFB facets in the experiment were uncoated, and the phases of these facet reflections were unknown. A number of simulations were therefore performed for combinations of facet phase reflectivities varying from 0 to 2π by increments of $\pi/4$. The facet reflectivities were found to have a considerable effect of the lasing spectrum and the pulsation characteristics. For many combinations of facet reflectivities, single mode operation was simulated over a wide range of injection currents, indicating that DFB effects are pronounced: this was observed by Möhrle *et al*, who measured the optical spectrum shown in Fig.(6-7), when the DFB was not pulsating. A typical simulated optical spectrum for facet reflectivities ($\pi/4$, $\pi/2$) is shown for comparison in Fig.(6-8).

When the two sections of the device were pumped with certain currents, Möhrle

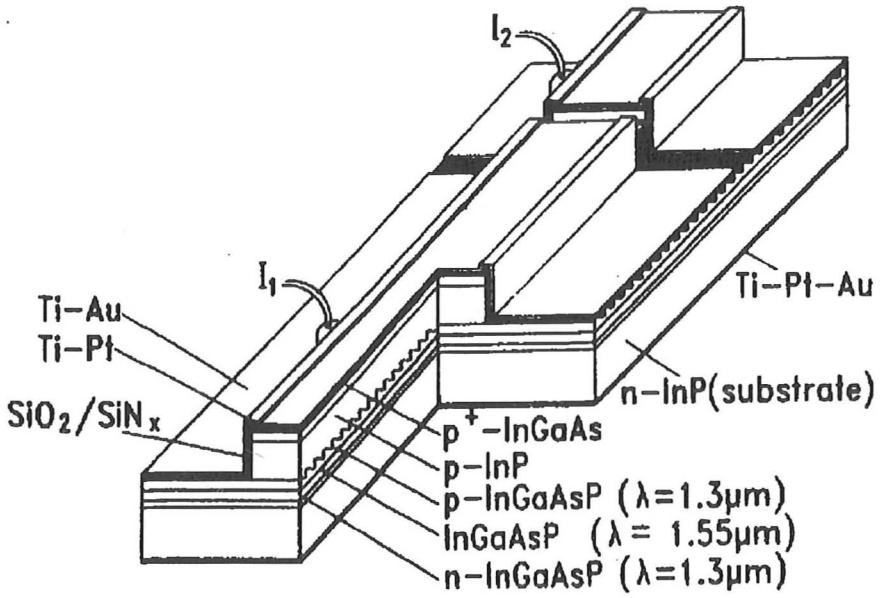

Figure 6-6: Structure of the ridge-waveguide two-section DFB lasers used by Möhrle *et al*, after [89].

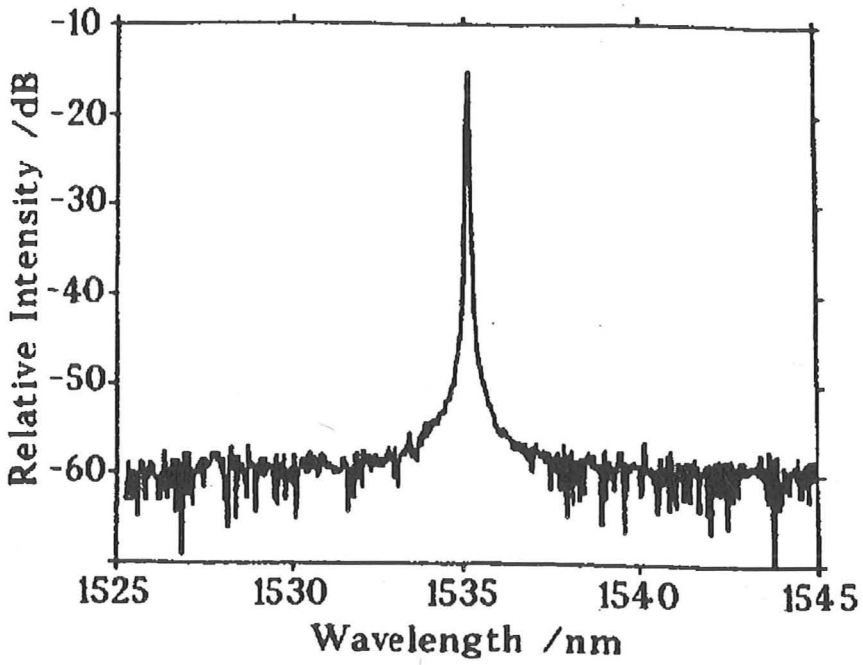

Figure 6-7: Optical spectrum of a DFB laser (non-pulsating regime) showing a large side mode suppression ratio (greater than 35 dB), indicating pronounced DFB effects. After [89].

Parameter (Uniform DFB)	Bulk
Facet reflectivities R1,R2	0.3
Coupling coefficient κ [cm^{-1}]	150
Bragg order m	1
Stripe width w [μm]	1.5
Active layer thickness [μm]	0.2
Laser length L [μm]	400
Confinement factor Γ	0.3
Effective index without injection $n_{e,0}$	3.2
Effective group index n_g	4.0
Internal absorption $\alpha_s[cm^{-1}]$	50
Differential gain a $[10^{-16}cm^2]$	2.5
Transparency carrier density $N_0[cm^{-3}]$	$1.8*10^{18}$
Non-linear gain coefficient $\epsilon[cm^3]$	1.0×10^{-17}
Material enhancement factor α_H	4
Inversion factor n_{sp}	2
Carrier lifetime τ [ns]	10
Bimolecular coefficient B $[10^{-10}cm^3/s]$	1
Auger Coefficient C $[7.5^{-29}cm^6/s]$	7.5

Table 6.2: Device Parameters for the self-pulsating DFBs.

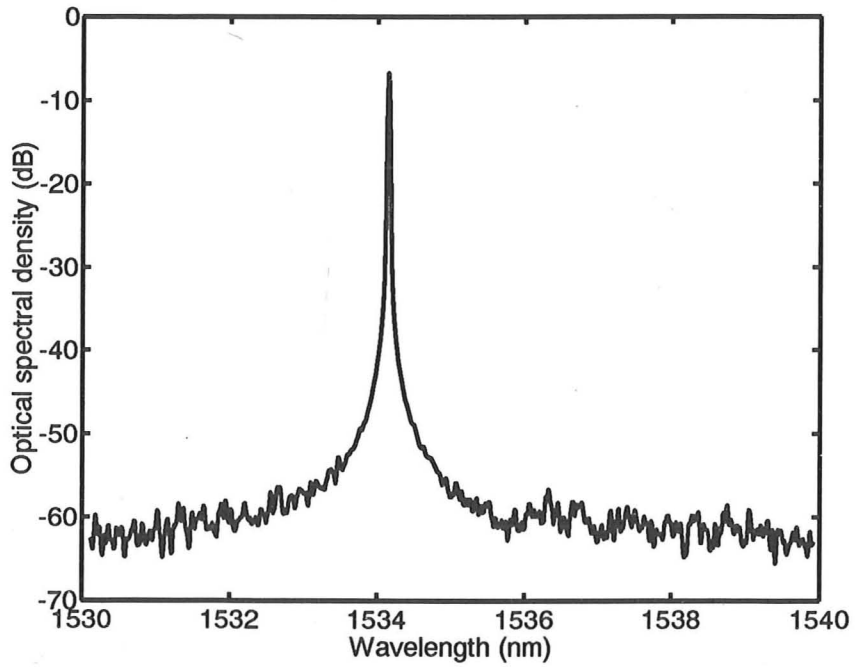

Figure 6-8: Simulated optical spectrum under similar injection conditions as in Fig.(6-7).

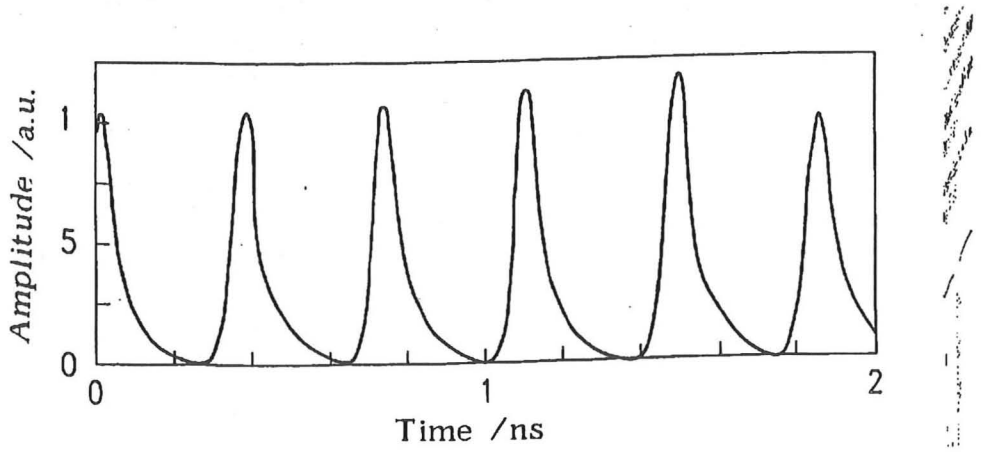

Figure 6-9: Observed pulsating facet power for currents 131.8 mA and 63.4 mA in the 330μm and the 70μm DFB sections respectively, after [89].

et al observed self-pulsations in the optical output from one laser facet, reproduced in Fig.(6-9). The currents producing self-pulsations were close to the currents leading to stable single mode operation.

Self-pulsation was simulated in a DFB laser with section lengths 70μm and 330μm. The facet phases were varied, and the regions for self-pulsation varied substantially with the reflection phases. For the facet phases $(0,\pi)$, self-pulsation was simulated at a similar injection level of (140 mA, 50 mA) in the 330μm and 70μm sections respectively. The power observed from the end of the 70μm section is shown in Fig.(6-10). The raw facet power data was in this case smoothed by a Gaussian filter of a width of 50ps, corresponding roughly to the response time of a typical fast photodiode. The facet power would otherwise display rapidly varying detail due to beating between the different laser modes. The shape of the pulses is similar, with a rise time shorter than the fall time. The frequency of the self-pulsation is similar to the experimental result, 3.2 GHz compared to 2.73 GHz observed by Möhrle *et al.* The optical power observed from the other facet was different, with a smaller extinction ratio.

The RF-spectrum measured by the experimentalists during self-pulsation is reproduced in Fig.(6-11). The first peak gives the frequency of the self-pulsation, and the other peaks are due to higher harmonics of the pulse shape. A simulated RF-spectrum evaluated from a 30 ns run of data is shown in Fig.(6-12).

Again, the shapes of the simulated and observed RF spectra are similar, due to the similar pulse shapes.

Möhrle *et al* also observed the optical spectrum of a self-pulsating DFB, which

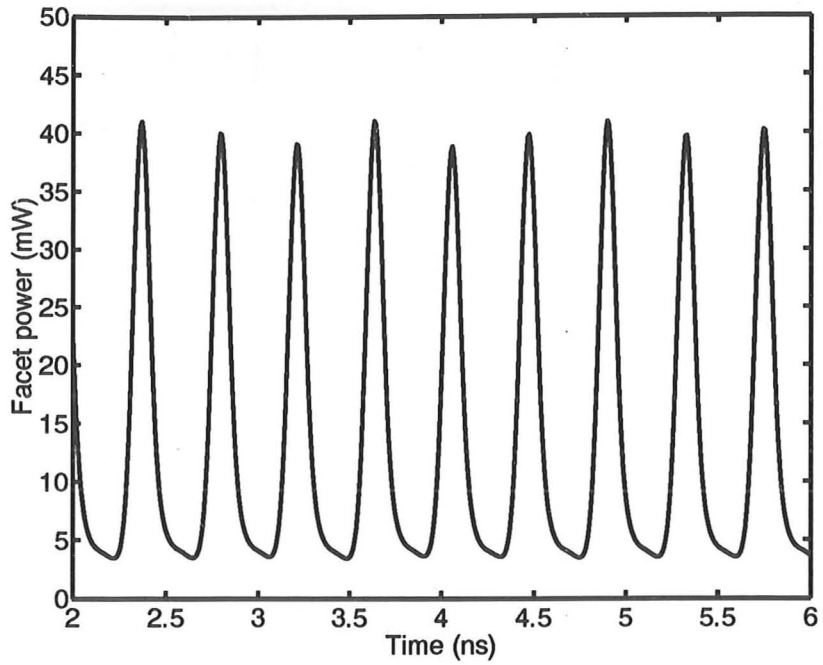

Figure 6-10: Simulated facet power for currents 140 mA and 50 mA in the 330μm and the 70μm DFB sections respectively.

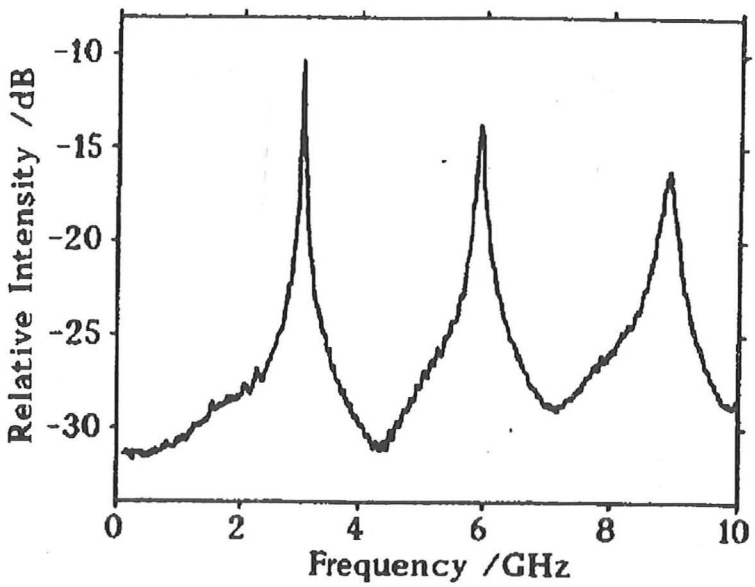

Figure 6-11: RF spectrum of self pulsating laser, after [89].

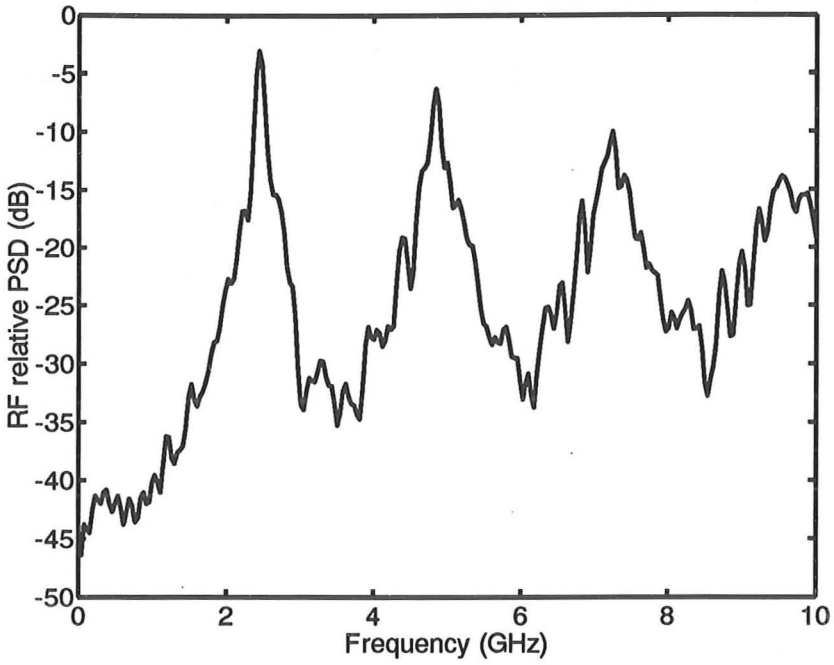

Figure 6-12: Simulated RF spectrum of self pulsating laser, same conditions as for Fig.(6-10).

showed two excited longitudinal modes, both broadened by chirping. No further published details concerning the self-pulsating optical spectrum were available, but the simulated self-pulsating DFB also displayed an optical spectrum with two excited modes, broadened by chirp. The optical spectrum for the self-pulsation under the same conditions as for Fig.(6-10) is shown in Fig.(6-13).

The regions of self-pulsation were then explored by Möhrle *et al*, this time in a symmetric device with two 200μm long sections. The observed injection currents for self-pulsation are shown in Fig.(6-14). The graph shows that the conditions for self-pulsation are symmetric with respect to an exchange of the drive currents in both sections, and that the islands for self-pulsation occupy small areas. The symmetry of the graph makes the possibility of self-pulsation being caused by defects unlikely, and reinforces the belief that self-pulsation in DFB lasers is distinct from that in Fabry-Perot lasers.

The regions for self-pulsation of a simulated DFB with two equal sections were examined for a number of different facet phase combinations. The facet phases were found to affect the self-pulsation significantly. Except for symmetric facet phases, the regions for self-pulsation were not at all symmetric with respect to interchanging the drive currents. An example is shown in Fig.(6-15), for the specific case of facet

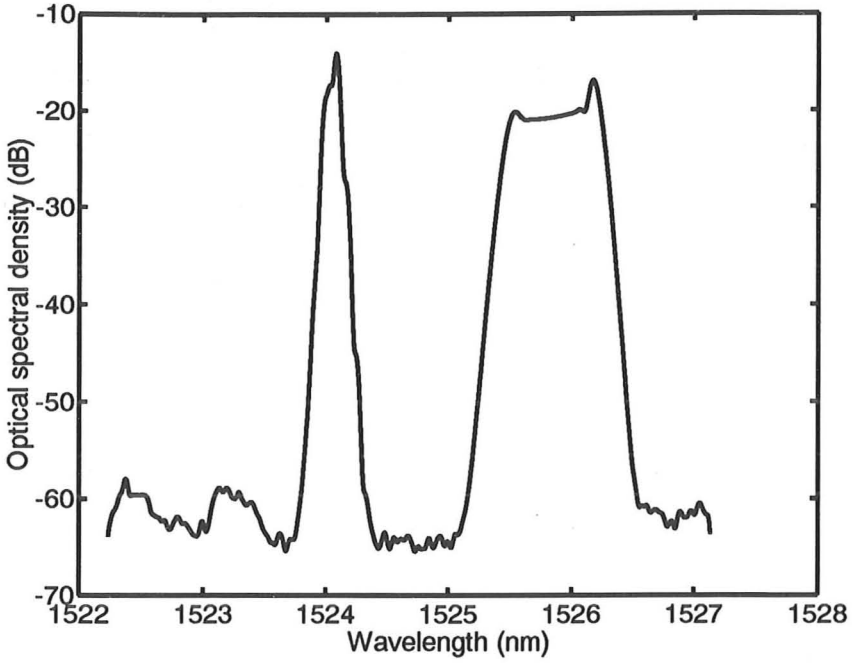

Figure 6-13: Simulated optical spectrum of self pulsating laser, same conditions as for Fig.(6-10).

phases ($\pi/4$ in section 1,$\pi/2$ in section 2). The regions for self-pulsation shown in this plot are those where the contrast ratio of the pulses is greater than 5.

Self-pulsation was also simulated in the same device with perfect anti-reflection coated facets. The device is then truly symmetric, and the regions for self-pulsation are shown in Fig.(6-16). These regions are not completely symmetric because the contrast ratio of the pulses from the same laser facet was used throughout to determine self-pulsation. The regions for self-pulsation in this case were considerably extended.

6.2.3 Mechanism for self-pulsation

The mechanism for self-pulsation in an anti-reflection coated symmetric device was examined. When the injection currents are equal, the laser operates in the +1 DFB mode, at the upper frequency edge of the DFB stop-band. This is due to spatial-hole burning, which in a high κL uniform DFB results in a lower Bragg frequency within the centre of the device: the +1 mode at the high frequency edge of the stopband is then better confined by the curving stopband than the -1 mode at the other edge of the stop band. When the power is increased, the hole burning in a DFB with

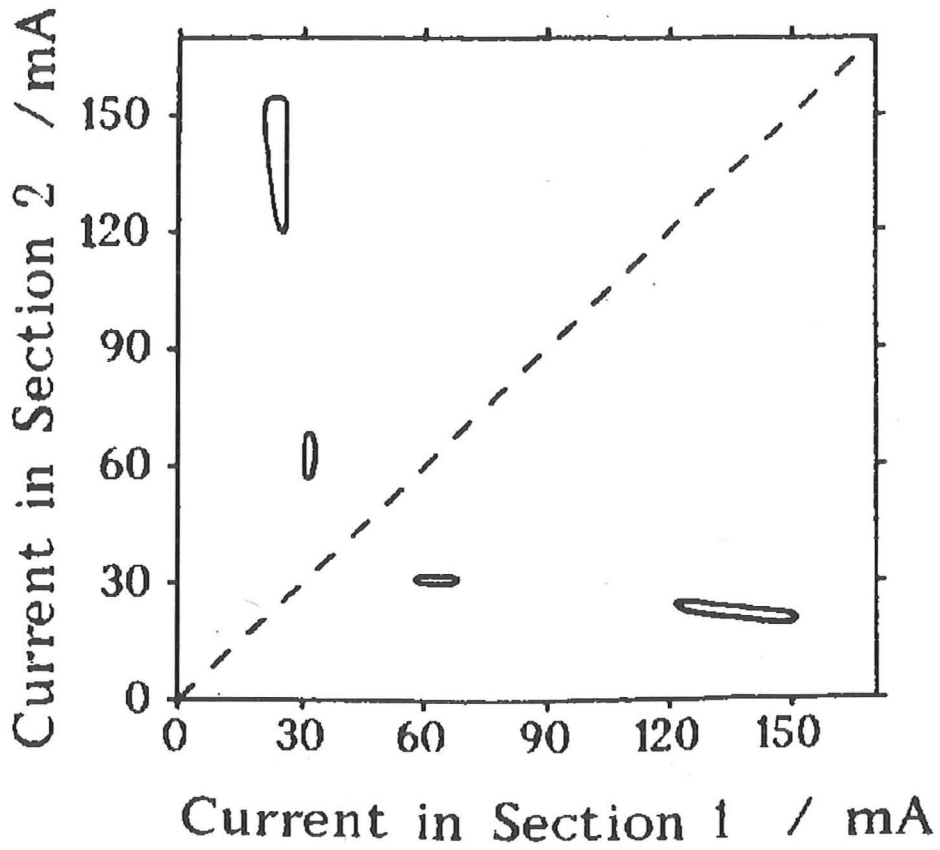

Figure 6-14: Current conditions for self-pulsation in a symmetric device. After [89].

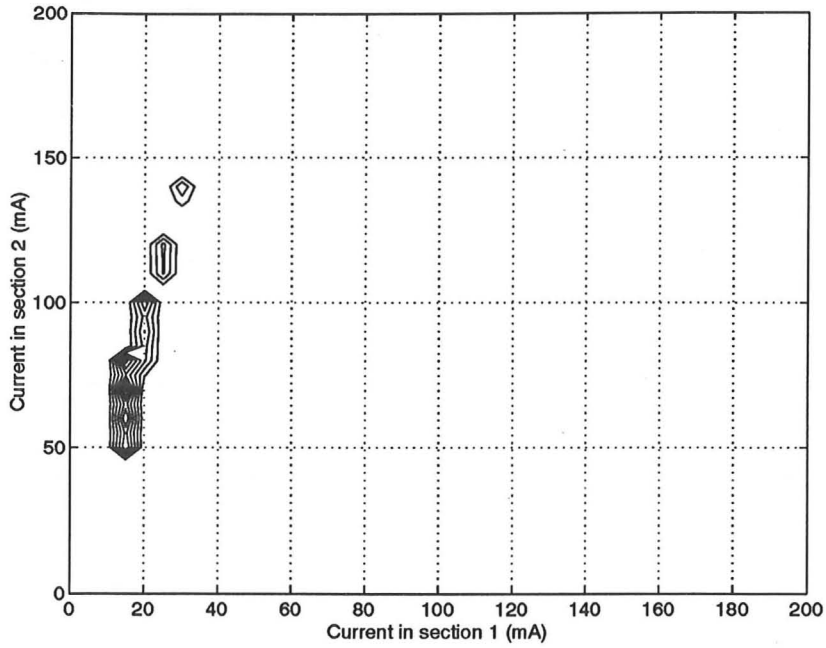

Figure 6-15: Regions for self-pulsation in a simulated DFB with facet phases ($\pi/4$,$\pi/2$).

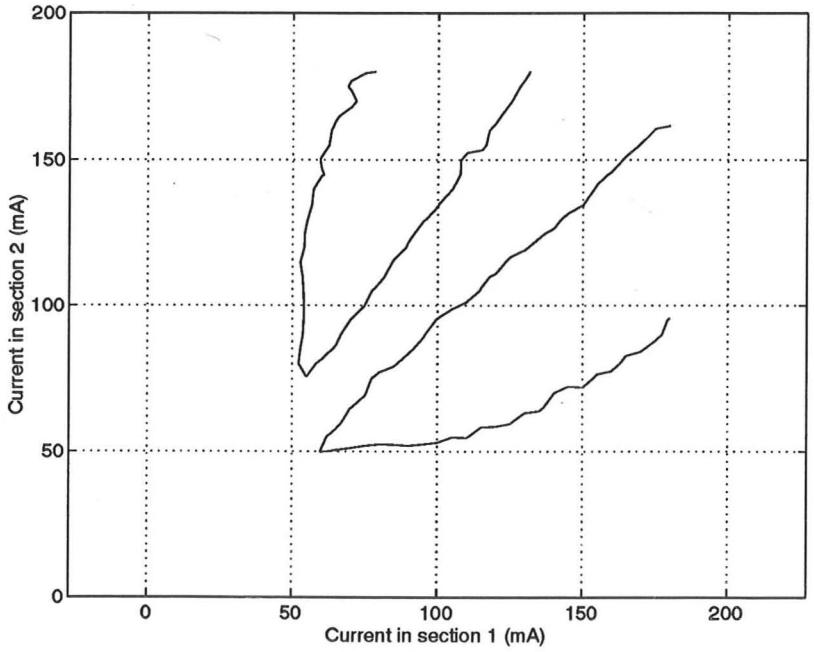

Figure 6-16: Regions for self-pulsation in a simulated DFB with anti-reflection coated facets.

$\kappa L > 3$ even causes the +2 or +3 modes of the DFB to start lasing as well, and longitudinal instability of the type predicted by Schatz [86] can also occur, possibly resulting in multimode operation.

As shown in Fig.(6-17), injecting a larger current I_2 in the right half of the laser than the current I_1 in the left half causes the stop band frequency to increase on the right of the laser. The photon density for the lasing (+1) mode then shifts to the left of the laser, accentuating the carrier density difference between the two sections. The optical power from the right facet falls at this point. When the difference between the two sections has become large enough, the (-1) mode starts lasing, and the optical power shifts to the right hand side of the laser, producing a pulse. The carrier density on the right hand side of the laser is then depleted by this pulse, and the process can be repeated. Figures (6-18) and (6-19) show the optical power from the facet of the highly pumped section and the corresponding frequency of the dominant mode. A mode switch is seen to occur at the beginning and the end of every pulse, and the low frequency mode displays a considerable chirp. The frequency of the dominant optical mode was obtained by smoothing the instantaneous frequency over a time longer than the beat period of the modes.

6.2.4 Self-pulsation: conclusion

Self-pulsation in DFB lasers has been modelled and the simulated results show qualitative agreement with the experimental results, except concerning the regions for self-pulsation in a symmetric device. The parameters of the modelled devices are typical for the structures and materials considered, but are only estimates, and better agreement could be achieved by adjusting the coefficients.

The causes for the disagreement between the experiment and the simulations for the regions of self-pulsation of the "symmetric device" are not known. One reason could be that the cleaved facet phases in the experimental device happened, by chance, to make the device very symmetric.

6.3 Comparisons: conclusion

Two different comparison were presented:

The European COST-240 modelling exercise provided an opportunity for a number of research groups to check their modelling tools by a detailed comparison of simulation results. Only D.C. and noise and small signal results were compared as

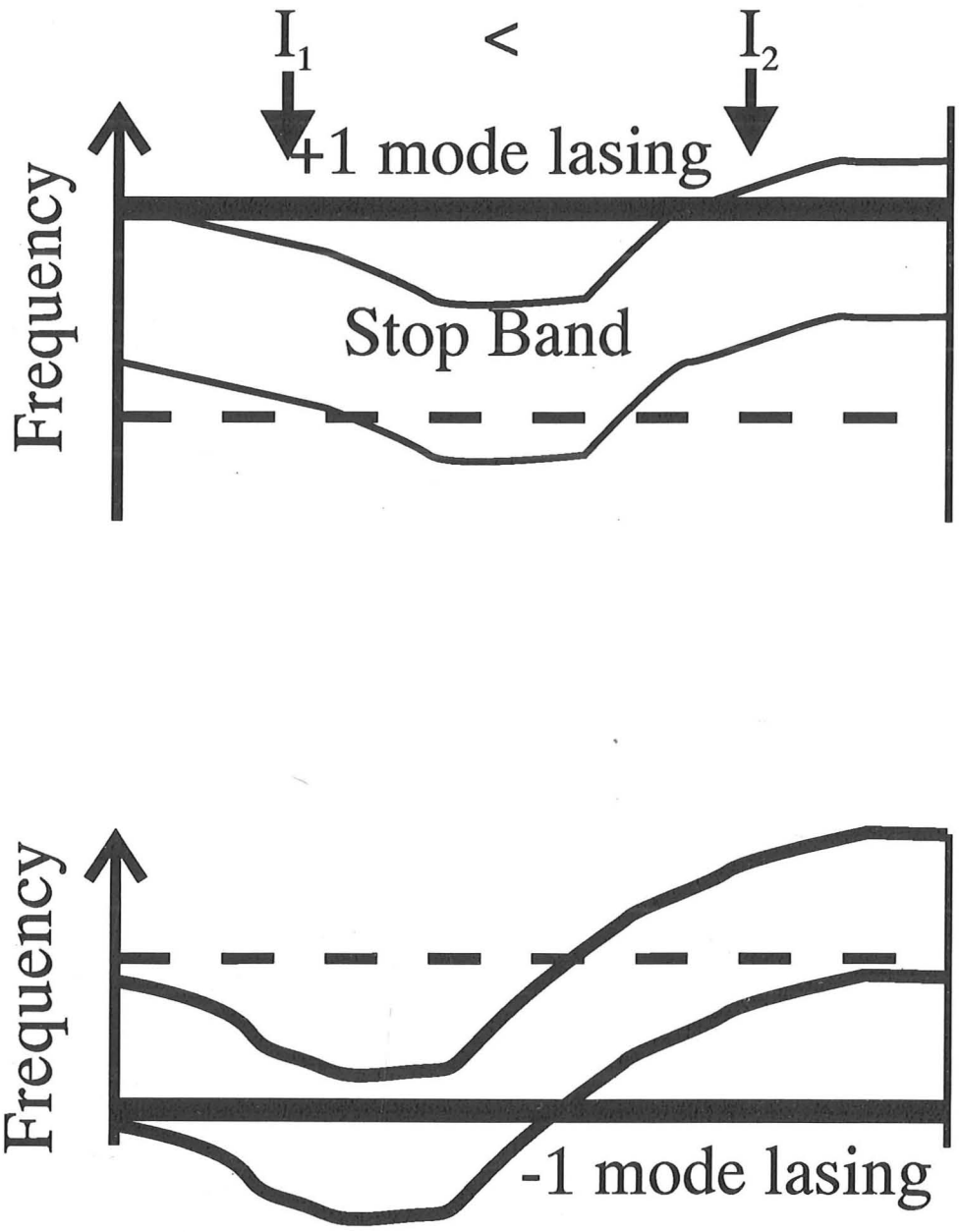

Figure 6-17: Mechanism for self-pulsation in terms of respective positions of the stopbands.

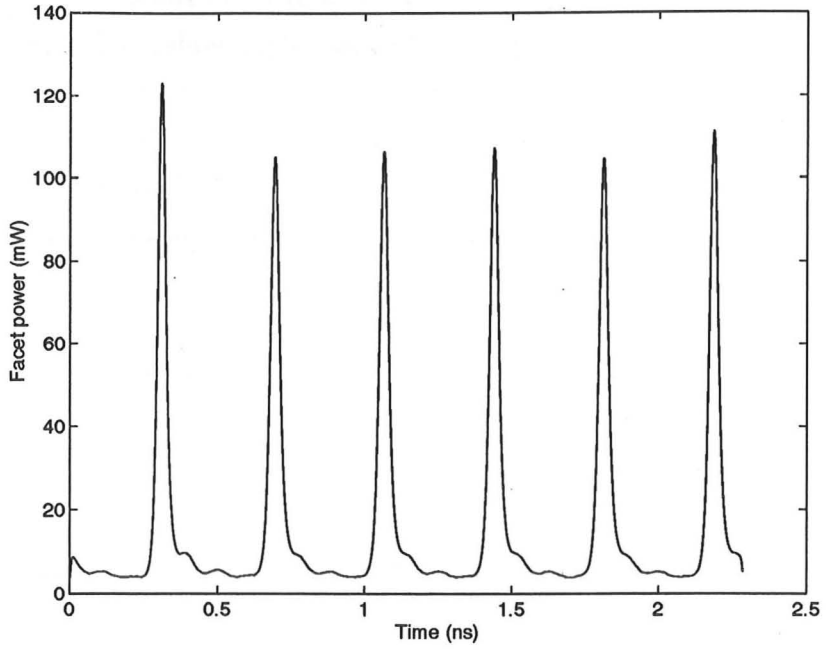

Figure 6-18: Optical power in the self-pulsating regime.

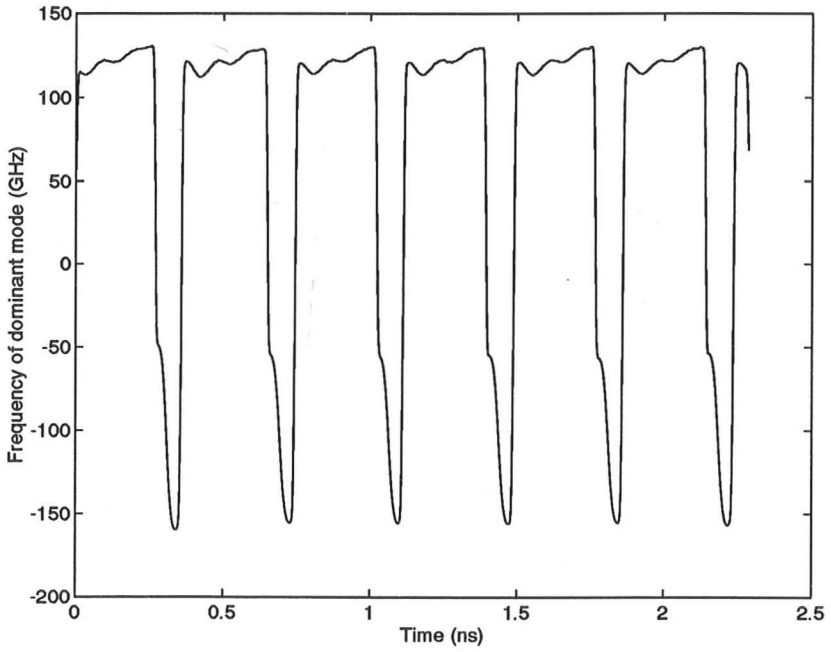

Figure 6-19: Frequency of dominant mode during self-pulsation showing mode switch.

large signal models are less common. The agreement between the time domain model results and those of some other models are very good, often within one percent. The linewidth simulations, showing linewidth rebroadening due to mode instability, agree well with those of the University of Gent and TFL, although the methods used differ substantially. The closeness of the agreement indicates that the numerical methods used by the time domain model are accurate.

Experimental measurements of self-pulsating DFB lasers were compared with simulations using the time domain model. Comparing experimental and modelling results of laser diodes is an intricate task: the models rely on a large number of device parameters which ideally would have to be measured precisely. A detailed knowledge of the device fabrication is also needed, but is not always available. The experiments have to be designed so as to minimize the dependence of the results on the measurement techniques, or at least to make sure that these dependencies are well understood. If some device parameters are not known with sufficient precision, then in some cases they can be adjusted to provide a close fit between experiment and simulation; this is usually a valid procedure when the number of unknown parameters is small so that they can be uniquely determined. When large numbers of parameters are unknown, an accurate quantitative comparison is of less benefit: by choosing parameters carefully, experiment and simulation can be often be made to agree, sometimes using very different sets of parameters.

Due to considerations of time, precise quantitative comparisons with experiment have not been carried out over the course of this Ph.D., and remain a subject for future work. A more qualitative comparison has been given instead, concerning self-pulsation in DFB lasers. This comparison has shown that some complicated aspects of DFB laser behaviour can be simulated by the time domain model. The speed of the model's algorithm, together with the increasing availability of cheap processing power, suggests that the time domain model can be used to study complex behaviour in laser diodes. In conjunction with experiments, this powerful numerical modelling could be used to advance our understanding of the phenomena to the point were analytic models providing a deeper insight could more easily be derived.

Chapter 7

Intensity noise and squeezing in laser diodes

Experimental work has demonstrated that sub-Poissonian photon statistics from laser diodes are possible [33]. The time-domain model presented in Chapter 2 was incapable of simulating such "squeezed light": the representation of the fields it used did not allow the simulation of light with sub-Poissonian statistics.

This is because when a stream of photons is incident upon a partially transmitting mirror, each photon is randomly and independently either transmitted or reflected. If a constant optical flux $I(t)$ represents a stream of regularly spaced photons *incident* upon the mirror, the *transmitted* flux $I_t(t)$ will not be constant, but will display random fluctuations, to account for the random reflections of the incident photons. A noise source must therefore be associated with the mirror. It is also found that noise sources must be associated with any radiation losses in the laser. The model in Chapter 2 did not include these noise sources associated with losses.

Instead, the model in Chapter 2 represented a Poisson stream of photons (photons incident upon the mirror, at times independent from one another) by a constant optical flux $I(t)$. The effect of a random reflection or transmission by a mirror, upon an incident Poisson stream of photons is to produce a transmitted stream of photons with Poisson statistics as well. So if the incident (Poisson) stream is represented by a constant flux $I(t)$, then the transmitted (Poisson) stream can also be represented by a constant flux $I_t(t)$, and no noise sources are necessary at the laser facets. The consequence of this, is that photodetection shot noise needs to be included at the detectors to recover the Poisson statistics represented by the constant flux $I(t)$.

The necessity of adding this photodetection shot noise at the detector means

that photon streams with sub-Poissonian statistics cannot be represented by a real flux $I(t)$. This chapter puts forward a new speculative theory whereby, in order to simulate squeezed light, fluctuations in the photon flux have two components. One component, associated with real fluctuations of $I(t)$, describes additional intensity noise, on top of the shot noise at the detector. The other component, associated with imaginary fluctuations of $I(t)$, has a negative average fluctuation power $< \delta I(t)^2 >$, and can therefore cancel the photodetection noise and simulate sub-Poissonian photon statistics.

This formalism for the optical fields, which allows complex fluctuations in the power, is known as the *positive P* distribution, and has been used to calculate photon statistics in other problems of quantum optics. Its new application to lasers, presented in this chapter, also requires complex fluctuations in the carrier density. Only the ensemble averages of these optical power and carrier densities are measured in reality, and these ensemble averages are found to be real, so that the theory does not predict complex values for measured quantities.

In this chapter, the new theory is described, and simulated intensity noise characteristics are presented for a variety of laser diode structures. The simulations reveal that the best possible reduction in intensity noise depends on the laser geometry: for some laser structures, like Fabry-Perot lasers with low facet reflectivities, it is indeed impossible to generate squeezed light. Simulations of intensity noise under large signal modulation are also presented.

7.1 Introduction

Relatively low intensity fluctuations enable semiconductor laser diodes to be used as good sources for optical-fiber communications and sensors. However, the relative intensity noise (RIN) power of the best laser diode source is not far below the maximum levels permitted by high quality analogue TV transmission [96] so that there is still a need for improved understanding about noise reduction.

Phase noise in a laser can usefully be described by classical optical fields where the phase is perturbed by random spontaneous events [14]. However, intensity noise really needs a quantum description of the shot noise and stimulated emission processes. Initial quantum theories of lasers [7, 24] appeared to indicate that intensity noise tended to the ideal shot noise limit at high optical powers, limiting the maximum signal-to-noise ratio for analogue transmission. Recently [33, 52, 97] it has been realized that intensity fluctuations below the shot noise level are achievable without

violating the uncertainty principle, because reduced intensity fluctuations simply increase the phase uncertainty. Such light is then said to be amplitude-squeezed.

When electrical current pumps a semiconductor laser with sufficiently high quantum efficiency, the low frequency noise in the current is directly converted into noise in the photon output. A noiseless pump leads to a noiseless output photon stream. By feeding current to a laser diode through a large enough series resistance, held at a low enough temperature, there is negligible shot and thermal noise in the current and amplitude squeezing has been observed [52, 98].

Various applications of the low noise in such squeezed light have been proposed: measurement of small changes in absorption [99]; improved interferometric measurements [100, 101]; improved signal-to-noise ratio of amplitude modulated transmission [102]. Indeed, a photon number state (the limit of intensity squeezing) realizes the maximum theoretical channel capacity in optical communications [103]. The drawback is that 3dB attenuation effectively removes the squeezing with Poissonian statistics again appearing.

Experimental results have demonstrated that relatively simple laser diode sources can emit amplitude squeezed light [52, 104] (up to 8.3 dB of amplitude squeezing [105]). Partition noise between modes limits the level of intensity squeezing in Fabry-Perot laser diodes [105, 106]. Suppressing these side modes by injection locking has improved the level of squeezing [106].

A realistic computer model is therefore required for laser diodes, in order to gain insight into the squeezing process. This paper extends previous work on a travelling wave, time domain model, based on quantum mechanical theory, to show how to simulate squeezed light combined with distributions of photon density, spatial hole burning, spatially distributed noise sources and many modes. Both steady state and large signal regimes are examined. A feature of our model is the use of quantized optical fields which are represented using the *positive*-P distribution [11, 107]. Intensity squeezed light is simulated through carrier densities and optical powers having complex fluctuations, but still having real mean powers. The mean square optical power can then be smaller than the square of the mean power. A time domain algorithm, related to that pioneered for standard laser diodes by Lowery [21], calculates both large signal and small signal noise characteristics for squeezed laser states.

Fabry-Perot (FP), Distributed Bragg Reflector (DBR) and, Distributed Feedback (DFB) lasers structures are examined. The simulations show that the device structure and the losses are more important in determining squeezing than expected

from lumped models (which predict that the lowest achievable intensity noise is given for a quiet pump, by the device quantum efficiency). This is due to spontaneous sources, producing excess output intensity fluctuations which are anticorrelated with fluctuations in the dissipated power (or power escaping from the rear facet of the laser), thus keeping the fluctuation in the total power (output + losses) equal to the fluctuation in drive current, as required by energy conservation. This effect prevents squeezed light output in some cases, and causes DFB lasers to be more noisy than FP lasers for squeezing. This is why the DBR appears a useful compromise, with performance similar to FP lasers, but single moded. Amplitude squeezing appears possible even with large signal modulation, a fact which is of particular interest in the transmission of analogue information.

This chapter first introduces the theory for squeezing. The extension of the theory to a large signal time-domain model is then discussed. Simulation results of intensity noise in FP, DFB and DBR laser diodes under C.W. and large signal modulation are presented.

7.2 Model for squeezing

Quantized optical fields can be represented in a form suitable for computation by using distribution functions [10]. The optical fields are then described by classical variables which are driven by stochastic Langevin noise sources. In the approach of Haken [9] Lax and Louisell [10, 24], the Glauber P-representation is used to describe the quantized optical mode by classical variables, allowing the optical fields to be described in semiclassical terms: a single mode laser is modelled by the following equations:

$$\dot{\alpha} = \frac{1}{2}\Big(g(N-N_t)-\gamma\Big)\alpha + F_\alpha(t), \tag{7.1}$$

$$\dot{\alpha^*} = \frac{1}{2}\Big(g(N-N_t)-\gamma\Big)\alpha^* + F_{\alpha^*}(t), \tag{7.2}$$

$$\begin{aligned}\dot{N} &= D - N/\tau_N - g(N-N_t)\alpha^*\alpha + F_N(t) \\ &- \alpha(t)F_{\alpha^*}(t) - \alpha^*(t)F_\alpha(t),\end{aligned} \tag{7.3}$$

where α is the optical mode amplitude, N is the carrier number, N_t is the carrier number at transparency, γ is the optical loss from the facet and g is the material gain constant.

The noise sources $F_\alpha(t)$ and $F_{\alpha^*}(t)$ are complex conjugates, have zero mean and

are Gaussian and delta-correlated:

$$< F_\alpha(t)F_\alpha(t') > = < F_{\alpha^*}(t)F_{\alpha^*}(t') >= 0, \tag{7.4}$$

$$< F_\alpha(t)F_{\alpha^*}(t') > = g(N - N_t)n_{sp}\delta(t - t'). \tag{7.5}$$

The carrier noise $F_N(t)$ is real, Gaussian, with zero mean:

$$< F_N(t)F_N(t') >= \Big(D' + N/\tau_N - g(N - N_t)\alpha^*\alpha\Big)\delta(t - t'). \tag{7.6}$$

Here D' determines the drive current fluctuations: for shot noise fluctuations, D' equals the drive D, but when the current noise is suppressed, $D' = 0$.

The quantum mechanical expectation values for the optical field mode are given by the stochastic ensemble averages:

$$< (a^\dagger)^m a^n >=< (\alpha^*)^m \alpha^n > . \tag{7.7}$$

The photon number, in particular, is $< a^\dagger a >=< |\alpha^2| >$. The normal ordering in Eq. (7.7) implies that the vacuum state is described by $\alpha = 0$ (the fields are zero when no photons are present). Another consequence is that shot noise must be added at the receiver to get the total fluctuation in the photodetection current [1]. Intensity squeezed light, which exhibits sub-shot noise photodetection current fluctuations over a given frequency range is impossible to simulate using the Glauber (semiclassical) P-distribution: the distributions corresponding to squeezed states of light, when they exist at all, are highly singular [7]. Considering the carrier noise correlation Eq. (7.6), we see that above a certain optical power, the right hand side will become negative, provided that the pump noise D' is sub-shot noise. This negative noise correlation is impossible to satisfy with real noise sources.

Other distribution functions could be used to simulate squeezed light: for instance the Wigner, or the Q-functions [11] could be used. One drawback is that these distribution functions include contributions from the vacuum fluctuations of the optical fields: their energy must be subtracted from the power $h\nu\alpha^*\alpha$ to get the accessible power for photodetection. It is also necessary to include noise sources associated with losses at the laser facets.

In this work an extension of Glauber's semiclassical distribution is used: the *posi-*

[1]This can be seen by inverting the laser equations (7.1,–7.3), with N clamped to 0, to provide absorption and thus simulate a photodiode. The drive current D is then negative, and is identified with the photocurrent. The carrier noise $F_N(t)$, according to Eq. (7.6), is then at the shot noise level, and is the photodetection noise.

tive P-distribution of Drummond and Gardiner [107], which provides a smooth transition from the intuitive semiclassical approach. The Glauber P-function $P(\alpha, \alpha^*)$ expresses the quantum mechanical density matrix ρ, as a diagonal superposition of coherent states $|\alpha>$ [42]:

$$\rho = \int d^2\alpha P(\alpha, \alpha^*)|\alpha >< \alpha|, \tag{7.8}$$

where the integration is over the whole complex plane. The *positive* P-distribution generalizes this superposition to include non diagonal elements:

$$\rho = \int d^2\alpha \int d^2\beta \, P(\alpha, \beta)|\alpha >< \beta^*|. \tag{7.9}$$

The joint distribution of two complex numbers, α and β, is now required to describe a quantum state. In our model, we may use the *positive* P-distribution simply by replacing α^* by β in Eqs. (7.1–7.3), that is allowing α and α^* to be no longer a complex conjugate pair. By doing this, we can always satisfy the carrier noise correlation (7.6) by making the noise source imaginary, when the correlation becomes negative. The laser equations are otherwise unchanged:

$$\dot{\alpha} = \frac{1}{2}\Big(g(N - N_t) - \gamma\Big)\alpha + F_\alpha(t), \tag{7.10}$$

$$\dot{\beta} = \frac{1}{2}\Big(g(N - N_t) - \gamma\Big)\beta + F_\beta(t), \tag{7.11}$$

$$\begin{aligned} \dot{N} &= D - N/\tau_N - g(N - N_t)\alpha\beta + F_N(t) \\ &- \alpha(t)F_\beta(t) - \beta(t)F_\alpha(t). \end{aligned} \tag{7.12}$$

The same spontaneous noise sources (7.5) are used.

In this formalism, the variables $I = \alpha\beta$, which describe the photon density, and N, which describes the carrier density, are allowed to be complex. The photon and carrier densities are obtained from these variables by averaging, and only ensemble averages like $< I >$ and $< N >$ have a physical meaning. These averages are real: for example, the variable I consists of a real average term I_0, plus a real fluctuation δI_r and an imaginary fluctuation $i\delta I_i$. The ensemble averages of the fluctuation terms are zero:

$$< I >= I_0 + < \delta I_r > + i < \delta I_i >= I_0. \tag{7.13}$$

The mean square photon density also is real:

$$\begin{aligned} < I^2 > &= < (I_0 + \delta I_r + i\delta I_i)^2 > \\ &= I_0^2 + < \delta I_r^2 > - < \delta I_i^2 > . \end{aligned} \tag{7.14}$$

However, the use of a complex fluctuation $i\delta I_i$, enables the photocurrent noise to be less than the shot noise level: the photocurrent I_D for a photodiode with an efficiency η is

$$I_D = \eta\gamma I + s_D = \eta\gamma(I_0 + \delta I_r + i\delta I_i) + s_D. \tag{7.15}$$

The term s_D is the photodetection shot noise, $< s_D^2 >=< I_D >= \gamma\eta I_0$ (see footnote 1). The total photocurrent noise $\delta I_D = s_D + \gamma\eta(\delta i_r + i\delta I_i)$ has a real mean power equal to:

$$< \delta I_D^2 >=< I_D > + \gamma^2\eta^2 \left(< \delta I_r^2 > - < \delta I_i^2 > \right). \tag{7.16}$$

Provided that $< \delta I_r^2 > - < \delta I_i^2 > < 0$, the photocurrent noise power can be less than the shot noise $< I_D >$. The minimum value allowed by the noise sources for this model, which corresponds to complete squeezing of amplitude fluctuations, is $< \delta I_r^2 > - < \delta I_i^2 >= -I_0/\gamma$ (see Appendix A). The photocurrent noise power is in this case:

$$< \delta I_D^2 >=< I_D > (1 - \eta). \tag{7.17}$$

This photocurrent noise power is thus always positive, and can be reduced substantially below the shot noise level only if the detector efficiency η, is close to unity. Ensemble averaging ensures that no imaginary values are predicted by the model for real physical quantities.

A small signal analysis using this formalism is given in Appendix A. It shows that our formalism gives the same answers as the more conventional approach in [33] with regard to fluctuations for a simple laser model.

7.3 Extension to the travelling wave model.

In Chapter 2, the quantized optical waves were described using the Glauber P-function by complex travelling waves, and were sampled and propagated around the laser cavity in time and space using a time domain algorithm similar to the Transmission Line Laser Model of Lowery [21]. To simulate squeezed light, two travelling-wave complex fields must be used to represent the propagating optical

fields. These travelling wave pairs are on average complex conjugates of one another, so that their product (the power flux), like the carrier density, is real on average, but exhibits complex fluctuations.The extension from Chapter 2 is straightforward, but a brief description is given here.

The coupled wave equations determine the spatial and temporal evolutions of the complex field pairs in a DFB. For the forward wave part of the optical fields these equations are:

$$\begin{aligned}\left(\frac{1}{v_g}\frac{\partial}{\partial t}+\frac{\partial}{\partial z}\right)F &= -\left(i\delta - b\Gamma(N-N_t)/2+\alpha_s/2\right)F \\ &+ i\kappa_{RF}R + G_F(z,t), \qquad (7.18)\\ \left(\frac{1}{v_g}\frac{\partial}{\partial t}+\frac{\partial}{\partial z}\right)F' &= -\left(-i\delta - b\Gamma(N-N_t)/2+\alpha_s/2\right)F' \\ &- i\kappa^*_{RF}R' + G^*_F(z,t). \qquad (7.19)\end{aligned}$$

For the reverse fields,

$$\begin{aligned}\left(\frac{1}{v_g}\frac{\partial}{\partial t}-\frac{\partial}{\partial z}\right)R &= -\left(i\delta - b\Gamma(N-N_t)/2+\alpha_s/2\right)R \\ &+ i\kappa_{FR}F + G_R(z,t), \qquad (7.20)\\ \left(\frac{1}{v_g}\frac{\partial}{\partial t}-\frac{\partial}{\partial z}\right)R' &= -\left(-i\delta - b\Gamma(N-N_t)/2+\alpha_s/2\right)R' \\ &- i\kappa^*_{FR}F' + G^*_R(z,t). \qquad (7.21)\end{aligned}$$

The symbols used are:

- the pairs $\{F(z,t), F'(z,t)\}$ and $\{R(z,t), R'(z,t)\}$ describe the forward and reverse propagating optical fields.
- δ accounts for changes in the refractive index due to changes in the carrier density,
- $b\Gamma(N-N_t)$ is the gain due to the carriers,
- α_s is the waveguide scattering and absorption loss,
- κ_{RF} and κ_{FR} are the coupling coefficients for reverse and forward waves respectively (zero in a Fabry-Perot laser).

- $G_F(z,t)$ and $G_R(z,t)$ are "spontaneous" Langevin noise sources, delta-correlated with powers like in Eq. (7.5). [2]

In the time domain model, the fields are sampled in space and time, at intervals Δz and $\Delta t = \Delta z/v_g$, where v_g is the waveguide group velocity:

$$F(n\Delta z, k\Delta t),\ R(n\Delta z, k\Delta t) \ \rightarrow \ F_{n,k},\ R_{n,k}. \tag{7.22}$$

The laser cavity of length L is thus divided into a number $N_S = L/\Delta z$ of sections. This sampling loses no field information, provided that the bandwidth of the fields, where the energy is significant, is smaller than the Nyquist bandwidth $B = 1/\Delta t$. The time domain model then estimates the values of the sampled fields at time step k, in terms of their values at the previous time step $k-1$, using the field equations (7.18–7.21): the simplest estimate is obtained by making the first order approximation [108, 109]:

$$\frac{\partial F}{\partial t} \rightarrow \frac{F_{n,k} - F_{n,k-1}}{\Delta t}, \quad \frac{\partial F}{\partial z} \rightarrow \frac{F_{n,k} - F_{n-1,k}}{\Delta z}. \tag{7.23}$$

This method of estimation is accurate for small enough sampling steps. For faster simulations, the sampling step must be increased, and the modelling results then are found to depend strongly on the number of sections used. A more accurate algorithm may be used by assuming that the fields vary in time as

$$\frac{\partial F}{\partial t} = \beta_F F(z,t), \quad \frac{\partial R}{\partial t} = \beta_R R(z,t). \tag{7.24}$$

where the complex instantaneous frequencies β_F and β_R for the forward and reverse fields may be estimated from the previous time step. The coupled wave equations (7.18,7.20) can then be integrated exactly between the points (t,z) and $(t+\Delta t, z+\Delta z)$: a transfer matrix is obtained relating the sampled fields $F_{n,k}$ and $R_{n+1,k}$ to the fields at the next time step $F_{n+1,k+1}$ and $R_{n,k+1}$. A DFB can then be modelled accurately using as little as 20 sections.

A digital filter is used to model the material gain curve. Rate equations are used

[2] On a microscopic level, forward and reverse spontaneous noise sources, which are due to fluctuating dipoles, are correlated. When the finite bandwidth and discrete sampling intervals of the travelling wave model are taken into account, uncorrelated noise sources should be used.

to model the changes in carrier density in the different sections of the laser:

$$\begin{aligned}\frac{dN(z,t)}{dt} &= J/ed - \frac{b\Gamma(N-Nt)}{1+\epsilon P}\Big(F'F + R'R\Big) \\ &- N/\tau_n - BN^2 - CN^3 - F_N(z,t). \end{aligned} \tag{7.25}$$

The carrier noise source $F_N(z,t)$ consists of two terms:

$$\begin{aligned}F_N(z,t) &= \Big(FG_F^*(z,t) + RG_R^*(z,t) \\ &+ F'G_F(z,t) + R'G_R(z,t)\Big) + F_N'(z,t). \end{aligned} \tag{7.26}$$

The first term is a noise source correlated with the field spontaneous noise sources $G_F(z,t)$ and $G_R(z,t)$, and expresses the power conservation of the spontaneous emission process. The carrier noise $F_N'(z,t)$ is uncorrelated with the field noise sources, and is a Gaussian white noise with correlation:

$$\begin{aligned}< F_N'(z,t)F_N'(z',t') > &= \Big\{D' + N/\tau_n + BN^2 + 2CN^3 \\ &- \frac{b\Gamma(N-Nt)}{1+\epsilon P}\Big(F'F + R'R\Big)\Big\} \\ &\times \delta(t-t')\delta(z-z'). \end{aligned} \tag{7.27}$$

The factor '2' in the Auger cubic recombination term is included because Auger recombination is a process which removes two carriers at a time, so its shot noise contribution is twice that of a one carrier process.

7.4 Noise analysis using the travelling wave model

The time domain model calculates the response of the noise driven optical fields in the laser to changes in drive current, as a function of time. Discrete Fourier transforms may be used, in order to examine the spectral information (e.g. power spectrum or linewidth) contained in the sampled fields. When the output of the laser is single moded, and the side modes are weak, it is possible using this model, to carry out a deterministic small signal analysis. To do this, all the noise sources are suppressed: the side modes which are below threshold, then vanish as they are no longer driven by spontaneous emission. Once the simulated laser has settled into this noiseless state, the responses of the power and phase of the fields to isolated noise

impulses, at different locations within the laser, can be monitored. The linearity in the small signal regime, together with the lack of correlation between different noise sources, is used to determine the mean fluctuations of the optical fields. This approach enables the influence of noise sources at specific locations within the laser to be determined individually.

This small signal analysis in fact enables the intensity noise to be calculated using the simpler, and faster algorithm described in chapter 3, which does *not* model optical intensities and carrier densities with complex fluctuations. This is because the response of the laser to an imaginary carrier noise impulse can be deduced from the response of the laser to a real carrier noise impulse. One must simply change the sign of the contribution of the carrier noise sources to the intensity noise spectrum. By changing the correlation for the carrier noise of "semiclassical" models like those in references [23, 110], and by changing the sign of their contribution to the intensity fluctuations, amplitude squeezed light can be simulated. This is, however, no longer the case when the small signal analysis is not applicable, as for example when the laser diode is multimoded, or in certain regimes of large signal modulation: the algorithm described in this chapter must then be used.

For example, to measure the intensity noise of the laser using the small signal analysis, the responses $\delta I(t) = I(t) - < I >$ of the power to impulses at the locations of the different noise sources is recorded. Due to the lack of correlation between the noise sources, the total intensity noise spectrum is the sum of the the intensity spectra for the different impulses. The responses $\delta I(t)$ are Fourier transformed to determine the power spectrum. The power spectrum of $\delta I(t)$ is calculated from its Fourier transform $\delta i(\omega)$:

$$\delta i(\omega) = \int_{-\infty}^{\infty} \delta I(t) \exp(-i\omega t)\, dt. \tag{7.28}$$

The power spectrum $P_I(\omega)$ is then generally taken to be the modulus square of this Fourier transform:

$$P_I(\omega) = \delta i(\omega) \times \delta i(\omega)^*. \tag{7.29}$$

In this model, we must calculate the power spectrum differently, in order to allow the negative power spectral density associated with a complex intensity fluctuation. We therefore define the power spectral density as:

$$P_I(\omega) = \delta i(\omega) \times \delta i(-\omega). \tag{7.30}$$

Laser Parameters		
Cavity length	L	300μm
Active region width	w	1.5μm
Active region thickness	d	0.1 μm
Gain $\times$ confinement factor	$b\Gamma$	$4 * 10^{-16}$ cm^2
Inversion parameter at n_{th}	n_{sp}	1.5
Transparency carrier density	n_t	$0.3 * 10^{18}$ cm^{-3}
Gain-refractive index coupling	α_H	5.0
Free space wavelength	λ	1.55 μm
Group refractive index	n_g	3.6
Gain curve FWHM	$\Delta\lambda$	20 nm
Carrier lifetime	τ_n	10 ns
Bimolecular coefficient	B	10^{-10} cm^{-1}s^{-1}
Auger recombination coeff.	C	10^{-29} cm^{-2}s^{-1}

Table 7.1: Parameters used to simulate squeezing in laser diodes.

Using this definition, the power spectrum of a real signal is unchanged, because if $\delta I(t)$ is real, $\delta i(-\omega) = \delta i(\omega)^*$. If the signal $\delta I(t)$ is imaginary, $\delta i(-\omega) = -\delta i(\omega)^*$, so that the power spectral density Eq. (7.30) is negative. The real and imaginary parts of the intensity fluctuations are uncorrelated, so the ensemble averaged power spectral density will be real, but, in general, negative as well as positive.

7.5 Simulation results

Table 7.1 lists parameters used (unless otherwise indicated) to simulate devices at low temperatures ($\approx$ 10K) where squeezing can be obtained. The low temperature particularly alters the transparency carrier density and the spontaneous emission factor from those for operation at normal room temperature.

7.5.1 Fabry-Perot lasers

According to a model which does not take into account the laser diode structure, like the one in Appendix A, determining the low frequency intensity noise achievable at high powers, is a trivial matter: the intensity noise reduction below the shot noise level (SNL) is simply equal to the quantum efficiency of the device.

In contrast, our model shows that the device structure *is* important in determining the lowest achievable intensity noise. To illustrate this, a symmetric FP laser

with no waveguide loss is modelled, for different facet reflectivities. A lumped model would predict a low frequency intensity noise from one facet equal to 50% of the shot noise level, irrespective of facet reflectivities R (with total pump noise suppression). Figure (7-1) shows the low frequency intensity noise from one facet at ≈ 30 times threshold versus R. There is a very strong dependence on R: indeed, for low reflectivities, the intensity noise is above the shot noise level. When the power from both facets is considered, the intensity noise is strongly squeezed, reduced to about 1% of the shot noise level, as expected. This indicates an anticorrelation between the noises from each facets. The dashed line in Figure (7-1) shows the intensity noise as calculated by the model of Chapters 2 and 3: no intensity squeezing is seen, nor can intensity squeezing be modelled. This is because the representation used in Chapter 2, like that used in distributed semiclassical models [29,30], cannot describe sub-shot noise drive current fluctuations, for which carrier noise with negative powers are required.

The large noise for low facet reflectivities is due to a strong contribution from the spontaneous noise sources, similar to the longitudinal excess spontaneous emission effect which affects the linewidth [26]. A new analytic formula is derived in Appendix B from a small signal analysis: the lowest achievable intensity noise from one facet is:

$$\left\{n_{sp}(1-R)^2/4R + 1/2\right\}\hbar\omega P, \tag{7.31}$$

where $\hbar\omega P$ is the shot noise level. This formula is plotted as the solid line in Figure (7-1), and agrees well with the modelling results. The more general formula for different facet reflectivities is given in Appendix B.

Differences between the model described here and semiclassical models, which are unable to simulate squeezed light, exist even when the simulated intensity noise is above the shot noise level for both models. Figure (7-2) shows the intensity noise calculated for a Fabry-Perot with negligible waveguide losses and a cleaved rear facet (R=0.3), as a function of the front facet reflectivity. The dashed line is the result for a noiseless pump current, while the solid line is the result calculated using a semiclassical model, which implicitly assumes shot-noise drive current fluctuations. Even though the intensity noise is, in both cases, greater than the shot noise level over the entire range of front facet reflectivities, the quantum treatment gives an intensity noise nearly half of that given by the semiclassical treatment, for low front facet reflectivities.

Until now all reported laser diode sources of squeezed light have been FP lasers

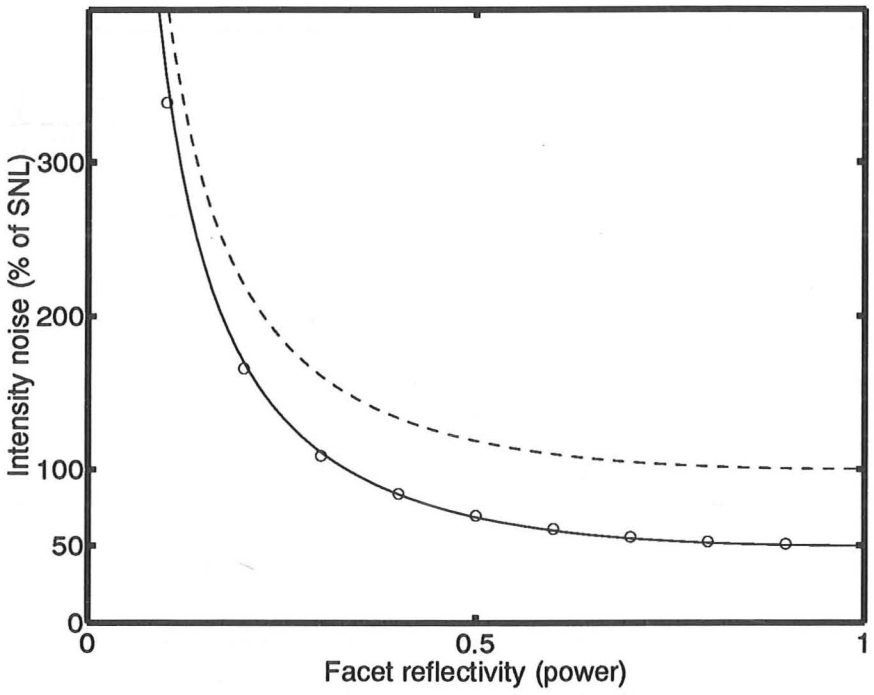

Figure 7-1: Intensity noise (% of shot noise level (SNL)) versus facet reflectivity R for lossless waveguide, symmetric FP lasers. Circles: modelling results, Solid line: analytic formula, Dashed line: with shot noise drive current fluctuations, as given by a semiclassical treatment. The facet power is $\approx$ 7.8mW for a drive current of 20mA (about 40 times threshold). The narrow gain curve at low T ensured single mode operation.

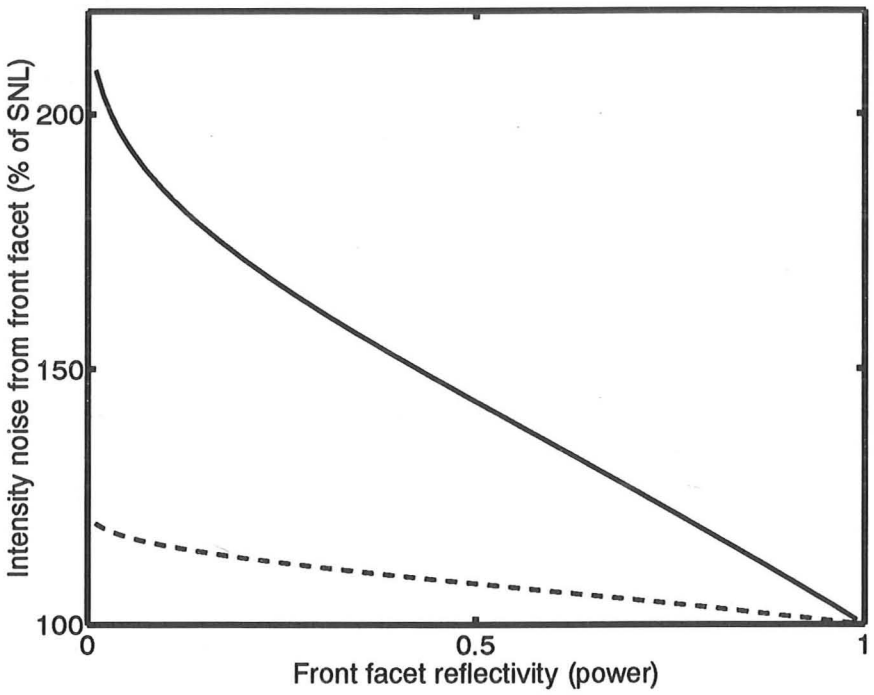

Figure 7-2: Calculated intensity noise as a percentage of the shot noise level (SNL) versus the front facet reflectivity. The waveguide is lossless, the back facet is cleaved (R=0.3), and n_{sp}=1.5.
Dashed line: quantum treatment with noiseless pump.
Solid line: semiclassical treatment, with shot-noise drive fluctuations.

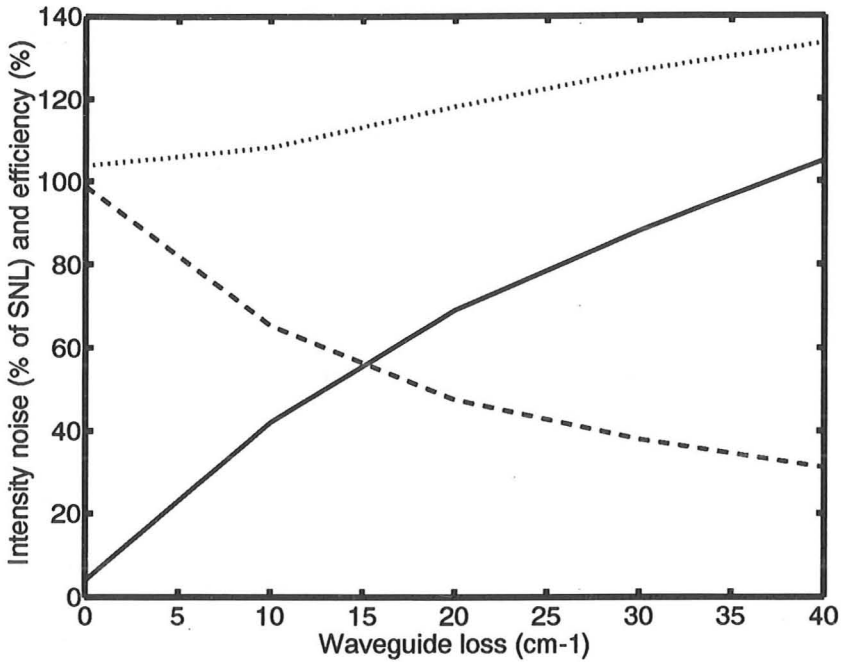

Figure 7-3: Calculated intensity noise (Expressed as a percentage of the shot noise level (SNL): solid line, for noiseless pump; dotted line, for a semiclassical treatment with shot noise drive current fluctuations) and quantum efficiency (dashed line) for a HR coated-Cleaved FP laser, versus waveguide loss α. The output power is 7mW, with a drive current about 40 times threshold.

emitting from an anti-reflection coated front facet and having a high reflection coated rear facet to enhance quantum efficiency. Accurate analytic formulas are more difficult to obtain for these more complex structures, and the effects of waveguide loss and the LR facet reflection are examined using our model. Figure (7-3) shows the intensity noise reduction at high powers (relative to the shot noise level) and the device quantum efficiency for different losses α, with a HR coating reflectivity of 0.99 and a cleaved facet reflectivity of 0.3. The amount of squeezing is quickly destroyed by increasing losses. For a loss of $40cm^{-1}$, the noise is greater than the shot noise, and again cannot be determined from the quantum efficiency alone. Figure (7-4) shows the effect of the LR coating reflectivity for a loss of $20cm^{-1}$. The quantum efficiency and noise relative to the SNL are plotted, showing that a LR coating achieves the best squeezing, in rough agreement with the quantum efficiency.

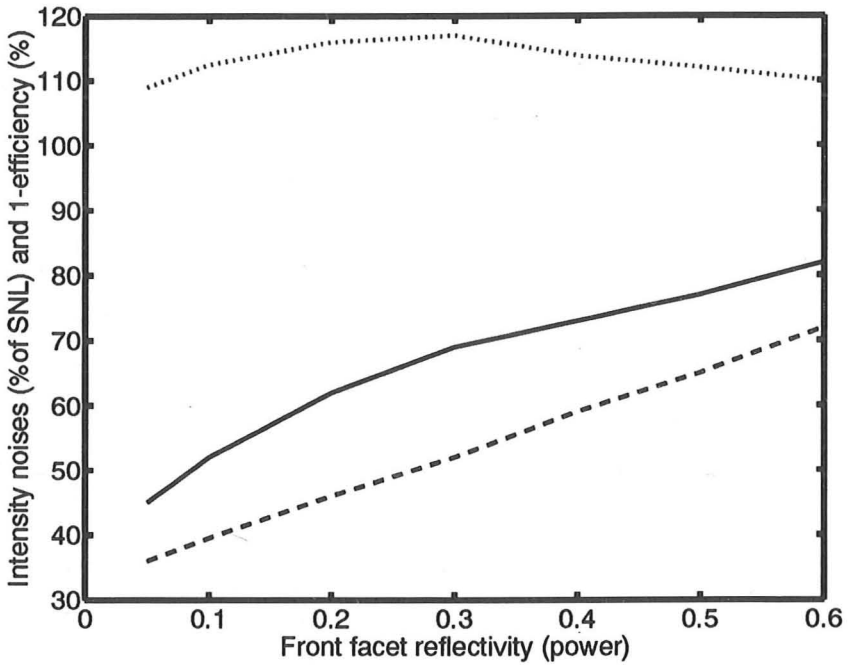

Figure 7-4: Calculated intensity noise (solid line: noiseless pump, dotted line: shot noise drive current) as percentage of the shot noise level, and (one minus the quantum efficiency = percentage losses) (dashed), for a HR-LR coated FP laser, versus the power reflectivity R of the LR coating. The waveguide loss was 20cm^{-1}, and the output power 8mW.

7.5.2 DFB lasers

Mode partition noise reduces the amplitude squeezing [104, 106]. Although the simplest multimode theory predicts that the low frequency noise for the total intensity is independent of numbers of modes excited, in practice this is not accurate. Single moded structures with no partition noise are therefore examined as potential squeezed light sources.

Single mode $\lambda/4$ shifted DFB's, AR coated on both facets, are first considered. In Fig. (7-5A), the low frequency intensity noise from one facet, at high power, for different values of the coupling κL is shown, while the quantum efficiency of the device is shown in Fig. (7-5B). The waveguide loss was $20cm^{-1}$. For low κL the noise is very large, and even for higher κL no squeezing is obtained. This is partly due to the waveguide loss, but also shows that DFB lasers have larger contributions from spontaneous emission sources. In this model, three independent noise sources contribute to the intensity noise: forward and reverse spontaneous emission sources (with strengths given by Eq. (7.5)), and the carrier noise sources, given by Eq. (7.27). The carrier noise contribution is negative at moderately high powers if the drive current fluctuations are suppressed, and contrives to reduce the intensity fluctuations. The strengths of the various spatially localized noise contributions along the laser cavity are plotted for κL=2 in Fig. (7-6). The contribution from the carrier noise sources in this device is strong only near the front facet (on the left, from which the power is observed), vanishing as the rear facet is approached. whereas the contributions from the spontaneous noise sources increase overall the further away they are from the front facet. It is argued that the squeezing is reduced by the evanescence created by the grating, which isolates conditions at one end of the laser from those at the other end.

In Figure 7-5(C,D) a uniform DFB structure with HR coated rear facet (R=0.99) and AR coated front facet (R=0) is considered. Fig. (7-5C) shows the intensity noise versus the coupling κL, while Fig. (7-5D) shows the device quantum efficiency. The waveguide loss was $20cm^{-1}$. The performance of this DFB device is on the whole inferior to that of the similar FP structure in Fig. (7-4), especially for $\kappa L > 1$.

7.5.3 DBR lasers

A single mode source which exploits the advantage of FP over DFB lasers for squeezing, is found by adding a passive DBR section to a FP laser. A device with 300μm DBR and FP sections, with a coupling $\kappa L = 1.5$ and zero loss for the DBR sec-

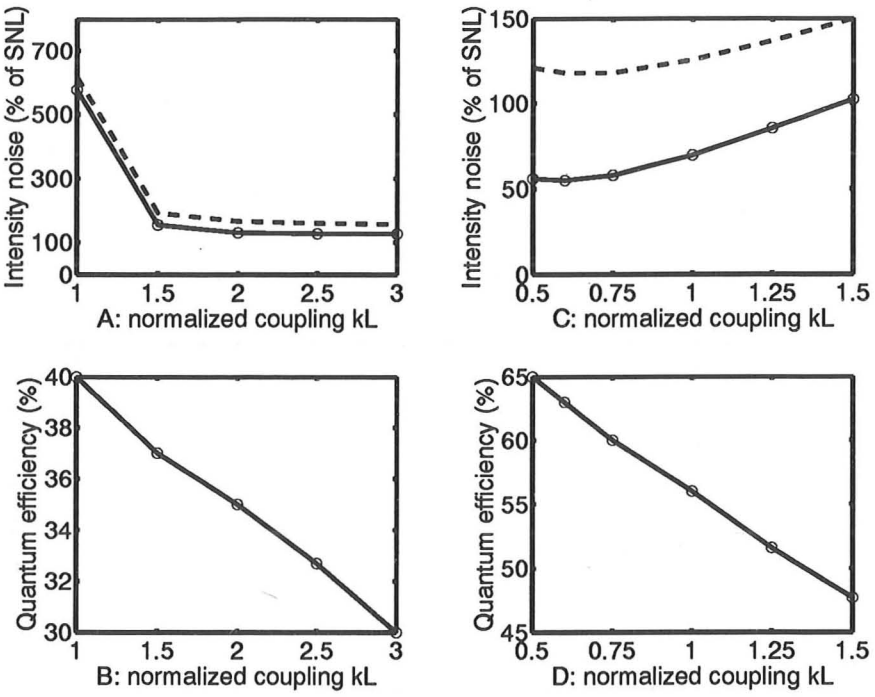

Figure 7-5: Calculated intensity noise (solid: noiseless pump, dashed: for shot-noise pump fluctuations given by the semiclassical treatment) and quantum efficiency for DFB lasers, versus grating coupling κL.

A,B: symmetric AR-coated $\lambda/4$ phase shifted DFB.

C,D: HR-AR coated uniform DFB.

For the HR-coated DFB, the phase of the reflection relative to the grating was kept at zero throughout, and single mode operation was obtained.

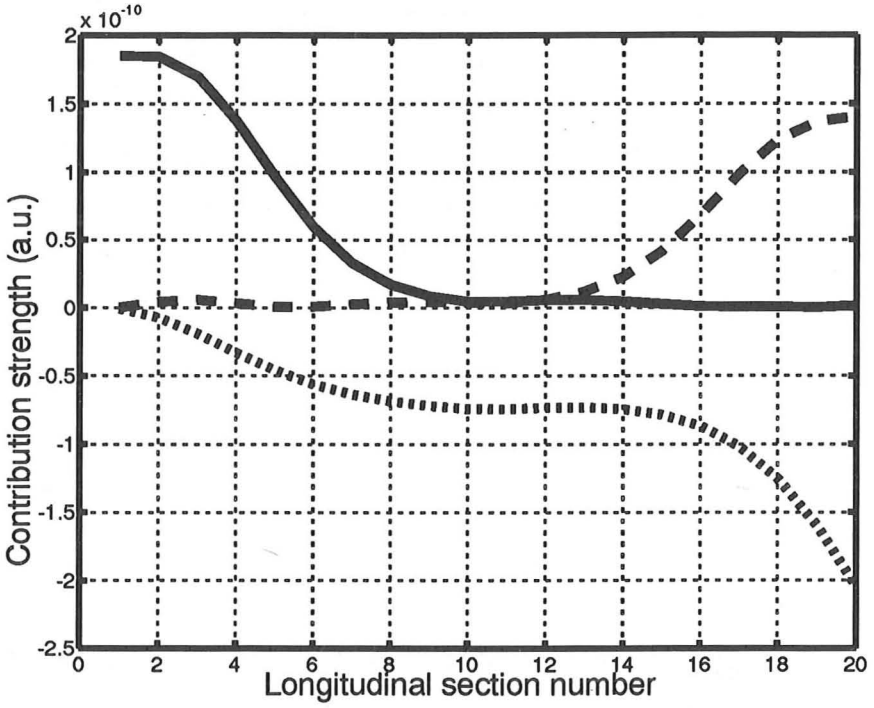

Figure 7-6: Contribution strengths of the different noise sources for a $\lambda/4$ DFB laser with $\kappa L = 2$. Solid: forward spontaneous emission noise. Dashed: reverse spontaneous emission noise. Dotted: carrier noise. The optical output is observed from the left (cleaved) facet. The optical output is observed from the left facet.

tion was simulated. The end of the DBR section is AR coated, and the FP end is cleaved (R=0.3). The level of squeezing with respect to the shot noise level at low frequencies was 2.5 dB, and the squeezing bandwidth at a power of 7mW was 5 GHz, indicating a performance similar to a FP laser.

7.5.4 Dynamic simulation of intensity noise

Intensity noise under large signal modulation is simulated because this is a regime which might be useful for low noise transmission of amplitude modulated optical signals. The FP device with a DBR section described in section 7.5.3 is biased at 20mA. The laser response to 3 successive drive current steps 0.5 ns long to 30, 25 and 20mA is monitored. Due to the stochastic noise sources, every simulation run is slightly different. The power responses to 50 different runs are averaged together, and the result is shown in Fig. (7-7). The deviations from the mean for each of the 50 runs are then calculated. Photodetection shot noise is added, and these deviations are individually Fourier transformed. The resulting power spectra are averaged to give the modulated intensity noise spectrum shown in Fig. (7.5.4).

Due to the varying power, the shot noise level is not well defined. However, 3dB of squeezing with respect to the shot noise level of the mean power is observed. We thus see that large signal modulation does not harm the level of squeezing significantly.

7.6 Conclusion: Intensity squeezing

A travelling wave, dynamic, large signal model for DFB, DBR and Fabry-Perot laser structures, which can simulate intensity noise, including amplitude squeezing has been demonstrated.

The work is an extension of intuitive semiclassical representations [21, 23, 110, 111], but now using the formalism of the positive P-distribution for the quantized travelling fields.

The lowest achievable intensity noise is seen to depend on the structure of the laser diode, and is generally higher than expected from the laser quantum efficiency. This is due to spontaneous noise sources which produce excess fluctuations in the output intensity, anticorrelated with fluctuations in the dissipated power, but keeping fluctuations in the total power (including losses) equal to those of the pump current.

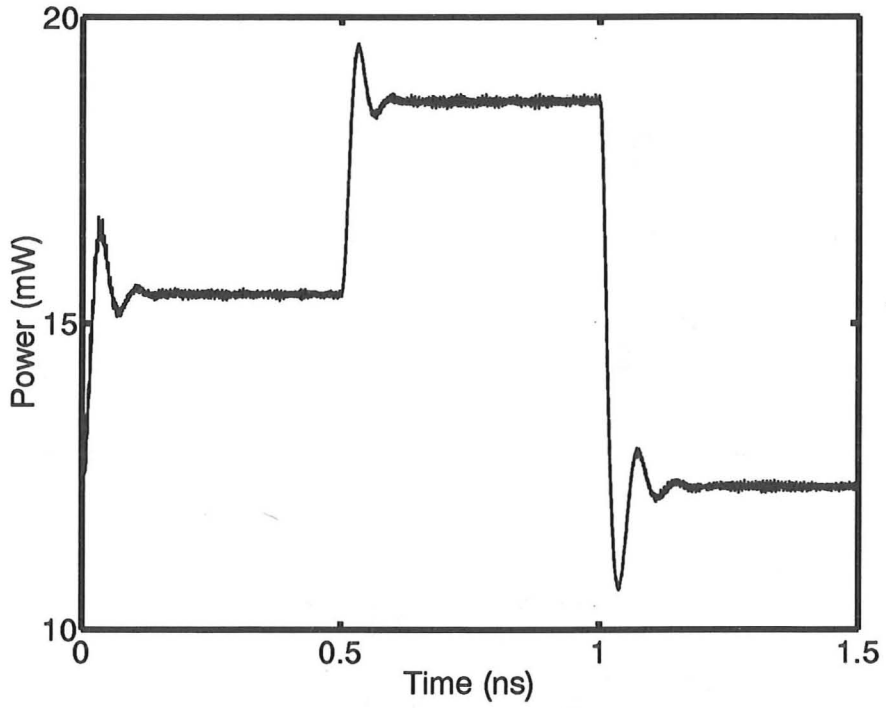

Figure 7-7: Average power response to large signal modulation of the FP-DBR device. Starting at 20mA, the response to three successive current steps of 0.5ns, to 30, 25 and 20mA is simulated.

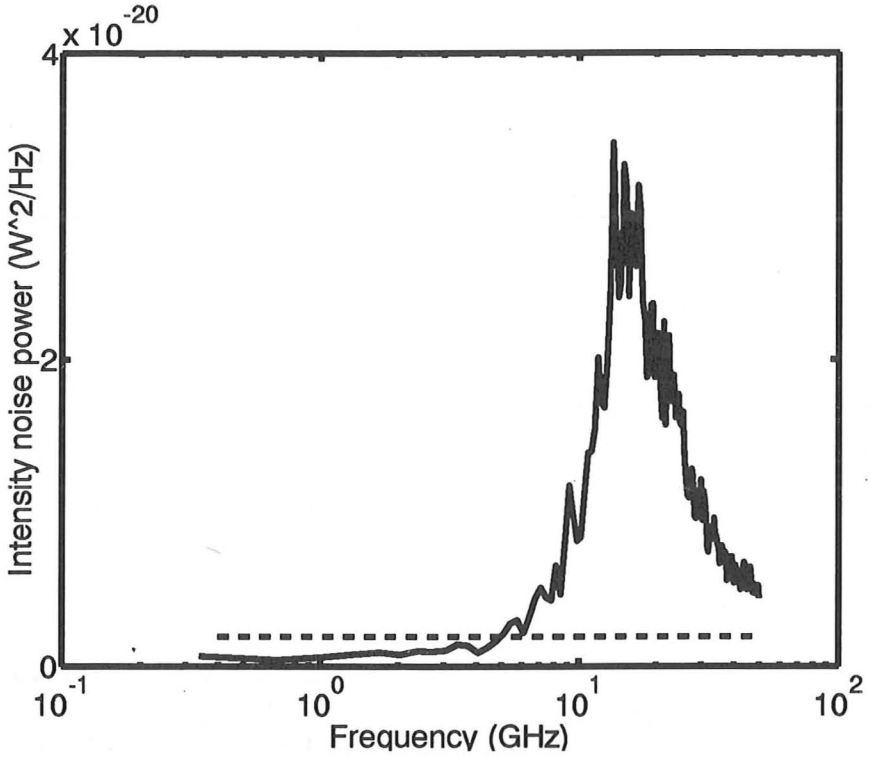

Figure 7-8: Intensity noise spectrum, including photodetection shot noise, for the modulated waveform of Fig. (7.7). Dashed line: shot noise level for a mean output power of 15 mW.

Three different structures of laser were investigated as potential sources of amplitude squeezed light. FP lasers show the best squeezing. However single frequency lasers are needed to remove the problems of mode partition noise. Although single moded, our simulations indicate that DFB structures are unlikely to be good sources of squeezed light, probably because of the evanescence of the optical fields within the grating. Laser diodes with a passive DBR section have the advantages of the FP diode but with negligible mode partition noise. It is however difficult to manufacture a DBR section with a reflectivity as high as that provided by a High Reflectivity coating on a Fabry-Perot laser. Intensity noise under dynamic large signal modulation was also investigated. The level of squeezing was not significantly affected by such modulation. With the available squeezing, the signal-to-noise ratio of amplitude-modulated transmissions should be able to be improved beyond the classical shot-noise limit, provided low loss transmission ($<$ 1dB) can be achieved.

Tromborg, Lassen and Olesen [112] have recently and independently derived an expression identical to (7.80) in Appendix B, which is the general case of the formula (7.31). They used a quantum formalism very different to the one presented here, where noise operators entering the laser through the facets are needed, as well as other noise operators which model absorption losses within the laser. This agreement between the work of Tromborg *et al* and the theory presented here helps to validate the present formalism which uses complex fluctuations in the variables representing optical power and carrier density operators.

7.7 Appendix A: Small signal analysis using the positive P-representation

The field and carrier rate equations (7.1-7.3) can be used to obtain a rate equation for the optical power $I = \alpha\beta$:

$$\dot{I} = g(N - N_t)I - \gamma I + F_I(t), \tag{7.32}$$

$$\dot{N} = D - N/\tau_N - g(N - N_t)I(t) - F_I(t) + F_N(t), \tag{7.33}$$

where the noise $F_I(t)$ is Gaussian, real, and zero mean:

$$< F_I(t)F_I(t') >= 2g(N - N_t)n_{sp} < I > \delta(t - t'). \tag{7.34}$$

The noise $F_N(t)$ is also Gaussian and zero mean, but is either real or imaginary, depending on the power and pump noise.

The small signal equations of motion obtained from (7.32-7.33) by putting $I(t) = I_0 + \delta i(t)$ etc... are:

$$\frac{d}{dt}\delta i(t) = \frac{\delta n(t)}{\tau_{st} + F_I(t),} \tag{7.35}$$

$$\frac{d}{dt}\delta n(t) = -(\frac{1}{\tau_N} + \frac{1}{\tau_{st}})\delta n(t) - \gamma \delta i(t) + F_N(t) - F_I(t). \tag{7.36}$$

Here τ_{st} is the net stimulated emission lifetime, $1/\tau_{st} = gI_0$, and γ is the cavity loss rate, related to the photon lifetime through $\gamma = 1/\tau_{ph}$. In the high power regime, the stimulated lifetime is much shorter than the carrier lifetime τ_N, and one can put $1/\tau \approx 1/\tau_{st} \approx 1/\tau_{st} + 1/\tau_N$. Taking the Fourier transforms, such as:

$$\delta I(\omega) = \int_{-\infty}^{\infty} dt\ \delta i(t) \exp(-i\omega t), \tag{7.37}$$

we solve the small signal equations in the frequency domain to get:

$$\delta I(\omega) = \frac{-i\omega\tau F_I(\omega)}{\gamma - \omega^2\tau + i\omega} + \frac{F_N(\omega)}{\gamma + i\omega - \omega^2\tau}. \tag{7.38}$$

The correlations for the noise sources, in the frequency domain, are from (7.34,7.6):

$$\begin{aligned} < F_I(\omega)F_I(\omega') > &= D_{II}\delta(\omega + \omega') \\ &= 2g(N - N_t)n_{sp}I_0\delta(\omega + \omega'), \end{aligned} \tag{7.39}$$

$$\begin{aligned} < F_N(\omega)F_N(\omega') > &= D_{NN}\delta(\omega + \omega') \\ &= \left(D' + N/\tau_N - g(N - N_t)I_0\right) \\ &\quad \times\delta(\omega + \omega'). \end{aligned} \tag{7.40}$$

This means that the frequency components of the intensity noise $\delta I(\omega)$ are correlated as:

$$< \delta I(\omega)\delta I(\omega') >= S_I(\omega)\delta(\omega + \omega'), \tag{7.41}$$

where

$$S_I(\omega) = \frac{\omega^2\tau^2}{(\gamma - \omega^2\tau)^2 + \omega^2}D_{II} + \frac{1}{(\gamma - \omega^2\tau)^2 + \omega^2}D_{NN}. \tag{7.42}$$

For Poisson pump fluctuations, at high power, $D_{NN} \approx 0$, which gives an intensity

noise spectrum:

$$S_I(\omega) = \frac{2\omega^2\tau^2\gamma I_0}{(\gamma - \omega^2\tau)^2 + \omega^2}. \tag{7.43}$$

As the power is increased, the stimulated lifetime τ decreases towards zero, so that the intensity fluctuation noise vanishes, and the output is coherent.

For suppressed pump fluctuations, $D_{NN} \rightarrow -\gamma I_0 \approx -D_{II}$, and the intensity fluctuation noise spectrum becomes:

$$S_I(\omega) = \frac{(2\omega^2\tau^2 - 1)\gamma I_0}{(\gamma - \omega^2\tau)^2 + \omega^2}. \tag{7.44}$$

The optical power output from the laser is in the ideal case just $O(t) = \gamma I(t)$, so that the output field fluctuations will have a power spectral density (assuming $\gamma \ll 1/\tau$, which is true at high enough powers):

$$S_O(\omega) \approx -\frac{< O(t) >}{\gamma^2\omega^2 + 1}, \tag{7.45}$$

i.e. the low frequency intensity noise is reduced to minus the shot noise level, and the squeezing bandwidth is equal to $\gamma = 1/\tau_{ph}$, the inverse of the photon lifetime, agreeing with Yamamoto's theory [33].

7.8 Appendix B: Analytic formulae for the intensity noise in Fabry-Perot lasers

Neglecting spatial hole burning, gain compression and waveguide losses, the minimum achievable RIN in Fabry-Perot lasers is calculated here.

First, a quantum amplifier model which includes carrier noise sources is presented. The corresponding small signal model is then derived by linearizing. This small signal model is incorporated into a Fabry-Perot cavity, and the intensity fluctuations are calculated.

7.8.1 Quantum amplifier model

The travelling wave forward optical flux inside the amplifying medium $I(z,t)$ experiences gain as it propagates from $z = 0$ to $z = L$, described by:

$$\Big(\frac{\partial}{\partial z} - \frac{1}{v_g}\frac{\partial}{\partial t}\Big) I(z,t) = b\Gamma\big(N(t) - N_t\big)I(z,t) + F_I(z,t). \tag{7.46}$$

This equation is obtained from the travelling wave equations for the forward fields Eqs. (7.18–7.21) with no coupling between the forward and reverse waves. b is the differential gain, Γ is the confinement factor, $N(t)$ is the carrier density at time t, assumed uniform between $z = 0$ and $z = L$, and N_t it the transparency carrier density. The noise source $F_I(z,t)$ satisfies:

$$< F_I(z,t)F_I(z',t') >= \hbar\omega n_{sp} 2b\Gamma\big(N(t) - N_t\big)\delta(z - z')\delta(t - t'), \tag{7.47}$$

which assumes that the noise sources at different spatial locations are uncorrelated, due to the short scattering length for the electrons in the semiconductor material [113]. The factor $\delta(t - t')$ means that the finite bandwidth of the spontaneous emission is neglected.

Integrating the travelling wave equation along the path of the field, $dz = v_g dt$, the output optical power $I(L, t + L/v_g) = I_o(t + L/v_g)$ is given in terms of the input power to the amplifier $I(0,t) = I_i(t)$ by:

$$\begin{aligned} I_o(t + L/v_g) &= \exp[(b\Gamma(N(t) - N_t)L]I_i(t) \\ &+ \int_0^L \exp[b\Gamma(N(t) - N_t)(L - z)]F_I(z, t + z/v_g)dz. \end{aligned} \tag{7.48}$$

This expression assumes that the carrier density $N(t)$ is uniform over the length L (no spatial hole burning), and that it does not change significantly over the very short integration time $\Delta t = L/v_g$. Call the gain $G = \exp[(b\Gamma(N(t) - N_t)L]$.

The second term on the right of the expression is a noise source $S_I(t)$, whose correlation is, using Eq. (7.47):

$$\begin{aligned} < S_I(t)S_I(t') > &= \int_0^L dz \int_0^L dz' \exp[b\Gamma\big((N(t) - N_t)(L - z) + (N(t') - N_t)(L - z')\big)] \\ &\quad < F_I(z, t + z/v_g)F_I(z', t' + z'/v_g) > \\ &= \hbar\omega n_{sp} 2b\Gamma(N(t) - N_t)\delta(t - t') \int_0^L \exp[b\Gamma\big(N(t) - N_t\big)(2L - z)]I_i(t) \\ &= \hbar\omega n_{sp} 2G(G - 1)I_t(t)\delta(t - t'). \end{aligned} \tag{7.49}$$

The carrier density varies according to:

$$\frac{d}{dt}N(z,t) = D - \frac{b\Gamma\big(N(t) - N_t\big)I(z,t) + F_I(z,t)}{\hbar\omega A} - N(z,t)/\tau_N + F_N(z,t), \tag{7.50}$$

where $D = I/q_e V$ is the drive, τ_N is the carrier lifetime, and A is the cross section

of the active volume $V = AL$. Assuming negligible spatial hole burning, the mean carrier density $N(t) = (1/L)\int_0^L N(z,t)dz$ changes according to:

$$\frac{d}{dt}N(t) = -\frac{I_o(t+L/v_g) - I_i(t)}{\hbar\omega V} + (1/L)\int_0^L F_N(z,t)dz. \tag{7.51}$$

The noise source $F_N(z,t)$ has the correlation derived earlier in this chapter (Eq. (7.6)):

$$< F_N(z,t)F_N(z',t') >= D'/A^2 + N(z,t)/A^2\tau_N - b\Gamma(N(z,t) - N_t)I(z,t)/(\hbar\omega A)^2, \tag{7.52}$$

where D' gives the pump noise ($D' = 0$ for a noiseless pump, D'=D for shot noise current fluctuations). This correlation can be negative when $D' < D$. The integrated carrier noise source $S_N(t)$ in Eq. (7.51) then has the correlation:

$$\begin{aligned} < S_N(t)S_N(t') > &= (1/L^2)\int_0^L dz \int_0^L dz' < F_N(z,t)F_N(z',t') > \\ &= \frac{\{D' + N(t)/\tau_N - (G-1)I_i(t)/(\hbar\omega)^2\}}{V^2}\delta(t-t'). \end{aligned} \tag{7.53}$$

To summarize, the amplifier is modelled by:

$$I_o(t+L/v_g) = G(t)I_i(t) + S_I(t), \tag{7.54}$$

$$\frac{d}{dt}N(t) = \frac{I_o(t+L/v_g) - I_i(t)}{\hbar\omega V} + \frac{I}{q_e V} - N(t)/\tau_N + S_N(t), \tag{7.55}$$

with $G(t) = \exp[b\Gamma(N(t) - N_t)L]$.

7.8.2 Small signal equivalent circuit

Equations (7.54,7.55) are linearized by putting:

$$I_i(t) = I_i + \delta I_i(t), \tag{7.56}$$

$$I_o(t) = I_o + \delta I_o(t), \tag{7.57}$$

$$N(t) = N + \delta N(t), \tag{7.58}$$

$$G(t) = G + G_N\delta N(t), \tag{7.59}$$

with, $\delta I_i(t) \ll I_i$etc..., and $G_N = dG/dN$. This gives:

$$\delta I_o(t+L/v_g) = G\delta I_i(t) + G_N I_i \delta N(t) + S_I(t), \tag{7.60}$$

$$\frac{d}{dt}\delta N(t) = -\frac{\delta I_o(t+v_g/L) - \delta I_i(t)}{\hbar\omega V} - \delta N(t)/\tau_N + S_N(t), \quad (7.61)$$

Converting $N(t)$, $I_i(t)$ and $I_o(t)$ to units of carrier number and photon flux respectively, instead of carrier density and power flux ($N(t) \rightarrow VN(t)$ and $I_i(t) \rightarrow I_i(t)/\hbar\omega$) makes the expressions simpler. In the frequency domain, these become

$$\delta I_o(s) = G\delta I_i(s)\exp(sL/v_g) + G_N I_i \delta N(s) + S_I'(s), \quad (7.62)$$

$$s\delta N(s) = I_i(s) - I_o(s) - \delta N(s)/\tau_N + S_N'(s). \quad (7.63)$$

The noise correlations are, for noiseless pump, high above threshold:

$$< S_I'(s)S_I'(s') > = 2n_{sp}G(G-1)I_i\delta(s-s'), \quad (7.64)$$

$$< S_N'(s)S_N'(s') > = \{D + N/\tau_N - (G-1)I_i(s)\}\delta(s-s')$$

$$\approx -(G-1)I_i(s)\delta(s-s'). \quad (7.65)$$

These equations can be represented by the small signal equivalent circuit shown in Fig. (7-9).

7.8.3 Equivalent circuit for a Fabry-Perot laser

The intensity noise in a Fabry-Perot laser is modelled using the circuit shown in Figure (7-10). The facet reflectivities $R_r = r_r^2$ and $R_l = r_l^2$ provide the optical feedback for the fields:

$$\delta I_1(s) = R_l \delta I_4(s), \quad (7.66)$$

$$\delta I_3(s) = R_r \delta I_2(s). \quad (7.67)$$

Considering the round trip gain, gives $G^2 R_r R_l = 1$. In the low frequency limit where $\exp(sT) = \exp(sL/v_g) \approx 1$, the following equations are obtained:

$$\delta I_2 = G\delta I_1 + S_{I1} + \frac{G_N I_1}{s}(\delta I_1 - \delta I_2 + \delta I_3 - \delta I_4 + S_N), \quad (7.68)$$

$$\delta I_4 = G\delta I_3 + S_{I2} + \frac{G_N I_3}{s}(\delta I_1 - \delta I_2 + \delta I_3 - \delta I_4 + S_N). \quad (7.69)$$

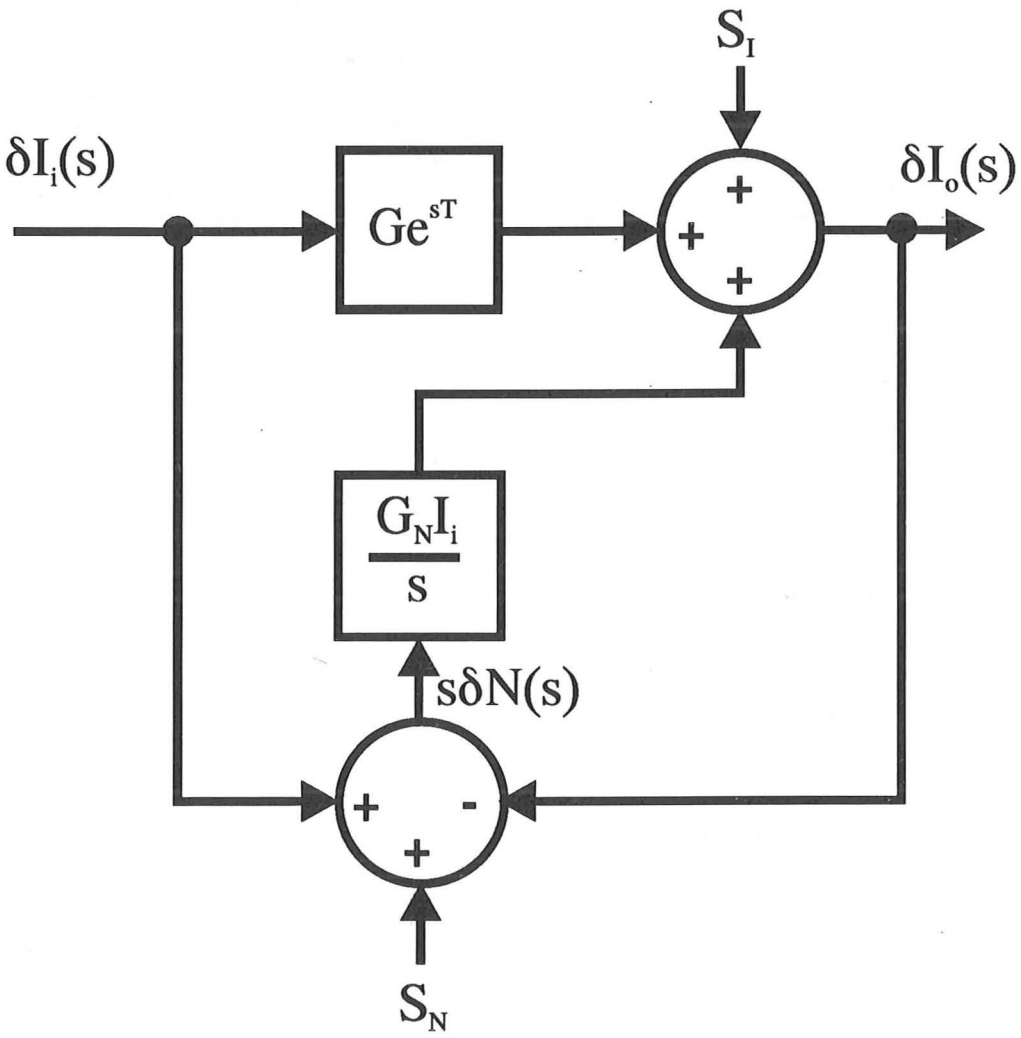

Figure 7-9: Small signal equivalent circuit for an optical amplifier.

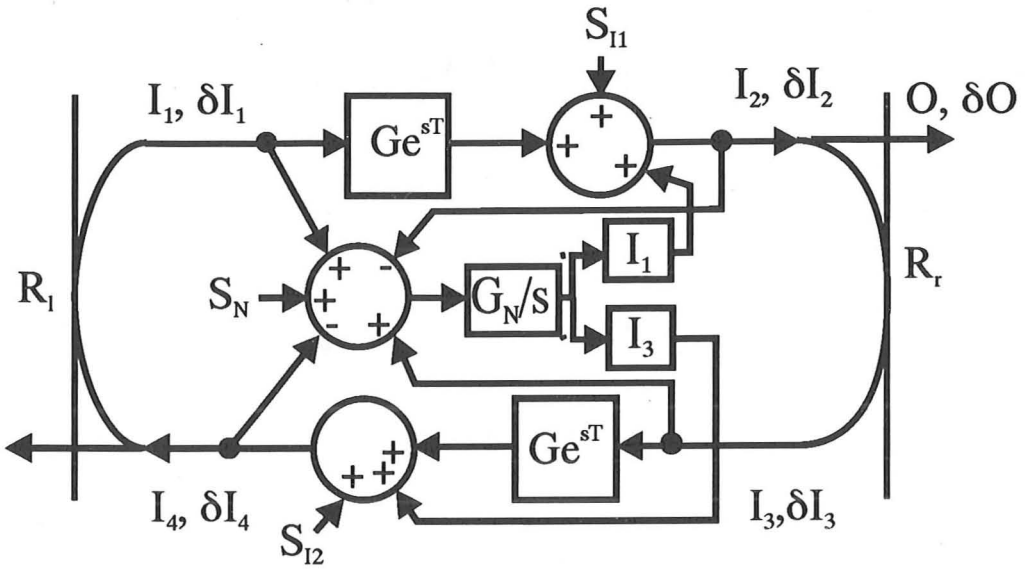

Figure 7-10: Small signal equivalent circuit for a Fabry-Perot laser.

Substituting using Eqs. (7.66,7.67) gives:

$$\begin{bmatrix} 1+G_N I_1(1-R_r)/s & -(GR_l+G_N(R_l-1)/s) \\ -(GR_r+G_N(R_r-1)/s) & 1+G_N I_3(1-R_l)/s \end{bmatrix} \begin{bmatrix} \delta I_2 \\ \delta I_4 \end{bmatrix} = \begin{bmatrix} S_{I1}+G_N I_1 S_N/s \\ S_{I2}+G_N I_3 S_N/s \end{bmatrix}. \quad (7.70)$$

Solving this and taking the low frequency limit $s \to 0$ gives for δI_2:

$$\delta I_2 = \frac{(1-R_l)I_3 S_{I1} - (1-R_r)I_1 S_{I2} + (GR_l I_3 + I_1)S_N}{I_1(1-R_r) + I_3(1-R_l) + G[(1-R_r)R_l I_3 + (1-R_l)R_r I_1]}. \quad (7.71)$$

The noise correlations derived earlier are:

$$< S_{I1}(s)S_{I1}(s') > = 2G(G-1)n_{sp}I_1\delta(s-s'), \quad (7.72)$$

$$< S_{I2}(s)S_{I2}(s') > = 2G(G-1)n_{sp}I_3\delta(s-s'), \quad (7.73)$$

$$< S_N(s)S_N(s') > = -\epsilon(G-1)(I_1+I_3), \quad (7.74)$$

where ϵ describes the pump noise: $\epsilon = 1$ for a noiseless pump, and $\epsilon = 0$ for shot noise drive current fluctuations. The noise sources are not correlated with one another.

The output power from the laser being $O = (1-R_r)I_2$ with a fluctuation $\delta O(s) =$

$(1 - R_r)\delta I_2(s)$, I_1, I_2, I_3 and I_4 can be expressed in terms of O:

$$I_1 = \frac{\sqrt{R_r R_l}}{1 - R_r} O = \frac{r_r r_l}{1 - r_r^2} O, \tag{7.75}$$

$$I_2 = \frac{1}{1 - R_r} O, \tag{7.76}$$

$$I_3 = \frac{R_r}{1 - R_r} O, \tag{7.77}$$

$$I_4 = \frac{\sqrt{R_r / R_l}}{1 - R_r} O = \frac{r_r / r_l}{1 - r_r^2} O. \tag{7.78}$$

The expression (7.71) can then be squared, and after simplifications we get:

$$< \delta O(s) \delta O(s') >= \left\{ \frac{1 - r_r^2}{(r_r + r_l)(1 - r_r r_l)} \left(\frac{n_{sp}}{2 r_l} (1 - r_l^2)^2 - \epsilon r_l \right) \right\} O \delta(s - s'). \tag{7.79}$$

Including the detection noise with a power O, and converting to power units from photon fluxes, the low frequency relative intensity noise for a lossless Fabry-Perot laser becomes:

$$RIN = \frac{\hbar \omega}{P} \left\{ 1 + \frac{1 - r_r^2}{(r_r + r_l)(1 - r_r r_l)} \left(\frac{n_{sp}}{2 r_l} (1 - r_l^2)^2 - \epsilon r_l \right) \right\}. \tag{7.80}$$

This formula is identical to the one independently derived by Tromborg, Lassen and Olesen [112] using a different quantum formalism.

Chapter 8

Maximum entropy spectrum for laser diodes

The previous chapters were concerned with computer modelling of laser diodes. This chapter, in contrast, reports the experimental demonstration of a new type of spectrometer. It uses the maximum entropy method of spectral estimation, which has already been used in Chapter 4 to estimate the spectra of simulated lasers.

The new type of spectrometer presented here uses computer interpretation of interference patterns. Its experimentally demonstrated resolution is currently sufficient to determine the optical spectrum of a two moded distributed feedback laser with 2 nm mode spacing. The spectrometer operates by transmitting the laser light through two pinholes to generate an interference pattern in the far field. The interference pattern is captured using an infra-red camera and is transferred to a computer. The spectrum of the light is extracted from this interference pattern using the maximum entropy method of spectral estimation.

8.1 Introduction

Optical spectrum analysers are widely used to monitor the spectra of optical signals, for example to characterize semiconductor laser diode sources for optical communications. Monochromators using diffraction gratings are generally used to determine optical spectra over a wide wavelength span, down to a resolution of typically 0.1 nm at infra-red communication frequencies. Precise optical alignment and accurate control of the diffraction gratings are required for these machines. This makes monochromators fragile, relatively expensive and bulky.

Monochromators use diffraction gratings as a wavelength selective element. The

numerous, evenly spaced corrugations on the grating act as secondary point sources, each one re-emitting the incident light from different spatial positions. The superposition of the radiation from these point sources creates a diffraction pattern, which is highly localized for a monochromatic beam. Unlike a diffraction grating, the present experiment uses just two point sources to produce a far field diffraction pattern.

The far field diffraction pattern from two point sources, for monochromatic light, is a set of nearly evenly spaced fringes, like the diffraction pattern from Young's slits. The diffraction pattern is due to the difference in the optical path length from each point source to a given point in the distance, so that the diffraction pattern is essentially the autocorrelation function for the light signal. If the diffraction pattern can be recorded, the autocorrelation function $C(\tau) =< E(t)E(t+\tau) >$ of the optical field for varying time lags τ is measured. The optical power spectrum $P(\omega)$ is the Fourier transform of the autocorrelation function, and so the optical power spectrum can be determined:

$$P(\omega) = \int_{-\infty}^{\infty} C(\tau) \exp(-i\omega\tau)\, d\tau. \tag{8.1}$$

The following sections describe how the diffraction pattern is recorded, and how the spectral information then is extracted. The principle behind the instrument presented here is similar to that behind the then new microwave network analyser demonstrated experimentally at Cambridge University Engineering Department by G. Luff [114, 115]. It consists of using a digital computer to process numerically the raw measured data. This allows one to correct for the inaccuracies of the measuring device by software, once a set of initial callibrations have been performed, and so relaxes the constraints on the precision of the manufacturing.

8.2 Experimental arrangement

The experimental arrangement used to capture the diffraction pattern is shown in Fig. (8-1). An optical fibre input is used for the spectrometer. A 50:50 fibre coupler splits the signal, and the cleaved ends of the coupler outputs are used as convenient point sources. The small diameter of single mode communications fibre, around 5 μm, ensures that the single pin-hole diffraction pattern does not interfere significantly with the required two-pin-hole diffraction pattern. The use of cleaved optical fibre ends, rather than pinholes or Young's slits, also permits greater luminosities to be achieved. The cleaved ends are held typically 20 mm apart, and an infra-red camera, without its objective, is placed 70 cm away to record the far field pattern,

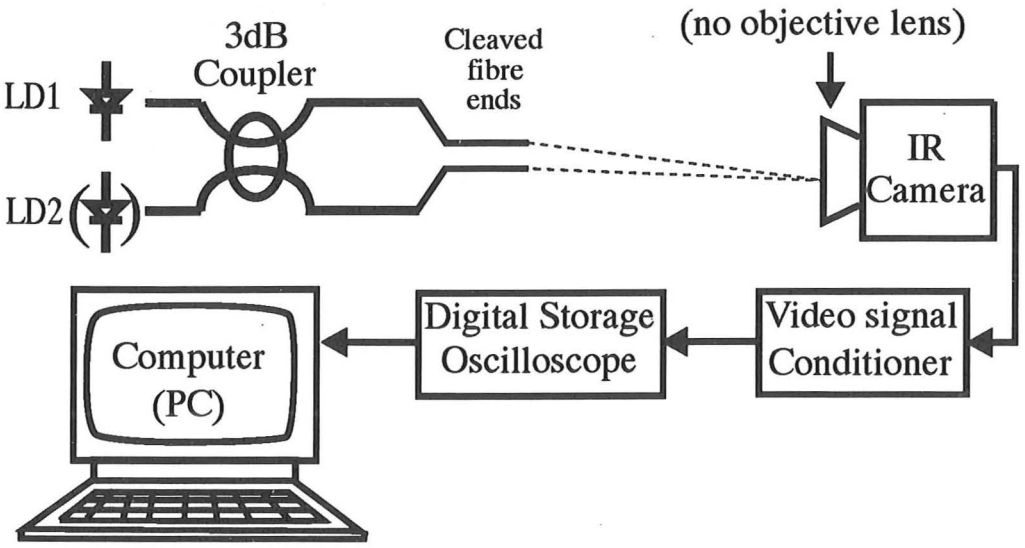

Figure 8-1: Experimental arrangement used to capture the field autocorrelation onto computer.

whose fringes are set up to be orthogonal to the line scan. A video signal conditioner is used to extract a single horizontal line of the camera signal, which is then digitized and sent to the computer by a Digital Storage Adapter. The camera resolution was sufficient to enable up to 300 diffraction fringes to be captured across the screen before the contrast ratio deteriorated excessively, and the camera resolution was of the order of 2500 pixels horizontally.

8.3 Processing the data

The signal autocorrelation function is obtained from the diffraction pattern by numerical filtering using the fast Fourier transform, to remove any low- frequency components, due to background levels, single pin-hole diffraction patterns, and the D.C. contribution of the mean optical power. Figure (8-2) shows an example of the measured autocorrelation function of the optical field: in this case the optical signal was generated by superposing the output of two single mode laser diodes emitting at 1.3μm and 1.55μm respectively. A beat signal resulting from the superposition is clearly seen. Performing a Fourier transform on this sampled autocorrelation function indeed reveals the two spectral components, as shown in Figure (8-3).

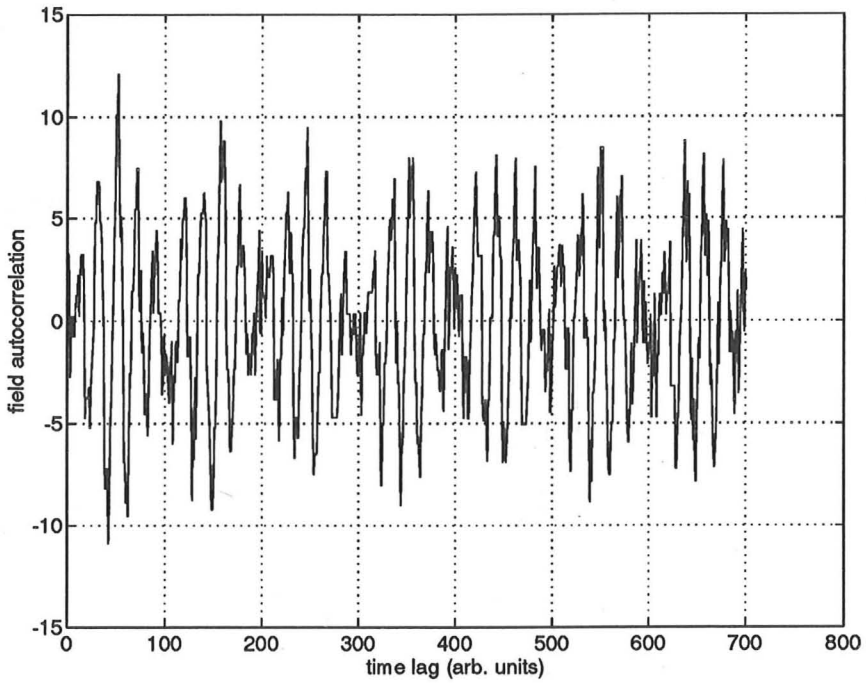

Figure 8-2: Measured field autocorrelation function for the superposition of two single mode optical fields at 1.3μm and 1.55μm respectively.

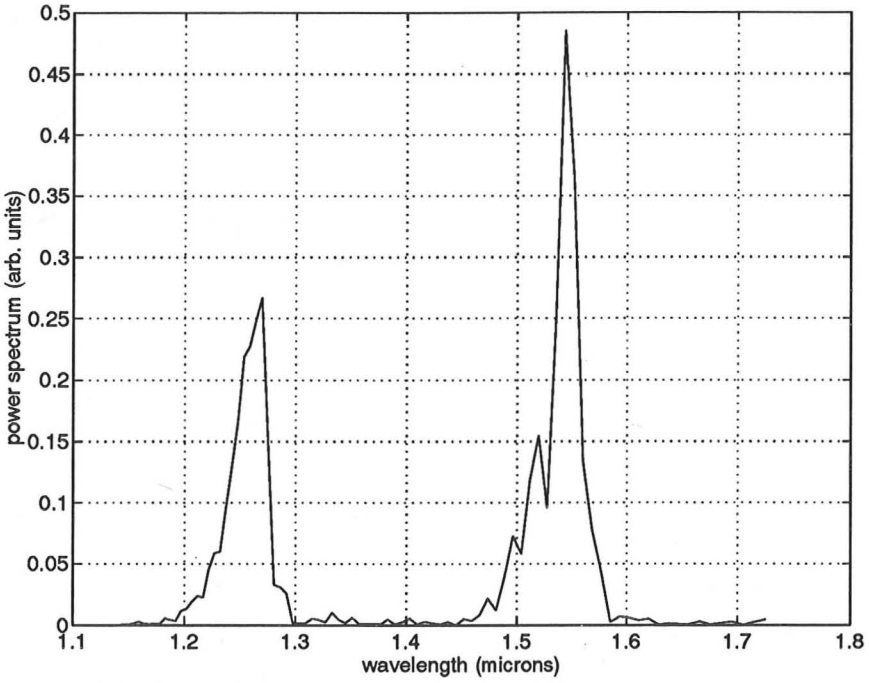

Figure 8-3: Discrete Fourier transform of the field autocorrelation shown in Fig.(8.2), showing components at 1.3 and 1.55 μm.

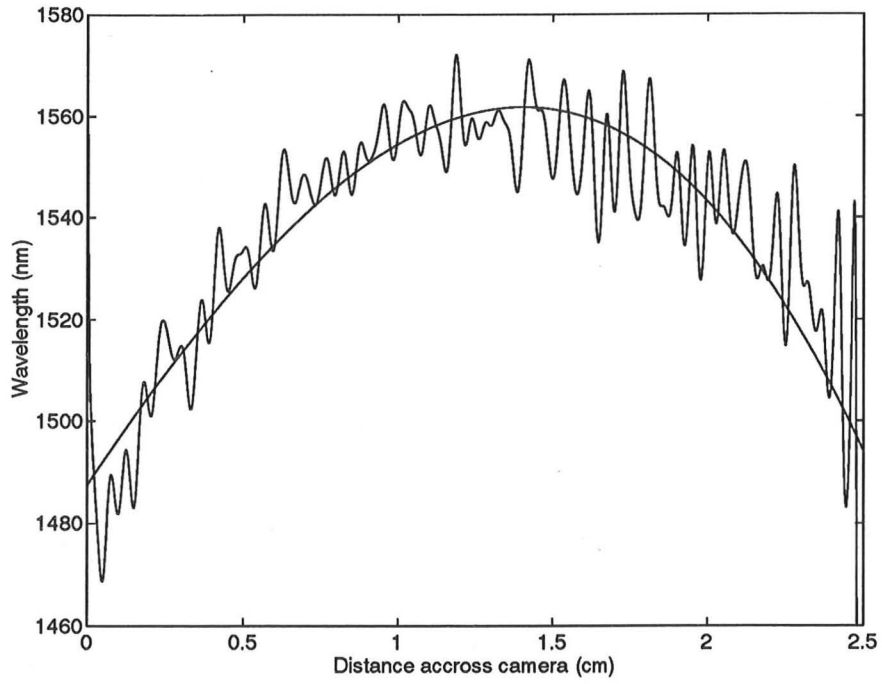

Figure 8-4: Change in the wavelength of the recorded diffraction pattern across the camera, showing chirp, and best fit to a third order polynomial.

8.3.1 Correction for chirping.

Distortions due to the geometry of the set-up, and to slight variations of the camera sweep rate, meant that for a monochromatic input, the diffraction pattern showed a wavelength chirp of about 4% across one recorded horizontal line, as shown in Fig. (8-4). This chirping caused a significant loss of resolution. Figure (8-5) shows the spectrum, estimated using a Discrete Fourier Transform, for a signal generated by two single mode lasers with wavelengths spaced 12 nm apart. The chirping broadens the modes, and confuses the spectrum. This variation in the spacing of the diffraction fringes across the camera, obtained with monochromatic light, was numerically fitted to a third order polynomial to obtain a set of correcting phase factors (see Fig. 8-4). The measured autocorrelation data were multiplied by these correcting phase factors to remove the chirp which otherwise would have significantly limited our instrument's resolution. The Discrete Fourier transform of the corrected autocorrelation function corresponding to Fig. (8-5) is shown in Fig. (8-6). The effect of the chirp is greatly reduced.

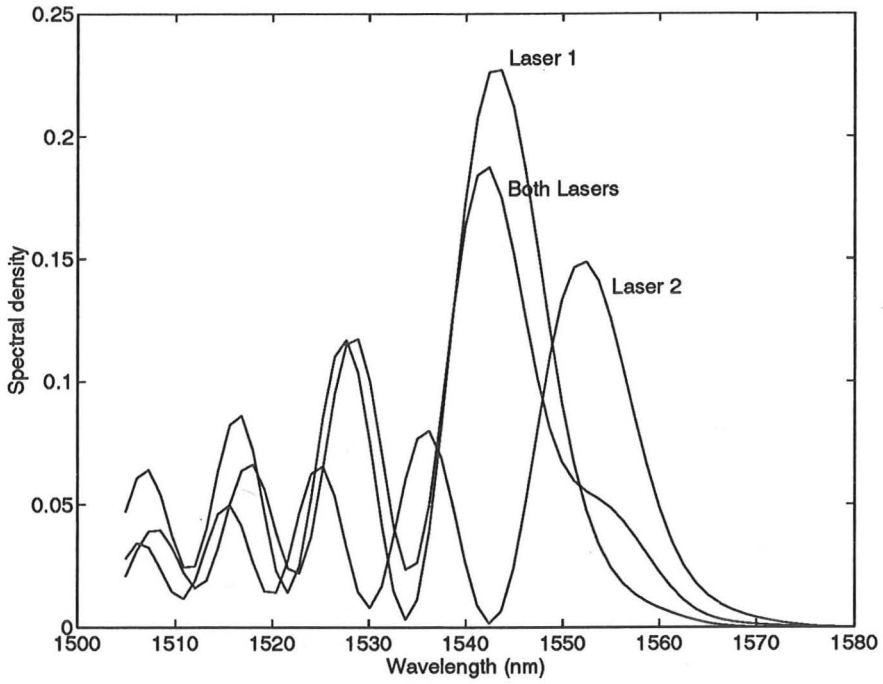

Figure 8-5: Measured spectrum for two lasers with wavelengths 12 nm apart, obscured by the chirping of the measuring instrument.

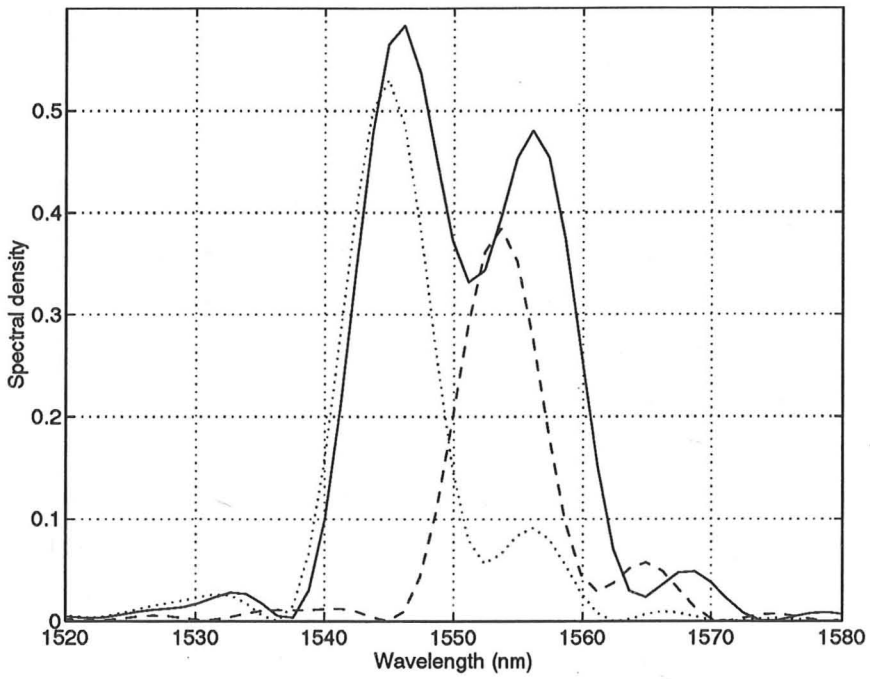

Figure 8-6: Measured spectrum for two lasers with wavelengths 12 nm apart, corrected for the chirping of the measuring instrument. Dots: Laser 1, Dashes: Laser 2, and Continuous line: Both lasers.

8.4 Reducing the windowing effect.

The properties of the autocorrelation function $C(\tau)$ make the power spectrum $P(\omega)$, given by Eq.(8.1), real and positive. However, due to measurement noise, and the difficulty of establishing the origin $\tau = 0$ for the autocorrelation function with sufficient precision, it is easier to evaluate $P(\omega)$ as the square root of the power spectral density $S(\omega)$ of $C(\tau)$:

$$P(\omega) = \sqrt{S(\omega)} = \left[\left| \int_{-\infty}^{\infty} C(\tau) \exp(-i\omega\tau) d\tau \right|^2 \right]^{1/2}. \tag{8.2}$$

This expression ensures that a real and positive power spectrum is obtained, and provides us with the freedom to choose the best method to evaluate the power spectral density $S(\omega)$.

The limited range for τ over which the autocorrelation $C(\tau)$ can be measured at one time by our apparatus, would mean that if $S(\omega)$ were evaluated using a fast Fourier transform, the resolution of our spectrometer would be severely limited. The fast Fourier transform-based methods of power spectral estimation implicitly assume that the autocorrelation of a signal is zero for time lags greater than the length of the available data record. The resulting windowing effect prevents closely spaced frequency components to be resolved. The slow fall-off around a strong frequency component may also mask weaker neighbouring signals. The maximum entropy method pioneered by Burg [81] overcomes these windowing effects, by effectively estimating the most probable values of the autocorrelation $C(\tau)$ for time lags greater than the length of the data record.

In the maximum entropy method, a number of poles P is chosen, and the spectrum is expressed as a rational function of frequency with P poles. Each pole can be used to fit a peak in the spectrum of the signal, possibly corresponding to a laser mode. The whitest spectrum (most random in the maximum entropy sense) which is consistent with the data, is chosen. A number of different algorithms have been developed to do this: the Yule-Walker and Burg methods are the oldest [81], and the forward-backwards least-squares method [82] has one of the highest resolutions. However, the performances of the different algorithms vary according to parameters like the Signal-to-Noise ratio, for example. The improvement in performance over Discrete Fourier Transform methods is apparent in Figure (8-7): here a test signal was generated by superposing 3 sinusoids with a frequency separation of 10^{-4} Hz, sampled at 1024 points 1s apart. The maximum entropy method (solid line) clearly

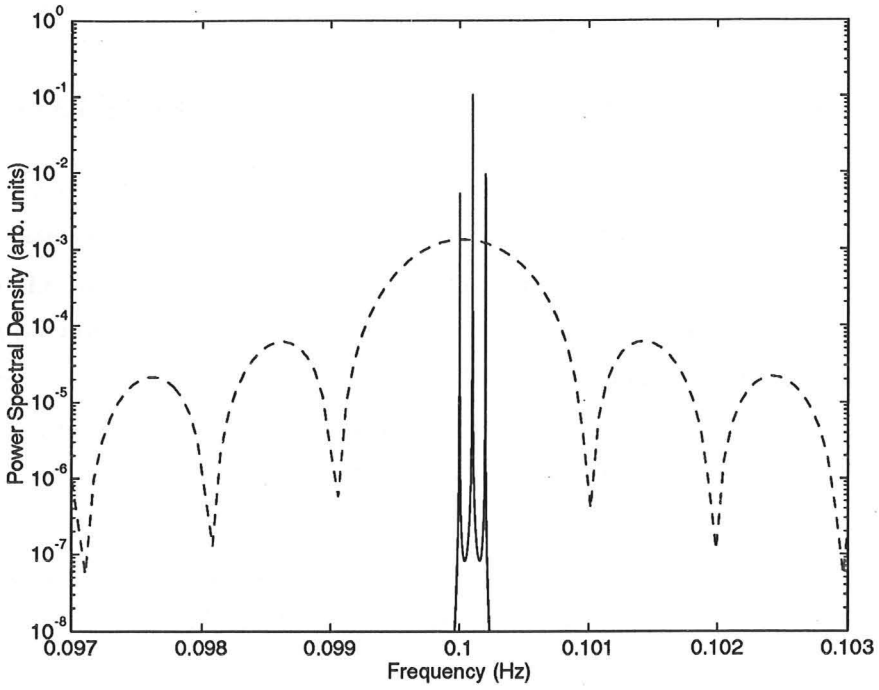

Figure 8-7: Spectra of three sinusoids spaced 10^{-3} Hz apart, estimated from 1024 samples with 1s sampling time. Solid line: Maximum entropy method (forward-backwards, 10 poles), Dashed line: Fast Fourier Transform (with no window to give highest resolution).

resolves the three components and gives the correct spacings, even if the height of the three peaks are not precisely equal. The Fourier transform method (dashed line), in contrast, has a resolution 10 to 20 times worse, and cannot resolve the three components. This is however an ideal case, with no noise present. The presence of noise can degrade the resolution of the maximum entropy method.

The Yule-Walker method was used here, and it is briefly described in Section 4.2, and in more detail in detail in references [82, 116]. It works by estimating, from the sampled data, a set of $P+1$ autocorrelation values for time lags 0 to P. The efficient Levinson-Durbin numerical algorithm is then used to obtain the whitest spectrum expressed as a rational function with P poles, which is consistent with the estimated autocorrelation values. The number of poles must be increased until the spectrum changes little, after which point the spectrum is judged to be realistic. Objective numerical criteria also exist [82] which try to select the necessary number of poles P to fit the data, also called the correct model order. The computation time for the

maximum entropy method depends on the number of poles, and is typically up to ten times longer than for the fast Fourier transform of the same length of data.

8.5 Measurements of laser spectra

In Fig. (8-8), a test signal was generated by using two single mode 1.55μm distributed feedback laser diodes, with lasing wavelengths separated by 12.9 nm, as the two inputs to the fiber coupler. The dotted line is the 2^{15}–point fast Fourier transform spectrum obtained by padding the measured 2450 data points with zeros. The solid line is the maximum entropy spectrum for 700 poles. The top figure shows the trace obtained using an Anritsu MS9701B optical spectrum analyzer. The fast Fourier spectrum shows side lobes due to the windowing effect, and it is clear that modes spaced less than 10 nm apart will be difficult to resolve using this method. The maximum entropy spectrum did not change significantly when the selected number of poles was between 400 and the maximum possible value of 2450, and the spectrum agrees well with the optical spectrum analyzer trace.

A second test signal was generated, this time using in one arm of the coupler, a two-moded uniform distributed feedback laser diode, with a 2.7 nm mode separation, and in the other arm of the fiber-coupler, a single moded distributed feedback laser diode. The top of Fig. (8-9) shows the trace obtained using the Anritsu optical spectrum analyzer, while the curve below is the maximum entropy spectrum with 2400 poles. The spectrum of the two-moded laser is clearly resolved. The spacings between the modes using the maximum entropy method are 2.4 and 8.7 nm, and compare with 2.8 and 7.6 using the commercial spectrum analyzer. The discrepancies in wavelength and modal power may be attributed to measurement noise, due, for instance, to the 8-bit quantizing of the digital storage adapter, and other distortions. More than 1800 poles were needed for the maximum entropy method to resolve the three modes, out of a maximum possible of 2450 (corresponding to the number of data points). This indicates that a resolution of about 2 nm is close to the limits of the initial instrument.

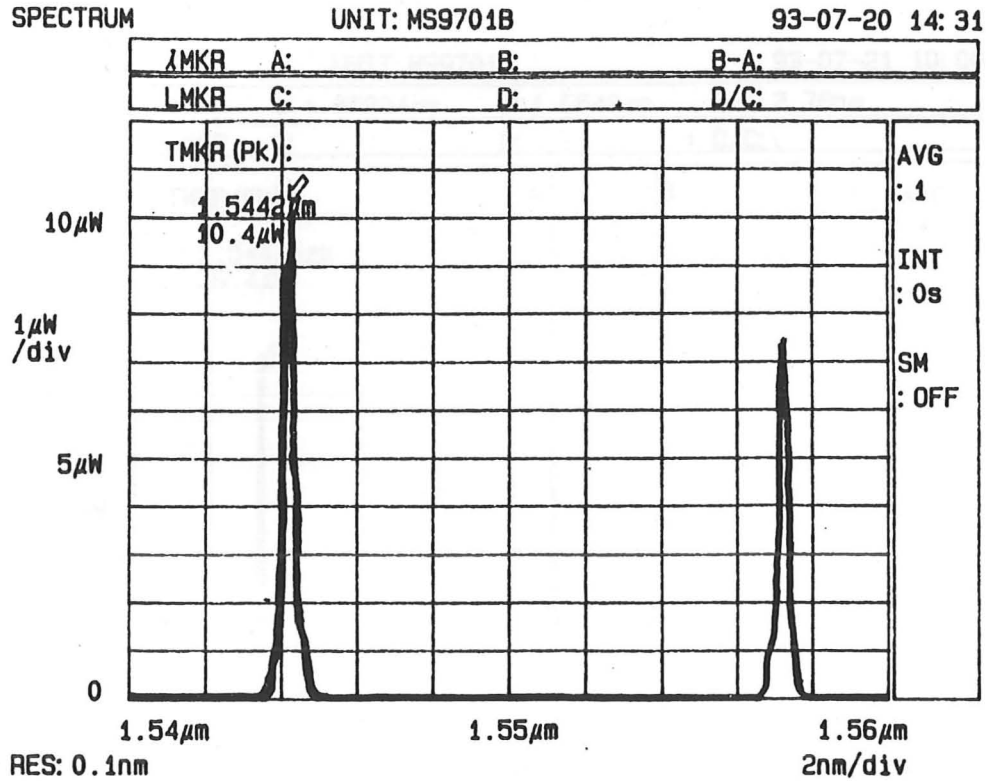

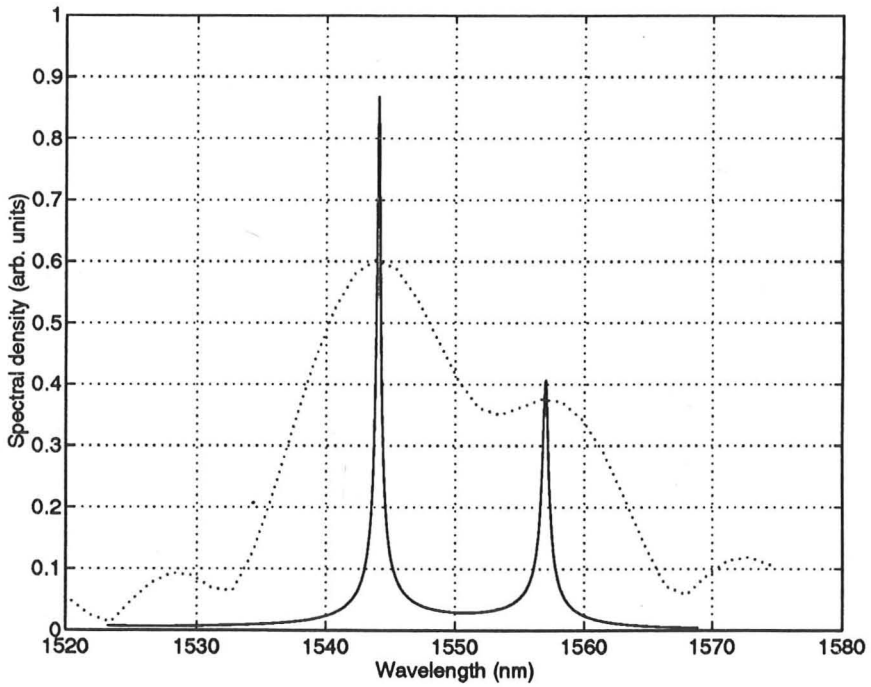

Figure 8-8: Comparison of maximum entropy method (solid), fast Fourier transform method (dotted) and commercial spectrum analyzer (above) spectra for a test signal consisting of the superposition of two single mode distributed feedback laser diode signals, 12.9 nm apart.

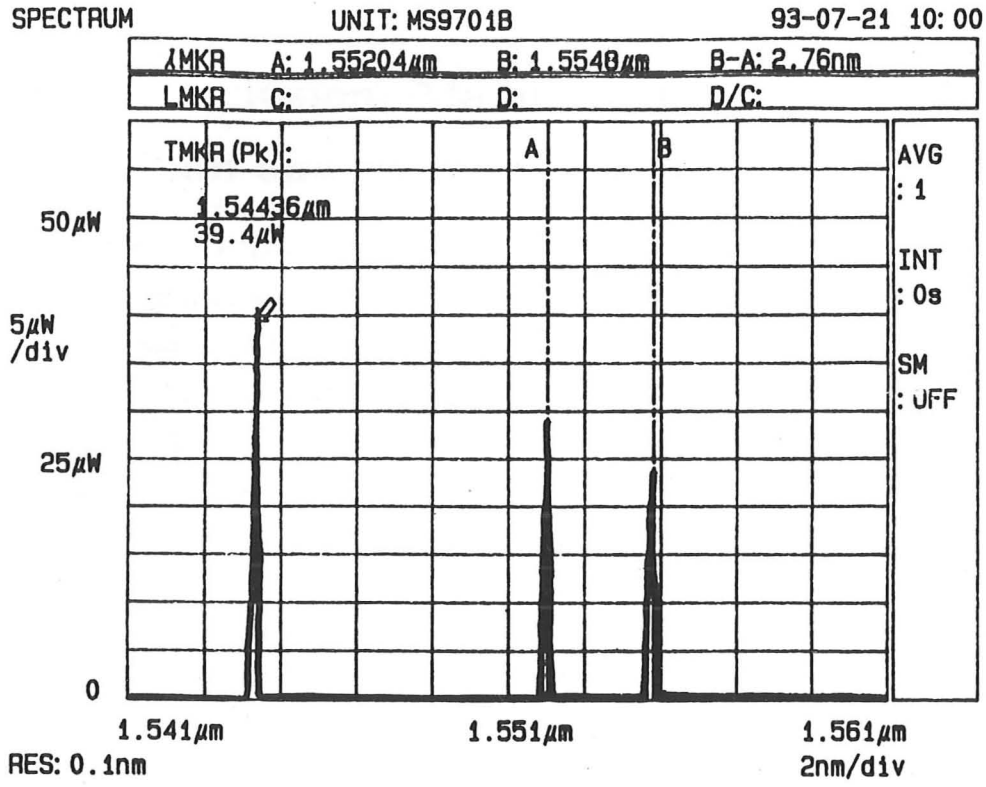

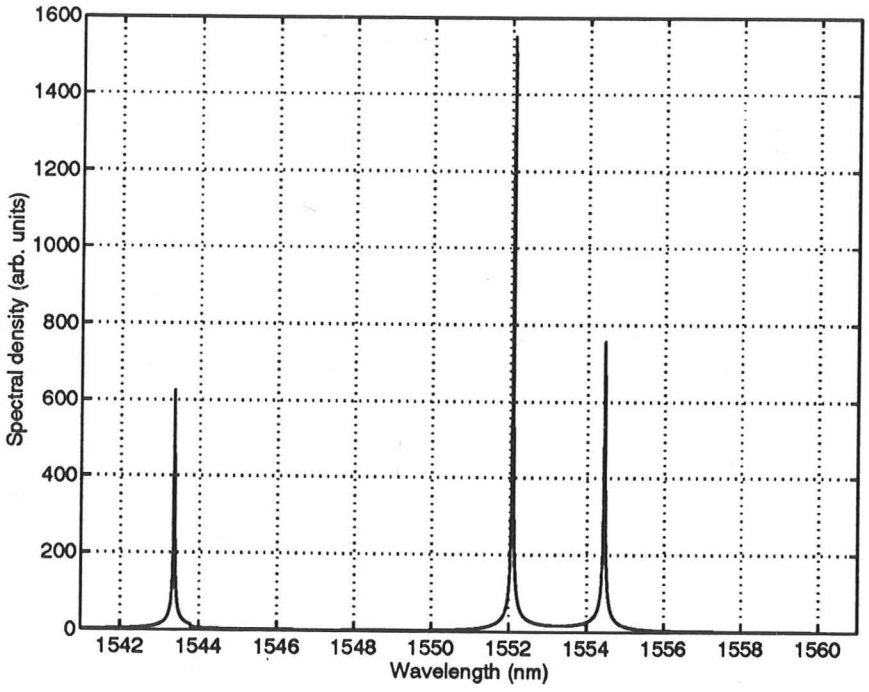

Figure 8-9: Maximum entropy method and commercial spectrum analyser trace (above) for a test signal made up of one single mode and one double mode distributed feedback laser.

8.6 Conclusion: Maximum entropy optical spectrum analyzer.

A new type of optical spectrum analyzer was demonstrated experimentally. The initial design presented here had a resolution just sufficient to measure the spectrum of a two moded DFB laser diode.

The instrument is potentially simpler and more robust than the spectrometers using monochromators, which are widely used in optical communications research laboratories. It does not require any moving parts, and provided the infra-red camera was replaced by a detector like a Charge Coupled Device array, it would be made entirely of solid state components whose performances continually improve while their prices keep decreasing. With an improved design, the resolution of the instrument could match that of commercial spectrum analysers. With the possibility of using software to compensate for distortions, after an initial set of calibrations, the manufacturing precision would need not be very high. The instrument is potentially a lower cost alternative to the present monochromator-based optical spectrum analysers.

However, a number of improvements are imperative before the instrument could become a commercial product. A resolution of 0.1 nm and a dynamic range of 30dB 0.5 nm from the peak would typically be required. In the present implementation, the resolution of the infra-red camera, and the noise due to digitizing (the digital storage oscilloscope used 8 bits per sample) and to the background radiation were two major factors limiting the resolution of our instrument. By using a detector with more lines horizontally (such as a long linear CCD array, capable of recording 1000 diffraction fringes), digitizing the signal with a 12 bit precision, and enclosing the instrument to shield from background radiation, the performance could be improved to meet the specifications.

Chapter 9

Conclusion

A set of new laser diode simulation tools, a discussion and some novel simulations of the intensity noise of laser diodes, and the experimental demonstration of a new type of optical spectrometer, were presented in this dissertation.

Modelling tools

The new time domain model presented in Chapters 2 and 3 was based upon quantum theory, to see whether the noise treatment of current semiclassical models (e.g. [23, 110]) could be improved. It is found that the semiclassical models are in agreement with quantum theory and with the time domain model presented here, as long as one does not try to simulate lasers whose drive current has sub-shot noise fluctuations. This is because the optical output could then exhibit sub-Poissonian photon statistics, and could not be simulated by semiclassical models.

The time-domain algorithm (first used for laser diodes by Lowery [21]) is used to implement the model in Chapter 3, and it allows strongly multimoded laser diodes and large-signal dynamic responses to be simulated. Improvements in the time-domain algorithm were presented in Chapter 3, consisting of the use of complex, instead of real, sampled optical fields, and of a transfer matrix method for DFB gratings. These improvements provide a greater accuracy and faster simulations. They enable simulations to be carried out in minutes, typically, on a desktop computer, making the model a powerful and interactive tool for researching and designing laser diodes.

The optical spectrum of laser sources is of great importance for optical fibre communications. The time domain model allows the detailed modelling of the spectral characteristics of laser diodes, but the spectral information in the output of the

model is not directly available. To extract this spectral information, Chapter 4 presented new applications of two spectral numerical methods: the Wigner distribution, and the maximum entropy method of spectral estimation. The Wigner distribution was found to provide the time-frequency representation of the optical fields with the highest combined resolution, an improvement on the methods used up till then. It was also suggested that the Wigner distribution could be used to enhance the time-frequency resolution of experimental chirp measurements, by deconvolution of the spectrometer's response. The maximum entropy method was found to display the static optical spectra of simulated laser diodes with a reduced noise and lower windowing effects, thus preventing the small features of the simulated optical spectra from being obscured.

Chapters 5 and 6 presented comparisons of the time domain model with other simulations and with experimental results. The first detailed comparison of simulations for multimoded DFB lasers under large signal modulation, was reported in Chapter 5. There, the time-domain model was found to agree closely with the Power Matrix Method, increasing our confidence in the simulations by these two very different large signal models. The second comparison, with the results reported by the COST laser modelling workshop, further increased confidence in the accuracy of the improved time-domain algorithm, and showed good agreement in noise calculations with models like CLADISS [23]. Reported experimental results, concerning self-pulsating DFB laser diodes, were then simulated in detail, for the first time, using the time domain model. Good qualitative agreement was found, highlighting the potential of this model for aiding research into the complex behaviour of DFB lasers.

Intensity noise

The quantum basis of the time-domain model presented in Chapters 2 and 3 showed that semiclassical models could not simulate the light output with sub-shot noise intensity fluctuations (squeezed light), which has been demonstrated experimentally [33]. In Chapter 7, a tentative new formalism, *enabling* the simulation of squeezed light in laser diodes, was presented. This new formalism permits more accurate calculations of intensity noise, and provides a better understanding of the effect of the laser structure on intensity fluctuations.

Simulation results were presented for a variety of laser structures. These indicated that DFB lasers were unlikely to be the sources with the lowest Relative Inten-

sity Noise. Another prediction is that intensity squeezing is *impossible* in symmetric Fabry-Perot lasers with facet power reflectivities below about 0.3, even with reduced waveguide losses. Analytic expressions for the intensity noise in simple Fabry-Perot lasers were derived, showing that this new formalism agreed with recent independent work by other researchers [112], who used a very different formalism.

Maximum Entropy Spectrum Analyzer

A new type of spectrometer using the maximum entropy method was presented. The apparatus was demonstrated experimentally and had a resolution sufficient to show the spectrum of a two moded DFB laser. With some design improvements, its spectral resolution and dynamic range could be improved to meet the specifications required for a useful commercial product. Composed entirely of solid-state components with no moving parts, the resulting instrument could be more robust and cheaper than spectrometers which use diffraction gratings. The building of the prototype for a commercial instrument could be the subject of future work.

Bibliography

[1] H. Statz and G. DeMars. Transients and oscillation pulses in masers. In C.H. Townes, editor, *Quantum Electronics*, pages 530–537, New York, 1960. Columbia University Press.

[2] R.S. Tucker and I.P. Kaminow. High-frequency characteristics of directly modulated InGaAsP ridge waveguide and burried heterostrucutre lasers. *J. Lightwave Tech.*, 2(4):385–393, 1984.

[3] M. Osinski and M. J. Adams. Transient time-averaged spectra of rapidly modulated semiconductor lasers. *IEE Proceedings:J-Optoelectronics*, 132(1):34–37, 1985.

[4] R. Nagaranjan, T. Fukushima, S.W. Corzine, and J.E. Bowers. Effects of carrrier transport on high-speed quantum well lasers. *Appl. Phys. Lett.*, 59(14):1835–1837, 1991.

[5] K. Shimoda, H. Takahashi, and C.H. Townes. Fluctuations in amplification of quanta with application to maser amplifiers. *Proc. Phys. Soc. Japan*, 12:686–700, 1957.

[6] D.E. McCumber. Intensity fluctations in lasers. *Phys. Rev.*, 141(1):306–322, 1966.

[7] M. Sargent III, M.O. Scully, and W.E. Lamb, Jr. *Laser Physics.* Addison Wesley (Reading Mass.), 1974.

[8] M. Lax. Classical noise V: Noise in self sustained oscillators. *Phys. Rev.*, 160(5):290, 1967.

[9] H. Haken. The semiclassical and quantum theory of the laser. *In Kay & Maitland, Eds.,* Quantum Optics, *Academic Press, London*, pages 201–321, 1970.

[10] W.H. Louisell. *Quantum Statistical Properties of Radiation.* John Wiley & Sons (New York), 1973.

[11] C.W. Gardiner. *Quantum Noise.* Springer-Verlag, Berlin, 1992.

[12] H. Dekker. Classical and quantum mechanics of the damped harmonic oscillator. *Physics Reports*, 80(1):1–112, 1981.

[13] D. Marcuse. Computer simulation of laser photon fluctuations: Theory of the single-cavity laser. *IEEE J. Quantum Electron.*, QE-20(10):1139–1148, 1984.

[14] C.H. Henry. Theory of the phase noise and power spectrum of a single mode injection laser. *IEEE J. Quantum Electron.*, QE-19(9):1391–1397, 1983.

[15] C.R. Mirasso, P. Colet, and M. S. Miguel. Dependence of timing jitter on bias level for single mode semiconductor laser under high speed modulation. *IEEE J. Quantum Electron.*, 29(1):23–32, 1993.

[16] K. Petermann. Calculated spontaneous emission factor for double heterostructure injection lasers with gain induced mode guiding. *IEEE J. Quantum Electron.*, QE-15(7):566–570, 1979.

[17] J. Arnaud. Natural linewidth of anisotropic lasers. *Opt. Quantum Electron.*, 18:335–343, 1985.

[18] S. Wang. Principles of distributed feedback and distributed Bragg-reflector lasers. *IEEE J. Quantum Electron.*, QE-10(4):413–427, 1974.

[19] H. Soda and H. Imai. Analysis of the spectrum behavior below the threshold in DFB lasers. *IEEE J. Quantum Electron.*, QE-22(5):637–641, 1986.

[20] G. Björk and O. Nilsson. A tool to calculate the linewidth of complicated semiconductor lasers. *IEEE J. Quantum Electron.*, QE-23(8):1303–1313, 1987.

[21] A.J. Lowery. New dynamic semiconductor laser model based on the transmission-line modelling method. *IEE Proceedings : J-Optoelectronics*, 134(5):281–289, 1987.

[22] T. Makino and J. Glinski. Transfer matrix analysis of the amplified spontaneous emission of DFB semiconductor laser amplifiers. *IEEE J. Quantum Electron.*, 24(8):1507–1518, 1988.

[23] P. Vankwikelberge, G. Morthier, and R. Baets. CLADISS–a longitudinal multimode model for the analysis of the static, dynamic, and stochastic behavior of diode lasers with distributed feedback. *IEEE J. Quantum Electron.*, 26(10):1728–1741, 1990.

[24] M. Lax. Fluctuations and coherence phenomena in quantum optics. In M. Chretien, E.P. Gross, and S. Deser, editors, *Brandeis Summer Institute in Theoretical Physics*, volume 2, pages 269–459. Gordon & Breach, N.Y., 1966.

[25] C.H. Henry. Theory of the linewidth of semiconductor lasers. *IEEE J. Quantum Electron.*, QE-18(2):259–264, 1982.

[26] K. Ujihara. Phase noise with output coupling. *IEEE J. Quantum Electron.*, QE-20(7):814–818, 1984.

[27] C.H. Henry. Theory of spontaneous emission noise in open resonators and its application to lasers and optical amplifiers. *J. Lightwave technology*, 4(3):288–297, 1986.

[28] A.E. Siegman. Excess spontaneous emission in non-hermitian optical-systems .1. laser-amplifiers. *Phys. Rev. A*, 39(3):1253–1263, 1989.

[29] A.E. Siegman. Excess spontaneous emission in non-hermitian optical-systems .2. laser-oscillators. *Phys. Rev. A*, 39(3):1264–1268, 1989.

[30] W.A. Hamel and J.P. Woerdman. Nonorthogonality of the longitudinal eigenmodes of a laser. *Phys. Rev. A*, 40(5):2785–2787, 1989.

[31] L.M. Zhang and J.E. Carroll. Large-signal dynamic model of the DFB laser. *IEEE J. Quantum Electron.*, 28(3):604–611, 1992.

[32] J.E.A. Whiteaway, G.H.B. Thompson, A.J. Collar, and C.J. Armistead. The design and assessment of $\lambda/4$ phase-shifted DFB laser structures. *IEEE J. Quantum electron.*, 25(6):1261–1279, 1989.

[33] Y. Yamamoto and N. Imoto. Internal and external field fluctuations of a laser oscillator: Part I-quantum mechanical Langevin treatment. *IEEE J. Quantum Electronics*, QE-22(10):2032–2042, 1986.

[34] G. H. B. Thompson. *Physics of Semiconductor Laser Devices.* John Wiley and Sons, New York, 1980.

[35] R. P. Feynman, R. B. Leighton, and M. Sands. *The Feynman lectures on physics*, volume II. Addison-Wesley, Reading, Mass., 1964.

[36] G.P. Agrawal and N.K. Dutta. *Long Wavelength Semiconductor Lasers.* Van Nostrand Reinhold (New York), 1986.

[37] B. Hüttner and S.M. Barnett. Dispersion and loss in a Hopfield dielectric. *Europhysics Letters*, 18(6):487–492, 1992.

[38] B. Hüttner, J.J. Baumberg, and S.M. Barnett. Canonical quantization of light in a linear dielectric. *Europhysics Letters*, 16(2):177–182, 1991.

[39] K.J. Blow, R. Loudon, S.J.D. Phoenix, and T.J. Shepherd. Continuum fields in quantum optics. *Phys. Rev. A*, 42(7):4102–4113, 1990.

[40] L.I. Schiff. *Quantum Mechanics.* MacGraw-Hill (New York), 1968.

[41] I. Abram and E. Cohen. Quantum theory for light propagation in a nonlinear effective medium. *Phys. Rev. A*, 44(1):500–517, 1991.

[42] R.J. Glauber. The theory of optical coherence. *Phys. Rev.*, 130(6):2529–2539, 1963.

[43] H.A. Haus. *Fields and waves in optoelectronics.* Mc Graw-Hill (New York), 1989.

[44] M. Ley and R. Loudon. Quantum theory of high-resolution length measurement with a Fabry-Perot interferometer. *J. Mod. Optics*, 34(2):227–255, 1987.

[45] K. Ujihara. Quantum theory of one-dimensional optical cavity with output coupling. Field quantization. *Phys. Rev.*, A12:148–158, 1972.

[46] K. Ujihara. Quantum theory of one-dimensional optical cavity with output coupling — V: Spontaneous emission. *IEEE J. Quantum Electron.*, 24(7):1367–1375, 1988.

[47] R. Loudon. Discrete-mode theory of quantum-optical processing. In Vilaseca and Corbalan [117], pages 2–13.

[48] J.R. Jeffers, R. Loudon, K.J. Blow, and S.J.D. Phoenix. Continuous-mode theory of quantum-optical processing. In Vilaseca and Corbalan [117], pages 14–26.

[49] R.J. Glauber. Amplifiers, attenuators, and the quantum theory of measurement. In E.R. Pike and S. Sarkar, editors, *Frontiers in Quantum Optics*, page 534. Adam Hilger, Bristol & Boston, 1986.

[50] R.J. Glauber. Coherent and incoherent states of the radiation field. *Phys. Rev.*, 131(6):2766–2788, 1963.

[51] R. Loudon. *The Quantum Theory of Light.* Clarendon Press (Oxford), 1983.

[52] Y. Yamamoto, S. Machida, and O. Nilsson. Squeezed state generation by semiconductor lasers. In Y. Yamamoto, editor, *Coherence, Amplification and Quantum effects in Semiconductor Lasers*, chapter 11, pages 461–538. John Wiley & Sons (New York), 1991.

[53] L.D. Landau and E.M. Lifshitz. *Electrodynamics of Continuous Media.* Addison-Wesley (Reading, Mass.), 1960.

[54] A. Yariv. *Optical Electronics (4th ed.).* Saunders College Publishing (Philadelphia), 1991.

[55] A.J. Lowery. Model for multimode picosecond dynamic laser chirp based on transmission line laser model. *IEE Proc. : J-Optoelectronics*, 135(2):126, 1988.

[56] H.A. Haus and S. Kawakami. On the "excess spontaneous emission factor" in gain-guided laser amplifiers. *IEEE J. Quantum. Electron.*, 21(1):63–69, 1985.

[57] I. H. Deutsch, J. C. Garrison, and E. M. Wright. Excess noise in gain-guided amplifiers. *J. Opt. Soc. Am. B*, 8(6):1244–1251, June 1991.

[58] J.P. Curtis and J.E. Carroll. Autocorrelation systems for the measurement of picosecond pulses from injection lasers. *Int. J. Electronics*, 60(1):87–111, 1986.

[59] E.P. Ippen, D.J. Eilenberger, and R.W. Dixon. Picosecond pulse generation by passive mode locking of diode lasers. *Appl. Phys. Lett.*, 37(3):267–269, 1980.

[60] H. Kogelnik and C.V. Shank. Coupled-wave theory of distributed feedback lasers. *J. Appl. Phys.*, 43(5):2327–2335, 1972.

[61] J.E.A. Whiteaway, B. Garrett, G.H.B. Thompson, A.J. Collar, C.J. Armistead, and M.J. Fice. The static and dynamic characteristics of single and multiple phase-shifted DFB laser structures. *IEEE J. Quantum Electron.*, 28(5):1277–1293, 1992.

[62] M Hillery, R.F. O'Connell, M.O. Scully, and E.P. Wigner. Distribution functions in physics: Fundamentals. *Phys. Rep.*, 106(3):121–167, 1984.

[63] T.C.A.M. Claasen and W.F.G. Mecklenbrauker. The Wigner distribution – a tool for time-frequency signal analysis: .1. continous time signals. *Philips Journ. of Research*, 35(3):217–250, 1980.

[64] N. Yen. Time and frequency representation of acoustic signals by means of the Wigner distribution function: Implementation and interpretation. *J. Acoust. Soc. Am.*, 81(6):1841–1850, 1987.

[65] T.C.A.M. Claasen and W.F.G. Mecklenbrauker. The Wigner distribution – a tool for time-frequency signal analysis:.2. discrete-time signals. *Philips Journ. of Research*, 35(4-5):276–300, 1980.

[66] T.C.A.M. Claasen and W.F.G. Mecklenbrauker. The Wigner distribution – a tool for time-frequency signal analysis: .3. relations with other time-frequency signal transformations. *Philips Journ. of Research*, 35(6):372–389, 1980.

[67] J.A. Johnston. Wigner distribution and FM radar signal-design. *IEE Proc. F: Radar and Signal Processing*, 136(2):81–87, 1989.

[68] K.H. Brenner and K. Wodkiewicz. The time-dependent physical spectrum of light and the Wigner distribution function. *Optics Commun.*, 43(2):103–106, 1982.

[69] M.I. Skolnik. *Radar Handbook.* McGraw-Hill, New York, 1970.

[70] K.H. Brenner and A.W. Lohmann. Wigner distribution function display of complex 1-D signals. *Optics Commun.*, 42(5):310–314, 1982.

[71] P.C. Sun and Y. Fainman. Real-time generation of the Wigner distribution of complex functions using phase conjugation in photorefractive materials. *Optics Lett.*, 15(17):941–943, 1990.

[72] P.T. Johnson. *Spectral Correlation of Semiconductor Lasers.* PhD thesis, Cambridge University, 1990.

[73] J. Ville. Théorie et applications de la notion de signal analytique. *Cables et Transmissions*, 2A:61–74, 1948.

[74] S.S. Abeysekera. Computation of the Wigner-Ville distribution for complex data. *Electron. Lett.*, 26(16):1315–1316, 1990.

[75] A.J. Lowery. Transmission-line laser modelling of semiconductor laser amplified optical communication systems. *IEE Proceedings: J-Optoelectronics*, 139(3):180–188, 1992.

[76] L. Cohen and T. E. Posch. Positive time-frequency distribution functions. *IEEE Trans. Acoustics, Speech and Signal Proc.*, ASSP-33(1):31–38, 1985.

[77] C. H. Page. Instantaneous power spectra. *J. Appl. Phys.*, 23(1):103–106, 1952.

[78] R. Gase and M. Schubert. Time-dependent spectra of ultra-short laser pulses. *Optica Acta*, 30(8):1125–1138, 1983.

[79] R. Gase. Time-dependent spectrum of linear optical systems. *J. Opt. Soc. Am. A*, 8(6):850–859, 1991.

[80] R. G. Baraniuk and D. L. Jones. A signal-dependent time-frequency representation: Optimal kernel design. *IEEE Trans. Signal Proc.*, 41(4):1589–1601, 1993.

[81] J.P. Burg. Maximum entropy spectral analysis. *Proc. 37th Meeting Society of Exploration Geophysicists*, (Oklahoma City), 1967. Reprinted in "Modern Spectrum Analysis", D. G. Childers, IEEE Press, 1978.

[82] S.M Kay and S.L Marple. Spectrum analysis – a modern perspective. *Proc. IEEE*, 69(11):1380–1419, 1981.

[83] E.T. Jaynes. On the rationale of maximum-entropy methods. *Proc. IEEE*, 70(9):939–952, 1982.

[84] J. Durbin. The fitting of time-series models. *Rev. Inst. Int. de Stat.*, 28:233–244, 1960.

[85] P.M.T Broersen and H.E. Wensink. On finite sample theory for autoregressive model order selection. *IEEE Trans. Signal Proc.*, 41(1):194–204, 1993.

[86] R. Schatz. Longitudinal spatial instability in symmetric semiconductor lasers due to spatial hole burning. *IEEE J. Quantum Electron.*, 28(6):1443–1449, 1992.

[87] X. Pan, H. Olesen, and B. Tromborg. Influence of nonlinear gain on DFB laser linewidth. *Electron. Lett.*, 26(14):1074–1076, 1990.

[88] H. Olesen, B. Tromborg, H. E. Lassen, and X. Pan. Mode instability and linewidth rebroadening in DFB lasers. *Electron. Lett.*, 28(5):444–446, 1992.

[89] M. Möhrle, U. Feiste, J. Hörer, R. Molt, and B. Sartorius. Gigahertz self-pulsation in 1.5 μm wavelength multisection DFB lasers. *IEEE Photon. Tech. Lett.*, 4(9):976–978, 1992.

[90] D. J. As, R. Eggemann, U. Feiste, M. Möhrle, E. Patzak, and K. Weich. Clock recovery based on a new type of selfpulsation in a 1.5μm two-section InGaAsP-InP DFB laser. *Electron. Lett.*, 29(2):141–142, 1993.

[91] M. Jinno and T. Matsumoto. All-optical timing extraction using a 1.5μm self pulsating multielectrode DFB LD. *Electron. Lett.*, 24(23):1426–1427, 1988.

[92] P.E. Barnsley and H.J. Wickes. All-optical clock recovery form 2.5 Gbits/s NRZ data using selfpulsating 1.58μm laser diode. *Electron. Lett.*, 28(1):4–6, 1992.

[93] P. E. Barnsley. NRZ format all-optical clock extraction at 3.2 Gbit/s using two-contact semiconductor devices. *Electron. Lett.*, 28(13):1253–1255, 1992.

[94] M. Ueno and R. Lang. Conditions for self-sustained pulsation and bistability in semiconductor lasers. *J. Appl. Phys.*, 58(4):1689–1691, 1985.

[95] U. Bandelow, H. J. Wünsche, and H. Wenzel. Theory of selfpulsations in two-section DFB laser diodes. *IEEE Photon. Tech. Lett.*, (To be published), 1993.

[96] K. Petermann. *Laser diode modulation and noise.* Kluwer Academic Publishers, Tokyo, 1988.

[97] J. Bergou, L. Davidovich, M. Orszag, C. Benkert, M. Hillery, and M.O. Scully. Role of pumping statistics in maser and laser dynamics: Density matrix approach. *Phys. Rev. A*, 40(9):5073–5080, 1989.

[98] W. H. Richardson and R. M. Shelby. Nonclassical states of light from a semiconductor laser operating at 4-K. *Phys. Rev. Lett.*, 64:400–403, 1990.

[99] M. Xiao, W. Ling-An, and H.J. Kimble. Detection of amplitude modulation with squeezed light for sensitivity beyond the shot noise limit. *Optics Letters*, 13(6):476–478, 1988.

[100] Y. Lai, H.A. Haus, and Y. Yamamoto. Squeezed vacuum from amplitude squeezed states. *Optics Letters*, 16:1517–1519, 1991.

[101] P. Grangier. Spectroscopy squeezed beyond the shot-noise limit. *Physics World*, 5(8):18–19, 1992.

[102] B. Saleh and M. Teich. Information transmission with photon-number-squeezed light. *Proc. IEEE*, 80(3):451–460, 1992.

[103] Y. Yamamoto and H.A. Haus. Preparation, measurement and information capacity of optical quantum states. *Rev. Mod. Phys.*, 58:1001–1020, 1986.

[104] M. J. Freeman, H. Wang, D.G. Steel, R. Craig, and D.R. Scifres. Amplitude-squeezed light from quantum-well lasers. *Optics Lett.*, 18(5):379–381, 1993.

[105] W.H. Richardson, S. Machida, and Y. Yamamoto. Squeezed photon number noise and sub-Poissonian electrical partition noise in a semiconductor laser. *Phys. Rev. Lett.*, 66:2867–2870, 1991.

[106] H. Wang, M. J. Freeman, D.G. Steel, R. Craig, and D.R. Scifres. Amplitude-squeezed light by injection-locking of quantum well lasers. *Postdeadline Papers, QELS'93, Baltimore, Maryland.*, paper QPD1-1/1, 1993.

[107] P.D. Drummond and C.W. Gardiner. Generalized P-representation in quantum optics. *J. Phys. A: Math. Gen.*, 13:2353–2368, 1980.

[108] A.J. Lowery, A. Keating, and C.N. Murtonen. Modelling the static and dynamic behavior of quarter-wave-shifted DFB lasers. *IEEE J. Quantum electron.*, 28(9):1874–1883, 1992.

[109] L.M. Zhang, S.F. Yu, M. Nowell, D.D. Marcenac, and J.E. Carroll. Dynamic analysis of radiation and side mode suppression in second order DFB lasers using time-domain large signal travelling wave model. *To be published, IEEE J. Quantum Electron.*, 1993.

[110] B. Tromborg, H. Olesen, and X. Pan. Theory of linewidth for multielectrode laser diodes with spatially distributed noise sources. *IEEE J. Quantum Electron.*, 27(2):178–192, 1991.

[111] D.D. Marcenac and J.E. Carroll. Quantum mechanical model for realistic Fabry-Perot lasers. *IEE proceedings: J-Optoelectronics*, 140(3):157–171, 1993.

[112] B. Tromborg, H. E. Lassen, and H. Olesen. Travelling wave analysis of semiconductor lasers: Modulation responses, mode stability and quantum mechanical treatment of noise spectra. *To be published, IEEE J. Quantum Electron.*, 1993.

[113] C.H. Henry. Phase noise in semiconductor lasers. *J. Lightwave tech.*, 4:298–311, 1986.

[114] G. F. Luff, P. J. Probert, and J. E. Carroll. Dual 7-port automatic network analyser with swept-frequency real-time response. *IEE Proc., Part A*, 134(7):587–594, 1987.

[115] G. F. Luff. *A real-time microwave network analyser using multiport techniques.* PhD thesis, Cambridge University Engineering Department, 1985.

[116] D. G. Childers, editor. *Modern Spectrum Analysis*, New York, 1978. IEEE Press.

[117] R. Vilaseca and R. Corbalan, editors. *Nonlinear Dynamics and Quantum Phenomena in Optical Systems.* Springer Verlag (Berlin), 1991.